SANDIA REPORT

SAND2007-0152
Unlimited Release
Printed September 2007

Sample Extraction and Injection with a Microscale Preconcentrator

Helena K. L. Chan and Alex L. Robinson

Approved for public release; further dissemination unlimited.

Sandia National Laboratories

Sample Extraction and Injection with a Microscale Preconcentrator

Helena K. L. Chan

Engineering Research Center for Wireless Integrated MicroSystems
The University of Michigan
Ann Arbor, MI 48109-2101

Alex L. Robinson
Advanced Sensor Technologies
P.O. Box 5800
Albuquerque, NM 87185-1425

Abstract

This report details the development of a microfabricated preconcentrator that functions as a fully integrated chemical extractor-injector for a microscale gas chromatograph (GC). The device enables parts-per-billion detection and quantitative analysis of volatile organic compounds (VOCs) in indoor air with size and power advantages over macro-scale systems. The 44 mm^3 preconcentrator extracts VOCs using highly adsorptive, granular forms of graphitized carbon black and carbon molecular sieves. The micron-sized silicon cavities have integrated heating and temperature sensing allowing low power, yet rapid heating to thermally desorb the collected VOCs (GC injection). The keys to device construction are a new adsorbent-solvent filling technique and solvent-tolerant wafer-level silicon-gold eutectic bonding technology. The product is the first granular adsorbent preconcentrator integrated at the wafer level. Other advantages include exhaustive VOC extraction and injection peak widths an order of magnitude narrower than predecessor prototypes.

A mass transfer model, the first for any microscale preconcentrator, is developed to describe both adsorption and desorption behaviors. The physically intuitive model uses implicit and explicit finite differences to numerically solve the required partial differential equations. The model is applied to the adsorption and desorption of decane at various concentrations to extract Langmuir adsorption isotherm parameters from effluent curve measurements where properties are unknown *a priori*.

3

Acknowledgements

Note: This report is a reprint of the doctoral dissertation submitted to the University of Michigan by Helena K. L. Chan in 2006. Alex L. Robinson served as the Laboratories-University liaison, and was not directly involved in performance of the work.

Contents

Appendix

Appendix

List of Figures

12

13

List of Tables

Chapter 1

INTRODUCTION

Air is essential for survival. Without it, a human being cannot remain conscious for more than a few minutes. It is hard to imagine something more immediately life-sustaining; yet the average adult and public health expert alike have little idea of what is in the $11,000\,\mathrm{L}$ of air that pass through a person's lungs, on average, in a single day. *What* is in the air—the public health effect of indoor air contaminants—provides the humanistic motivation for this thesis research. The scientific motivation comes from *how* to analyze complex constituents in air—the technique of gas chromatography. And finally, the pursuit of air analysis at the *microscale* is driven by a vision: to shrink a $10\,\mathrm{kg}$, $200\,\mathrm{W}$ laboratory system into a $<0.1\,\mathrm{kg}$, $10\,\mathrm{mW}$ on-site system, taking advantage of advanced silicon micromachining and integrated electronics technology.

This thesis is about a microscale preconcentrator that supports the vision of a monolithic, microscale gas chromatograph (μGC). The application of the μGC is real-time analysis of 30–40 trace-level, volatile organic compounds (VOCs) listed as indoor air contaminants by the United States Environmental Protection Agency (US EPA). The 10-year vision is to integrate the μGC with associated microprocessing and wireless data transmission capability to form a low-power ($10\,\mathrm{mW}$) wireless integrated microsystem (WIMS) [1]. The critical functions of the preconcentrator are to extract compounds at parts-per-billion (ppb) levels from air and inject them at parts-per-million (ppm) concentrations for separation and detection via the microcolumns and sensor arrays. VOC capture at ppb-levels and subsequent thermal desorption at higher ppm concentrations in μL volumes are prerequisite to μGC ppb detection limits and high separation efficiencies.

The hypothesis of this work is that the solution to sample extraction and injection for the WIMS μGC is a thermally desorbed, Si micromachined preconcentrator using granular carbon adsorbents. Intuitively, pursuing a preconcentrator of this type at the microscale offers the opportunity to take advantage of rapid integrated heating, temperature sensing, and low dead volume. To explore these advantages, this research follows two paths of inquiry that are interrelated: the first demonstrates the usefulness of the preconcentrator for real-time μGC; the second furthers the understanding of microscale materials and designs for packed-bed adsorbers.

Dissertation Approach

The contributions of this research can only be appreciated by understanding the following:

- Application - What do we build and why?
- Technology - How do we build it?
- Engineering - How do we make a better microdevice and model it?

This dissertation investigates each of these elements to elucidate the impact of this research on the field and to provide tools with which future researchers can use to build upon this work. This research is interdisciplinary, so we will not assume prior familiarity with specialized terminology. Our approach is to comment on application, technology, and engineering in roughly that order. Ideally, research would partition into the categories as neatly separated as the bullet points suggest; in practice, these elements confound each other.

The continuous fabric of application, technology, and engineering is what constitutes the intangible experience that we have gained while pursuing this research. To communicate the nuances of this work and to keep a lively discussion, we opt to move freely between them. In the end, our solution is to introduce concepts and mathematics along the way, in each chapter, rather than in a single chapter at the start, via a delivery devoid of context.

Contributions

As a preview of the chapters to come, these are the contributions of this work:

- A unique system-level analysis that interconnects the requirements of all the analytical components (sample capacity and chromatographic plate height).
- The first demonstration of dynamic, exhaustive extraction, preconcentration, and injection of trace-level VOCs with a preconcentrator.
- The development of wafer-scale quantitative adsorbent loading technology and solvent-tolerant wafer-level Au-Si eutectic bonding, enabling the first wafer-level integrated preconcentrator.
- The construction of the first physically-based model for micropreconcentrator extraction and injection.
- The first temperature-programmed micropreconcentrator effluent-curves for extraction of a material property using the newly developed device model.

In terms of usefulness to μGC, the microscale preconcentrator is the first of its kind to provide exhaustive extraction of ppb-level VOCs from air. It is also the first to successfully perform high concentration and narrow injections, truly applicable to real-time μGC. The broader contribution of this research to the field is the development of a physically intuitive microdevice model. Novel quantitative adsorbent loading technology facilitates material

and structural investigations, and the preconcentrator itself is used to probe physical properties of materials and models of microscale structures.

Chapter Outlines

Our ultimate goal is to comment on the fundamental operational limits of microscale packed-bed preconcentrators. The authority of our commentary is to be backed by empirical evidence from a novel microdevice, and each chapter signposts our way to this destination:

- Chapter 2 reviews the basics of gas chromatography and ends with an equation to describe the separation efficiency of the μGC.
- Chapter 3 puts this work into the context of VOC analysis using μGC, and describes the component-level architectural choices to satisfy the demands for functional microsystem integration.
- Chapter 4 explains the macroscale model and previous preconcentrators developed for VOC analysis. It also presents evidence that the macro- to microscale assumption does not work and outlines the resulting approach to tackle the gap in understanding for packed-bed microscale adsorbers.
- Technology development is given in Chapter 5.
- Chapter 6 is about system interfacing, with an emphasis on thermal isolation of the microdevice from its surroundings to lower its energy usage.
- Chapter 7 is a brief summary of the last half of the dissertation.
- The customized instrumentation that we have developed for microdevice characterization is the subject of Chapter 8.
- Chapter 9 presents the first model for a microscale preconcentrator, and it is based on a one-dimensional representation of the adsorbent bed.
- The experience that we have gained is put to work in Chapter 10 where we examine the prospect of a new microdevice that is both energy efficient and suitable for high-speed narrow-bore μGC.
- The dissertation concludes with a summary of contributions in Chapter 11.

Synopsis

For researchers who are familiar with VOC analysis or gas chromatography, this section is a brief synopsis of the progression of this work. This is the only aside in this dissertation where terminology is not introduced before use, and is included to provide an accelerated orientation for those already in the field.

The preconcentrator follows two of its Michigan predecessors in its approach of scaling down a granular-adsorbent capillary-tube preconcentrator to the microscale to achieve a

given capacity. Figure 1.1 shows the progression of preconcentrator research in this thesis. The ability to scale assumes that the adsorptive capacity model is valid in both the macro- and microscale domains, and to validate the model requires knowledge of the adsorbent mass inside the device. So until now, this assumption has not been questioned due to manufacturing limitations: prior microfabrication processes did not allow for the quantification of adsorbent mass in the device. The adsorbent mass was optimistically assumed to be correct, and the adsorptive capacity was not measured.

The present research begins by probing this macro- to microscale design assumption. Measurements of a microchannel prototype debunk the notion of macro- to microscale applicability for the adsorptive capacity model. With hindsight and data in hand, the reason is intuitively simple: the macroscale tube preconcentrator is a single long packed bed, while the microchannel prototype is many short variable flow restriction beds in parallel. Therefore, the effective adsorptive capacity of the device is reduced to the channels of least fluid resistance.

Without a valid capacity model, the two choices are to build a microscale device that looks more like a tube or to develop a new model for microscale devices. This research takes the average of these choices by implementing a design with cavities in series for adsorbents. This simpler configuration is used to investigate mass and heat transfer tradeoffs in preconcentrator operation. In addition, a new microfabrication technology of adsorbent-solvent loading is developed to know how much adsorbent is in each device. The loading technology enables batch fabrication, and for the first time, granular adsorbent preconcentrators are integrated at the wafer-level. With the adsorbent mass and integrated temperature sensors, we perform meaningful breakthrough measurements and develop a physically-intuitive model to describe the preconcentrator.

Thus, the cavity-based preconcentrator is used as a tool to understand material and microscale device properties and to provide arguments for a new vertical in-line packed-bed design. Rather than taking a macroscale design and geometrically shrinking it to the microscale, the new methodology is bottom-up, based on the knowledge that we have accumulated through this research.

Thesis Progression

Design

Empirical Adsorptive Capacity Model for Tubes

System, Application, and Technologically-Driven Specifications

Si Cavity Microheater, Heat Exchanger, and Variable Pressure Designs

Scaling

Wafer Bonding Technology

Si Cavity Microheater Preconcentrator

Fundamental Limits

Scaled Tube Model Not Applicable!

Quantitative Adsorbent Loading Technology

Thermodynamics

Adsorbent Properties
No implied time/length scales

$\Delta H_{ads} \rightarrow I^2 R\, t \rightarrow m\, C\, \Delta T \rightarrow \Delta H_{des}$

Kinetics

Rate Tradeoffs
Time/length dependent

$\partial T / \partial t$ vs. $\partial q / \partial t \rightarrow C(z,t)$

Future Generation

How to create an energy efficient structure?

How to select an operating point?

Si Inline Vacuum-Isolated Preconcentrator

Figure 1.1. Thesis research progression.

Chapter 2

PRELIMINARIES

Every field oscillates between dormant periods and noisy growth. During dormancy, a field subsists on incremental improvements, surviving in the background of its research world. The opposite occurs during growth: the Midas touch abounds. From monetary support to publications populating journals—everything is hot. Historically, research in new technology follows a progression: inventing, applying, and modelling. A useful physical understanding quantifies device operational limits and requires a deep and holistic view—from fundamental material properties to a device model. The power of quantified fundamental operational limits impels the progression to begin anew. What perturbs the field into noisy growth are the efforts of researchers to open the next stage in the progression, wherever the field resides. So the philosophical goal of this dissertation is twofold: to show breadth by explaining where the field is in the cycle, and to show depth by solving a difficult problem to propel the field forward.

The first step is this chapter on chromatography, meant to be a microcosm of the whole dissertation. The concepts and mathematics of gas chromatography (GC) introduced here are applicable to preconcentrators. And while the field of basic GC has stepped through the stages, from invention to physical modelling, the field of microscale preconcentration has not; microscale preconcentration resides in the application stage of development. Therefore, the great opportunity before us is to move preconcentrators from proof-of-concept application to a physical understanding of fundamental operational limits. To facilitate this move, we pursue two lines of thought and action: we bring together GC and preconcentrator theories to open a new phase of activity in models based on fundamental physical processes; and in parallel, we design and develop a new preconcentrator to quantify material and structural properties at the microscale.

Chromatography

Here we distill the essentials of chromatography and review the mathematical language for retention and dispersion useful for a unified discourse on μGC separation efficiency. During this discussion, there are two big-picture ideas to keep in mind. Chromatography is a method that uses *two phases* to *separate components* in a mixture; and separation occurs if the equilibrium constants between components are different [2] [3].
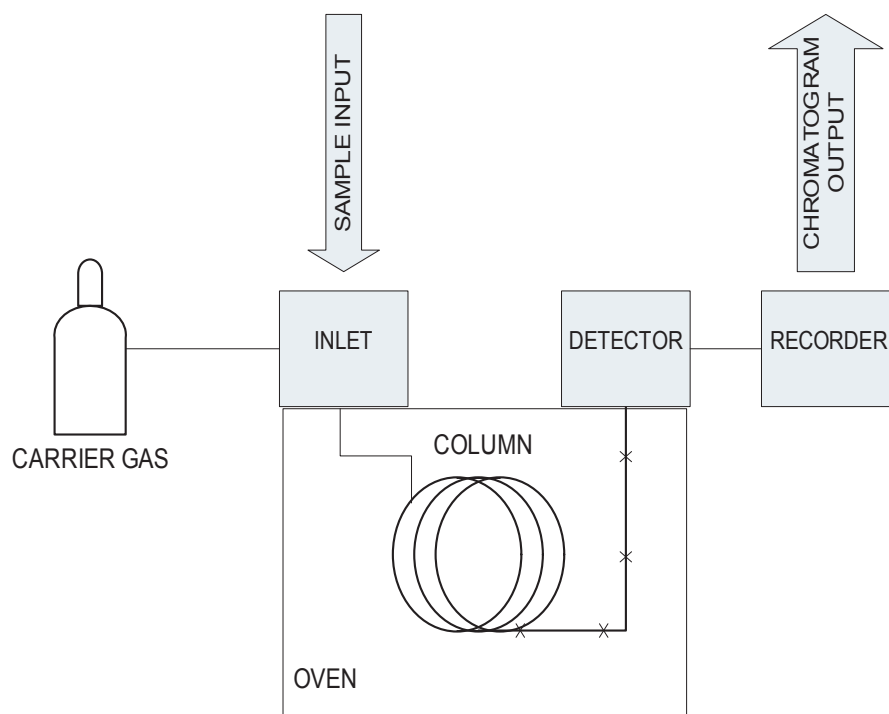
Figure 2.1. Schematic of a gas chromatograph.

Figure 2.1 shows the major parts of a gas chromatograph. In GC, the mixture is introduced at the inlet located on the front of the column and continuously pushed through the column by flowing carrier gas. There are many types of GC columns, and for the μGC we use a wall-coated open-tubular column (WCOT). With a WCOT column, the two phases are a carrier gas (mobile phase) and a liquid coating (stationary phase) on the column wall. The mobile phase brings the mixture components (solutes) in contact with the stationary phase so that gas-liquid interfacial interaction—called partitioning—occurs. The degree of partitioning between the solutes in the mobile and stationary phases characterizes its retention. A greater retention means that a solute spends more time "sticking" (or partitioning) to the stationary phase-coated wall. Therefore, a more highly retained solute emerges from the column later than one with less retention. And the result is that the solutes in the mixture separate as they travel along the column, finally exiting the end (eluting) at different times. The detector measures solute elution and the recorder plots the concentration as a function of time, giving a chromatogram of the separated components.

GC can be divided into two branches based on the scale and end-goal for separation: analytical chromatography for small-scale separation and quantification, and preparative chromatography for industrial-scale purification and refining. For WIMS we are concerned with analytical GC for VOC analysis. Analytical GC models are unlike those for preparative chromatography, that use high concentrations and a large mass of materials. The difference is that of linearity (for analytical chromatography) and nonlinearity (preparative chromatography) for the description of equilibrium between each component in the mobile phase and the stationary phase [2]. For now, we will focus on a linear idealized system description for analytical chromatography with μGC.

Retention explains how solute mixtures can separate if each constituent has a different affinity for the stationary phase. This is because each solute spends a different amount of time interacting with the stationary phase. The amount of retention is determined by the equilibrium thermodynamics of the solute-stationary phase pair. The distribution (partition) coefficient and the dependence of this coefficient on concentration for a fixed temperature (isotherm) fully characterize retention. The plate theory of chromatography described in the next section uses the assumption of equilibrium and retention to empirically model the shape of an elution curve.

However, retention alone is not enough. If it were, then any solute pair with differing retention could be separated with a sufficiently long column. In reality, while differences in retention act to move solutes apart, there also exist physical processes that act to merge the solute bands as they migrate down the column—sources of dispersion. Excessive band broadening can result in overlap and loss of chromatographic resolution. Therefore, the chromatographer's job is to balance the effects of retention and dispersion to achieve separation between solutes. Due to the limitations of empirical plate theory, physically-based models that account for both dispersion and retention will be discussed in the section on the rate theory of chromatography.
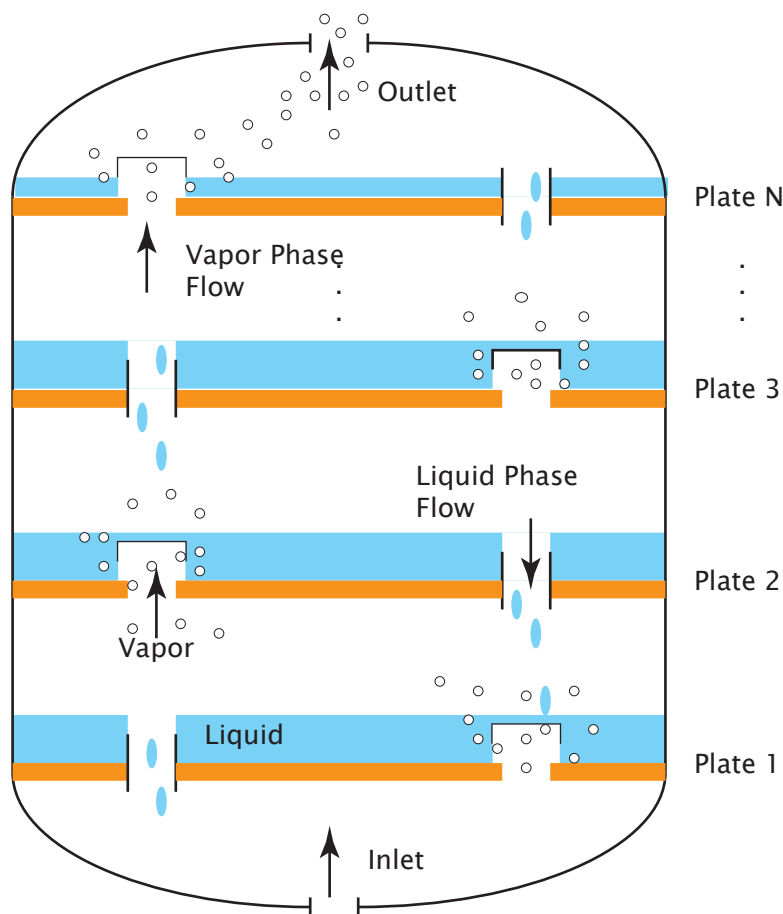
Figure 2.2. Diagram of a fractionating distillation column.

Plate Theory

The plate theory of chromatography has its roots in distillation columns [4] [5] [6]. We will trace plate theory to its origins in distillation to grasp its virtues and limitations, and to absorb the nomenclature inherited from it by modern gas chromatography. All of the assumptions for distillation plate theory remain the same for its application to GC.

In distillation, liquids are separated by their boiling points. A fractionating distillation column consists of a tower with a series of plates shown in Figure 2.2. The liquid mixture with components of similar boiling points is at the heated bottom. The lowest boiling point component vaporizes first, rising up through the plates and condensing on them. A tap at the top collects the distilled vapor by cooling it. The higher in the column a plate resides, the colder it is so that the vapor is purest at the top of the column; it follows that a taller column (greater number of plates) results in purer vapor.

Plate Height

The original purpose for plate theory was to calculate the column height (i.e., number of plates) to distill a set purity [4]. In 1922, W. K. Lewis computed the theoretical number of plates by considering the following: mass balance between adjacent plates (i.e., what vaporizes off a lower plate condenses on the adjacent upper one, and vice versa—what drips off the upper plate falls back down onto the lower plate), and *assume* equilibrium between the vapor and liquid phases on a plate. Though physically inaccurate, the assumption of equilibrium enables simple mathematics, and plate theory is useful as an empirical description of plate and overall column efficiency.

Lewis recognized that the assumption of equilibrium has no physical basis, and that the value of plate theory lies in its application to empirical data and designs based on measurements. This is best summed up in his own words [4]:

> It is obvious that in practice equilibrium will not be reached between vapor and liquid. The number of plates actually needed for a given enrichment divided into the number theoretically necessary according to these formulas may be called the plate efficiency of the column ... It is necessary only to determine from experimental operating data upon existing columns the influence upon k [plate efficiency] of type of plate, rate of flow of vapor and of reflux, etc., in order to be able to use these equations in problems of column design with safety and assurance.

That year, W. A. Peters measured several distillation columns, including a packed tower with no plates, to compare his data with the theoretical column efficiency calculated via Lewis' method [5]. In so doing, he coined the term "height of equivalent theoretical plate," modernly rephrased as height equivalent to a theoretical plate (HETP). For Peters' packed tower with no plates, the HETP described the section of packed material necessary to achieve the distillation power of a theoretical plate where equilibrium between vapor and liquid phases was assumed.

Today in gas chromatography, we use the number of plates N and HETP H to describe the separating power of a column. It is a useful empirical measure for the efficiency of a particular separation, and the number of plates is computed after recording a chromatogram. The greater the number of plates, the greater the separation efficiency so that highly complex mixtures can be analyzed. The relation between N and H is simple: $H = L/N$ where L is the length of the column.

Elution Profile

The object of distillation is to purify, while for analytical chromatography it is to separate for analysis. Analysis consists of measuring chromatograms: solute concentration versus

time as each component elutes from the column end. So for chromatography, the plate concept from distillation is of limited utility; a long column with many plates has higher separation efficiency, but nothing is said about the solute concentration profile emerging from the column end. This problem was solved by A. J. P. Martin and R. L. M. Synge in 1941.

The 1952 Nobel prize in chemistry was awarded to Martin and Synge for inventing partition chromatography. In their 1941 paper on liquid-liquid chromatography (one example of partition chromatography, another being WCOT GC) they took the plate concept of distillation to a new level [6]. Borrowing the ideas of mass balance, equilibrium between two phases—this time a liquid and a liquid—and HETP from distillation, they applied it to a *series* of successive "plates." Like Peters, there were no plates in their system, so they conceptualized a plate as an ideal mixing cell for the liquid-liquid phases. Their object was to describe the shape of an eluting band. Just as distillation plate theory assumed equilibrium between vapor and liquid phases, so too did they assume for mathematical purposes, equilibrium between their liquid solutes and liquid stationary phase. By considering a *large* number of plates, Martin and Synge formulated the band shape as a Poisson distribution.

A modern-day chromatogram is pictured in Figure 2.3. Retention time identifies components by their elution order, and the retention factor can be obtained from the chromatogram as:

$$k' = \frac{t_R - t_m}{t_m} \tag{2.1}$$

where the time for an unretained solute to elute from the column, called the hold-up time, is t_m, while the retention time is t_R. The definition of the retention factor is the ratio of the solute mass in the stationary phase to the mass in the mobile phase.

The peak width influences the resolution between adjacent peaks and the number of solutes that can be realistically separated (peak capacity). Finally, the area under the concentration curve gives the mass of solute.

The elution profile is the concentration at the Nth plate, and when the total number of plates is large, the Poisson distribution tends to a Gaussian [7]. The elution profile for the ith solute is:

$$C_i = C_{max} \exp\left(-\frac{X^2}{2\sigma^2}\right) \tag{2.2}$$

where C_{max} is the concentration at the peak maximum (a function of the initial pulse fed at the beginning of the column), the standard deviation is σ, and X is the difference from the peak maximum. This equation can be expressed equivalently in terms of plates, time, or length units as shown in Table 2.1. In the table, v is the dimensionless cumulative mobile phase volume, $t_{R,i}$ is the retention time of the ith solute, H is the plate height, L is the length of the column, and N is the number of plates.
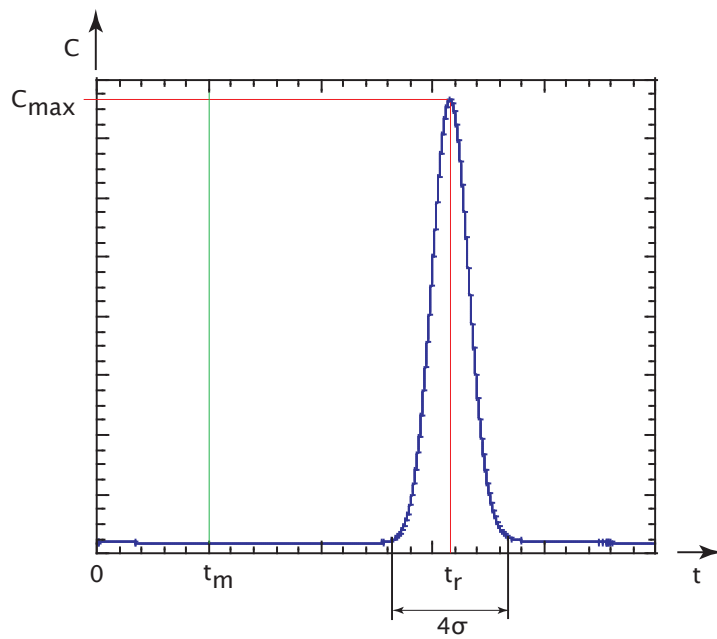
Figure 2.3. Example chromatogram illustrating the concepts of hold-up time of an unretained compound t_m, solute retention time t_r, baseline peak width 4σ, and peak concentration C_{max}.

Table 2.1. Gaussian Distribution Parameters for Plate Theory

Units	Dependent Variable	X	σ
Plates	v	$v - N$	$\sqrt{N}$
Time	t	$t - t_{R,i}$	$t_{R,i}\sqrt{\frac{H}{L}}$
Length	z	$z - L$	$\sqrt{HL}$

The concept of retention is embodied in v, which is the amount of mobile phase per plate required to push the solute to the end of the column. Intuitively this volume depends on how well the solute is retained in the column and increases with the retention factor k'.

Of great importance for separation is the width of the eluting band and the factors that contribute to band broadening. Ideally, two solutes with different retentions should separate due to equilibrium considerations, but in practice, band broadening can inhibit the resolution of the peaks. We have seen how the elution curve of plate theory accounts for flow velocity, retention, and number of plates. However, like distillation plate theory, chromatographic plate theory is limited in predictive power because of its dependence on the equilibrium assumption.

Martin and Synge, and later, James and Martin laid claim to the enormous swath of inventing, applying, and empirically modelling partition chromatography [8]. However, there still remained the need to have a physically-based model to optimize separations.

Rate Theory

Researchers recognized that the practical use of plate theory for optimizing separations was hampered by its lack of physical grounding. So in parallel with the development of separation techniques, others in the field worked on physical models—rate theory [9] [10].

Rate theory has replaced plate theory to model chromatographic systems. But as mentioned earlier, the terminology of plate theory is still what we use to describe column efficiency. Rate theory looks at both equilibria and kinetics: equilibrium isotherms and mass transfer rates. And the fundamental approach is to solve the differential mass balance equation for solutes in the mobile phase to obtain the elution profile.
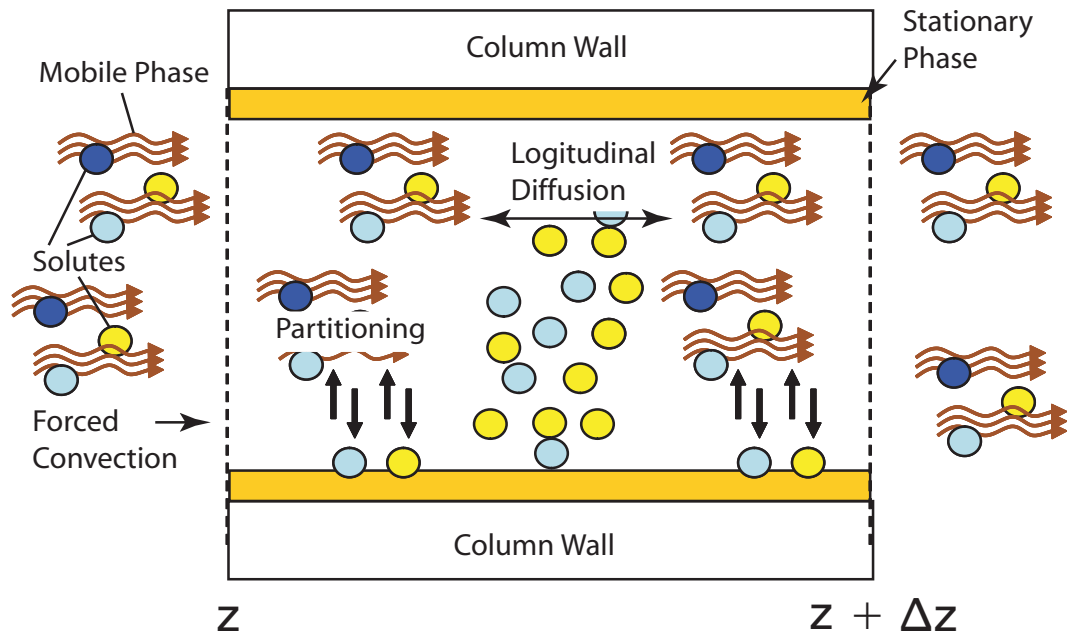
Figure 2.4. A differential length of column showing the mechanisms affecting the net number of solutes in the section; forced convection into and out of the section, free convection (dispersion) in the center of the section due to concentration gradients, and accumulation due to partitioning of solutes into and out of the stationary phase on the column wall.

Gas Phase Mass Balance

The mass balance equation is vital because it will model the preconcentrator in the chapters to come. The mass balance equation for the solutes travelling down a column has the same form as the equation of charge balance in a semiconductor encountered in solid-state electronics (e.g., for deriving the ideal diode equation). In this case, mass replaces charge, and generation/recombination is replaced by a partitioning term. The mechanisms affecting the gas phase solute concentration are illustrated in Figure 2.4.

Note the variety of symbols about to be used for solute concentrations:

- q is the instantaneous solute concentration in the stationary phase
- q^* is the value of q in equilibrium with the instantaneous solute concentration in the mobile phase, c
- $\bar{q}$ is the average value of q
- q_s is the saturation value of q
- c is the instantaneous solute concentration in the mobile phase

- c^* is the value of c in equilibrium with the instantaneous solute concentration in the stationary phase

Just as in the charge balance equation, the mass balance equation has a diffusion term (dispersion), a drift term (convection), and accumulation term (partitioning) as shown below [11]:

$$-D_L\frac{\partial^2 c}{\partial z^2} + \frac{\partial(uc)}{\partial z} + \frac{\partial \bar{q}}{\partial t} + \frac{\partial c}{\partial t} = 0 \tag{2.3}$$

where D_L is the longitudinal diffusion coefficient, c is the concentration of solute in the fluid phase (gaseous phase) [mol/cm^3], z is the coordinate along the length of the bed [cm], u is the interstitial fluid velocity [cm/s], $\bar{q}$ is the average solute sorbed into the stationary phase on the column wall [mol/cm^3], t is time [s].

To solve this equation requires additional relations for the partitioning term which is in general a function of the solute concentration in both the stationary and mobile phases: $\frac{\partial \bar{q}}{\partial t} = f(q, c)$. These relationships are the equilibrium and kinetic behaviors of the solute at the stationary phase-mobile phase interface. The equilibrium relationship between the concentrations in the stationary and mobile phases is given by the equilibrium isotherm, $q^* = f(c)$. And the kinetic behavior is described by a model for the *rate* of mass transfer between these two phases.

Figure 2.5 highlights the differences between analytical and preparative chromatography on several physical assumptions that affect modelling. In this work, we operate in the realm of analytical chromatography so that from now on, we will deal with a linear, isothermal system, with constant fluid velocity across the mass transfer zone. For information on models dealing with non-trace systems, the reader is referred to [11], [12], [13], [14].

A linear isotherm means that:

$$\frac{q^*}{q_s} = bc \tag{2.4}$$

where b is a proportionality constant (Henry's law constant at low concentrations). Physically, a linear isotherm means that the amount of solute in the stationary phase required for equilibrium increases linearly with mobile phase solute concentration.

For a WCOT column, we consider a single mass transfer resistance to encompass finite mass transfer rates in both the stationary and mobile phases:

$$\frac{\partial \bar{q}}{\partial t} = k(q^* - q) \tag{2.5}$$

where k is the mass transfer coefficient describing the rate of mass transfer. This equation means that the average change in stationary phase solute concentration is linearly propor-
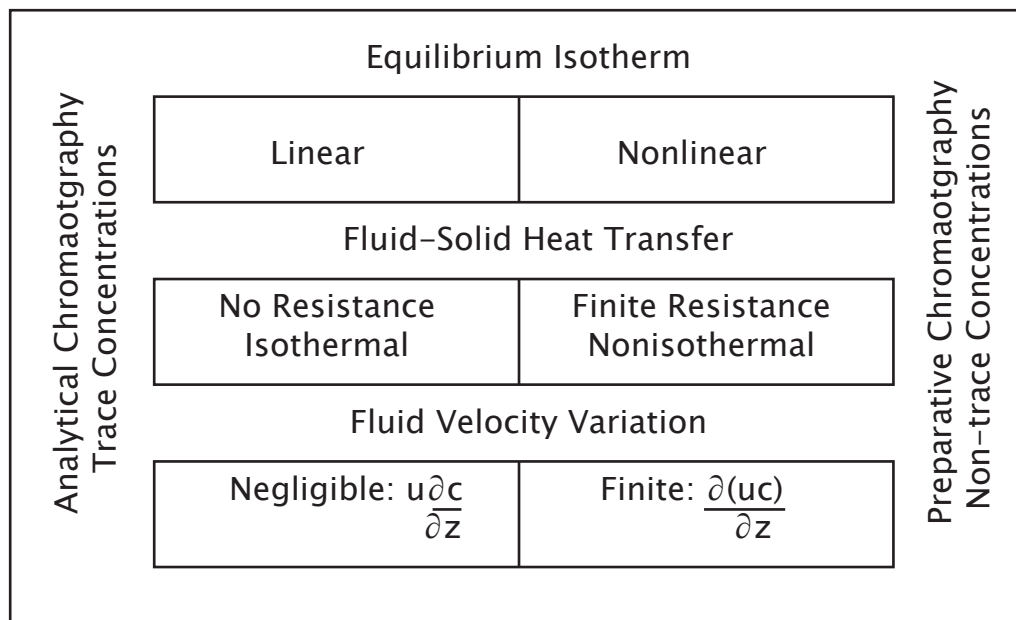
Figure 2.5. Comparison of analytical and preparative chromatography.

tional to the difference between the instantaneous and equilibrium solute concentrations. In other words, the farther from equilibrium, the faster the mass transfer rate.

van Deemter Equation

The term HETP exists today because of seminal work in 1956 by J. J. van Deemter, F. J. Zuiderweg, and A. Klinkenberg, who linked the solution to the mass balance equation with the Poisson distribution (turned Gaussian for large N) of Martin and Synge [10]. They built on L. Lapidus and N. R. Amundson's general solutions to the mass balance equation, $c(z, t)$ [9]. Lapidus and Amundson considered the following:

- Finite axial dispersion: $-D_L \frac{\partial^2 c}{\partial z^2}$
- Linear mass transfer rate: $\frac{\partial \bar{q}}{\partial t} = k(q^* - q)$

Rather than looking at the solute concentration at every point along the column, van Deemter and coworkers honed in on the elution profile, $c(L, t)$ resulting from a delta function input at the column entrance $z = 0$. They elegantly expressed the solution as a Gaussian and noted that the Gaussian of plate theory expressed in length units had a standard deviation $\sigma_l = \sqrt{HL}$. So they equated the standard deviation that they obtained from the mass balance equation with that of plate theory to give what is now known as the van Deemter equation:

$$H = \frac{\sigma_l}{L} = A + \frac{B}{u} + Cu \qquad (2.6)$$

where L is the column length, A, B, and C are parameters that describe band broadening for packed columns (multi-path dispersion, longitudinal diffusion, mass transfer resistance in the mobile phase, and mass transfer resistance in the stationary phase), u is the linear velocity. The first equality restates the plate theory definition for the standard deviation in length units. It says that the height equivalent to a theoretical plate, H, is the variance of the elution curve per unit length. The second equality says that this variance per unit length can be described by the phenomena of longitudinal diffusion, finite mass transfer resistance, and linear velocity. The beauty of their equation is that *the band broadening processes are independent of each other so that the total elution curve variance is the sum of variances from the dispersion sources.*

Thus, H and the number of plates N—the measure of separation efficiency—can be obtained from a chromatogram by measuring the elution curve band width which is $4\sigma_l$. And furthermore, the experimental plot of H as a function of linear velocity u shows how to optimize the separation efficiency of a column.

Models for μGC

We are done with the tools for column efficiency! But what about the separation efficiency of a μGC *system* that includes the injector, detector, and recorder electronics? There is a simple solution. Recall the new picture of the elution curve; it is a Gaussian where we attribute the column variance to the sum of variances from the dispersion sources. So we postulate the same for a GC system: the elution curve remains a Gaussian, and its variance is the sum of the column and extra-column variances. This is precisely what G. Gaspar and coworkers did in 1978 [15]. They expanded the equation for H for WCOT columns (the Golay equation) to include different types of extra-column band broadening:

$$H = \frac{B}{\bar{u}} + C\bar{u} + D\bar{u}^2 \tag{2.7}$$

where H is the variance per unit length [cm], and D is the new term for extra-column dispersion sources [s^2/cm]. B is for longitudinal dispersion [cm^2/s], C is for finite mobile phase and stationary phase mass transfer resistance [s], and $\bar{u}$ is the average linear velocity along the length of the column [cm/s]. Note that unlike the packed column of van Deemter, a WCOT column has no multi-path dispersion arising from nonuniform flow via packing (A term).

The expanded form of the equation is shown to illustrate the dispersion sources in detail:

$$H = \frac{2D_g}{\bar{u}} + \left[\frac{1 + 6k' + 11k'^2}{24(k'+1)^2} \frac{r^2}{D_g} + \frac{2}{3} \frac{k'}{(k'+1)^2} \frac{d_f^2}{D_s} \right] \bar{u} + \frac{\tau^2}{L(k'+1)^2} \bar{u}^2 \tag{2.8}$$

D_g is the binary diffusion coefficient for the solute in the mobile phase, k' is the retention factor, r is the column radius, D_s is the stationary phase diffusion coefficient, d_f is the stationary phase film thickness, L is the column length, and τ is the extra-column dispersion expressed as a time. Optimizing a modern-day separation typically entails selecting a proper stationary phase, column radius and length, stationary phase thickness, and carrier gas as well as minimizing extra-column band broadening sources. In practice, chromatographers graph H as a function of $\bar{u}$ for an isothermal chromatogram (column at constant temperature), called a Golay plot, to find the conditions for minimum H. The minimum plate height H gives the best separation efficiency since the number of plates $N = L/H$ is greatest.

The next chapter uses Equation 2.8 in conjunction with data from Golay plots for Si-glass microcolumns to compute the effect of finite injection from the preconcentrator (not a delta function) on system separation efficiency. The same technique can be applied for other extra-column band-broadening sources such as detector dead volume and detector response time, although the latter is negligible nowadays with high-speed microelectronics.

Summary

This chapter provided a rapid-fire review of gas chromatographic concepts and mathematics. We looked at distillation to understand the physical significance of the terms plate height and number of plates that are used in GC today. And distillation plate theory had the biphasic equilibrium assumption that was reapplied to chromatography. By going through some of the historical highlights we noticed a trend in development; empirical models (equilibrium-based plate theory) were replaced by physical ones that allowed separation optimization (rate theory) as the field matured. The end of the chapter culminated in a way to describe the separation efficiency of the GC system via the summation of variances.

The rest of this thesis parallels the progression of this chapter. Surveying the literature, we will observe a lack of physically-based models for the preconcentrator's adsorptive behaviour. With that in mind, we have the goal of constructing a physical model for the microdevice. But first we use an empirical model—the Wheeler equation—to make a microdevice with the hopes that it will satisfy μGC needs, as well as provide insights into physical processes. The mass balance equation for the column will be reapplied to the preconcentrator to describe its step function response (breakthrough curve) for adsorptive capacity. The language of partition chromatography will be translated into that of gas-solid adsorption. The end of the thesis will culminate in a description of preconcentrator adsorption efficiency based on physical processes to optimize future microscale packed bed designs.

Chapter 3

SYSTEM CONTEXT

Good technology must have an application. Technology and application together are always extant in academic discourse. But rarely is another engineering constraint discussed; who decides the application? Who for this research is the University of Michigan's Engineering Research Center for Wireless Integrated Microsystems (WIMS-ERC), funded by the National Science Foundation (NSF). The vision of a microscale gas chromatograph (μGC) as an autonomous wireless integrated microsystem (WIMS) is one of the backbones of the ERC, and the goal of the WIMS μGC to be the first monolithic microscale system provides the impetus for our microscale preconcentrator research.

The WIMS ERC also gives all efforts in support of the μGC a bold exhortation: to engineer a *novel component* and integrate it into a *functional microsystem.* "Novel component in functional microsystem" is an oxymoron. Novel technology by definition is unproven and cannot function reliably: conversely, a functional system is built by using proven and standard technology. This duel between component novelty and system functionality makes our research exciting. And in the big picture, we recognize that we are a part of an educational experiment to create a real system in an engineering-team environment. The result of this extra dimension of challenge is an education enriched by exposure to system engineering.

With the duality in mind, this chapter explains the component-level architectural choices to satisfy the need for integration into a functional microsystem. This means looking at the application and science-based contexts for the microscale preconcentrator. It turns out that the application-based context of VOC analysis gives sample extraction requirements, while the science-based context of GC gives sample injection requirements. The result is a novel component: a microscale granular carbon preconcentrator that embodies sample extraction and injection in a single unit.

WIMS μGC System

The volatile organic compound (VOC) analysis application comes from the public health arena, and the US EPA publishes methods on how to perform analyses using bench-scale laboratory systems [16]. A summary of the pertinent methods selected in relation to the GC technique is in Table 3.1. The methods shown in the table use flame ionization detectors

(FID) and mass spectrometers (MS) for detection and quantitation, typical of bench-scale instruments. Sample extraction makes use of cryotraps, tube preconcentrators, and canister sampling without preconcentration. These well-documented methods form the foundation for the specifications for the WIMS μGC. By selecting EPA methods as the basis, the resulting system has a well-defined function recognized by the public.

Table 3.1. EPA Methods

Method	Target Compounds	Extraction Media
TO-3 (GC/FID)	VOCs	Cryotrap
TO-17 (GC/FID)	VOCs	Single/Multi-bed Adsorbent
TO-1 (GC/MS)	VOCs	Tenax adsorbent
TO-2 (GC/MS)	VOCs	Molecular Sieve Adsorbent
TO-13A (GC/MS)	Polycyclic Aromatic Hydrocarbons	Polyurethane Foam
TO-14A (GC/MS)	non-polar VOCs	Canister
TO-15 (GC/MS)	polar/non-polar VOCs	Canister

All of the EPA methods rely on field sampling onto extraction media followed by transfer to a laboratory instrument for analysis—hours or days after sampling. Commercial instruments are increasingly field-portable with sizes ranging from laptop computers to large suitcases as seen in Table 3.2, but they also discretize sample extraction and injection into two steps [17], [18].

The unique *microscale* solution for on-site VOC analysis is to combine sample extraction and injection into a single device. In fact, the ability to accomplish on-site analyses without human intervention in the transfer of sample from extraction media to GC inlet rests solely on the analytical front-end: the preconcentrator in this work. Figure 3.1 illustrates what the microscale preconcentrator replaces—a tube preconcentrator *and* the thermal desorption unit to desorb it, mounted on the inlet of a bench-scale GC [19].

It is a tautology to say that an engineered μGC requires system analysis of separation efficiency. Yet this chapter is the first analysis of its kind for a micropreconcentrator. This observation is no mistake. Benchscale GCs are infinitely tweakable, and a chromatographer must be at its side to get it to separate and analyze. In practice, no chromatographer puts pencil to page to compute complete GC specifications prior to running a separation. The microscale GC is an attempt to *alter the technique of GC itself.* By engineering it as an autonomous microsystem, we have to develop and use a system description for GC like no other.

For sample extraction and injection, it is no different. We are using microelectronics technology to create a single extraction and injection microdevice that needs no chromatog-

Thermal
Desorption
Unit

Tube
Preconcentrator

Heating
Block

GC Oven

FID

Cryofocusing
Trap

GC Column
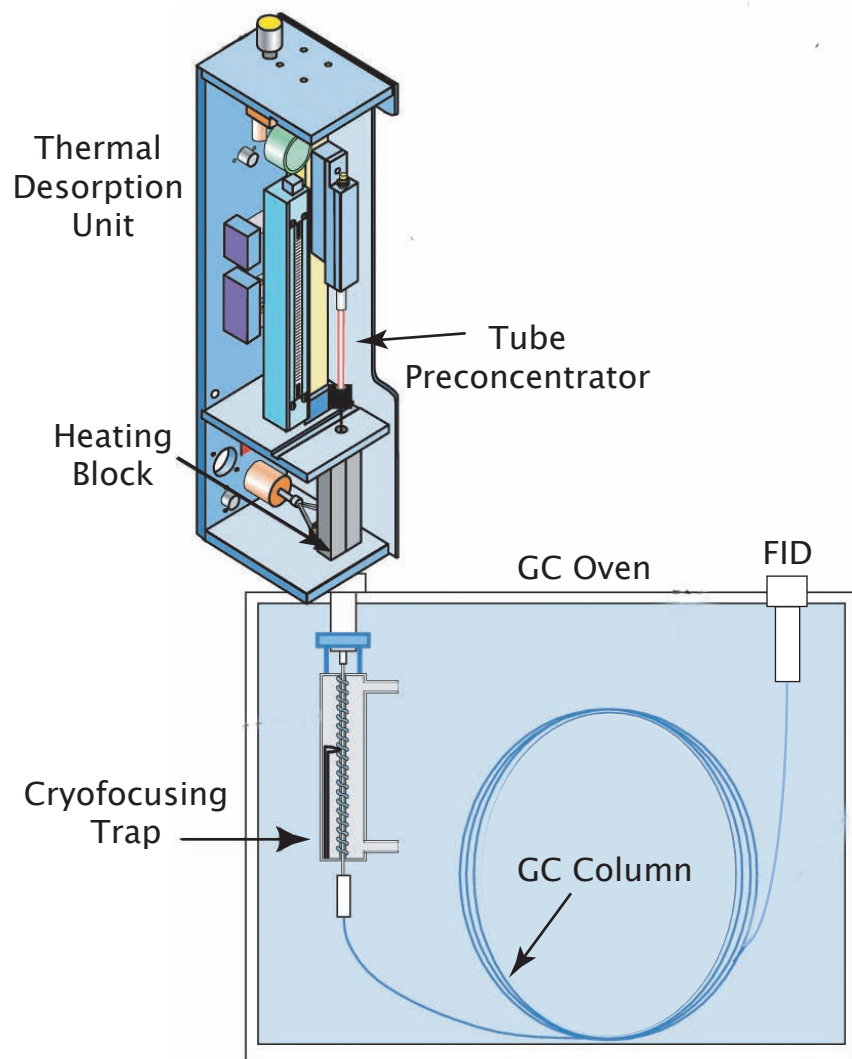
Figure 3.1. Schematic of a thermal desorption unit for a tube preconcentrator mounted on a bench-scale GC inlet.

Table 3.2. Portable-GC System Comparison

Parameter	Units	Varian CP-3900	Agilent 3000	WIMS
Injector Volume	μL	1 - 10	1 - 10	1 - 10
Injector Heating	°C	30 - 110	-	30 - 300
Column Heating	°C	30 - 180	15 - 180	20 - 200
Detector	-	micro-TCD	micro-TCD	sensor array
Detector Volume	μL	0.2	0.24	2
Detection Limit	ppm	10	10	0.1
Linear Dynamic Range	-	10^6	10^6	-
Dimensions	cm^3	$28 \times 15 \times 30$	$15.5 \times 36.4 \times 41.3$	200
Voltage	V	12	15	3
Power	W	180	130	0.1
Weight	kg	5.2	16.6	< 0.1

rapher to operate it or carry it from the field to the laboratory. The premise is that the micropreconcentrator simplifies the process and saves the human from intervening in extraction and injection. A new kind of near-real-time indoor analysis will then be possible.

Let us take a moment to review the process that we simplify and reduce via micropreconcentration. The multi-step sequence for an adsorbent tube preconcentrator begins at a field site. The tube preconcentrator, like a drinking straw filled with grain, is attached to a pump so that air is sucked through and VOCs can stick to the adsorbents. After sampling, the tube is manually removed from the pump and its ends are capped to keep VOCs from diffusing out of the tube. The tube is brought to the analysis laboratory and loaded into a thermal desorption unit (TDU) for injection like the one in Figure 3.1.

The TDU is a complex instrument that houses mechanics to automatically load the tube preconcentrator into a preheated block when injection is to begin. Launching the tube into the block coincides with a high flow rate carrier gas flush through the tube. And since the desorbed sample volume is large, a split inlet and cryofocusing trap are used to narrow down the plugwidth and sample mass to sizes more palatable for the GC column.

Without loss of functionality, this research attempts to replace the TDU with a micropreconcentrator. However, we do not mirror the benchscale GC by implementing cryofocusing. The amount of human intervention necessary to maintain a liquid nitrogen source for the microsystem would indeed seriously undermine our argument for autonomy. Figure 3.2 is a simplified depiction of the sample extraction (adsorption) cycle of the preconcentrator: (a) the adsorbent bed is clean, (b) adsorbates in the air flow through the bed, (c) and (d) adsorbates adsorb into the adsorbent, accumulating over the sampling period until it ends.
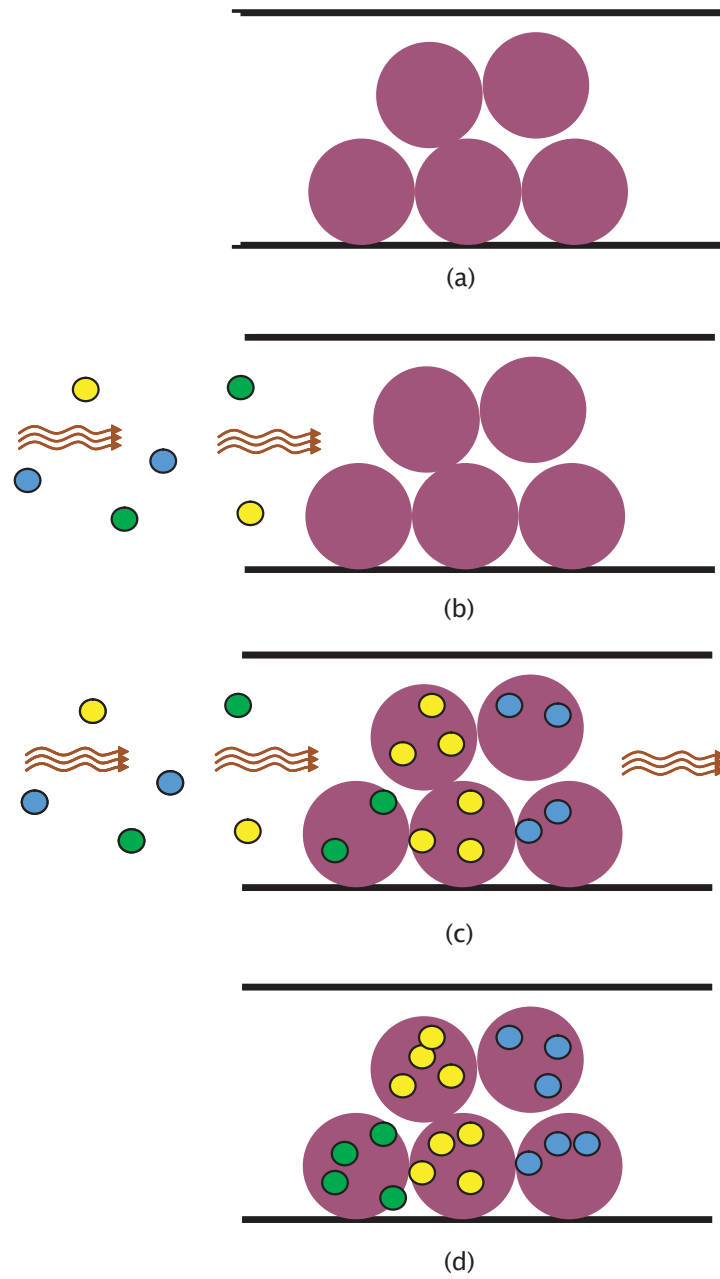
Figure 3.2. Illustration of the adsorption process of a preconcentrator.

The sample injection process is illustrated in Figure 3.3: (a) the preconcentrator is heated, (b) the adsorbates desorb, (c) air is pushed through the device, constituting injection into the microcolumn, (d) the bed is clean and ready for another sampling cycle. The next section reviews the analysis cycle of the whole microsystem to show how the architecture is able to support a preconcentrator that acts as a sample extractor and injector.

Analysis Cycle

The WIMS μGC analytical system drawing is shown in Fig. 3.4. The analysis cycle consists of sample extraction, injection, component separation, and detection. The key component, in addition to the preconcentrator, behind the ability to include sample extraction in the analysis cycle is the micropump. It is the micropump that we use for sampling and then reuse for analysis. Where conventional methods have a pump for field sampling, and a cylinder of carrier gas for analysis, the WIMS system uses a micropump to pull air for sampling and the same micropump to push air for analysis—ambient air is the carrier gas for the μGC.

- **Particle Filtration** The porous Si inlet filter provides a tortuous path for air so that the pressure drop is low while particles of 0.3 to $1\,\mu$m in diameter are trapped before they reach the other analytical components and wreak havoc [20], [21].
- **Calibration** The calibration source is a porous Si reservoir filled with n-decane connected to a diffusional path to the inlet of the preconcentrator [22]. It provides ppb-levels of decane during the analysis for sensor array calibration to temperature and drift.
- **Gas Pumping and Valving** The electrostatic parylene micropump pushes and pulls gas through the system at $25\,$mL/min for a 0.5 atm pressure drop [23], [24]. Thermopneumatic microvalves provide the means to shutoff the inlet and open the split vent during the analysis. A microvalve at the junction of the two columns allows pressure programming during separations [25], [26].
- **Extraction** The pump pulls air containing ppb-levels of VOCs into the preconcentrator, and the VOCs adsorb onto the carbons inside of the microdevice.
- **Injection** The preconcentrator heats rapidly to desorb the VOCs to higher concentrations, and the pump pushes the ppm-level VOC plug into the microcolumn.
- **Separation** The constituents of the VOC mixture each have their own retention, or characteristic amount of interaction (partitioning) with the liquid stationary phase coating on the microcolumn wall. Tuning retention and controlling dispersion make the constituents separate as they traverse the length of the column and emerge from the end temporally separated.
- **Detection** The emerging solutes partition into the Au-thiolate monolayer-protected nanoparticles so that the nanoparticle distance, and thus tunneling current, changes giving a measurable response for detection [27], [28].
- **Microprocessing** The WIMS microcontroller controls component heating and sensor readout, both resistive and capacitive, while the RF link provides wireless data
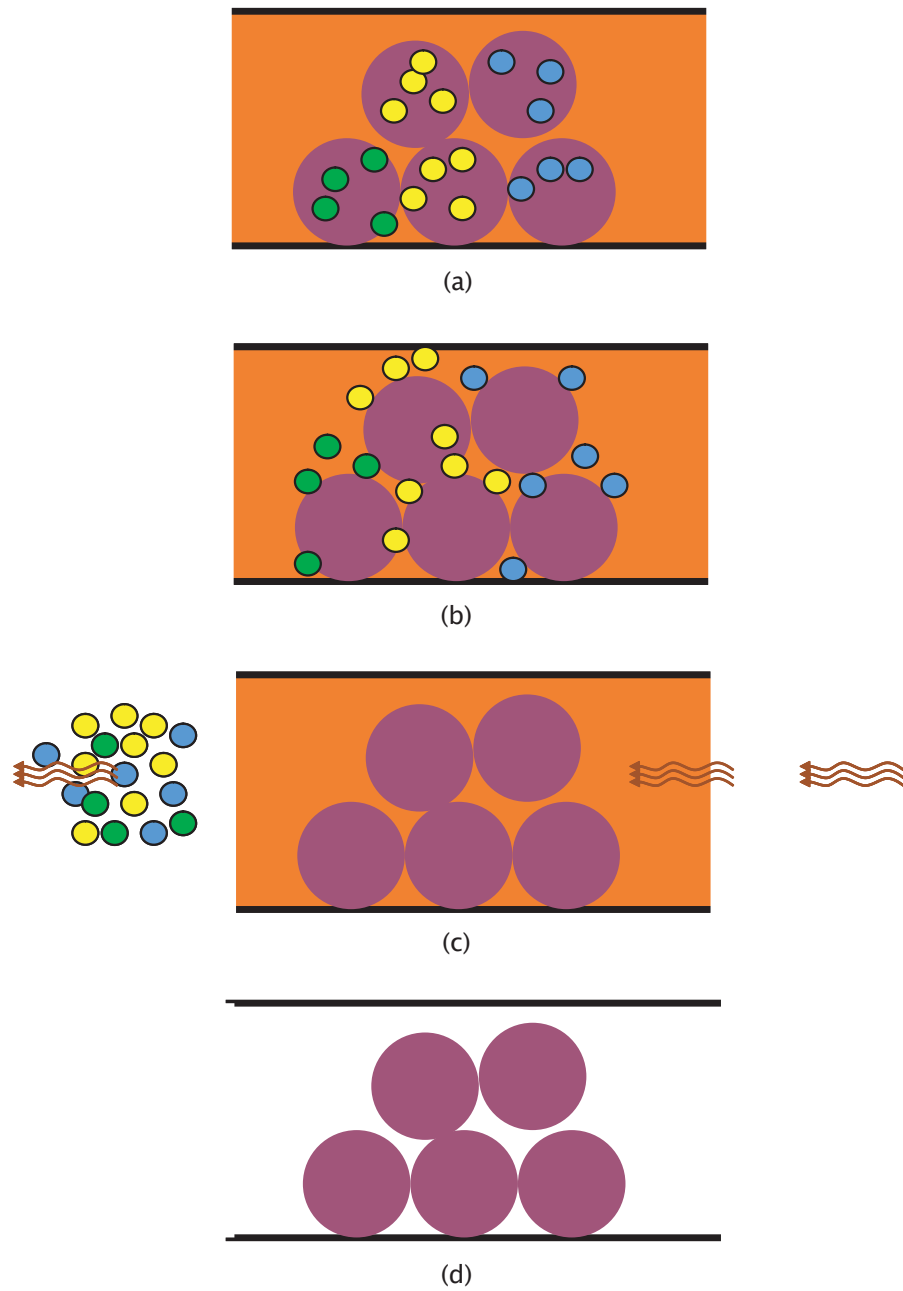
Figure 3.3. Illustration of the thermal desorption process of a preconcentrator.

transmission to a remote computer.

The average power consumption goal is an agressive 10 mW, while the total volume of the system is targeted for 1cm^3. Unique to the WIMS μGC is the fact that adsorption and partitioning are the fundamental phenomena behind each of these functions. Adsorption—the enrichment of a vapor phase at a gas-solid interface relative to the vapor phase—accounts for preconcentration. Partitioning accounts for separation and detection and is the enrichment of a vapor phase at a gas-liquid interface relative to the vapor phase. This observation will be revisited in our discussion of component tradeoffs.

The present trend is that research institutions are implementing state-of-the-art combined extraction and injection devices for on-site analyses; most startup companies doing MEMS-based miniaturized GC are commercializing microvalve injection-only technology shown in the first Si micromachined GC of Terry and coworkers at Stanford University in 1979 [29]. Both of these will be discussed in the next chapter.

Extraction Methods

VOC analysis provides sample extraction choices for this research. There are several classifications for GC sample extraction methods shown in Figure 3.5. These include the medium into which extraction occurs (membrane vs. solid adsorbent), sampling condition (dynamic vs. static), and degree of extraction (equilibrium vs. exhaustive) [30]. The microfabricated preconcentrator here uses solid adsorbents, with dynamic sampling for exhaustive extraction of VOCs from ambient air. The driving force behind these choices is the desire for **quantitative analysis of complex mixtures of trace-level VOCs**.

The choice of a solid sorbent over a membrane goes with exhaustive extraction since membranes are thin, inherently giving lower adsorptive capacity. The sampling medium extracts *all* the compounds of interest from air when it is exhaustive. This contrasts with equilibrium extraction methods, such as solid phase microextraction (SPME), where only a fraction of the compounds are extracted [31], [32]. In SPME, analytes partition between the headspace and a polymer, and in macroscale systems, the SPME device is transferred to the inlet of the GC column and heated to thermally desorb the analytes [33], [34]. The importance of this equilibrium method for microscale, portable instruments is its potentially low power for subsequent injection. The low adsorptive mass and weak adsorption give rise to low desorption temperatures, thereby reducing power requirements. Equilibrium extraction is a possible solution for analyzing a few compounds with the WIMS μGC if the sensor array limits of detection (LODs) are already in the 100 ppb range. However, because of LOD limitations and the quantitative analysis requirement, exhaustive extraction is the viable solution.

The major benefit of exhaustive extraction is that quantitative analysis is easy. The relationship between the input analyte concentration and the preconcentrated, injected sample

concentration is simple. This is because all of the compounds from the sample stream are captured in the preconcentrator. The input concentration can be back-calculated from the flow rate, sampling time, and preconcentration factor for the analytes—all of which are known. This is the opposite of equilibrium extraction with its preferential and competitive adsorption problems. Since only a fraction of analytes are captured into the adsorbent, the adsorbed fraction of *each* compound must be known beforehand, in order to back-calculate the input concentration for quantitative analysis. This makes equilibrium extraction virtually impossible to use for the quantitative analysis of complex vapor mixtures where amounts and compositions are unknown beforehand. However, in this work, with exhaustive extraction, the preconcentrator adsorbs/desorbs all the compounds to enable quantitative analysis.

An extraction method that uses dynamic sampling has a sample that flows continuously into a device (5 to $100\,\mathrm{mL/min}$) to dynamically equilibrate with the medium for extraction, such as an adsorbent bed. In the static approach, such as in diffusive samplers, or SPME, there is no pump to draw gas in contact with the adsorbent. The sampling depends on diffusive flow (1 to $3\,\mathrm{mL/min}$) to equilibrate the extraction medium with compounds of interest. Dynamic sampling offers potentially higher preconcentration factors than static methods for the same sampling time, since a higher flow rate means that a larger volume of analytes are sampled into "contact" to the adsorbents for extraction.

System Limits of Detection

The system limit of detection (LOD) for a given compound is the lowest concentration that can be quantitatively measured. The LOD is different for each VOC because the sensor array response, to first order, depends on volatility as a partition process. Therefore, the system LOD comes from the sensor array detection limits and the preconcentration factor, about to be defined. The present WIMS sensor array consists of four chemiresistors which are interdigitated $15\,\mu$m-wide evaporated Cr/Au lines spray-coated with Au-thiolate monolayer-protected nanoparticles (MPN) [27].

The LOD for GC is commonly defined as the concentration of solute that results in a signal-to-noise ratio (S/N) of three. If the detector measures a signal with a S/N of three, then the probability of that signal being legitimate (representing a solute) is 99% [35]. The role of the preconcentrator is to boost the S/N seen by the sensor array, and it accomplishes this by taking a low concentration input and desorbing it at a higher concentration. Hence, the overall LOD for the system is lowered. The ratio of desorbed concentration to input sample concentration is defined as the preconcentration factor, PCF,

$$PCF = \frac{m_{des}/V_{des}}{m_{in}/V_{in}} \tag{3.1}$$

where m and V denote the mass and volume of the desorbed or input compounds respec-

tively. Note that m_{in}, V_{in} describe the adsorptive capacity of the preconcentrator. They are the amount of VOC that can be exhaustively extracted without breakthrough—the passing of VOCs through the preconcentrator without getting trapped. The preconcentration factor describes the ability of the preconcentrator to boost the concentration of input compounds to a level detectable by the sensor array.

The overall system detection limit is the sensor array detection limit divided by the preconcentration factor:

$$LOD_{sys} = \frac{LOD_{SA}}{PCF} \tag{3.2}$$

In terms of sample injection, the ideal preconcentrator would inject a high concentration of analytes in as small a volume as possible; the volume requirement is described in the next section on sample injection.

The LOD is useful for comparison among detectors and can be measured or computed from the noise and the sensitivity of the detector, which is the slope of the detector response vs. solute concentration. However, for practical GC, we are interested in the linear range of the detector, the concentration range over which the sensitivity varies no more than $\pm 5\%$. We want to know the lowest and highest concentrations measurable by the μGC. The LOD of the detector usually coincides with the start of the linear range. However, this is not the case for the Au MPN sensor array of Q.-Y. Cai and E. T. Zellers, whose published account gives different values of the LOD and the start of the linear range [28]. More recent data from new generations of WIMS sensor arrays are forthcoming and will undoubtedly change the requirements for preconcentrators in the future.

The necessary system detection limit is subject to debate because indoor air has a wide range of VOC concentrations depending on the scenario under study [36]. For WIMS, we have converged on the ppb range. However, even the distinction between a detection limit of 100 ppb versus 10 ppb involves important system tradeoffs. A lower LOD of 10 ppb requires higher preconcentration factors, but has less adsorptive capacity. A higher LOD of 100 ppb increases the adsorptive capacity requirement by ten-fold over 10 ppb, but requires less preconcentration for sensor array detection. Our preconcentrator is developed for the 100 ppb LOD since we recognize that our approach is unique for its exhaustive extraction ability and we wish to emphasize it.

For that earlier WIMS sensor array, the linear response range is tabulated in Table 3.3 along with their computed LODs for Au nanocluster chemiresistor arrays in $60\,\mu$L detector cells and various VOCs [28]. The preconcentration factors are computed for a 100 ppb system detection limit for both the minimum concentration for linear range, and the minimum detectable concentration for the chemiresistor arrays. The table shows that the range of preconcentration factors is wide: from 1 to 170 when considering limits of detection, and 200 to 600 (much higher) when considering linear range. There is nothing that disallows us from using a detector outside of its linear range; however, one can imagine that operating in a non-linear regime comes at the expense of a few more look-up tables in the WIMS mi-

crocontroller to convert the signal into a concentration (rather than a single multiplicative factor, for example). The maximum preconcentration factor dictates the minimum adsorbent mass for the device. Therefore, the target for a 100 ppb detection limit, assuming the more stringent linear-range operating regime, is a preconcentration factor of 600 for highly volatile compounds (acetone) and 200 for low volatility compounds (m-xylene).

Table 3.3. Preconcentration Factors for 100 ppb LOD for VOCs on Au-octanethiol Chemiresistor Arrays

Compound	p_v	Linear Range	PCF	LOD	LOD PCF
	[Torr]	[ppm]	-	[ppm]	-
Acetone	231	60-2000	600	17	170
2-butanone	72	20-800	200	3.1	31
Ethanol	58	60-1600	600	3.2	32
Isooctane	49	40-800	200	0.7	7
Trichloroethylene	47	20-80	200	0.7	7
1,4-dioxane	40	20-800	200	0.8	8
Toluene	28	20-800	200	0.3	3
Perchloroethylene	18	20-80	200	0.3	3
n-butyl acetate	12	20-40	200	0.3	3
Chlorobenzene	12	20-80	200	0.2	2
m-xylene	8	20-400	200	0.1	1

Sample Injection

While preconcentration factor and output solute concentrations are of utmost importance when considering the sensor array-preconcentrator relationship, the extent (volume or time) of the desorption plug is the vital link between the preconcentrator and the column. Concentration is important for column overload considerations but takes a backseat for the moment. As explained in Chapter 2, initial GC separation theory assumed that the sample at the column inlet was a delta function. It is interesting to note that a host of equations sprang up as alternatives to van Deemter's as researchers tried to test its applicability—no one quite got the van Deemter curve of H vs. $\bar{u}$ because they all overlooked the fact that their real GCs had extra-column variances not included in the idealized model [3].

Guiochon pointed this out in his note on the mathematical modifications to account for a finite sample volume [37], and later Gaspar and coworkers verified and expanded this to include other extra-column variances including finite detector response times, recorder

electronics, and detector dead volume [15]. First introduced at the end of Chapter 2, the equation for the plate height (H), a measure of separation efficiency for the μGC system, is repeated here for convenience:

$$H = \frac{2D_g}{\bar{u}} + \left[\frac{1 + 6k + 11k^2}{24(k+1)^2} \frac{r^2}{D_g} + \frac{2}{3} \frac{k}{(k+1)^2} \frac{d_f^2}{D_s} \right] \bar{u} + \frac{\tau^2}{L(k+1)^2} \bar{u}^2 \tag{3.3}$$

where H is the variance of a Gaussian peak per unit length [cm], the first term on the right accounts for longitudinal dispersion [cm^2/s], the second term accounts for dispersion due to finite mobile phase and stationary phase mass transfer resistance [s], and the last term is for extra-column variance [s^2/cm]; $\bar{u}$ is the average linear velocity along the length of the column [cm/s], D_g is the binary diffusion coefficient for the solute in the mobile phase (e.g., nonane in air), k is the retention factor, r is the column radius, D_s is the stationary phase diffusion coefficient, d_f is the stationary phase film thickness, L is the column length, and τ is the extra-column dispersion expressed as a time. Note that for simplicity, mobile phase compressibility is not taken into account in this equation (i.e., the Martin-James pressure correction factors are left out).

The designation "extra-column variance" is a superset of "extra-column sources of band broadening." For example, a finite injection volume is technically not a source of band broadening in and of itself. Sources of band broadening are physical dispersion processes such as parabolic velocity profiles in open tubes or turbulent mixing in flow restrictions and extreme bends in connections. Because of the summation of variances, it is not necessary to know the physical process behind a finite injection volume to account for its effect on overall system efficiency. This is a double-edged sword. On one hand, we can compute the effect of a finite injection volume on separation efficiency and visualize it as a sample that occupies a finite number of plates along the column. On the other hand, we need to be careful in making any generalizations from operational parameters that we artificially put into the expression for sample variance to get the units to work out for the H equation.

Here we will consider only the preconcentrator's contribution and not other extra-column variances. Its contribution is primarily from the desorption plug width rather than the dead volume per se. Dead volume of extra-column connections and detector cell volumes is commonly quoted by chromatographers because usually large dead volume can cause dispersion, which is detrimental to separation efficiency. This is easy to appreciate for the case of a concentration-sensitive detector where a large detector cell will cause the eluting solute to be averaged over the entire cell volume. And for connecting tubes one can visualize dispersion from the parabolic velocity profile across the tubes. However, the effect of the dead volume of the sample injector is not as intuitive.

The low dead-volume of microscale preconcentrators has been often quoted in the past as one of its microscale virtues, and typically researchers cite their estimates for dead volume without further explanation. However, the intentional implication that a small dead-volume is good without qualification deserves to be examined further. It is reasonable to assume that adsorbents occupy a certain volume and that since adsorption occurs within the whole

bed that the interstitial volume must be swept out in order to effect desorption. So dead volume in a sense of the volume of mobile phase that must be flowed through the device to sweep out the interstitial space is reasonable and coincides with the definition of dead volume for columns. However, in general the effect of dead volume on separation efficiency is not easy to quantify. Dead volume adversely impacts separation efficiency when it contributes to solute band broadening. If a solute band goes through a dead volume with little or no dispersion, say rapid flow through a heated section of capillary, then the denigration of overall system separation efficiency is trivial. Therefore, the important metric is not the dead volume alone but also the desorbed volume from the preconcentrator.

Unfortunately, the desorbed volume from an injection device is exceedingly difficult to predict. So perhaps that is why for a fall-back, researchers cite the dead volumes in their devices or connecting tubes. For reference, the dead volume of this device is $1.70\,\mu\text{L}$, while for comparison $1.04\,\mu\text{L}$ was the dead volume for a previously developed single-stage prototype [38]. In later chapters, we will present the measurements of desorbed volumes, more relevant for commentary on system separation efficiency.

To make some relevant computations to describe the effect of finite volume on separation efficiency, we will take some parameters measured for actual microcolumns. The parameters supplied for this calculation are from an actual measured Si/glass column that has been described in [39] and is summarized in Table 3.4. In order to keep as many of the parameters valid from that experiment as possible, we back-calculate the stationary film thickness from equation (3.3) as $1.5\,\mu\text{m}$. A chromatographer would say that this is somewhat pessimistic; typical narrow-bore film thicknesses are on the order of $0.1\,\mu\text{m}$ [40]. The assumption of air as carrier gas reflects the WIMS indoor air application.

Table 3.4. Calculation Parameters For Dispersion Calculations

Parameter	Symbol	Units	Value
Stationary Film Thickness	d_f	μm	1.5
Stationary Phase	-	-	PDMS
Carrier Gas	-	-	Air
Retention Factor	k	-	5

A sample of finite extent with a standard deviation in time units (τ) is accounted for in the equation. Recall that the standard deviation of a solute elution curve (a Gaussian) is a quarter of the base peak width so that it is easily obtained from a single vapor desorption response. The last term in equation (3.3) is denoted H_d in the following plots to account for finite injection volume, while H_{min} is the variance per unit length without the finite injection volume.

Figure 3.6 shows the effect of finite sample variance on a $25\,\text{cm}$ PECVD column with an

inner diameter of $90\,\mu$m. The left y-axis is the finite sample variance H_d and the intrinsic column variance H_{min}, while right y-axis shows the ratio of H_d to H_{min}. The importance of this ratio is that a generally cited rule of thumb for standard bore separations is to have the extra-column variance σ_{ec}^2 (from dead volumes, sample injection, detector cell volumes, electronic response time) be no more than 10% of the column variance, σ_c^2 [3]. Therefore, the 10% level is where we would like to operate, and that gives us an idea of the injection plugwidth that we can afford if we are to preserve separation efficiency.

The case of H_{min} and H_d/H_{min} for a standard bore microcolumn $3\,$m-long with the empirically derived parameters (except τ) is shown in Figure 3.7. In contrast to the $25\,$cm column, the effect of a finite sample is much less detrimental to the separation power of the column. Looking at the H_d/H_{min} ratios for a given time standard deviation, say 10%, the time extent of the injection plug for the $25\,$cm needs to be half that of the $300\,$cm column. When we consider the optimal column flow rates, this translates into an order of magnitude difference in injected volume. This is shown in the comparison of the standard and narrow bore microcolumns of Table 3.5 with V_{inj} being the sample injection volume which is equivalent to a 10% length variance ($k = 5$, PDMS/air).

Table 3.5. Comparison of the Standard and Narrow-bore Micro-columns

Parameter	Symbol	Units	L = 300 cm, $r_{eq} = 109\,\mu$m	L = 25 cm, $r = 45\,\mu$m
Minimum Plate Height	H_{min}	cm	0.039	0.0353
Linear Velocity	$\bar{u}_{opt,ic}$	cm/s	8.91	9.87
Hold-up Time	t_m	s	33.65	3.04
Number of Plates	N	-	7692	708
Volumetric Flow Rate	v_{opt}	mL/min	0.2	0.04
Injection Volume	V_{inj}	μL	2.42	0.11

Analysis Time

Besides separation efficiency, total analysis time for the μGC is another practical specification. After all, the analysis time defines how real-time a system is—the time over which the sample is averaged, in essence. So what effect does a finite sample have on the ability to accomplish a separation, say in $1\,$min? For the general case, the most highly retained compound will determine the total separation time via:

$$t_{r,last} = \frac{L}{\bar{u}_{opt}}(k_{last} + 1) \qquad (3.4)$$

where $t_{r,last}$ is the retention time of the last compound to elute, L is the column length, $\bar{u}_{opt}$ is the optimal average linear velocity (we are assuming that we operate at the optimal velocity, otherwise it would be $\bar{u}$), k is the retention factor of the last solute, and the equation is from the definition of the retention factor.

Peak Capacity

Finally, peak capacity indicates the complexity of an anlysis in terms of how many analytes we can separate and quantify in a mixture on a chromatogram using the μGC. The peak capacity N_p is defined as the number of equally spaced peaks that can fit on an isothermal chromatogram for a given resolution R_s. It gives us a first-order estimate of how many components we can separate. In practice with temperature and pressure programming, where resolution is sacrificed for speed, the actual number of peaks is different.

A sample of finite variance changes the peak capacity via its contribution to the minimum plate height H in the equation shown below. Each peak is assumed to be Gaussian in shape, and from plate theory we obtain:

$$N_p = 1 + \frac{1}{4R_s}\sqrt{\frac{L}{H}} \ln\left(\frac{t_r}{t_m}\right) \tag{3.5}$$

where $R_s = \Delta t_r/4\sigma = 1.5$ for baseline separation, L is length [cm], H is height [cm], t_r is the critical pair solute retention time [s], and t_m is the column hold-up time [s]. (A baseline separation is defined as that where $R_s = 1.5$ meaning that the spacing between peaks is 6σ.)

Figure 3.8 provides a view of the peak capacity as a function of sample dispersion expressed as τ for the $300\,\text{cm}$ Si/glass standard-bore microcolumn and the $25\,\text{cm}$ PECVD narrow-bore microcolumn. The plot shows the intuitive result that the shorter the injection plug width from the preconcentrator, the better. The peak capacity of the $300\,\text{cm}$ Si/glass column is about three times that of the narrow-bore $25\,\text{cm}$ PECVD column. This serves as a reminder that the ultra-rapid separations of short, narrow-bore columns are not geared toward complex vapor mixtures with 30 to 40 components.

Summary

We have discussed GC limits of detection, separation efficiency, analysis time, and peak capacity from the point of view of μGC. Just as the autonomous, monolithic microsystem is unique, so too are the requirements for the sample extraction and injection device: the micropreconcentrator. The micropreconcentrator must take in 10 to $100\,\text{ppb}$ concentrations of VOCs and deliver them in narrow injections ($0.1\,\text{s}$ for narrow-bore fast microcolumns, $1\,\text{s}$)

for longer standard-bore microcolumns at high concentrations in the hundreds of ppm. The remainder of this thesis uncovers whether these requirements are compatible and practical given the finite sample mass capacity for a microcolumn, along with a unique extraction and injection model for the all-in-one micropreconcentrator.
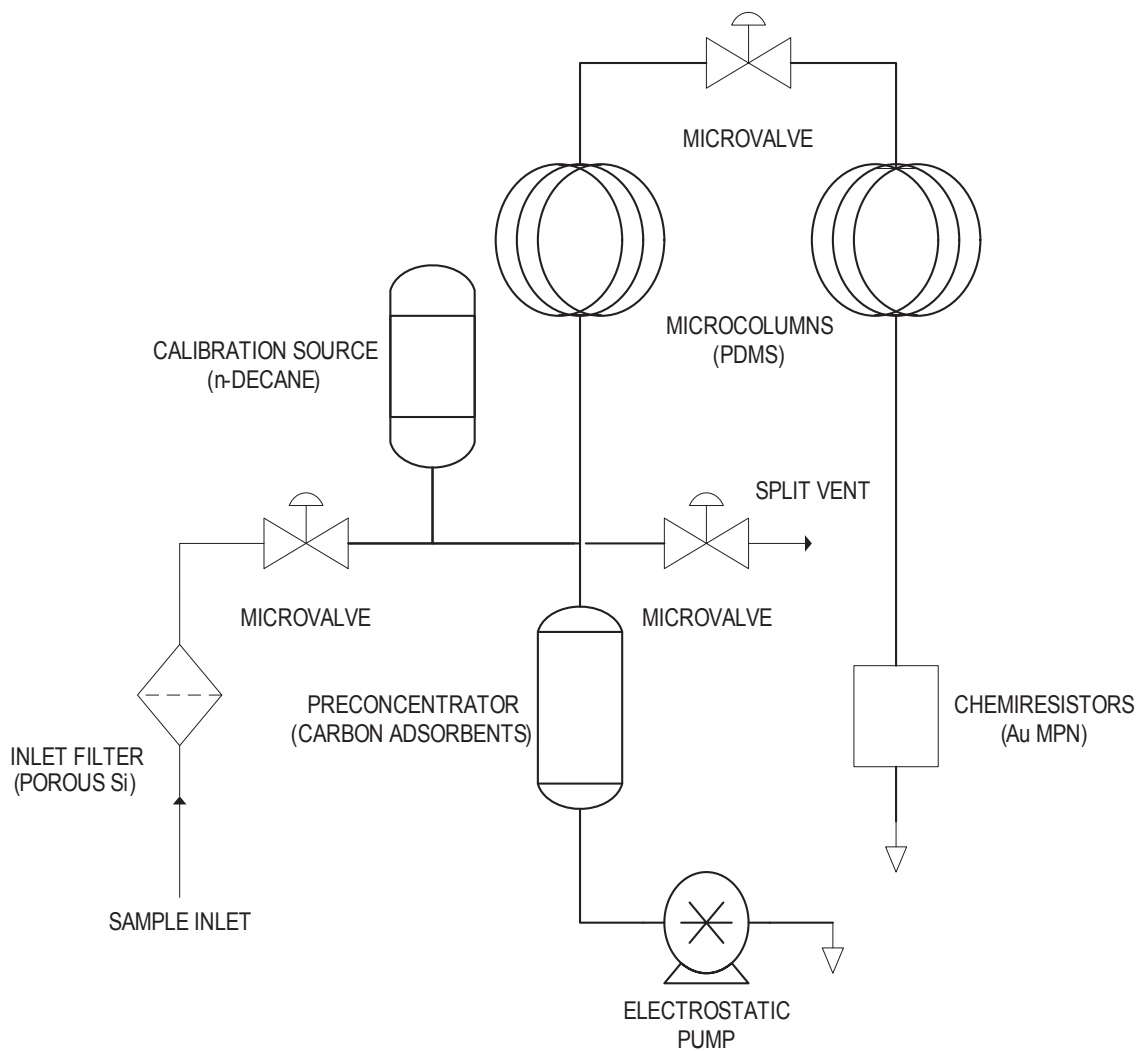
Figure 3.4. μGC system diagram
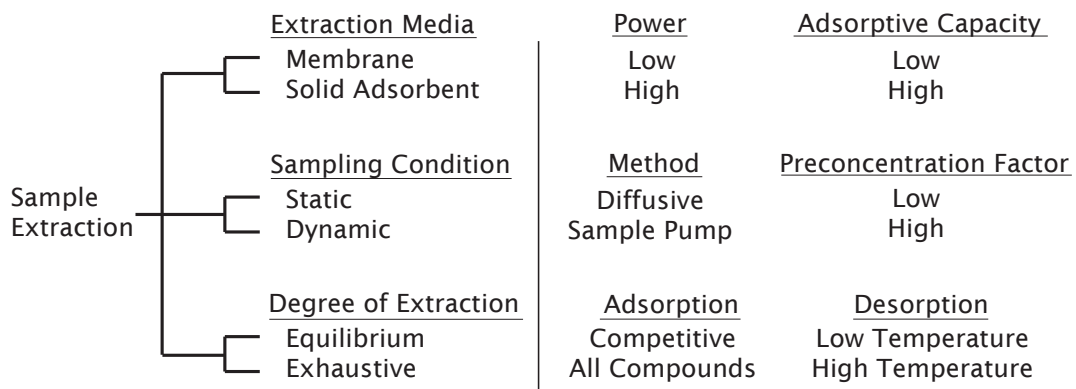
Figure 3.5. Sample Extraction Choices
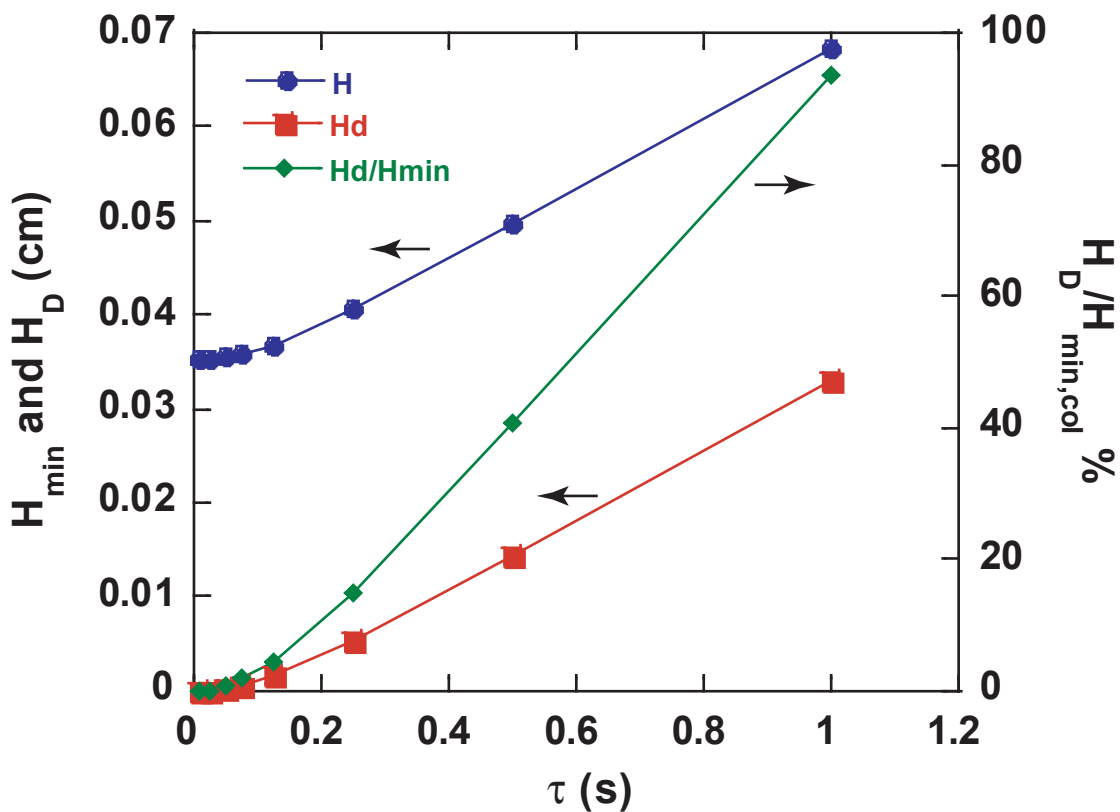
Figure 3.6. A plot of the minimum plate height and the height contribution due to finite sample injection band width (left y-axis). The ratio of the height contribution due to finite sample and intrinsic column only plate height (right y-axis), both as a function of time calculated for a PECVD 25-cm-long PDMS/air/Si column and solute retention factor of $k = 5$.
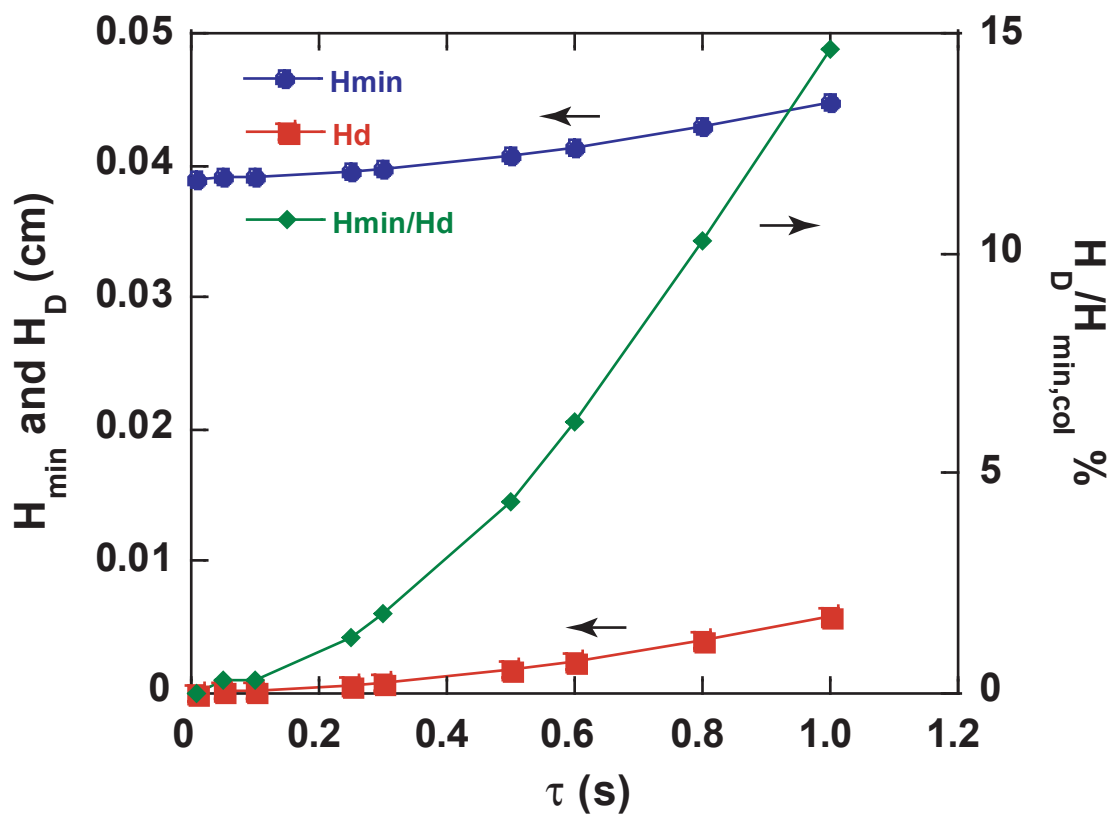
Figure 3.7. Minimum plate height (total) and plate height due to finite sample as a function of τ for a Si/Glass microcolumn of length $300\,\mathrm{cm}$.
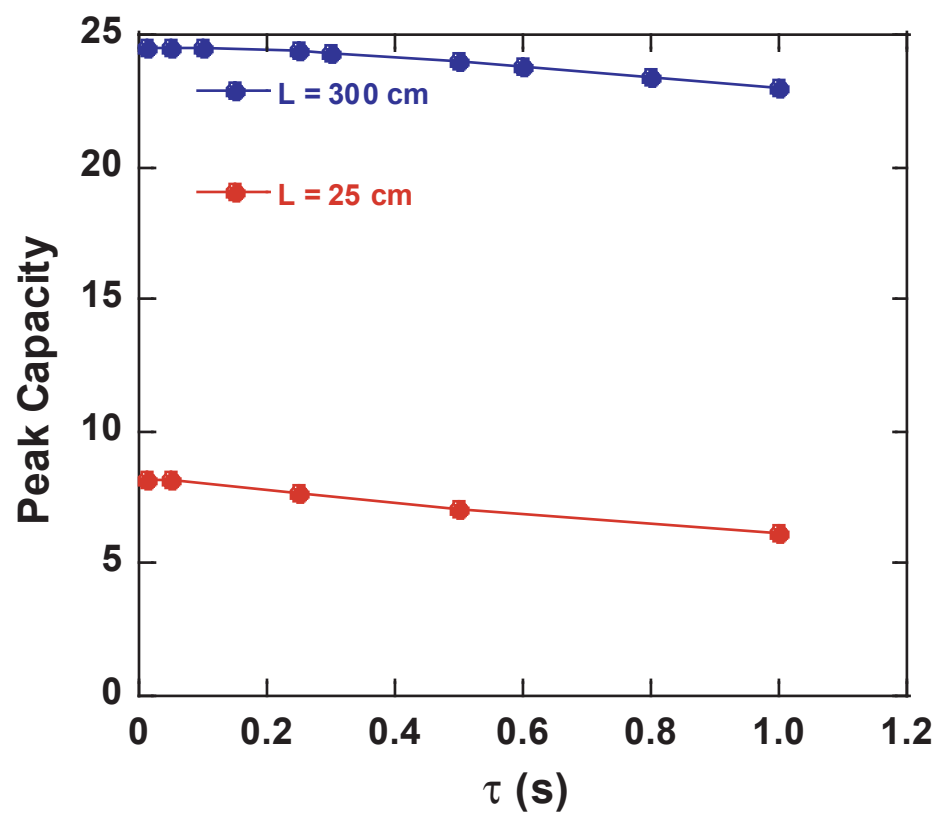
Figure 3.8. Peak capacity as a function of τ for a Si-Glass microcolumn with a length of $300\,\text{cm}$, and a PECVD microcolumn with a length of $25\,\text{cm}$.

Chapter 4

MICROSCALE PRECONCENTRATORS

A microscale preconcentrator that both exhaustively extracts and injects narrow samples is unique to this work. Exhaustive extraction and narrow sample injection represent opposite extremes for adsorbent-adsorbate interaction. For exhaustive extraction of a wide volatility range of VOCs, interaction should be strong; yet for low-power thermal desorption of these same compounds, interaction should be weak. The challenge for preconcentrator design is the classic "chicken before the egg" conundrum. A proven design model with adsorbent-adsorbate interactions does not exist precisely because no device has been made, and yet a design must be done. Normally, the lack of design model *a priori* is typical of research. But in this case, the preconcentrator needs to fit into a functional microsystem.

To escape the conundrum and to build a device, a conjecture has been made by previous researchers: to scale down a macroscale model to the microscale, emphasizing adsorptive capacity (i.e., exhaustive extraction) rather than sample injection. This chapter reviews the approach of this work; a cavity-based scaled design is implemented to probe the validity of the scaling conjecture. This chapter also gives the historical context for microscale extraction and injection devices to explain the gap in the literature regarding design models.

Preconcentration

The fundamental mechanism behind preconcentration in this research is physical adsorption, or physisorption. Physisorption is due to weak, intermolecular nonspecific and specific forces between the gaseous phase, called the adsorbate, and the solid surface, termed the adsorbent. A simplified view of how the adsorbent inside a preconcentrator preconcentrates is diagrammed in Figure 4.1 via hypothetical adsorption isotherms.

A typical adsorption isotherm's y-axis is the equilibrium adsorbed amount of adsorbate (solute) per gram of adsorbent normalized to the maximum adsorbable amount (also g/g), q^*/q_0, and the x-axis is the partial pressure of the adsorbate normalized to the saturation vapor pressure for a fixed temperature, p/p_0 (equivalently expressed in terms of concentration as C/C_0). In simple terms, the adsorption isotherm tells us the equilibrium distribution

of the adsorbate in the gas and solid (adsorbent) phases for a fixed temperature and partial pressure. During extraction at room temperature, the adsorbent takes up adsorbate because physisorption is a spontaneous, exothermic process; during injection the adsorbate flies off the adsorbent because the high thermal desorption temperature imparts kinetic energy to the adsorbates to escape the adsorbent. A big-picture discussion of physisorption and its relation to thermodynamics is in Appendix A. Generally, the isotherms for exact concentrations and adsorbent-adsorbate pairs are measured. However, we do not have the luxury to make equilibrium isotherm measurements since we do not have the apparatus. And it is for that reason, that previous researchers have turned to the approach of scaling macroscale results published by others, for adsorbent mass selection. We do note that properties whould at least theoretically be attainable from microdevice measurements.

Adsorbent Selection

The selection of granular carbons for adsorption in the preconcentrator is driven by the following considerations:

- Preferential adsorption of nonpolar adsorbates (e.g., saturated hydrocarbons) over water (which exists in indoor air) → carbon
- Weak adsorption (for low desorption energy requirements) → physisorption
- Rapid adsorption/desorption kinetics → granular form
- Good thermal stability with repeated regeneration → graphitized carbon blacks
- Reproducible, commercial source

The simplest synopsis of the difference between carbon and other major industrial adsorbents such as activated alumina or silica gels is that "like dissolves like." Because their surfaces are nonpolar or weakly polar, carbonaceous adsorbents are the best in terms of preferential adsorption of nonpolar adsorbates [41]. Figure 4.2 is a series of scanning electron micrographs (SEMs) of the adsorbents used in this work.

Generally, carbonaceous adsorbents are as diverse in pore structure and adsorptive properties as their biomass and synthetic precursors: wood, peat, coal, coconut shells, polymers, etc. The major categories are:

- Graphitized carbon black (GCB): (used in this work) GCBs are produced from petroleum and coal-tar pitches under inert gas ambients and high temperatures. They are almost purely carbon as opposed to the other types of carbon adsorbents, and lamellar constituent molecules (LCM) are parallel to the surfaces of the carbon blacks [42]. The space between these graphitic regions is quite large so that by International Union of Pure and Applied Chemistry (IUPAC) definitions, GCBs are macroporous (width $> 50\,\mathrm{nm}$). The surfaces of GCBs are as close to energetically homogeneous as can be found amongst the carbon adsorbents, and their high degree of graphitization makes them able to tolerate high regeneration (thermal desorption) temperatures. It
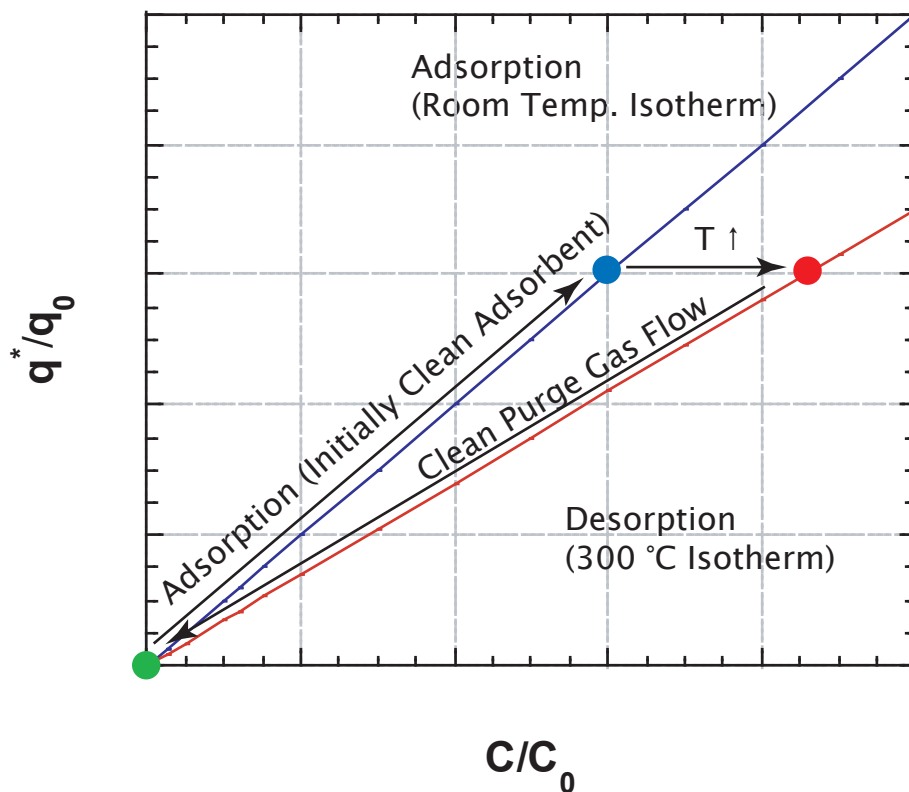
Figure 4.1. Concept diagram showing the preconcentration process on two linear (hypothetical) adsorption isotherms. During sampling, an initially adsorbate-free preconcentrator traps the influent adsorbate (finite concentration C) ; Once sampling ends, the preconcentrator is heated to $300\,^\circ$C bringing it to the high temperature isotherm; The adsorbed amount is out of equilibrium with the purge gas (zero concentration) so that it desorbs from the adsorbent bringing it back to its adsorbate-free state.
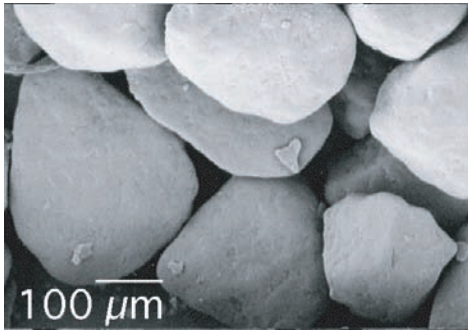
Carbopack B
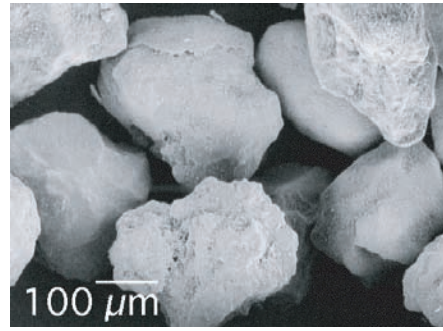
Carbopack X
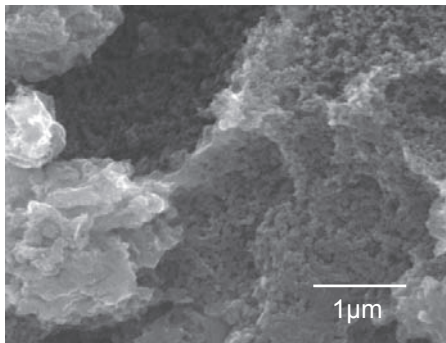
Close-up of Carbopack B
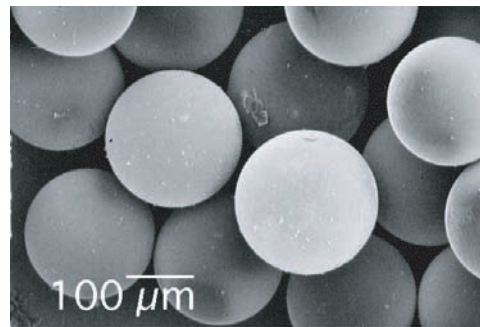
Carboxen 1000

Figure 4.2. SEMs of the carbon adsorbents in this work.

is their thermal stability and extremely weak adsorption which makes them useful for our application in terms of regeneration.

- Carbon molecular seives (CMS): (used in this work) CMS are on the other extreme of porosity. They are amorphous carbons produced from synthetic precursors with micropores that are several adsorbate molecular diameters in size. These provide highly energetic adsorptive sites and the surfaces of CMS are energetically heterogeneous. The highly energetic sites enable the capture of light hydrocarbons for preconcentration.

- Activated carbon (AC): (interesting for future work)
  ACs are microporous, amorphous carbons that come in forms such as fibers and cloths. The maximum temperature of $200\,^\circ$C is lower than graphitic carbons, but adsorption/desorption kinetics are rapid due to small $10\,\mu$m diameter fibers.

- Carbon nanotubes (CNTs): (interesting for future work)
  CNTs have attracted attention as a potential hydrogen storage material for fuel cells [43]. For VOC mixture adsorption however, CNTs are not well-understood [44]. Not only are there many configurations for CNTs, but amorphous carbons in the synthesis process also effect adsorption. Intellectually interesting possibilities such as controlling pore sizes to tailor adsorption capacities have yet to materialize. One unique opportunity for a microdevice such as the preconcentrator is to be a platform for investigating a nanoscale material such as CNTs *as synthesized*. Current nanoscale adsorbent characterization follows the macroscale paradigm of separating synthesis from characterization. A microdevice like the preconcentrator can combine synthesis and property extraction so that nanoscale materials can be probed *in situ*.

Adsorbent Properties

Prior tube preconcentrator work and literature available from vendors has led us to select the adsorbents summarized in Table 4.1. Properties of the Carbopack B and Carbopack X (both GCBs) and Carboxen 1000 (CMS) used in this work are compiled from information supplied by the manufacturer (Supelco, Inc., Bellefonte, PA, USA) and a nitrogen adsorption study on these adsorbents [45]. According to the IUPAC definition, the width of a micropore is $< 2\,$nm, mesopore 2 to $50\,$nm, and macropore $> 50\,$nm.

From Table 4.1 the graphitized carbons have no microporosity, in contrast to the CMS and activated carbons used extensively in air purification and respirator applications. Surface area and porosity are not as simple as they seem. Adsorbents cannot be conceptualized as flat two-dimensional surfaces, nor can their porosity be viewed like holes in Swiss cheese. For adsorption, it is the spaces between bunches of atoms that are important. At the macroscale these adsorbents are what we think of as solids without holes. With Swiss cheese, we can get a ruler, measure the hole size, calculate the volume, and we only get one answer. However, at the atomic scale, measuring the spaces between clusters of bonded atoms is not easy—the answer we get depends on the ruler we use. The surface area we obtain

Table 4.1. Adsorbent Properties

Property	Units	Carbopack B	Carbopack X	Carboxen 1000
Carbon Type	-	GCB	GCB	CMS
Internal surface area	m^2/g	100	240	1200
Density	g/mL	0.35	0.41	0.48
Micropore Diameter	nm	N/A	10	1-1.2
Microporosity	cc/g	N/A	N/A	0.44
Mesoporosity	cc/g	N/A	0.62	0.16
Macroporosity	cc/g	N/A	N/A	0.25
Degradation Temperature	$^\circ$C	527 (800K)	477 (750K)	-
Vapor pressure range	Torr	0.01 - 29	29 - 95	95 - 231
Required mass	mg	1.2	0.8	0.64

depends on the probe molecule. Arbitrarily, as the "standard" for superficial comparison between adsorbents, we use nitrogen as the probe. This is called the Brunnauer-Emmett-Teller (BET) surface area, so named after the researchers who developed the mathematics for an adsorption isotherm describing multi-layer adsorption.

It is understood that from an application point of view, the actual surface area "seen" by a particular adsorbate will depend on its size relative to the pore sizes and pore size distributions of the adsorbent. In other words, the BET surface area does not tell what the pore sizes are, or how they are laid out in the adsorbent. Both of those things are critical for capacity and kinetics (rates of adsorption and desorption) in actual devices. Therefore, design models derived from fundamental properties are not seen in the literature, and the approach is to build first, measure later.

Kruk and coworkers have measured the BET surface areas and TGA profiles of several of the Supelco Carbopack adsorbents [45]. The adsorption potential of a monolayer is also calculated for nitrogen as $5.3\,\mathrm{kJ/mol}$ for Carbopack B and $5.11\,\mathrm{kJ/mol}$ for Carbopack X. The degradation temperature from the weight loss profiles given in the paper is $477\,^\circ$C for Carbopack X, and this is an important fabrication constraint in terms of bonding temperature for the silicon sealing wafer.

Prior Art

A summary of microfabricated preconcentrators for combined extraction and injection is given in Table 4.2. What distinguishes this work is its 100 ppb exhaustive extraction ability, wide volatility range, and short injections. The approach is dynamic, exhaustive ex-

traction for quantitative analysis, while other researchers in the field have pursued devices for dynamic, *equilibrium* extraction for their respective compound identification-only applications. The earliest Si micromachined GCs used timed microvalves to introduce a set volume of sample into the column [29], [46], [47]. These timed microvalves are injection-only systems while new research efforts are focusing on extraction from the ambient and injection.

The table is an oversimplified comparison because the devices are for different applications and the parameters depend on operating conditions. Often the value of the parameters in the table are not static, but moving targets with system tradeoffs. For example, the WIMS $25\,\text{mL/min}$ sampling flow rate and sampling time of $10\,\text{min}$ are flexible targets with which to measure progress. A system engineer would call this a baseline design knowing that these could just as easily be $2.5\,\text{mL/min}$ and $1\,\text{min}$ with appropriate trades in the sensor array domain. The problem is that the literature has little commentary on tradeoffs and design choices—the indispensable know-how that only comes with a physical understanding of the microdevices. The next paragraphs go into as much detail as the literature offers in its description of the virtues and limitations of these devices. However, as shown in the table, parameters reported are not comprehensive nor are they consistently defined between papers, so that it is difficult to truly compare the designs. This lack of a common language to describe micropreconcentrators underscores the fact that the field remains in proof-of-concept mode.

Table 4.2. Microfabricated Preconcentrator Comparison

Parameter	Units	Sandia	Kim et. al.,	Present Work
Target Compounds	-	DMMP	BTEX	30 - 40 VOCs
Sampling Flow Rate	mL/min	3	7	25
Sampling Time	min	1	N/A	10
Extraction Concentration	ppm	5	5 - 20	0.1
Adsorbent	-	Sol gel	OV17 polymer	GCB
Form	-	Thin-film	$2.4\,\mu\text{m}$ thin-film	$200\,\mu\text{m}$ particle
Bed Length	cm	0.25	16	8
BET surface area	g/m^2	1000	N/A	100 - 1200
Desorption Temperature	$^\circ\text{C}$	250	120	300
Heating Rate	$^\circ\text{C/s}$	1000	12	30
Desorbed Volume	μL	250	N/A	60
Desorption flow rate	mL/min	3	N/A	2
Preconcentration Factor	-	500	14	5000

The device reported by Kim and coworkers from New Jersey Institute of Technology is a
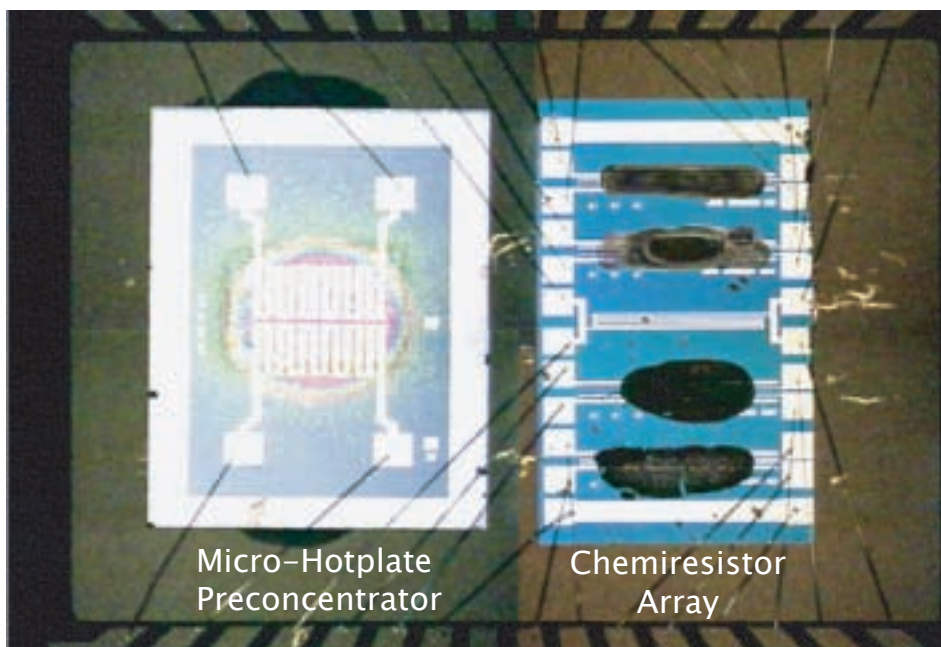
Figure 4.3. Sandia National Laboratories' micro-hotplate pre-concentrator and chemiresistor array wirebonded in a dual-inline package

dynamic, equilibrium extraction device [48]. It uses a polydimethylsiloxane (PDMS) coating, which is a material often used for GC column coatings that has low adsorptive capacity and low desorption temperature of $120\,^\circ$C. Hence, they report limited preconcentration factors and very small breakthrough volumes for benzene, toluene, ethylbenzene, and xylene (BTEX).

Sandia National Laboratories has developed several versions of a microscale hotplate-based preconcentrator for dynamic equilibrium extraction and sample introduction for GC analysis of targeted chemical warfare agents [49], [50], [51], [52]. Their first preconcentrator uses a silica gel adsorbent for targeted chemical warfare agent detection such as dimethyl methyl phosphonate (DMMP) [49]. Its size is $4.5\,\text{mm}$ by $6.5\,\text{mm}$ and has a heated area of $2.5\,\text{mm}$ by $2.5\,\text{mm}$. The sample collection time is 30 to $60\,\text{s}$ for an input 5 ppm concentration, and the thin-film membrane design has heating rates up to $1000\,^\circ\text{C/s}$. The rapid heating rate is achieved with a very low thermal mass configuration since the target application is chemical warfare agent detection. The power for this heating rate has not been reported. The emphasis is not quantitative analysis but response speed and short cycling time. Therefore, the adsorbent material is determined by detection thresholds. This emphasis on detection is shown in the preconcentrator-sensor array combination of Figure 4.3, where there is no column to separate analytes [50]. Sandia has also developed technology to demonstrate preconcentration with carbon nanotubes on the hotplate design [51].
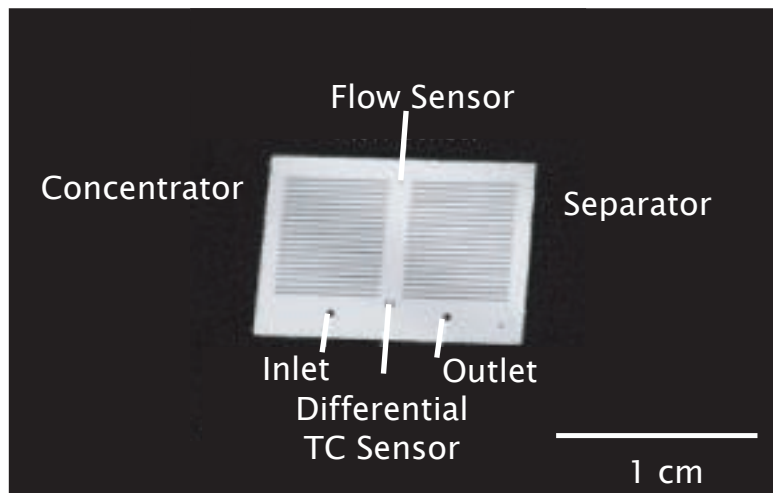
Figure 4.4. Honeywell phased preconcentrator

As a part of the Defense Advanced Research Projects Agency (DARPA) Micro Gas Analyzer (MGA) program, Honeywell has created a coated membrane-in-channel preconcentrator, integrated with a thermal conductivity detector and separation column, shown in Figure 4.4. This, too, is a dynamic equilibrium extraction device but with a twist on the injection concept. The concept behind their preconcentrator is to use heating in stages along the channel, timed precisely with the flow of the desorbed plug to boost the concentration higher than normally achievable with such a coating-based adsorbent. Details are scarce in the literature, but two speculations can be made about this scheme: to achieve successively high concentrations as the plug travels along the channel, the temperature of each stage must be higher than the last (adsorption equilibrium considerations) so that thermal isolation is of great importance; and furthermore, the plugwidth must be known *beforehand* to optimize the flow rate and stage heating since the geometry of the channel remains fixed. The latter speculation suggests that it is not easy to reap the benefits of the scheme; the physical size of the plug must match the volume in a given heating stage. One can imagine that the plugwidth can be detrimentally dispersed if it spans several heating stages that have fired in sequence to create a temperature gradient along the plug. If the end of the plug is colder than the front (closer to the outlet), then the desorption from the end will be slower, thus dispersing the peak and lowering the concentration.

The alternative preconcentrators just described are the low power and low adsorptive capacity cousins of our microdevice. Our system objective to analyze complex mixtures of VOCs quantitatively means that competitive adsorption cannot be tolerated. And all of the thin-film designs, like SPME reviewed in Chapter 3, have low adsorptive capacity. In other words, they exhibit competitive adsorption in the face of complex mixtures. Thus, the critical requirements of injection plugwidths and preconcentration factor drive us toward an architecture that is inherently more energy-demanding by virtue of the sheer amount of
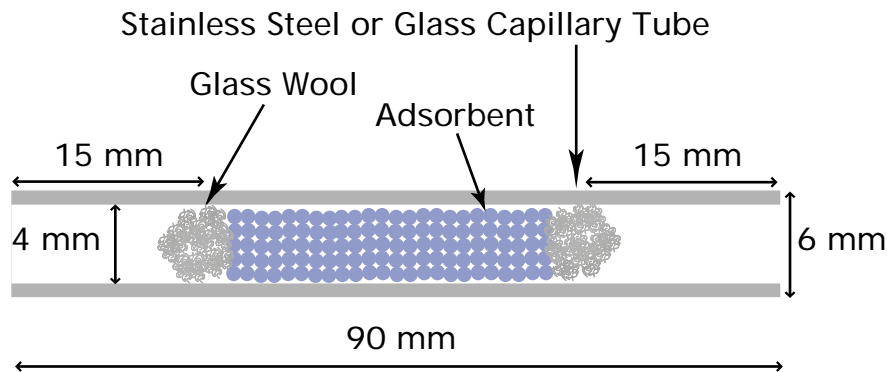
Figure 4.5. Schematic of a macroscale packed capillary tube pre-concentrator.

adsorbent necessary to exhaustively extract a large quantity of VOCs from air.

Michigan Preconcentrators

The Michigan microscale preconcentrators have their beginnings in the world of capillary tube preconcentrators. The tube preconcentrator, as diagrammed in Figure 4.5, is commercially available for dynamic exhaustive extraction and quantitative analysis for laboratory bench-top instruments [53], [54], [55]. The dimensions in the diagram highlight the inherently large dead volumes of these tubes, $\approx 380\,\mu\mathrm{L}$. Since bench-top instruments are not portable, real-time on-site sampling and analysis are not practical. As a result, for EPA indoor air monitoring methods, the solid adsorbent tubes are taken to field sites to capture the analytes, brought back to the laboratory, and placed in a thermal desorption unit to inject the sample for GC analysis [56]. These TDUs have typical maximum heating rates of $100\,^{\circ}\mathrm{C}/\min$, maximum temperature of $400\,^{\circ}\mathrm{C}$, and $600\,\mathrm{W}$ of power for the heating block [19]. The ability to use a TDU at the inlet of a GC requires the use of a cryotrap to focus the sample at the head of the column. Chromatographers have constructed alternatives to TDUs and called them heated traps [57]. These devices are optimized to achieve the smallest possible plugwidth via ultra-high heating rates. From an engineering standpoint, these plugwidths come at the expense of variable AC transformers that crank hundreds of Watts in power [58].

The design of the microscale preconcentrators follows a technique used in both large-scale adsorbers and tube preconcentrators. This design approach is known as the length of unused bed (LUB) technique for large-scale preparative chromatography and the Wheeler equation

for adsorptive capacity in tube preconcentrators. Both of these will now be explained.

Length of Unused Bed (LUB)

The length of unused bed (LUB) design technique is widely used in industrial-scale adsorbers for removal of trace impurities from gas streams [11] [12] [14]. The idea is that for removal (exhaustive extraction) the parameter of highest importance is the breakthrough time—the time when the exit (effluent) concentration rises above a predefined fraction of the input (influent) concentration when the adsorber is fed a Heaviside function concentration of adsorbate. In this technique, several packed adsorption columns are constructed with different bed lengths (masses) and the breakthrough time is measured for a fixed input concentration and flow rate. Since the plot of breakthrough time versus the bed length is linear, it is simple to use for the scale-up of the laboratory-scale model results. Generally LUB is a useful technique provided that the operating conditions and packed bed construction remain the same between the laboratory and large-scale adsorbers.

Wheeler Model

The LUB method is also used (under a different name) in industrial hygiene and indoor air analysis to describe the exhaustive extraction ability of packed tube preconcentrators. The straight-line plot of breakthrough time t_B against adsorbent mass W for a set fractional exit concentration C_x/C_0, is given by an expression called the Wheeler equation [59] [60]:

$$ t_b = \frac{W_e}{C_0 Q} \left[W - \frac{\rho_b Q}{k_v} \ln \left(\frac{C_0 - C_x}{C_x} \right) \right] \tag{4.1} $$

where W_e is the kinetic saturation capacity (dynamic adsorbed amount of adsorbate per gram of adsorbent) [g/g] for the selected ratio of C_x/C_0, W is the adsorbent mass [g], k_v is the first-order adsorption rate constant [min^{-1}], C_0 is the inlet concentration [g/cm^3], and C_x is the outlet concentration [g/cm^3].

The use of this equation consists of plotting the breakthrough time as a function of adsorbent mass in order to experimentally extract the kinetic saturation capacity W_e and the first-order adsorption rate constant k_v; these values are then reapplied to estimate the breakthrough time for other bed masses. The Wheeler equation is also commonly recast in terms of volume for exhaustive extraction. In addition, researchers have simplified the form of the equation by changing the term inside the logarithm from $(C_0 - C_x)/C_x$ to simply C_0/C_x. This is the called modified Wheeler equation:

$$ V_B = \frac{W_e W}{C_0} \left[1 - \frac{1}{k_v \tau} \ln \left(\frac{C_0}{C_x} \right) \right] \tag{4.2} $$

Table 4.3. Mesoscale 3-stage Preconcentrator Characteristics

Property	Units	First Stage	Second Stage	Third Stage
Adsorbent	-	Carbopack B	Carbopack X	Carboxen 1000
Adsorbent Mass	mg	8	2.5	1.8
Microcavity Volume	μL	22.85	6.09	3.73
Cavity Length	mm	21.90	5.86	3.61
Residence Time	ms	54.60	14.46	9.00
Input Sample Concentration	ppb	100		
Desorption Temperature	°C	300		
Dead Volume	μL	45		

where V_B is the breakthrough volume [L], and τ is the residence time [min]. Today, it is rarely pointed out that by changing the term inside the logarithm, the equation no longer approaches 1 as the time goes to infinity, mostly because researchers are more interested in the time or volume for breakthrough rather than the shape of the curve. The result is that the modified Wheeler equation has no physical meaning and does not describe a real breakthrough curve if we rearrange it to express the concentration as a function of time.

Application to Microscale Preconcentrators

The Wheeler equation has been described in detail because the results of a tube preconcentrator study by C.-J. Lu and E. T. Zellers have been applied to all of Michigan's microscale preconcentrators [54]. They packed their own multi-adsorbent tube preconcentrators and measured exhaustive extraction and desorption of VOCs; typical in industrial hygiene, they fit their measured breakthrough volumes to the modified Wheeler model [59]. A summary of the characteristics of their multi-stage adsorbent tube preconcentrator is tabulated in Table 4.3 [54].

The scaling of results from that study have provided the adsorbent mass requirements for all of the Michigan microscale preconcentrators, beginning with the parallel-microchannel single-stage device built by W.-C. Tian and coworkers, shown in Figure 4.6 [38]. This first device had a single adsorbent bed (single-stage) with parallel channels and used a hybrid anodically-bonded glass and silicon stack with Teflon tape for inlet and outlet gas connections. Table 4.4 summarizes the dimensions and adsorbent mass of this single-stage preconcentrator. The dead volume (not including the intraparticle void volume) is significantly less than its macroscale tube counterpart.

The second prototype was also a parallel microchannel configuration, but with three stages to demonstrate preconcentration of a wide vapor pressure range of VOCs, like the multi-
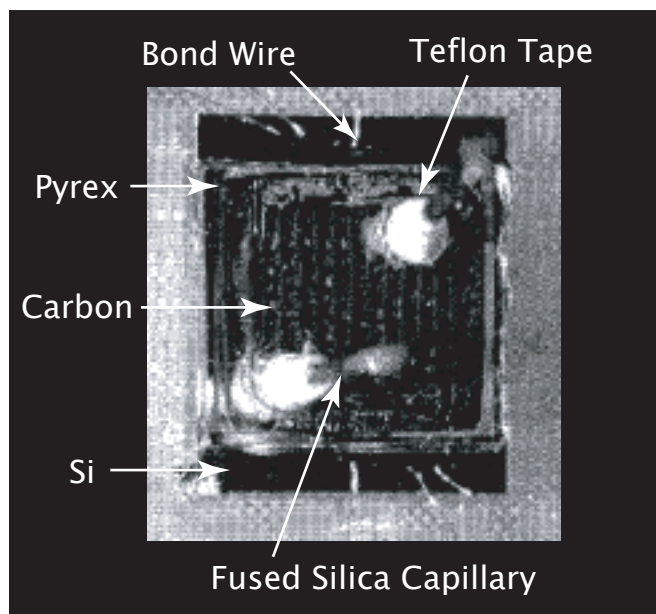
Figure 4.6. Si-glass anodically-bonded, granular carbon preconcentrator.

Table 4.4. Microscale Single-stage Preconcentrator Characteristics

Property	Units	First Stage
Adsorbent	-	Carbopack X
Adsorbent Mass	mg	1.8
Microcavity Volume	μL	3.73
Cavity Length	mm	3
Input Sample Concentration	ppm	100
Desorption Temperature	°C	250
Dead Volume	μL	1.0442

Table 4.5. Wheeler Model Parameters from Mesoscale Experiments

Parameter	Symbol	Units	Carbopack B	Carbopack X	Carboxen 1000
Kinetic Adsorption Capacity	W_e	g/g	0.189	0.371	0.802
Rate Constant	k_v	min^{-1}	43068.69	64411.08	150671.50

bed adsorbent tube [61]. Table 4.5 shows the Wheeler model parameters from a series of breakthrough experiments performed on the graphitized carbons and carbon molecular seive for the mesoscale tube preconcentrators [55]. The particle size used in the mesoscale capillary work was 250 to 425 μm for the longest dimension for Carbopack X, and 180 to 250 μm for the longest dimension for Carboxen 1000 and Carbopack B. For the current work, the longest dimension is between 180 to 212 μm for all adsorbents. The experiments were performed using a 43-compound VOC mixture at a 100 ppb concentration and 100 mL/min sampling flow rate. Using these Wheeler model parameters and substituting the new WIMS μGC sampling flow rate of 25 mL/min gives the necessary bed masses for the three-stage *microscale* preconcentrator shown in Figure 4.7 [61].

By selecting the bed masses of a microdevice based on tube preconcentrator data, the key underlying assumptions are the following:

- The mass transfer rate (k_v) does not depend on particle size nor the flow rate (Q) through the adsorbent bed.
- The flow variations through a microdevice are similar to a tube preconcentrator.
- The kinetic saturation capacity (W_e, dynamic adsorbed amount of adsorbate per gram of adsorbent) for the selected ratio of $C_x/C_0 = 0.1$ does not depend on the flow rate (Q) through the adsorbent bed.

In summary, W.-C. Tian and coworkers contributed to the field of microscale preconcentrators by creating the first single and three-stage parallel-microchannel preconcentrators with granular carbon adsorbents. And in order to build these prototypes, they scaled the empirical results of tube preconcentrators and reapplied the Wheeler equation. In terms of fabrication technology, they developed manual dry filling techniques for loading the carbons into the microchannel structures. The dry filling technique was compatible with Si-glass anodic bonding, and Au-Au bonding via rapid thermal annealing at 850 °C, both at the die-level. Finally, their analytical results showed that preconcentration of VOCs spanning a vapor pressure range of three orders of magnitude can be done at the microscale.

Initial Experiments

The predecessor Michigan prototypes have left some intriguing questions:
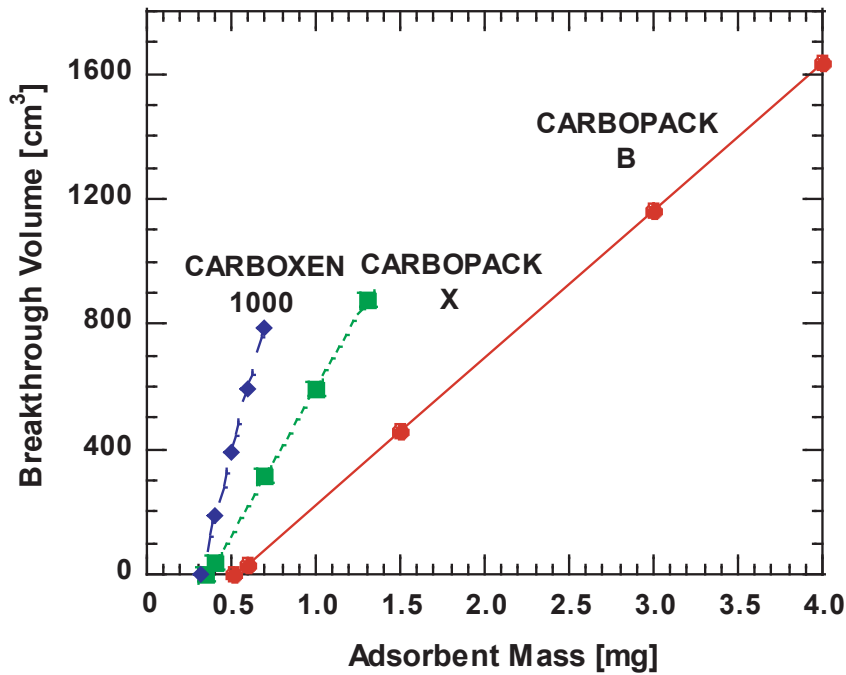
Figure 4.7. Breakthrough volumes for Carbopack X, Carbopack B, and Carboxen 1000 in a capillary tube preconcentrator.

- Can the microdevice perform exhaustive extraction? and if so, how does its adsorptive capacity compare with the scaled results of the Wheeler equation?
- Is the Wheeler equation valid at all for this design?
- What injection plugwidths are attainable via these microscale packed beds?

With these questions in mind, the first experiment in this research was to refabricate the multi-stage channel design and perform an exhaustive extraction (breakthrough curve) measurement. In the parallel microchannel design, the microchannels are $380\,\mu$m deep and $220\,\mu$m wide to accommodate single rows of adsorbent particles. The channels are bulk micromachined via deep reactive ion etching and several channels in parallel comprise a given stage in the preconcentrator structure [61].

For a breakthrough curve measurement, the preconcentrator is fed a constant concentration adsorbate, and the outlet is monitored for that adsorbate. Exhaustive extraction means that there is a finite time for which the adsorbate does not appear at the outlet. And a breakthrough curve is a set of outlet concentrations as a function of time as the inlet is fed the step function concentration. Figure 4.8 shows a room temperature breakthrough curve of 200 ppb of m-xylene in air drawn through a parallel microchannel design packed with
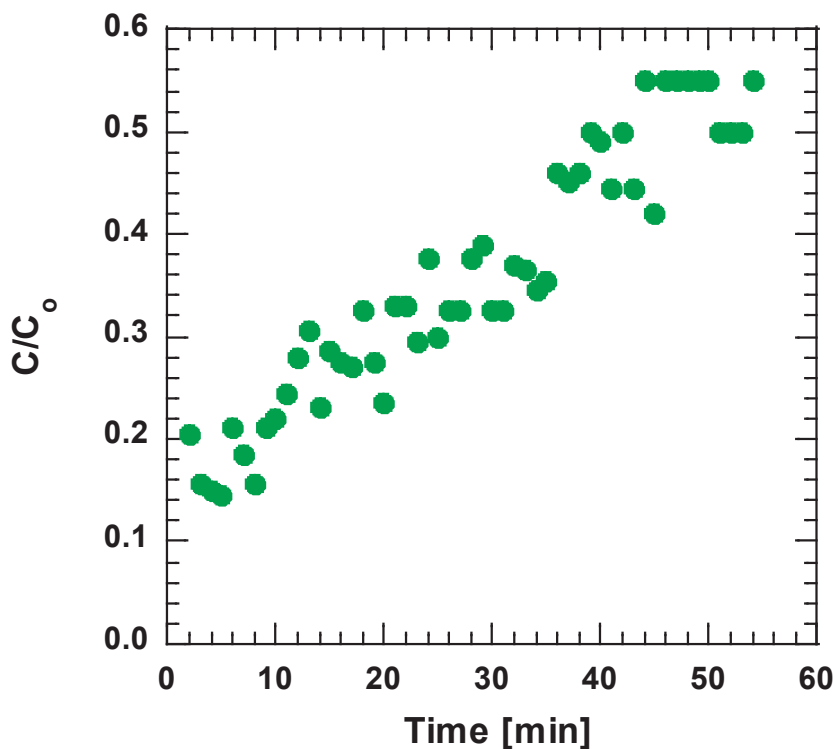
Figure 4.8. Measured breakthrough curve for Carbopack X at a
flow rate of 5 mL/min in the parallel microchannel design.

Carbopack X at a flow rate of $5\,\mathrm{mL/min}$. The concentration is 200 ppb rather than 100 ppb in order to facilitate peak integration from the measured chromatograms. The flow rate is five times lower than the initial WIMS μGC target of $25\,\mathrm{mL/min}$, and demonstrates that even under the low flow condition, which favors exhaustive extraction, instantaneous breakthrough occurs in this microdevice.

Instantaneous breakthrough means that the downstream concentration is non-zero immediately upon the start of feeding a finite concentration. The initial output concentration should be zero if the extraction is indeed exhaustive. The repeatable results of this breakthrough curve measurement made us realize that there were little or no models to describe the inner-workings of microscale preconcentrators and that the simple use of scaling was naively optimistic. In retrospect, the fluidic layout of parallel microchannels to contain and uniformly heat adsorbents, along with manual adsorbent loading, inherently introduces short paths for the input sample gas mixture. Thus, the effective adsorbent capacity was reduced and premature compound breakthrough was measured. The breakthrough was determined by the least-loaded microchannel and not by the total amount of adsorbent mass in the device, hence it could not be easily used for quantitative analysis without characterizing the amount of effective adsorbent material.

These results suggests that the assumption of similar flow variation between the tube preconcentrator and the microscale design cannot be made. The failure of that assumption implies that scaling the macroscale tube preconcentrator data to the microscale via the Wheeler equation is invalid for this case. It is important to make the distinction that the instaneous breakthrough results do not mean that the Wheeler model does not work within the microscale. It could be possible that by packing several parallel microchannel devices and measuring their breakthrough volumes, that one could discern a trend usable for other parallel microchannel preconcentrators. However, given practical experience with packing and the small microchannel to particle diameter ratio of these designs this scenario is unlikely.

Research Focus

The previous sections have surveyed the field of microdevices for combined extraction and GC injection with an emphasis on exhaustive extraction devices for VOC analysis. Followup measurements of refabricated Michigan prototype designs have exposed a lack of design models for microdevices in general, the need for adsorbent-adsorbate interaction data, and the means for obtaining the data at the microscale. In Chapter 2 on the development of chromatography, we made a general observation: the maturation cycle of a research field consists of invention, application, and empirical/physical modeling. With the survey behind us, we are poised to point out the current state of microscale preconcentrators and how our work advances the field.

The present state of microscale preconcentrators is that proof-of-concept is emphasized while microdevice models are scarce in the literature. Therefore, a beautiful opportunity exists in the areas of validating empirical models and developing models based on physical processes. Going from proof-of-concept to a device for empirical/physical modeling is not trivial. It implies repeatable, reliable microdevice operation, controllable manufacturing, and instrumentation that can interface with and test the state of the art. Thus, the focus of this research is to build a microdevice and the instrumentation that satisfies these requirements so that we can fundamentally understand microscale packed bed designs via experiments and models. These goals are listed below:

- **Application**
  - To show the first exhaustive extraction of VOCs in air using a microscale preconcentrator.
  - To demonstrate the first narrow sample injections from a packed bed microdevice.
- **Empirical and Physical Models**
  - To test the validity of scaling the adsorbent mass from macroscale tube preconcentrators to microscale designs.
  - To develop a model of microscale adsorber dynamics (finite mass transfer resistances) and adsorbent equilibrium properties (adsorption isotherms) to predict

the concentration profile exiting the bed (breakthrough curve).

To tackle these tasks requires new microfabrication technology to quantify the adsorbent mass, new instrumentation, and measurements that can probe the true injection plugwidth from the preconcentrator. So as our departure point, we have chosen to keep the bed masses the same as the parallel channel prototype and to develop the technology to make meaningful measurements of adsorbent and preconcentrator properties.

Chapter 5

TECHNOLOGICAL ADVANCES

The road to understanding preconcentrators begins with the adsorbent mass. There is no heat capacity or adsorption capacity measurement that makes sense without it, and no model is possible without these properties. Measuring milligram masses with 10's of μg resolution adds nontrivial process complexity for microdevices. The difficulty resides with handling and contamination control throughout the weighing process. Contamination from a single fingerprint contributes about $100\,\mu$g of added mass to a measurement. Therefore, mass measurement requires that the process of introducing the adsorbent be clean. Vibrations from walking by an instrument, drafts, and dust must also be strictly kept to a minimum for a sensitive analytical balance to give reliable results.

The practical difficulty for incorporating mass measurement into the fabrication process is probably the main reason that proof-of-concept microdevices leave it out. We notice a dearth of design models in the literature even though technically, design models can exist with adsorptive properties from the macroscale. Verification, though, does require the adsorbent mass in the microdevice to be known. Since our goal is to understand the microdevice, and mass is so fundamental, we begin by solving this technological problem: how to have a fabrication process that includes reliable adsorbent mass measurement. This chapter describes newly developed *quantitative* adsorbent-solvent loading technology that enables microscale exhaustive extraction and sample injection measurements to mean more than they have in the past. No less important are the additional design problems for this research listed below. Each one addresses a critical need left behind by the predecessor preconcentrators in the field.

- To create a reliable structure that interfaces reversibly (i.e., can be removed from packaging) with a laboratory GC to obtain mass transfer data. This allows functional verification prior to μGC system integration and facilitates making models for the device.
- To integrate reliable, repeatable temperature sensors into the device for heat transfer measurements.
- To develop a wafer-level integration process to improve manufacturing throughput.
- To build a thermally-isolated hybrid package to improve power consumption for rapid heating.
- To build measurement setups that interface with the preconcentrator and do little to alter its native performance.

This chapter reviews the structure for the preconcentrator and the technology to build it. Chapter 6 goes over system interfacing, modular testing for functional verification, hybrid packaging for thermal isolation, and thermal models.

Existing Adsorbent Loading Technology

Granular and pelletized forms of graphitized and molecular sieve carbons are used for quantitative analysis at the macroscale, such as purge and trap tubes for VOC extraction from liquids and multisorbent tubes for air sampling [62] [63]. To determine the mass of carbon inside a glass or stainless steel tube, the tube is weighed before and after the carbon loading. The loading process for granular carbons is to pull them via house vacuum into a tube where one end is plugged with glass wool and a stainless steel mesh screen. The wool and the screen prevent adsorbent escape through that end. Once the desired amount has been vacuumed into the tube, the other side is also plugged with wool and a screen. Typically, tube preconcentrators hold up to $10\,\mathrm{mg}$ of adsorbent granules and the diameter of the granules is $500\,\mu\mathrm{m}$ in order to avoid prohibitively high pressure drops across the adsorbents [64] [55]. From our own experiments with constructing glass tube preconcentrators, we found that for low adsorbent masses $< 1\,\mathrm{mg}$ the pressure drop can be significantly determined by the glass wool packing density.

The present work uses a multiple-sorbent configuration for quantitative trapping of VOCs, but it uses finer mesh size adsorbents with diameters of 180 to $212\,\mu\mathrm{m}$ to improve compound uptake rates. Our preconcentrator consists of three stages loaded with 0.8, 1.0, and $1.5\,\mathrm{mg}$ of adsorbent, respectively, and includes integrated heaters and Pt resistance temperature detectors. A vacuum loading method is not practical for a wafer-level process at the microscale because a single wafer has many die. The small 180 to $212\,\mu\mathrm{m}$ diameters of the granules makes physical tweezer manipulation impossible and the desire to preserve the mesh size of the adsorbent precludes any method of assembly that will crush or alter the granule size. Therefore, adsorbent manipulation in a controllable fashion is the key processing technology for the production of microfabricated preconcentrators based on granular adsorbents.

Previous microfabricated preconcentrators with granular adsorbents were integrated at the die level using a stencil mask and an Al-foil funnel dry-fill method [38] [61]. In the dry fill method, a Si through-etched stencil is placed on top of the die to cover adjacent stages while a given stage is being loaded with the carbons being dropped from the Al foil funnel that is manually positioned and has an opening $\approx 2\,\mathrm{mm}$ in diameter. Preventing inter-stage mixing or cross-contamination of one type of adsorbent in another stage is absolutely critical to the successful implementation of a multistage preconcentrator. The point is that compounds are to be trapped onto the adsorbent beds in the order of increasing volatility so that desorption is efficient. The lowest volatility (high boilers) are to trap onto Carbopack B, while the highest volatility (low boilers) should trap on Carboxen 1000. Were the CMS Carboxen 1000 to taint the Carbopack B bed, the low volatility compounds would imme-

diately get sucked into the micropores where they would be more difficult to desorb. The result would be to nullify the benefit of the macroporous Carbopack B. Figure 5.1 shows a stencil on an empty microchannel preconcentrator. The stencil mask is a cut-out rectangle and the microchannel device below it has the rows of Si slats to contain single rows of adsorbent particles.
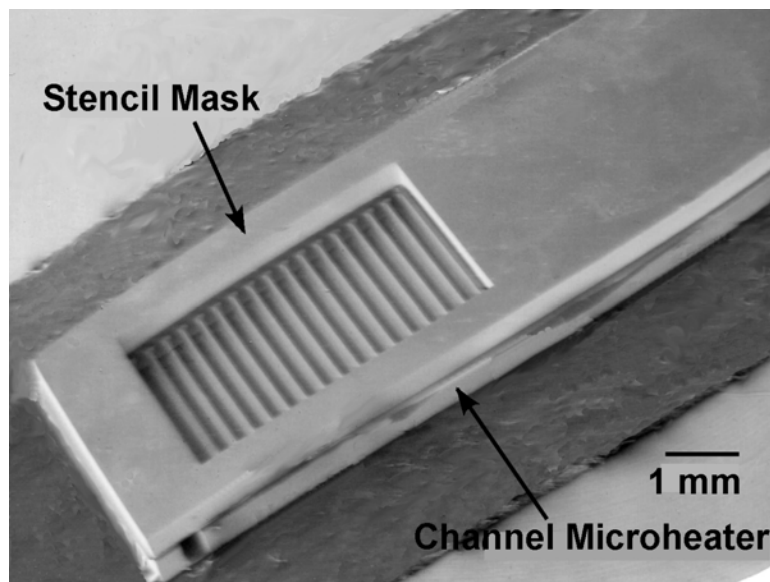
Figure 5.1. Predecessor Si channel microheater covered with Si stencil mask for dry loading. The slats are part of the channel preconcentrator structure while the stencil mask is a rectangle etched away in the Si.

The stencil masks are necessary because of the spread in trajectories of the falling granules from the funnel and the tendency for elastically-colliding granules to bounce onto the die surface as well as into adjacent stages. The processing strategy that enables device construction with the dry fill technique is to over-fill a given stage and then remove excess granules using an electrostatically charged probe. However, the drawback is that the amount removed cannot be precisely controlled. Figure 5.2 shows a microchannel preconcentrator during the dry filling process. Once the microchannel die is full, a Si sealing die with an evaporated Au bonding layer is manually placed on top, and the assembly is bonded in a rapid thermal annealing chamber at $850\,^{\circ}\mathrm{C}$ for $3\,\mathrm{min}$ [61].

Our first attempts included two approaches: to include carbon weighing prior to filling, and to implement before-and-after weighing of a loaded microstructure. Both of these attempts failed. Trying to incorporate a measured amount of carbons via the funnel method did not work, and the major reason was that of random trajectories and lack of control for particles falling through the funnels. In fact, even in the scientific literature, researchers are still working on the dynamics of grains falling through tapered openings—the so-called
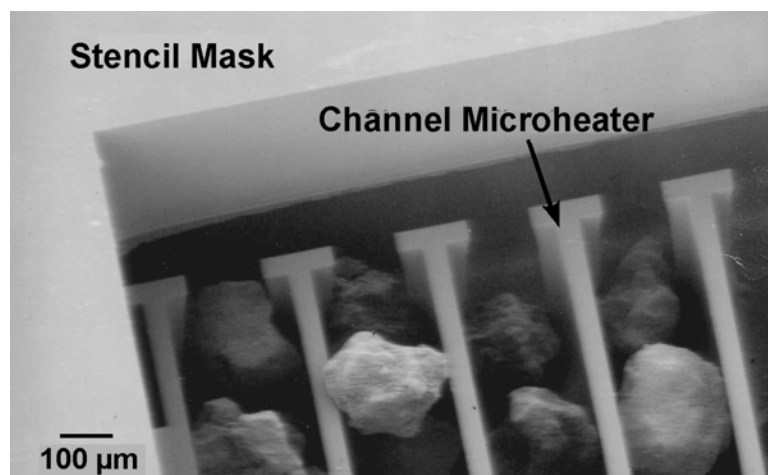
Figure 5.2. Dry filling of carbon adsorbents using stencil mask in the predecessor parallel microchannel preconcentrator. The slats are part of the channel preconcentrator structure while the stencil mask is a rectangle etched away in the Si.

hour-glass tick or silo hiccup problem [65], [66], [67].

The results of the hourglass papers, while interesting, were difficult to use practically because of the varied shapes of our carbons. So we moved on to the approach of measuring the microchannel device before and after carbon loading. While this was successful for single stage devices, electrostatic charging made it impossible to do multiple stage devices where the same structure had to be pulled out of the analytical balance, recovered with another stencil mask, loaded, and weighed again. Grounding methods met with limited success. Because of the extensive handling involved with manually placing, aligning, and removing the stencil masks, interstage contamination proved to be difficult to prevent.

The present work overcomes these problems and is the first demonstration of a wafer-scale integrated, microfabricated granular-adsorbent preconcentrator. This demonstration is made possible by a new wafer-scale adsorbent-solvent cavity filling method and Si-Au bonding, which is robust to filling-solvent outgassing during the bonding cycle. Intellectually-interesting heat exchange chamber and variable-pressure-drop preconcentrator structures have been fabricated, but the cavity microheater structure is the one that is optimally filled using the new loading technique. The new adsorbent-solvent loading method consists of mixing the adsorbent with a solvent for filling, and allowing the force of gravity to pull a single drop at a time from a tapered needle (rather than injecting multiple drops). This method has several advantages over its dry filling counterpart: electrostatic interactions between carbons are avoided during loading, the surface tension of the solvent acts to keep the carbons in the cavities, successive filling is possible by administering multiple drops of the adsorbent-solvent mixture, and interstage mixing is kept to a minimum without the use of through-etched stencil masks to cover adjacent cavities.

Even after the successful demonstration of loading adsorbent particles into the cavity microheaters, the challenge of bonding the filled wafers remains. The removal of the solvent from the carbon adsorbents is critical in order to preserve the adsorptive capacity of the carbons and to enable the bonding process to occur without contamination problems. Since the preconcentrator is cycled to a temperature of $300\,°C$ during thermal desorption and a hermetic seal is necessary to ensure that only the inlet can allow VOCs to enter the preconcentrator, the Si-Au eutectic bonding system was investigated for this application. The critical difference between the present application for Si-Au eutectic bonding and other studies reported in the literature is the presence of granular carbons with residual amounts of 2-propanol which are expected to outgas in a vacuum bonding environment.

The techniques developed in this work are generalizable to microscale packed bed reactors and to wafer bonding in the presence of solvents. The next sections present the experimental details and analysis of these technological developments.

Cavity Microheater Fabrication

To address the challenge of flow nonuniformity during the vapor trapping cycle posed by the parallel microchannel and slat configurations of the above-mentioned large capacity preconcentrators, the present work features a large cross-sectional area, series microcavity structure for the stages, and a new method for filling and sealing the microcavities at the wafer scale to improve adsorbent distribution uniformity. Table 5.1 summarizes the design characteristics of this device. The target mass in each stage is $1.2\,mg$ of Carbopack B, $0.8\,mg$ of Carbopack X, and $0.64\,mg$ of Carboxen 1000. The bed length and depth are $2.58\,mm$ and $450\,\mu m$, respectively, while the width of each of the beds corresponds to the amount of adsorbent needed to cover the vapors of its volatility range. The width of the Carbopack B bed is $4270\,\mu m$, Carbopack X $2405\,\mu m$, and Carboxen 1000 $1570\,\mu m$. The corresponding internal volumes are 4.41, 2.54, and $1.63\,\mu L$, to accommodate the desired adsorbent mass necessary for preconcentration [68].

The heater is the bulk Si structure itself and the doped regions for ohmic contacts to the Si are on the backside of the device. During heating, current flows through the bulk Si. Temperature measurement during device operation is critical since one of the primary functions of the device is to rapidly heat the carbon particles for thermal desorption of preconcentrated compounds. The Pt resistance temperature detector (RTD) is chosen for temperature sensing due to its linearity, ease of readout, stability over time and environmental factors, and simplicity of fabrication. The Pt RTDs are located on the backside of the device, isolated from the bulk Si with a thermal oxide. Lead resistance error is mitigated through the use of a four-wire configuration (two contacts for source current, and two for voltage measurement), and the nominal resistance at room temperature is chosen to be $4.5\,k\Omega$ to take advantage of the measurement range with best resolution of our instrumentation. The self-heating error of the Pt RTDs for a $100\,\mu A$ input current is 0.45Ω which is equivalent to $0.02\,°C$ when the temperature coefficient of resistance (TCR) is $4060\,ppm/\,°C$. The

Table 5.1. New 3-stage Characteristics

Property	Units	First Stage	Second Stage	Third Stage
Adsorbent	-	Carbopack B	Carbopack X	Carboxen 1000
Microcavity Volume	μL	4.41	2.54	1.63
Cavity Width	μm	4270	2405	1570
Residence Time	ms	10.60	5.95	3.89
Cavity Length	μm	2580		
Input Sample Concentration	ppb	100		
Desorption Temperature	°C	300		
Dead Volume	μL	1.70		

TCR of the Pt RTDs was measured inside an oven with a thermocouple in contact with the sample, which soaks for 30 min at the given temperature to ensure thermal equilibrium. The accuracy of the thermocouple and readout circuitry is ± 1 °C, which indicates that self-heating error is not of consequence relative to the calibration error of the thermocouples and the oven used for RTD calibration.

The microcavity preconcentrator is fabricated from two Si substrates: one for the micro-cavities and integrated resistance temperature detectors (RTDs), and another for sealing the cavities and providing gas inlet/outlet flow ports. Figure 5.3 shows the components of the preconcentrator relevant to the gas flow path. The top is an illustration of the sealing wafer whose fluidic function is to provide the inlet and outlet gas interface to external components via fused silica capillaries. The bottom shows an SEM of a plasma-etched Si cavity microheater with a stage for Carboxen 1000, Carbopack X, and Carbopack B from left to right. Each cavity is bounded by pillars which keep the adsorbents in their respective cavity. Flow channels between each channel direct the vapors to the rows of pillars along the tops and bottoms of each cavity. The dimensions of the cavities are designed to accommodate the mass of carbon adsorbent necessary to achieve exhaustive extraction of 100 ppb levels of 30 to 40 VOC-mixtures present in indoor air samples of interest to the US Environmental Protection Agency [69]. The Carbopack B cavity width is $4270 \, \mu$m, Carbopack X $2405 \, \mu$m, and Carboxen 1000 $1570 \, \mu$m while the lengths of each cavity are $2580 \, \mu$m. The corresponding volumes of each stage are: 4.41, 2.54, and $1.63 \, \mu$L [61].

The Si cavity microheater, with integrated temperature sensors and heater electrical contacts on the backside, is etched from the frontside using reactive ion etching to a depth of $450 \, \mu$m. It is then filled with adsorbents in the cavities and subsequently sealed at the wafer-level using Si-Au eutectic bonding. The sealing wafer provides gas inlet and outlet ports, which are formed by reactive ion etching of Si, for connection to the rest of the μGC system.
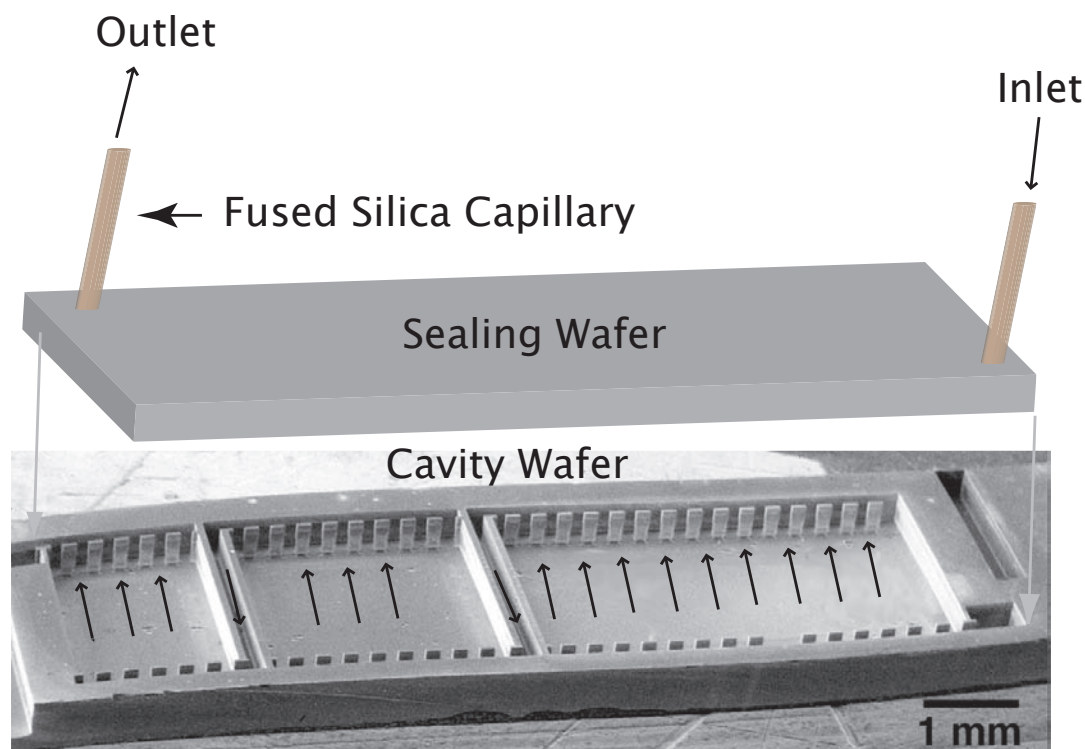
Figure 5.3. Flowpath illustration for the preconcentrator. The sealing wafer has fused silica capillaries at the inlet and outlet (top), while the 3-stage cavity microheater has a meandering flow path through alternating cavities ($450\,\mu$m deep and fabricated by deep reactive ion etching of Si).

Adsorbent Granule Loading into Cavity Microheaters

Wafer-scale cavity filling technology is the first challenge for wafer-level preconcentrator integration. The implementation of adsorbent-solvent loading involves choosing a solvent, an orifice size, and an angle.

Orifice Diameter

Based on empirical studies of particles in liquids and the drop sizes which result from different orifice sizes, and the known minimum dimension of $1580\,\mu$m by $2580\,\mu$m for the Carboxen 1000 microcavity, the orifice size range was chosen to be 0.3 to $2.5\,$mm in diameter for a polypropylene needle [70]. The needle has two tapers: the main body has a $5°$ taper, and the last 3 mm at the tip has a taper of $50°$ with an orifice diameter of $0.3\,$mm.

With this orifice size, a solvent is chosen for single drop release characterisation. The Bond number, Bo, is a dimensionless parameter that describes the relative importance of the gravitational force vs. surface tension for the release of the drop and is given as [71].

$$\text{Bo} = \frac{\rho g r_0^2}{\sigma} \tag{5.1}$$

where ρ is the liquid density$[\text{g/m}^3]$, g is the gravitational constant $(9.81\,\text{m/s}^2)$, r_0 is the diameter of the orifice [m], and σ is the surface tension [N/m]. The surface tension and corresponding computed Bond numbers for several candidate solvents are tabulated in Table 5.2. The Bond numbers highlight the choice of 2-propanol as the solvent for the adsorbent-solvent mixture due to its high Bond number, implying that the release of the drop from the orifice is facilitated easily through gravitational force. For low Bond numbers, the surface tension force is greater than the gravitational force, thereby acting to keep the droplet inside the needle. Additional considerations for the selection of 2-propanol are its high volatility (low boiling point), which facilitates easier removal from the carbon adsorbent, and fewer residues compared with acetone. CMOS grade 99.5% 2-propanol is used for all experiments since it has a low $4\,\text{ppm}$ residue after evaporation, small water content 0.05%, low count of 8 particles $> 1\,\mu\text{m}$ in size in a liter bottle, and 50 particles $> 50\,\mu\text{m}$ in size in a liter bottle.

Table 5.2. Bond Number for Various Solvents with $r_0 = 1.5\,\text{mm}$

Solvent	σ [N/m]	Bo
2-propanol	0.0217	0.798
Methanol	0.0226	0.772
Ethanol	0.0228	0.763
Acetone	0.0237	0.736
Benzene	0.0289	0.667
Water	0.0728	0.302

Figure 5.4 shows a plot of the volume necessary to release a single drop of 2-propanol from the tapered needle with different orifice sizes. There are two distinct regions on the plot, which correspond to the tradeoff between ease of release and the surface area for evaporation. For orifice sizes below $1\,\text{mm}$, the diameter of the polypropylene needle is obtained by using stainless steel syringe needles of different gauges to enlarge the existing opening since it is difficult to achieve small diameters by cutting the needle. In the larger orifice diameters, the needle is cut in the $5°$ region and bored out to give its circular shape, eliminating the initial $50°$ taper. During the experiment, a $10\,\mu\text{L}$ micropipette is used to drop $10\,\mu\text{L}$ increments of 2-propanol into the needle every $5\,\text{s}$ until a single drop is released. The $50°$ taper orifices below $1\,\text{mm}$ follow the expected trend of increasing ease of drop
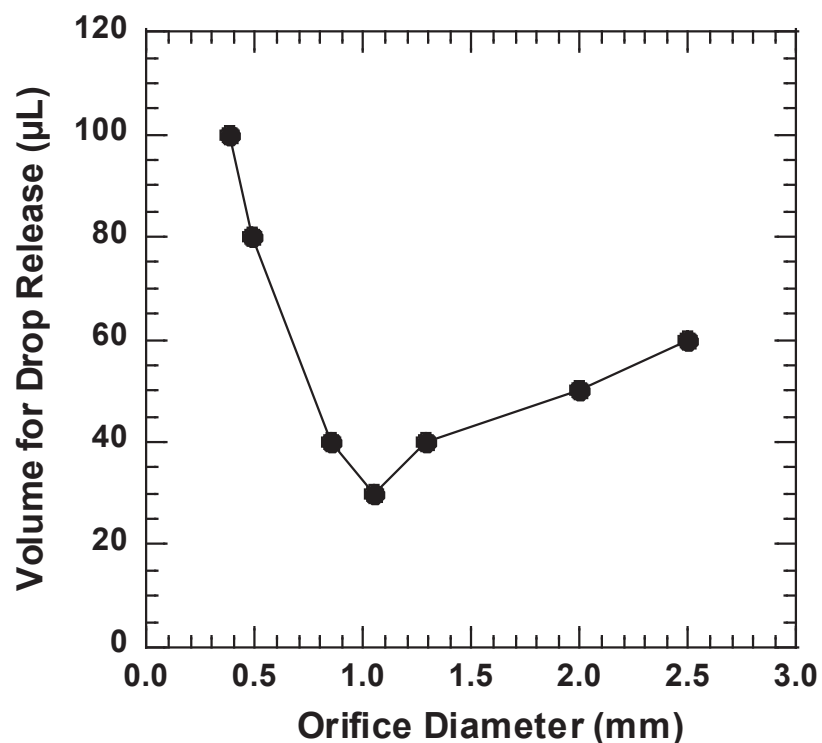
Figure 5.4. Volume for single drop release as a function of orifice diameter.

release for larger orifice diameter as the Bond number highlights. For the larger orifices ($1\,\text{mm}$ and above), the amount needed to release a single drop increases, and we observe the formation of a meniscus at the orifice opening due to the larger area for evaporation from the orifice tip.

From these results, we have chosen to use a $0.85\,\text{mm}$ diameter orifice. While 2-propanol is trapped by Carboxen 1000, it is among the highest volatility compounds trapped by this adsorbent in our application. Therefore, it can be removed with the appropriate outgassing techniques discussed in the next section.

Cavity Filling

Figure 5.5 is a schematic of the adsorbent filling method used to fill multiple cavity microheaters across a $100\,\text{mm}$ Si wafer. Each preconcentrator consists of three stages with each type of carbon residing in its own cavity as shown in the schematic. Preparing the adsorbent-solvent mixture consists of weighing the desired amount of carbon into a watch glass with an analytical balance and then filling the watch glass with 2-propanol. A syringe with tapered needle is used to draw the adsorbent-solvent mixture for introduction
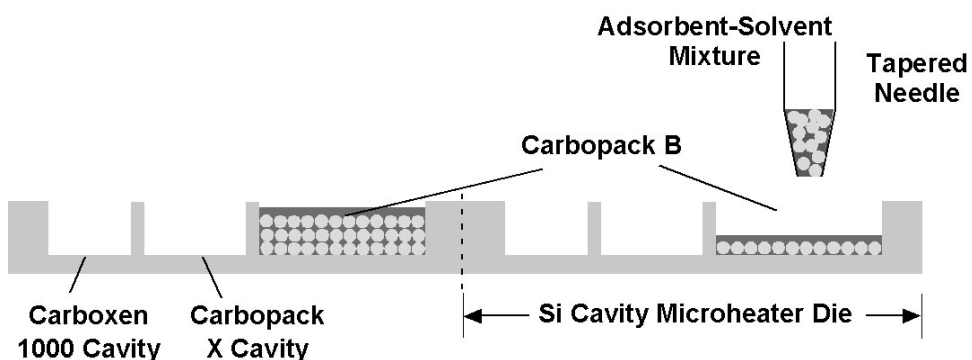
Figure 5.5. Schematic of wafer-scale adsorbent-solvent filling method with tapered needle.

into the microcavities. Each cavity (or stage) has its own quantity of adsorbent measured into its own watch glass so that the object of syringe filling is to dispense all of the contents of the glass into the cavity. Drawing up the mixture using a syringe prevents crushing of adsorbents.

The microcavities are sufficiently large that needle positioning is accomplished manually. An orifice diameter of $0.85\,\mathrm{mm}$ gives enough alignment tolerance that droplet positioning is easily achieved with or without the use of a stereo microscope. In addition to manual positioning, we have also successfully demonstrated droplet positioning and release by attaching the needle to the arm of an x, y, z micropositioner (Newport). However, the positioning accuracy of this method is not necessary for our current structure dimensions (1570 to $4270\,\mu\mathrm{m}$ by $2580\,\mu\mathrm{m}$), so we elect to use the simpler and faster manual positioning technique.
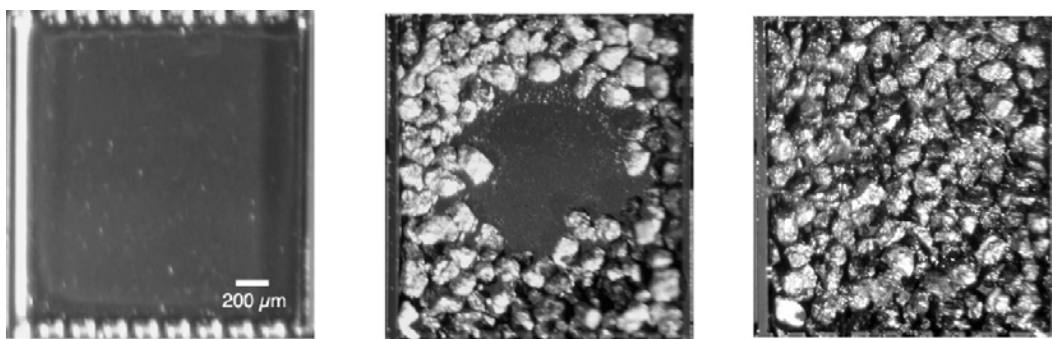
Figure 5.6. Filling of a $2580\,\mu\mathrm{m} \times 2580\,\mu\mathrm{m}$ Si microcavity with 180 to $220\,\mu\mathrm{m}$-diameter Carbopack X using the new adsorbent-solvent filling technique.

After administering a drop of a given adsorbent-solvent mixture, some of the solvent is allowed to evaporate at room temperature for $1\,\mathrm{min}$ before the introduction of the next drop in order to prevent overfilling of the cavity. If excess solvent flows into adjacent empty cavities and a faster filling process is desired, it can also be removed via capillary action by using a glass capillary tube if evaporation is too slow. The orifice size is $0.85\,\mathrm{mm}$ so that a single drop with carbons does not exceed the volume of the cavity in question.

Figure 5.6 shows the successive filling of 180 to $220\,\mathrm{mm}$ (longest dimension) Carbopack X granules into a microcavity over a time duration of $5\,\mathrm{min}$. Figure 5.6 (a) shows the empty $2405\,\mu\mathrm{m}$ by $2580\,\mu\mathrm{m}$ microcavity. This adsorbent-solvent filling method has the advantages of controllable filling and surface tension self-redistribution of the carbons as the 2-propanol evaporates. In a dry loading method, vibration is necessary to redistribute and settle the carbons to the bottom of the cavity. In this adsorbent-solvent method, the evaporating solvent redistributes the carbons towards the minimal energy configuration according to surface tension phenomena. This is seen in Fig. 5.6 (b) where the cavity is $5/8$ full and carbons move toward the walls of the Si cavity as the solvent evaporates. Figure 5.6 (c) shows the cavity completely filled with two layers of carbons evenly distributed in its interior.

A filled three-stage cavity microheater is shown in Figure 5.7 where from left to right, the stages are Carbopack B, Carbopack X, and Carboxen 1000. With the tremendous improvement in trajectory control and elimination of electrostatic interactions between carbons, interstage contamination is no longer a problem. The input sampled air with analytes to be trapped flows first through the Carbopack B stage as directed by the etched pillars which define the flow into and out of the cavity. The input air then flows into the next stage of adsorbents via $150\,\mu\mathrm{m}$ wide interstage connecting channels as shown in the figure, finally exiting the device at the end of the Carboxen 1000 stage.

The complete process of weighing, preparing the mixture, and filling takes about 20 to $30\,\mathrm{min}$ for a three-stage device and less time for a single stage device. The bulk of the time is not in the filling, but in the weighing of the adsorbent for each cavity. Great manual dexterity, attention to detail, and patience are required for this process. However, it is important to remember that this is an advance, for dexterity and patience did little to compensate for the inability to measure the adsorbent mass with the dry-fill method.

Wafer-Level Bonding and Process Integration

The second critical technology for wafer level integration of granular adsorbent preconcentrators is residual solvent outgassing and subsequent cavity sealing. The preconcentrator requires a high strength bond capable of withstanding repeated $300\,^{\circ}\mathrm{C}$ cycling during thermal desorption. A natural choice for preconcentrator integration is Si-Au eutectic bonding, where two Si wafers can be bonded together using Au above the eutectic temperature $(363\,^{\circ}\mathrm{C})$ of the Si-Au system.
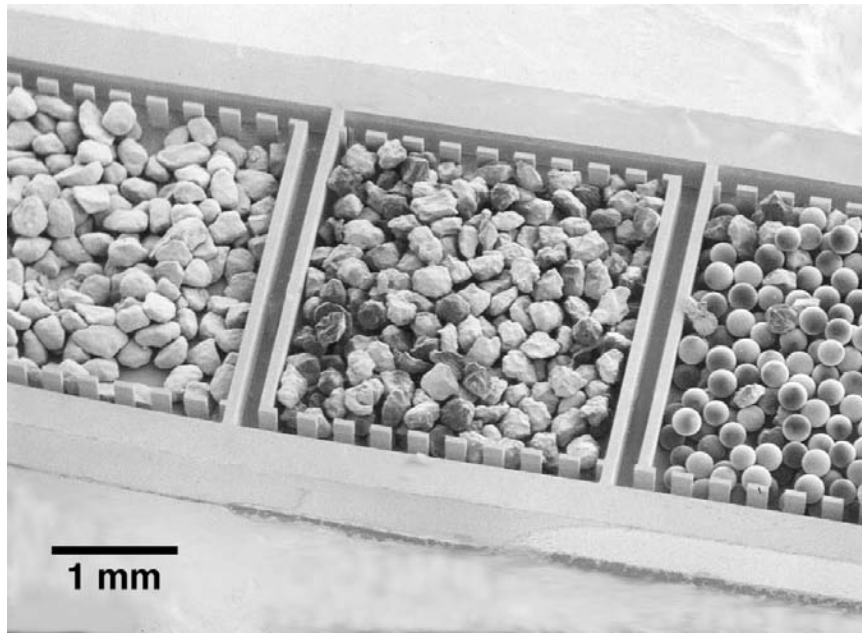
Figure 5.7. Three stages of microcavities filled with carbon adsorbents using adsorbent-solvent technique

Material Choice and Pre-bond Cleaning

It is well known that the Si surface must be free of oxide or other thin film contaminants in order for this bonding method to be successful [72]. Si-Au eutectic bonding of MEMS is typically done in vacuum chambers with clean surfaces [73], [74], [75] [76]. However, predating MEMS and wafer-bonding technologies, Si-Au eutectic has been used extensively in die-attach performed in *ambient* atmospheres so that for successful bonds the Si die is mechanically scrubbed into the Au preform to break up oxides or surface contaminants [77]. Our application, like die-attach, is not optimally clean during the bonding process due to solvent outgassing. But unlike die-attach, mechanical scrubbing cannot be used since the cavities contain the granular adsorbents which will spill out of the cavities.

Our initial characterizations of Si-Au eutectic bonding with a single Au-coated substrate and various solvent removal methods for the solvents in the carbons gave poor bonding yield. We analyzed these samples with energy dispersive x-ray analysis (EDX) and found heavy traces of organics and oxides on the bonding surfaces. Although strictly not a true surface analysis technique, the EDX results still provide evidence to support our view that the thermal decomposition of residual 2-propanol left byproducts to oxidize the uncoated Si surface [78]. For this reason, we have developed an outgassing scheme and Si-Au eutectic bonding with Au on both substrates at temperatures from 380 to $400\,°\text{C}$. This combination mitigates the need for scrubbing of the Si surface, which is expected to have solvent and oxide films, and to achieve a high bond strength from Si-Au interdiffusion. Various Au

thicknesses and outgassing sequences are experimentally evaluated for bonding yield. For a 100% bonding yield, defined as the successful hermetic sealing of all the loaded cavity microheaters on a given wafer, the empirically determined sufficient conditions are $0.5\,\mu$m of Au on the cavity wafer and $1.5\,\mu$m of Au on the sealing wafer, and solvent removal using the combination of baking on a hotplate at $300\,^\circ$C followed by one day at a vacuum of $115\,$Torr prior to wafer level alignment and bonding. Prebond preparation of the sealing wafer consists of O_2 plasma cleaning at $250\,$mTorr with $100\,$W rf power and 20% O_2 in Ar for $1\,$min.

Eutectic Bonding

Bonding is performed at a chamber pressure of $30\,$mTorr. In order to remove moisture and other adsorbed species in the bond chamber, the bonding process begins with two pump and N_2 purge cycles. Once the chamber has been pumped down to base pressure of $30\,$mTorr, heating for $300\,^\circ$C thermocompression bonding commences. At $300\,^\circ$C, a $1500\,$N force is applied to the wafers and held for $5\,$min which is typical for thermocompression bonding [79] [80]. The next stage is heating to $400\,^\circ$C (above the eutectic point of the Si-Au system) in order to achieve Si-Au interdiffusion for strong bonding. This temperature is permissible for the carbon adsorbents since thermogravimetric analyses of these carbons have shown degradation to begin at $477\,^\circ$C [45]. The force remains applied throughout the second stage; the time at $400\,^\circ$C is $45\,$min. Upon completion of the bonding cycle, the force is removed and the chamber is vented and purged with N_2 for faster cooling than in vacuum. Cooling takes $1.5\,$h to reach $150\,^\circ$C, after which the bond chamber is opened and the sample is removed and allowed to cool to room temperature.

Figure 5.8 shows an SEM of a polished cross-section of the Si-Au eutectic. The Si that has diffused into the dense Au during this process is clearly seen in the crystals of Si inside the Si-Au eutectic region in the center of the micrograph. And it is the interdiffusion that makes the bond strong and hermetic, both properties desired for the preconcentrator process.

Process Integration

The overall preconcentrator process flow is given in Figure 5.9. The heated microcavities are fabricated in double side polished p-type (100) Si with a wafer thickness of $500\,\mu$m and resistivity of $1-10\,\Omega\,$cm. A $2\,\mu$m-thick thermal oxide is grown as a boron doping mask for backside ohmic contacts and as a cavity plasma etching mask on the frontside (furnace parameters for growth are in Appendix B). The reason for the thick thermal oxide is for high dry etch selectivity. The large open etch area on the wafer brings down the overall etch rate so that the time is long and a hard oxide mask is necessary. Shallow boron diffusion is performed for $45\,$min at $1175\,^\circ$C for the contact areas on the backside, and the borosilicate glass (BSG) formed during diffusion is removed by plasma etching using $100\,$W rf power
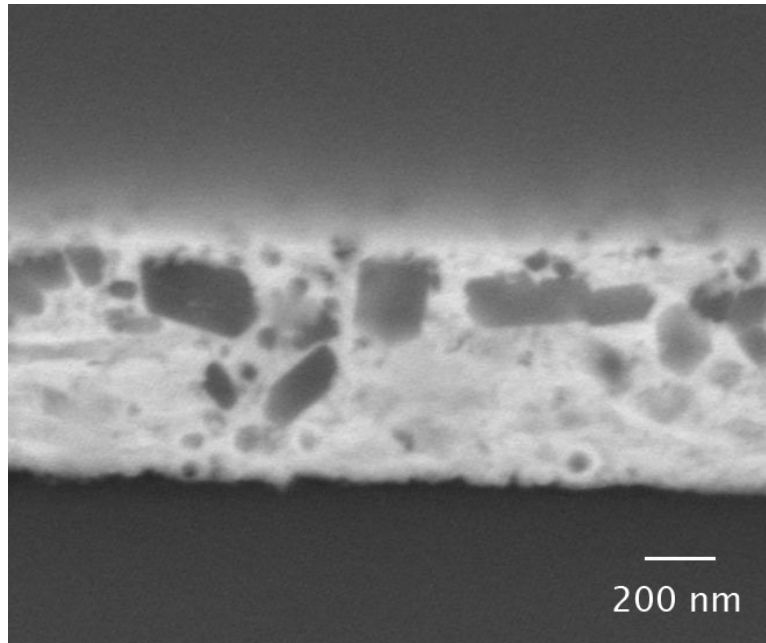
Figure 5.8. Polished cross section of Si-Au eutectic bonding from a device wafer.

with $15\,\mathrm{sccm}$ of CF_4 and $15\,\mathrm{sccm}$ CHF_3 at a pressure of $40\,\mathrm{mTorr}$ for 110 min. Electron beam evaporation of Ti/Au $100/1000\,\text{Å}$ and lift-off completes the RTDs and ohmic contacts to the backside of the microcavities, which are subsequently annealed in an oven for $2\,\mathrm{h}$ at $400\,°\mathrm{C}$.

On the frontside, the microcavity oxide etching mask is patterned via dry etching as described above, and the microcavities are etched using the Bosch process [81]. The depth of the cavities requires two dry etches, the first one at with a fast etch rate, and the second one to preserve a good sidewall profile. The latter etch consists of a $13\,\mathrm{s}$ SF_6 etch step with a stage power of $25\,\mathrm{W}$ ramped at $-0.1\,\mathrm{W/min}$, a source power of $800\,\mathrm{W}$, and a flow rate of $160\,\mathrm{sccm}$ is alternated with a $7\,\mathrm{s}$ C_4F_8 passivation step with $600\,\mathrm{W}$ of source power and a flow rate of $85\,\mathrm{sccm}$ for $2\,\mathrm{h}$ to complete the $450\,\mu\mathrm{m}$ etch depth. Finally, the frontside oxide dry etch mask is removed via wet etching for $25\,\mathrm{min}$ in buffered hydrofluouric acid (BHF) and Cr/Au $500/5000\,\text{Å}$ is evaporated for thermocompression bonding.

The sealing substrate shown in Figure 5.10 is a double side polished p-type (100) Si wafer and its purpose is to seal the microcavities as well as provide the inlet and outlet ports for gas flow through the device. The bull's eye configuration of the ports is particularly important because it mechanically secures the fused silica capillaries while preventing polyimide sealant from wicking up inside the capillary during our capillary-to-port sealing process. Previous researchers have successfully implemented this scheme for microfluidic interconnects [82].
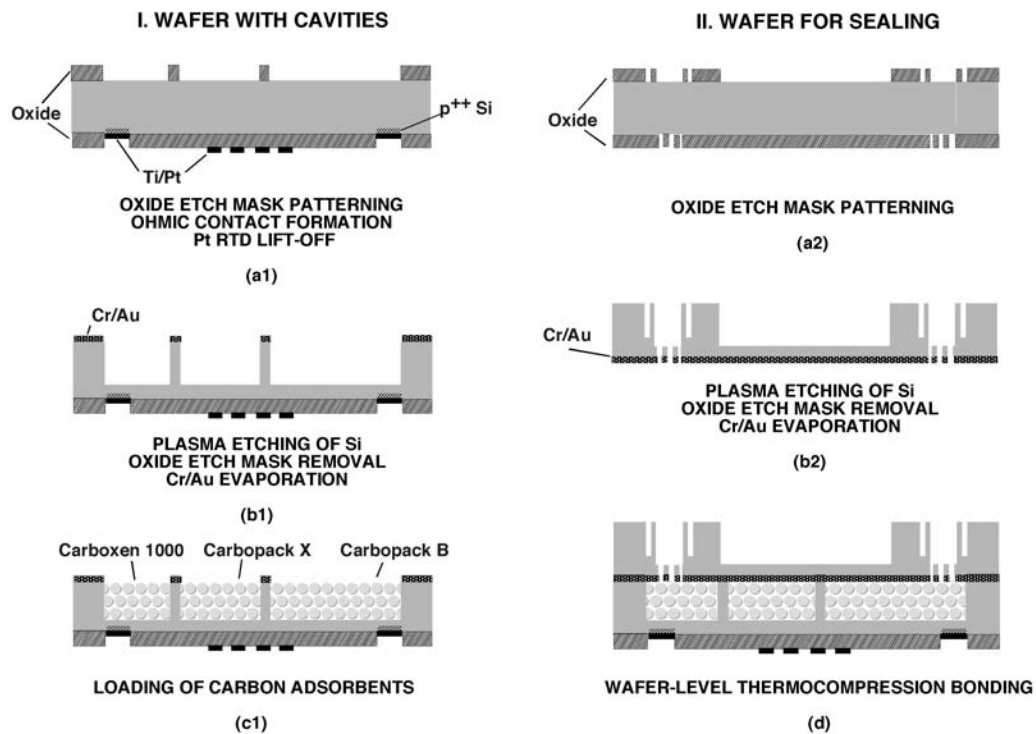
Figure 5.9. Preconcentrator process flow.

A $2\,\mu$m thermal oxide is grown as a plasma etching mask for both the front and back side of the sealing substrate. Like the cavity substrate, the etch area is large as can be seen in Figure 5.10 where the center recessed cavity is etched to reduce the thermal mass of the sealing substrate that seals the microcavities below. The etching masks are patterned via plasma etching using the CHF_3 and CF_4 chemistries as described previously. The Bosch process is used to etch both the front and back sides to open the fluidic ports and to reduce thermal mass. The thermal oxide dry etching mask is removed by wet etching in BHF, and a Cr/Au $500/5000$Å layer is evaporated for thermocompression bonding.

The loading process proceeds as described in the previous section. An analytical balance is used to weigh the carbons into curved watch glasses for each stage. Then 2-propanol is added to the watch glass after weighing so that the needle can draw up the carbons and load them into the cavities. Transport of the loaded microcavity wafer is accomplished via an aluminum foil-lined container. Prior to wafer handling, tweezers and gloves are electrostatically discharged. During bond alignment, the rough alignment step (called "preadjust") is skipped because wafer movement at mm separations increases the probability of carbons falling out of the cavities. Instead, the wafers are brought into $30\,\mu$m separation before alignment to make sure that the carbons remain inside the cavities. Bonding proceeds under the conditions described in the previous section once alignment is accomplished.

A sealed cavity microheater without granular carbons is shown in Figure 5.11 with the
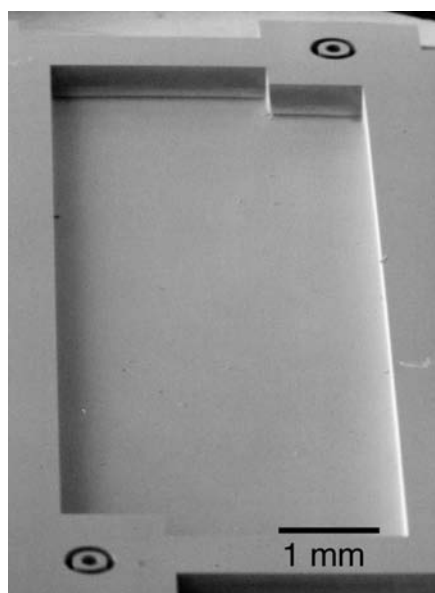
Figure 5.10. Si sealing wafer with plasma etched inlet and outlet ports for gas flow

sealing membrane partially removed to reveal the cavities below. Having a membrane rather than a solid Si piece reduces the thermal mass of the structure to reduce power consumption during microdevice heating. The gas inlet and outlet bull's eye ports for fused silica capillaries are on the two opposite diagonal corners corresponding to the Carbopack B and Carboxen 1000 cavities respectively.

After dicing, the die are removed and $430\,\mu$m o.d. high-temperature-polyimide-coated fused silica capillaries are scored and placed into the etched gas flow ports. Care is taken to cut the capillary ends as flush as possible to prevent polyimide sealant from wicking up inside the capillary. Three layers of polyimide sealing resin are used to seal the capillaries in place, and gross flow verification and leak testing is performed by immersing the device in a beaker of deionized water while pumping air through it.

Summary

In this chapter, we have shared the advances in microfabrication technology that have enabled us to construct the first wafer-level integrated cavity-based preconcentrator. We have eliminated interstage contamination problems, implemented wafer-scale loading, and incorporated adsorption mass measurements into our fabrication process. We saw that the adsorbent-solvent loading method introduced its own problem: how to seal devices that had residual solvents. But in the end, we developed a robust and compatible bonding process
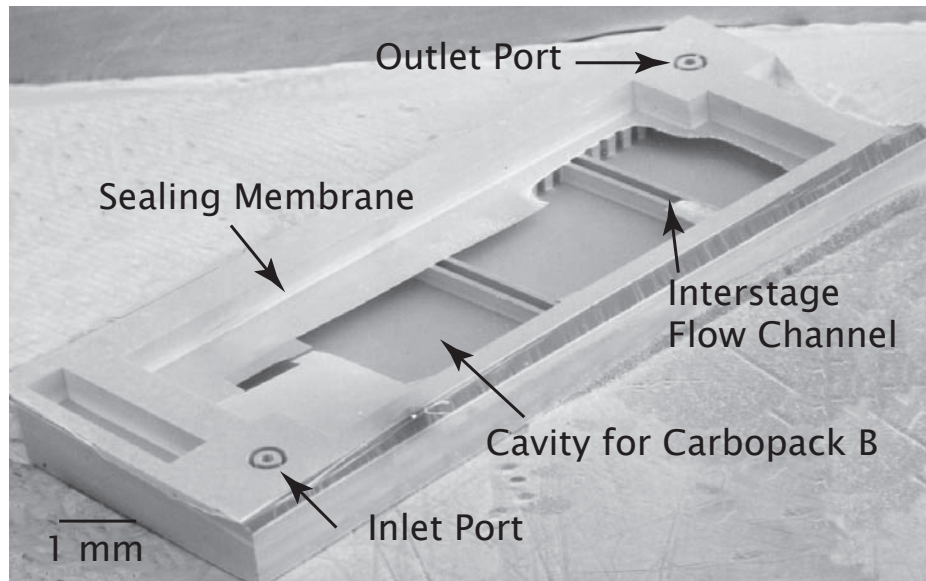
Figure 5.11. Unfilled three-stage preconcentrator with sealing membrane partially removed to reveal cavities below.

with a maximum temperature of $400\,^{\circ}\mathrm{C}$, less than half of the $850\,^{\circ}\mathrm{C}$ in the RTA approach of die-level predecessors.

Chapter 6

SYSTEM INTERFACES

The preconcentrator requires electronic and fluid flow interfaces for the macro- and micro-worlds, interchangeably. This requirement for macro-/micro- interchangability is driven by the pursuit of integrating a novel component into a functional microsystem: the macro-interface is for optimizing a preconcentrator's performance with a benchscale GC, and the micro- interface is for integrating that same device into the μGC. Note that in a production environment, we would not need to test and integrate the *same* device, and that in prototype component research, interfacing to the macro- world is enough for proof-of-concept. Hence the need for macro-/micro- world interchangability is unique in our context of pursuing component novelty and microsystem integration simultaneously.

The solution is to have two packages: a 16-pin hybrid package for the benchscale GC and a leadless chip carrier (LCC) for the μGC. And interchangability is accomplished via imper-manent mounting technology for the macro-world 16-pin hybrid package. Both the 16-pin hybrid and the LCC must be robust and work with the physical constraints (dimensions and form factor) of their respective systems. But not only must the packages be robust—the implicit daunting challenge is to create a preconcentrator that is functionally reliable and robust to copious amounts of handling for verification, optimization, and microsystem integration. If microsystem integration is to be taken seriously, the preconcentrator cannot be a research prototype in the fragility-in-handling sense. For this reason, we thermally isolate the preconcentrator via packaging rather than with a microscale isolation structure. Where there is no microfabricated thermal isolation, a thermally isolated package helps the preconcentrator save power for the portable microsystem. This chapter discusses these packaging schemes to shed light on two non-analytical μGC system interface metrics: energy usage and pressure drop. Along the way, relevant theory and calculations will be presented.

Packages

Figure 6.1 shows the effect of a preconcentrator without thermal isolation on the underlying substrate (printed-circuit board). The prototype single-stage Si-Glass prototype preconcentrator in the figure has electrical and gas flow ports on the same side making it difficult to implement mechanically robust thermal isolation [38]. As a result, the substrate not only is
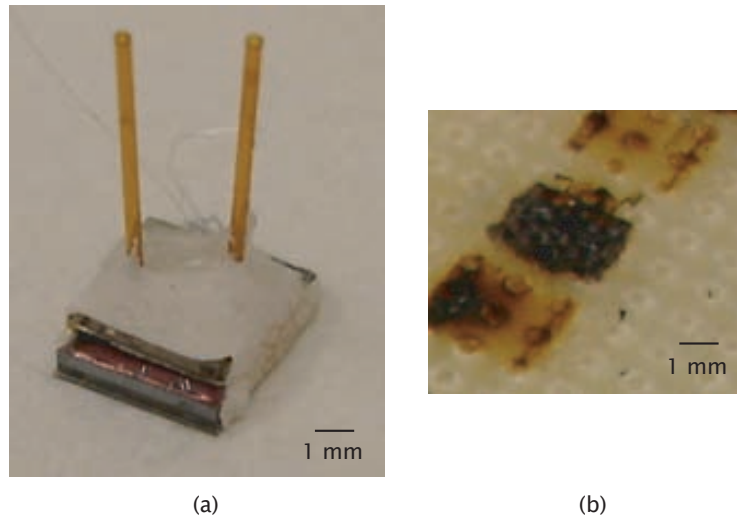
Figure 6.1. (a) Single stage Si-glass preconcentrator encapsulated in epoxy with same-side gas flow ports and electrical connections, (b) printed-circuit board testing substrate after prototype was heated to $300\,°\mathrm{C}$.

a heat sink but is also burned from the $300\,°\mathrm{C}$ desorption temperature. Therefore, the new approach is an opposite-side gas flow and electrical connection scheme to use the gas flow lines for isolation from the package. This is shown in Figure 6.2 where the preconcentrator is mounted in a macro-world 16-pin hybrid package.

To avoid direct-contact heat sinking requires the capillaries to act as preconcentrator standoffs from the package. From a heat transfer point of view, the greater the standoff distance the better, since a longer path to the package (heat sink) means a greater thermal resistance. However, as the standoff distance increases, so does the dead volume of the length of capillary. In the end, the desire for low dead volume trumps heat transfer so that the standoff distance we implement is $1\,\mathrm{mm}$. A $1\,\mathrm{cm}$-length of $320\,\mu\mathrm{m}$ capillary contributes $0.8\,\mu\mathrm{L}$ of dead volume while $1\,\mathrm{mm}$ gives $0.08\,\mu\mathrm{L}$ (0.05% of the preconcentrator's intrinsic dead volume). While the dead volume scales with length L, the heat loss goes as $1/L$ so that $1\,\mathrm{cm}$ is preferred for less heat transfer. However, once we consider wirebonding constraints, our choice of a $1\,\mathrm{mm}$ air gap isolation is doubly reasonable. Conventional ultrasonic wedge wirebonding has a step-height limit on the order of mm's and requires a mechanically stable surface. Therefore, to achieve an isolated preconcentrator while being able to wirebond means that the preconcentrator must be propped up with a removable sliver of support material during wirebonding. The slivers of material for this process are pieces of Si wafers which are carefully slid underneath the preconcentrator during the first step of packaging: affixing the fused silica capillaries to the drilled holes with water-soluble epoxy that is air dried. The water-soluble epoxy and the wirebonds, both reworkable, allow the preconcentrator to be removed from the 16-pin hybrid and repackaged into the LCC for μGC
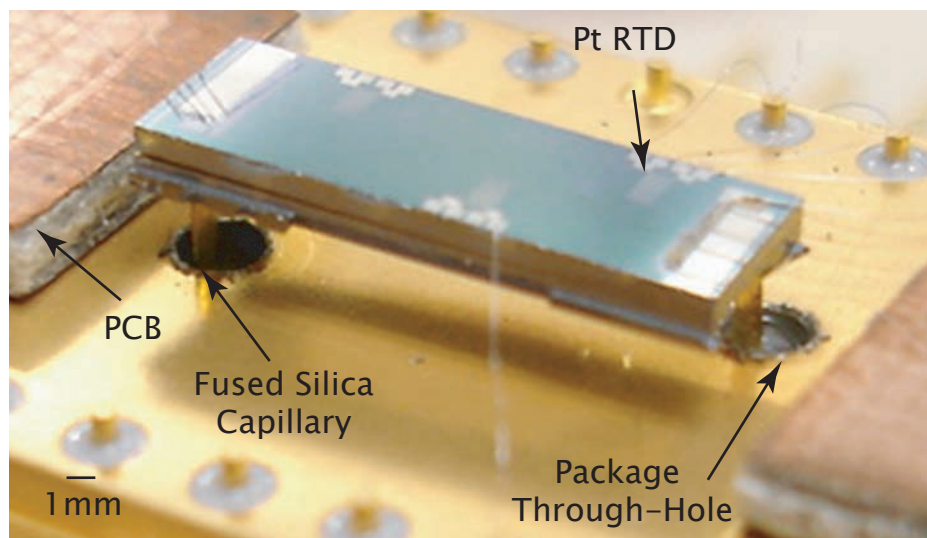
Figure 6.2. Side view of a quantitatively loaded microscale granular carbon preconcentrator mounted in a hybrid package with a 1 mm air gap.

integration.

Once the capillaries support the preconcentrator in the package, 6 to 8 Al wirebonds connect the preconcentrator to the PCB pieces for high current handling. The packaged preconcentrator plugs into a modular testing board pictured in Figure 6.3 (a) and custom-developed for reuse in several experimental setups: preconditioning, extraction and injection, heat transfer, and pressure drop. Figure 6.3 (b) illustrates the use of the 16-pin hybrid package and modular testing board in a custom fixture for heat transfer measurements in vacuum, while (c) shows a close-up of the electrical and gas flow feedthroughs on our custom-built testing fixture.

The μGC preconcentrator package is a leadless chip carrier (LCC) diagrammed in Figure 6.4. Its surface mountability makes it ideal for low dead-volume connection to the Si-glass microfluidic substrate. And for the same reason, it is a poor macro-world package because of the difficulty in reworking the electrical connections—the LCC would need to be soldered on and off of a PCB for testing while keeping the base of the LCC clean and flat for μGC integration. With the 16-pin hybrid, the pins allow easy plugging in and out of the testing board. Just as in the 16-pin hybrid, the capillaries are used as standoffs to leave a $1\,\mathrm{mm}$ air gap beneath the device and the package, while providing fluidic connection, this time to the underlying Si-glass microfluidic substrate. Solder paste at the LCC base provides electrical contact to the substrate.
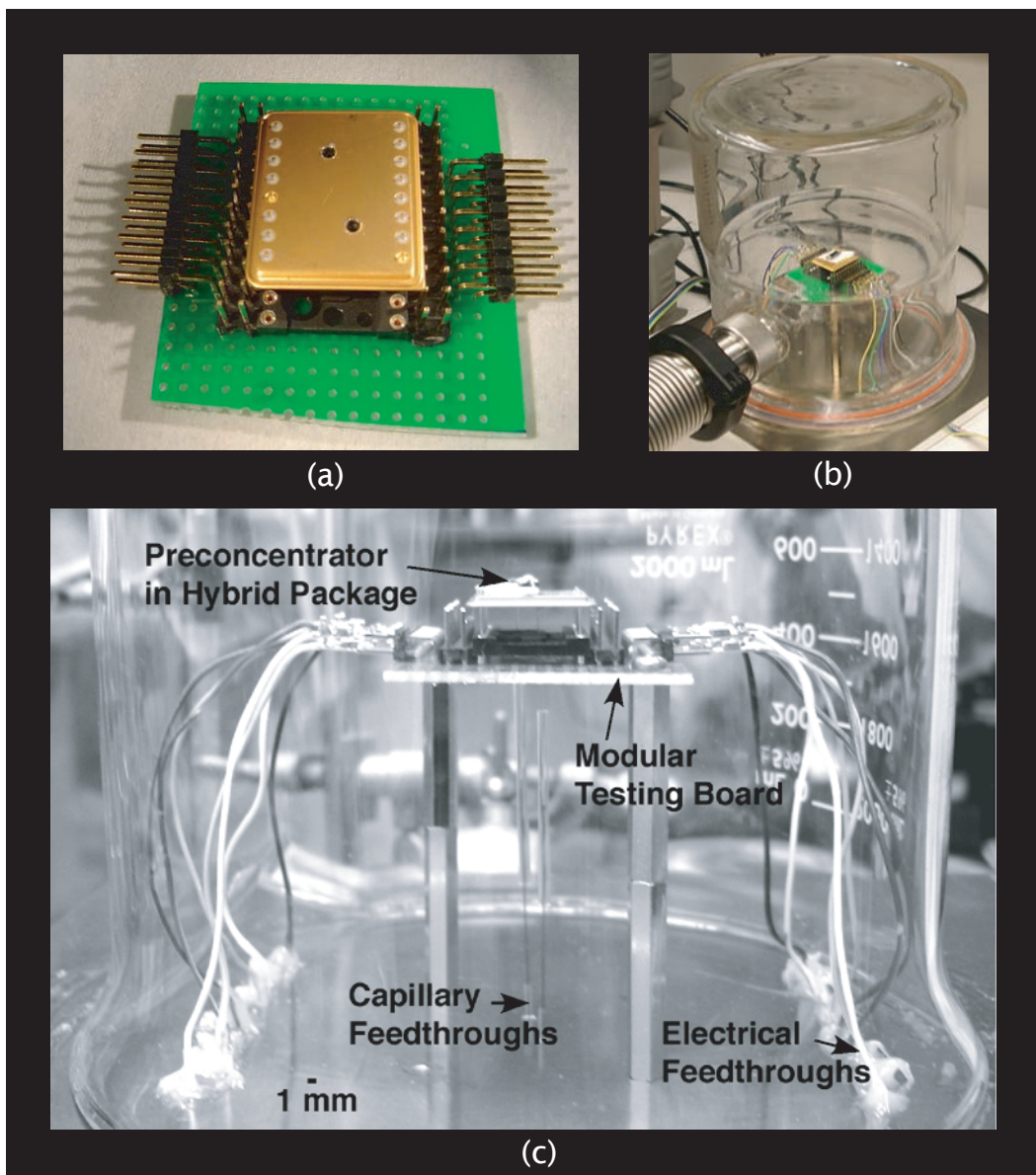
Figure 6.3. (a) 16-pin hybrid package in modular testing board where pins and sockets provide reusable electrical connections for extraction/injection and heat transfer measurement setups. (b) Preconcentrator packaged in a 16-pin hybrid and interfaced with the modular testing board for vacuum heat transfer measurements in a bell jar. (c) Custom heat transfer measurement fixture with capillary gas-flow and electrical feedthroughs, shown covered with a Pyrex beaker to eliminate error due to inadvertent forced convective heat loss from drafts in circulated room air.
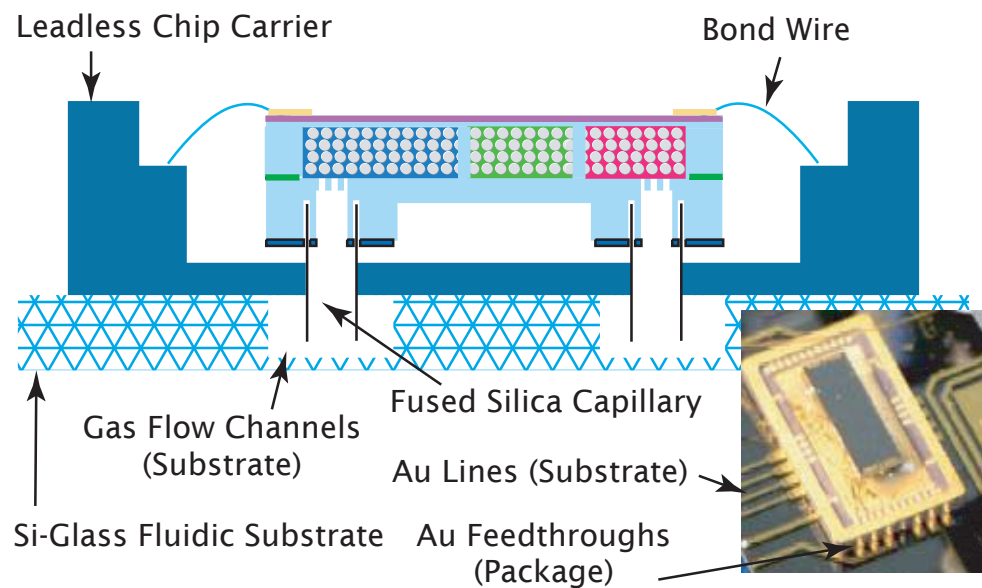
Figure 6.4. Schematic of the preconcentrator gas flow interface to the WIMS μGC fluidic substrate. Preconcentrator mounted in a leadless chip carrier on a Si-glass substrate showing the electrical interface lines (inset).

Steady-State Heat Transfer

This section outlines the heat transfer analysis for the present device and its implications for a next generation device. Understanding micropreconcentrator heat transfer is critical from the system point of view, where energy use should be kept to a minimum due to finite power source lifetime. We compute the sources of heat transfer from an isothermal device because we have a good grasp on the material properties and external transfer mechanisms. Although a model of internal heating dynamics involving adsorbent particles would be ideal, the combined fluid flow, mass, and heat transfer problem for a believable internal dynamic model is exceedingly complex and warrants a dissertation of its own. An understanding of steady-state loss gives insight into device designs and enables conclusions about system interface effects, so that is our object in this analysis.

The cases to consider for the heat transfer problem can only be understood in the light of microdevice operation scenarios. The operational scenarios are the following:

- **Sample extraction** The microdevice is at room temperature so that heat transfer modeling is not necessary.
- **Sample injection** During thermal desorption of the micropreconcentrator, power is applied to heat the device to $300\,^\circ\mathrm{C}$ where it is held with no flow for under 1 min.

Figures 6.5 and 6.6 point out the heat transfer paths for steady-state loss from the preconcentrator. Conduction, free convection, and radiation all play a role in heat loss for the microdevice and these are outlined in the next sections.

Radiation

Radiative loss is given by:

$$Q_{rad} = \sigma \epsilon A (T_s^4 - T_\infty^4) \tag{6.1}$$

where σ is the Stefan-Boltzmann constant, ϵ is the surface emissivity, and A is the radiating surface area. Radiation is considered for all the surfaces of the preconcentrator. For an over-estimate of radiative effects, we consider a worst-case emissivity of one, which is that of a black-body. Since the emissivity of single-crystal Si is generally a complex function of doping and temperature, it is difficult to justify a particular selection. So we select $\epsilon = 1$ to learn the upper-bound for the radiative loss contribution. This is shown in Figure 6.7 where the x-axis is the surface temperature in Celsius. Radiation can be virtually eliminated in future designs through the use of a low emissivity coating such as thin-film Au with $\epsilon = 0.05$ and we will come back to this shortly.
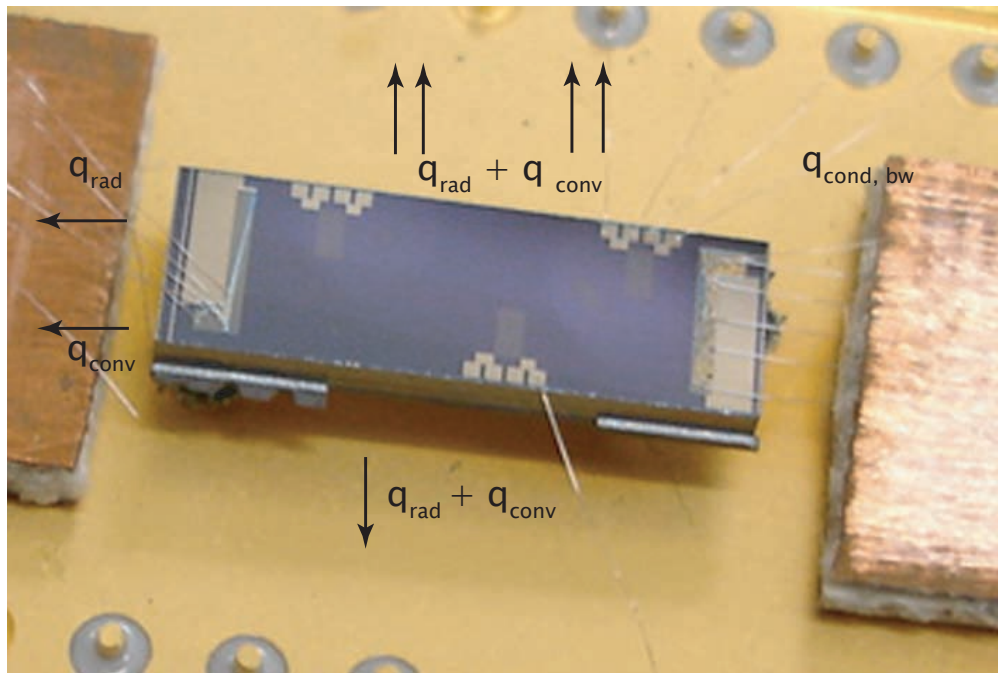
Figure 6.5. A top-view picture of lateral heat transfer paths from the preconcentrator.

$$q_{rad} + q_{conv}$$

$$q_{cond, fs} \qquad q_{cond, air}$$

Preconcentrator

Package
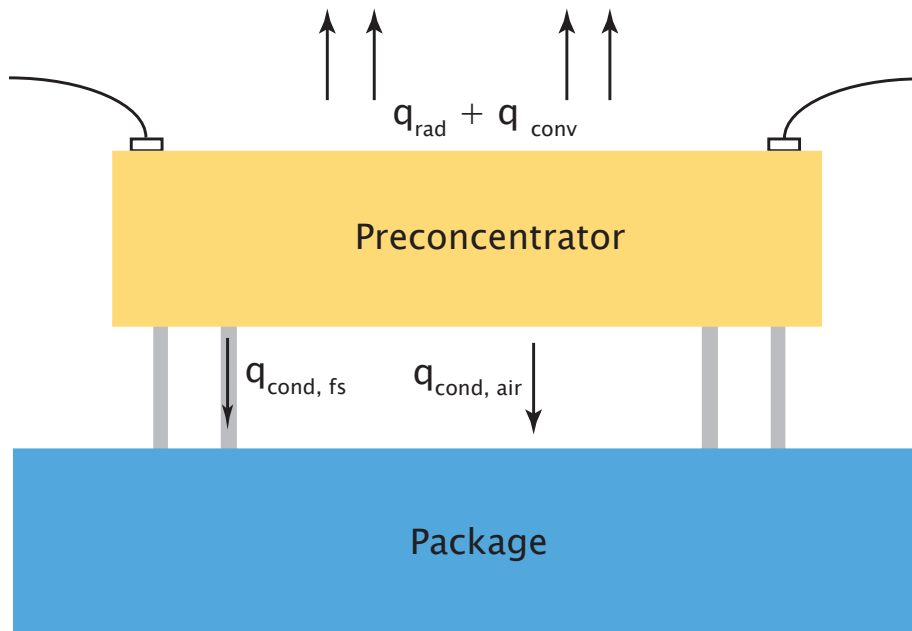
Figure 6.6. Side-view schematic showing the vertical heat transfer surfaces from the preconcentrator.

Conduction

The heat loss due to conduction, Q_{cond} in [W], is given by:

$$Q_{cond} = kA(T_s - T_\infty)/L \tag{6.2}$$

where k is the temperature dependent thermal conductivity of the material, A is the area through which conduction occurs, T_s is the temperature of the preconcentrator surface [K], and T_∞ is the surrounding ambient temperature, and L is the length geometry of interest. Heat conduction is considered for the air underlying the device to the package, the fused silica capillaries from the device which are epoxied to the package, and the electrical connections from the device to the package as shown in Figures 6.5 and 6.6. For the conduction through the air and the fused silica capillaries, $L = 1\,\text{mm}$ which is the distance between the device and the gold coated hybrid package. The area is $4\,\text{mm}$ by $11\,\text{mm}$ for air and the cross-sectional area of the $320\,\mu\text{m}$ i.d. and $450\,\mu\text{m}$ o.d. fused silica tubes. Figure 6.7 shows the contribution of conductive loss. Reduction of the static air conduction loss beneath the microdevice can be implemented via vacuum encapsulation while reducing fluidic interconnect loss requires a specialized fluidic scheme at the microscale.

Natural Convection

In natural convection, heat is transfered via fluid motion due to temperature gradients causing buoyancy forces to compete with gravitational forces to move the fluid. The energy balance and momentum balance equations are coupled in this case [83]. The Churchill and Chu correlation for vertical heated plates allows an estimate for the heat transfer coefficient which describes the free convection from the surface of the preconcentrator. The correlation is given below and correlates the Nusselt number with the Rayleigh and Prantdl numbers of over four orders of magnitude in Rayleigh numbers for heated plates [83].

The Rayleigh number describes whether the flow is laminar or turbulent in convection. It is the product of the Grashof and Prandtl numbers. The Prandtl number tells the relative importance of the inertial (viscous) forces to the buoyancy forces. When $\text{Pr} \leq 1$ then the thermal boundary layer thickness is approximately equal to the fluid boundary layer thickness, but when Pr is large then the fluid boundary layer can be greater than the thermal boundary layer. The viscosity of the fluid is high so unheated fluid will get dragged by the moving heated fluid when Pr is large. β describes thermal coefficient of expansion of the fluid, which in this case is air. The Rayleigh number is given by:

$$\text{Ra} = \frac{g\Delta T L^3 \beta}{\alpha \nu} \tag{6.3}$$

where g is the gravitational acceleration constant $9.81\,\mathrm{m/s^2}$, ΔT is the temperature difference [K], L is the length [m], β is the thermal coefficient of expansion of the fluid, which is $1/T$ when we assume that air is an ideal gas, α is the thermal diffusivity $[\mathrm{m^2/s}]$, and ν is the product of the kinematic viscosity and the thermal heat capacity for the air $[\mathrm{m^2/s}]$. The heat transfer coefficient is subsequently calculated by using the length scale relevant to the problem L, and then multiplied by the area to obtain the heat loss [84].

$$h = \frac{\mathrm{Nu}k}{L} \tag{6.4}$$

$$\mathrm{Nu} = 0.68 + 0.67\,\mathrm{Ra}^{1/4}\left[1 + \left(\frac{0.492}{\mathrm{Pr}}\right)^{9/16}\right]^{-4/9} \tag{6.5}$$

where Ra is the dimensionless Rayleigh number, and Pr the dimensionless Prandtl number. The contribution of natural convection is shown in Figure 6.7 where the x-axis is the surface temperature in Celsius. Future vacuum encapsulation of the preconcentrator will eliminate this heat loss mechanism. The sum of the contributions computed from the foregoing equations is also plotted in Figure 6.7.

The experimental measurement of steady-state heat loss is shown in Figure 6.8 under different ambients from atmospheric pressure to $50\,\mathrm{mTorr}$. These heat loss measurements are characterized in a vacuum bell jar, and for vacuum, the data are collected over several hours to reach thermal steady state. Temperature measurements are made with the Pt RTDs on the backside of the preconcentrator. The Pt RTDs are calibrated inside a convection oven with a K-type thermocouple in contact with the backside of the device to measure the device temperature. Ni/Cr wires of 5 mil diameter and insulated with silica insulator are used for the four-wire RTD feedthroughs.

At a reduced pressure of $50\,\mathrm{mTorr}$, the power required to maintain a steady-state temperature of $300\,^\circ\mathrm{C}$ is $0.65\,\mathrm{W}$compared with $1.5\,\mathrm{W}$ at atmospheric pressure. This is a 57% decrease that highlights the virtue of vacuum packaging the device. Exploring the idea of further reducing loss, we can imagine gold-coating the device to minimize radiation. Figure 6.9 shows the measured $50\,\mathrm{mTorr}$ data along with the computed steady-state loss for the case of a gold-coated preconcentrator in vacuum. This improved ideal condition allows the maintenance of $300\,^\circ\mathrm{C}$ with $0.47\,\mathrm{W}$, which is one-third of the present power consumption with no coating at atmospheric pressure.

Figure 6.10 shows the power plotted against temperature achieved at one minute heating in $20\,^\circ\mathrm{C}$ ambient air for atmospheric pressure and a $\mathrm{N_2}$ flow of 10 mL/min through the device, and no flow with the device under a rough vacuum of $2.75\,\mathrm{Torr}$. The initial power required is higher than the steady-state power needed to maintain the temperatures of interest because the air surrounding the immediate vicinity of the device is cold. Typical flow rates of interest for the preconcentrator during desorption are $\leq 2\,\mathrm{mL/min}$ for splitless injection into a standard-bore Si-glass $3\,\mathrm{m}$ microcolumn [39]. Therefore, the demonstration of very
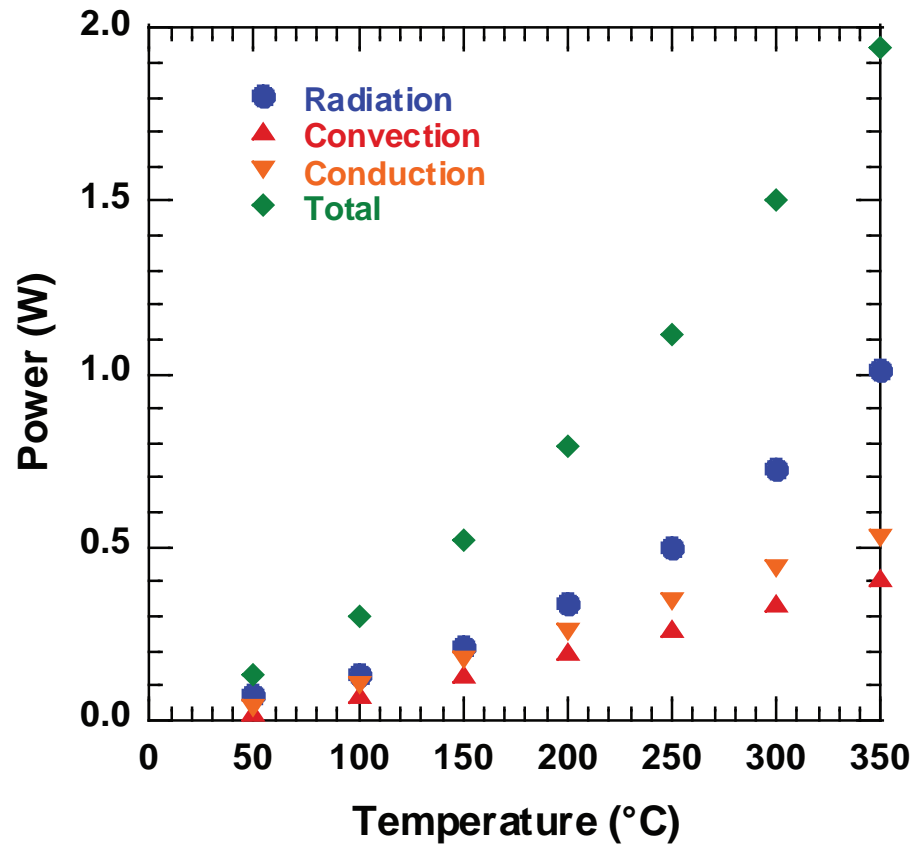
Figure 6.7. The computed contributions of steady-state radiative, convective, and conductive heat loss for the preconcentrator as a function of final temperature.
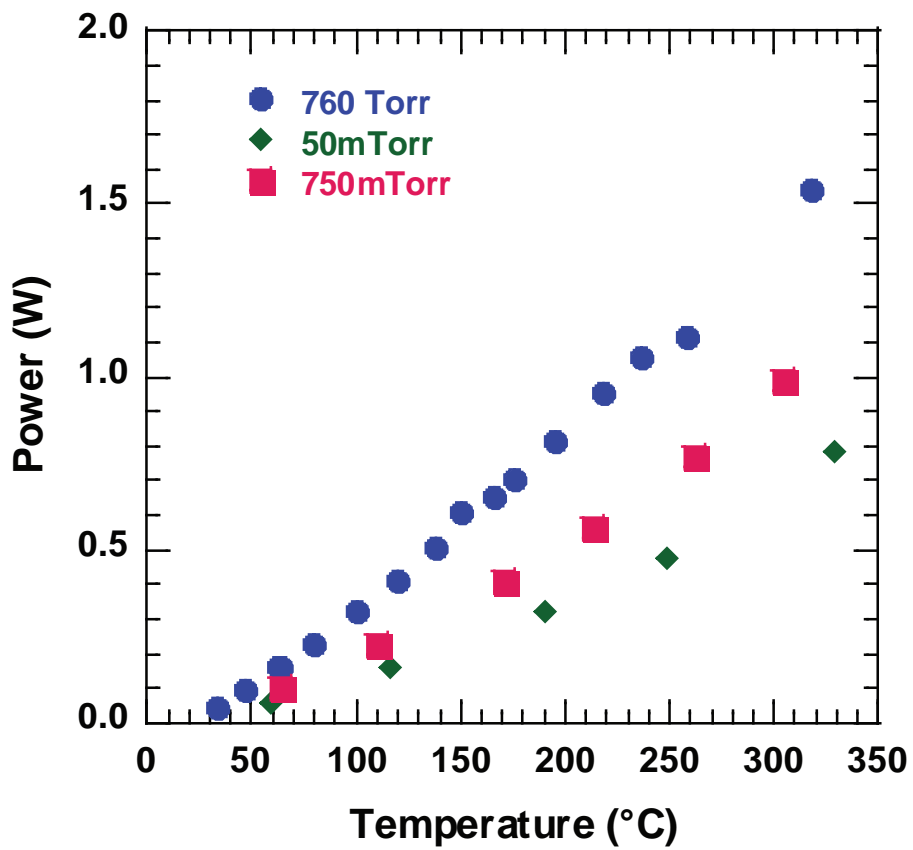
Figure 6.8. Applied power for heating in thermal steady-state at atmospheric and reduced pressures measured using integrated temperature sensors.
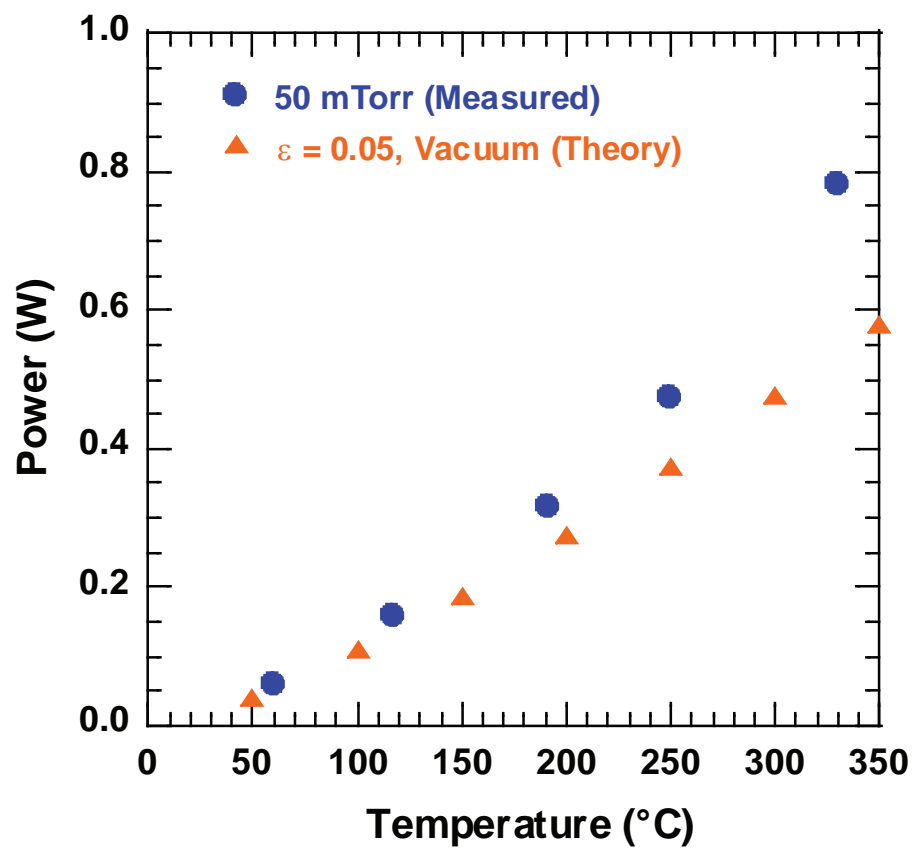
Figure 6.9. Comparison 50 mTorr experimental data for steady-state heating and computed heat loss for a gold-coated, vacuum encapsulated preconcentrator.
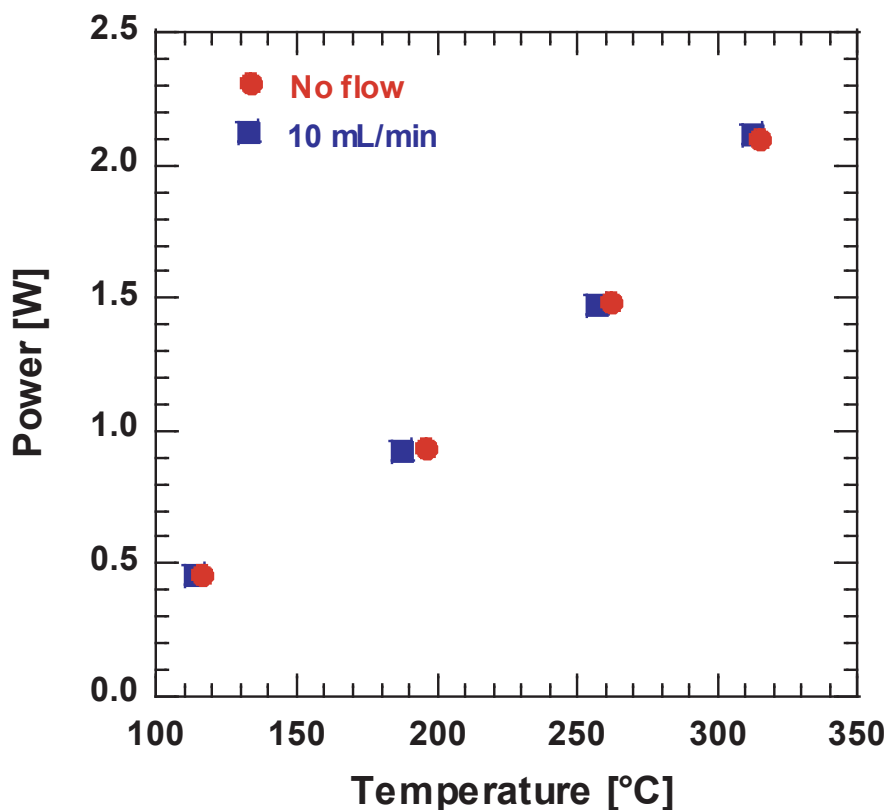
Figure 6.10. Measured power as a function of temperature for
1 min heating of a 3-stage filled microcavity preconcentrator under
no flow and 10 mL/min flow conditions.

little increased power needed at $10\,\mathrm{mL/min}$ as shown in the figure, supports the notion that forced convective loss in the device at these flow rates is relatively small compared with other heat loss mechanisms such as free convection, conduction, and radiation.

Transient Thermal Response

The transient thermal response is of interest because of heating during the sample injection mode of heating the preconcentrator to $300\,°\mathrm{C}$. The heating rate during desorption has a direct affect on the rate of desorption of the captured compounds from the adsorbents. Rapid heating rates are desired to achieve narrow bandwidths of high concentration compounds from the preconcentrator. The transient heating characteristic is shown in Figure 6.11 where the heating rate as a function of applied power is given for a device with vertical orientation. The results show a significant improvement of this preconcentrator over its single-stage prototype for the same application. Where the single-stage prototype
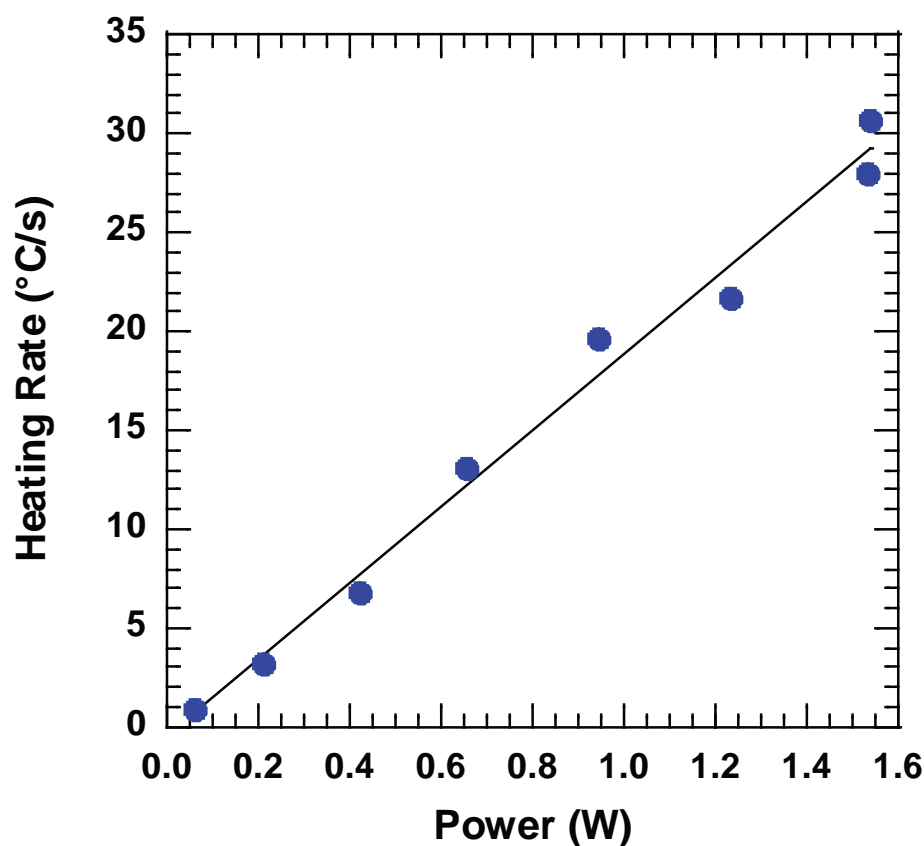
Figure 6.11. 3-stage filled preconcentrator heating rates at atmospheric pressure measured using integrated temperature sensors as a function of applied power.

needed $2.25\,W$ to achieve a desorption temperature of $250\,°C$ with a $15\,°C/s$ heating rate, the present device needs only $1.2\,W$ to achieve the same temperature and a faster heating rate of $23\,°C/s$ [38].

Pressure Drop

The wafer-level carbon loading technique along with the solvent removal and combination thermocompression/eutectic bonding process have enabled the first wafer-level integrated granular adsorbent preconcentrator. An important preconcentrator performance metric directly related to the packing of adsorbent beds is the pressure drop-flow rate relationship since it will be integrated with a microfabricated pump in the WIMS μGC.
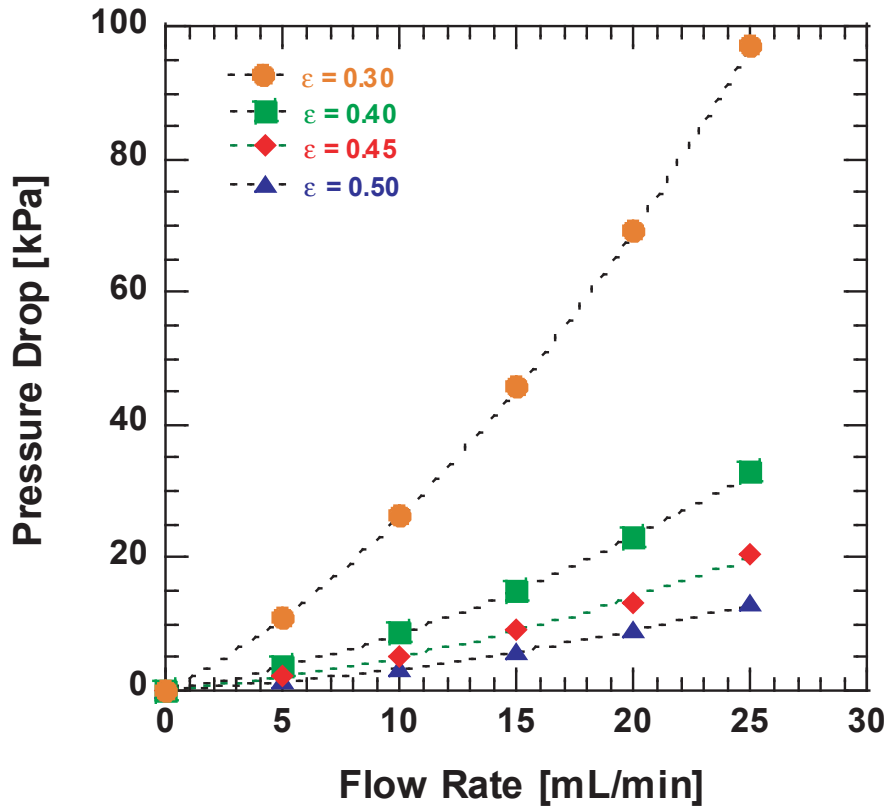
Figure 6.12. Calculated pressure drop against atmosphere at outlet as a function of flow rate for different void fractions.

The Reynold's number for a packed bed is given by:

$$\mathrm{Re}_p = \frac{D_p \nu' \rho}{\mu(1 - \epsilon)} \tag{6.6}$$

where D_p is the particle diameter, ν' is the superficial linear velocity, ρ is the density of air, μ is the kinematic viscosity, and ϵ is the void fraction.

The Ergun equation for pressure drop in packed beds is given by [85]:

$$\Delta p = \left(\frac{150}{\mathrm{Re}_p} + 1.75 \right) \left(\frac{1 - \epsilon}{\epsilon^3} \right) \left(\frac{G''^2}{D_p \rho} \right) \Delta L \tag{6.7}$$

where G' is the mass flow rate and ΔL is the bed length. A pressure flow relation computed with a mean particle diameter of $200\,\mu\mathrm{m}$ for a packed bed of spheres based on the Ergun equation, and with different packing void fractions is shown in Figure 6.12.
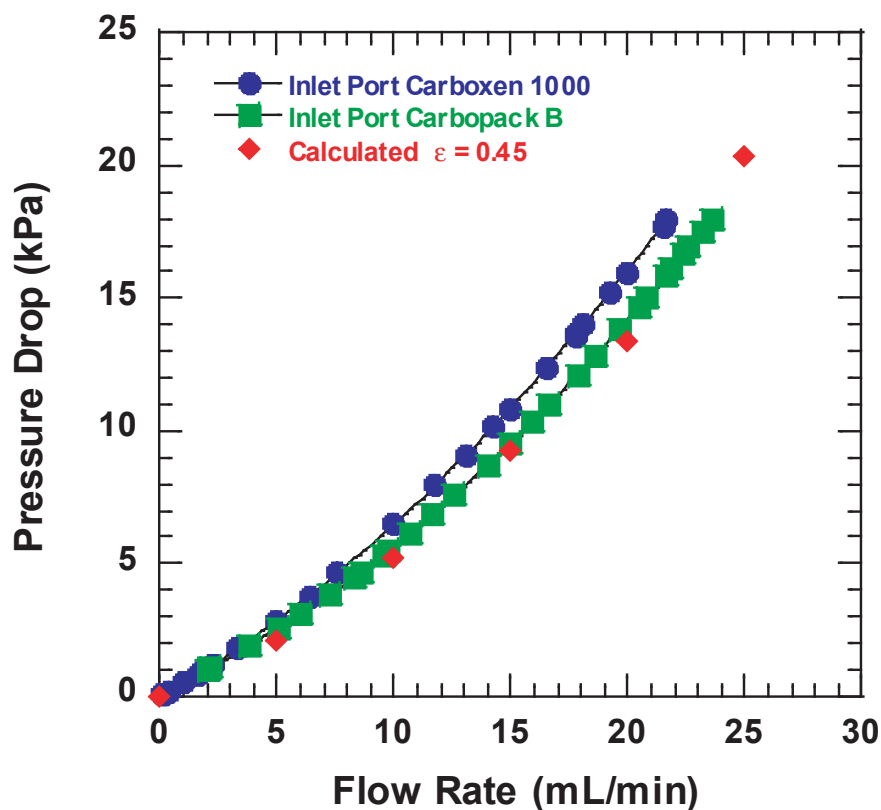
Figure 6.13. Pressure drop against atmosphere at outlet as a function of flow rate.

The pressure drop is experimentally obtained by using a supply of dry N_2 whose flow rate is controlled by a needle valve, and a digital manometer and flow meter connected the inlet. The outlet of the preconcentrator is left at atmospheric pressure. The pressure drop of the connecting Tygon tubing and fused silica capillaries is first measured to subtract their contribution from the measurement of the sealed preconcentrator. The resulting pressure drop-flow rate relationship from a sealed preconcentrator is shown in Figure 6.13. The measured data shows that the preconcentrator pressure drop is within the limits of the micropump design for the WIMS μGC of 20 to $50\,\text{kPa}$ since it has a $20\,\text{kPa}$ pressure drop for a $25\,\text{mL/min}$ flow rate. We show the closest fit void fraction of 0.45 on the plot for comparison purposes. The void fraction of 0.45 falls within the bounds of the random loose packing void fraction of 0.44 and the hexagonal close packing void fraction of 0.26 [86].

113

Summary

In this chapter, we made the case for the necessity of robust electrical and gas flow interfaces, as well as the need to implement two packages to address testing at the macroscale and integration at the microscale. A modular testing board was developed to allow reuse in many testing environments: flow/no-flow, vacuum ambient, conventional GC, and pressure drop.

Of all the analytical components, the preconcentrator is the hottest at $300\,°C$ and needs the fastest heating rate on the order of 30 to $100\,°C/s$, whose upper-bound is only limited by the need for a portable power source. The power is linearly proportional to the heating rate, so that the practical approach to reducing the power during operation with the present device without modification to the fabrication is to use stop-flow. In this scheme, the gas flow is stopped so that the device can reach $300\,°C$ with a lower applied power. For example, instead of applying $3.2\,W$ to achieve $300\,°C$ in $10\,s$, we can stop the flow for $20\,s$ and apply $1.6\,W$ of power to get to $300\,°C$. The total energy usage remains the same. Flow resumes to push the desorbed compounds out after the microdevice reaches $300\,°C$.

We have also analyzed how power consumption can be significantly cut down in the future with microdevice improvements such as gold coating, and vacuum encapsulation. We can conceive of implementing a vacuum package with the existing LCC or hybrid packages with standard package lids or cans. While microscale thermal isolation is worthy in its own right for power reduction, the simplest way to reduce power is to shrink the device size since all heat loss mechanisms scale with surface area. Chapter 10 will explore this idea of scaling.

Chapter 7

MIDPOINT

Chapters 2-6 circumscribed this research's problem-space—what are the fundamental operational limits for microscale packed-bed preconcentrators? Each chapter drew a different angle to this central problem as recapped below:

- Chapter 2 introduced the language and concepts of GC. We will reapply GC theory to preconcentrators in Chapter 9 to develop models that can be used to examine fundamental physical processes in the device.
- Chapter 3 placed the preconcentrator into its μGC and VOC analysis contexts. These contexts give us reference metrics for discussing fundamental preconcentrator operational limits: exhaustive extraction volume, injection plugwidth, preconcentration factor, and power consumption.
- Chapter 4 reviewed prior work in the field. We note an absence of device models in the literature. We identified adsorbent property verification at the microscale and model development as target areas for contribution.
- In Chapter 5 we observed that not knowing the adsorbent mass was a major roadblock for developing any microdevice model. We developed a new adsorbent-solvent method for quantitative loading of our microcavity preconcentrator to break down this barrier and to solve the interstage contamination problem of the dry-fill technique. In addition, we improved manufacturability by developing an outgassing scheme to make robust Si-Au eutectic bonding the method of choice for wafer-level integration of these preconcentrators.
- In Chapter 6 we developed micro- and macroscale interfaces to allow us to begin meaningful measurements of structural and material properties. We also took a first-pass look at the way these interfaces affect the thermal performance of the microdevice since isolation is not built-in at the microscale.

Now we reach a pivot point for this dissertation. The newly-built micropreconcentrator carves a path to encompass our solution-space: the material properties and device model that comprise our answer to the physical limits of microscale packed bed designs. With known adsorbent mass, integrated heating, temperature measurement, and custom GC interfaces, we use the device as a tool to learn about its own limits.

Chapter 8

INSTRUMENTATION AND EVALUATION

The preconcentrator is *itself* a complex microsystem. To probe, elicit, and record a response from it requires special instruments and measurement techniques. The development and construction of these instruments and techniques are the subject of this chapter. Our observation is that state-of-the-art technology requires new instrumentation to measure it. And since instrumentation has its own concepts and terminology, we will learn yet another language—this time for microdevice measurements.

Our present discussion is not a treatise on experiments; we will not delve into detail sufficient for the uninitiated to go into the laboratory and produce quality results. For new practitioners and the curious, Appendix C on Laboratory Techniques provides details on measurement procedures, their rationale, and common pitfalls to avoid. We have been priveleged with the opportunity to build our own instrumentation and to perform our own measurements. So it is with the spirit of appreciation that we share what we have learned through this process, both in this chapter and in the appendix.

Input and Output

We begin by specifying the input stimulus and the output recorder. The input to the preconcentrator is the vapor generation source, generally categorized into two clases: dynamic and static.

- **Dynamic**
  An example is a fritted bubbler with mixing chambers and flow controllers to dilute a saturated vapor down to the desired concentration. Controlling the temperature of the bubbler is critical for maintaining the same starting concentration, so that it is usually placed in an isothermal bath.
  Dynamic generation is superior to static generation for its ability to generate repeatable and specific concentrations. However, the price of dynamic generation is complexity, cost, and safety. It requires several thousand dollars of mixing and flow control equipment, consumes copious amounts of high purity gas, and needs several

thousand dollars more for laboratory safety measures because of potentially high vapor concentrations and dilution vent streams inherent in the system.

- **Static**

  The twenty-dollar static solution makes use of the Tedlar bag used in EPA standards for collecting indoor air samples. Static methods are inexpensive, simple, and used for indoor air analysis applications. The idea of static preparation is to fill a bag with dilution gas to a known volume and then to inject a liquid into the bag for vaporization to a given concentration. There are no vent streams or bubblers so that the liquid solvent consumption is low, and an exhaust hood is not required. The main costs associated with this method are the liquid syringe and the dry gas meter, which admittedly is $1700. Low-cost comes at its own price—bags suffer from the inability to dial in a precise and repeatable concentration, being limited by the skill of the operator in performing liquid injections and bag dilution.

The static method is our choice because of its simplicity and laboratory safety constraints. We recognize that we will not be able to dial in a concentration that is the same between compounds. But we note that we will always measure the bag concentration using a calibrated detector to know what our skill has afforded us to prepare. And we see the silver lining in the fact that as along as we can produce a range of concentrations, we will be able to extract properties from our data.

The input probes that we will send in are of two types, depending on whether we are performing quantitative or qualitative measurements. Here, quantitative narrowly refers to those measurements that require mass calibration of our flame ionisation detector (FID). The need for quantitation arises from the object of these measurements—physical properties that characterize adsorbent-adsorbate interactions. For material property and model verification, our input probes are a homologous series of alkanes: saturated hydrocarbons with a chemical formula of C_nH_{2n+2}. The absence of polar molecules and molecules of vastly different orientation will keep us focused rather than dispersed into chemical investigations of molecular shape and charge interactions that are patently outside the scope of this work. Our focus is on compound volatility—the ease with which a compound can vaporize—and its influence on preconcentrator behavior. And for a homologous series of alkanes, the volatility decreases with increasing carbon number. In other words, a higher carbon number means higher boiling point, and that is equivalent to a lower vapor pressure. The expectation is that a compound that is easy to vaporize will be difficult to adsorb and a compound that is difficult to vaporize will be easy to adsorb. Thus, our compound selection spans a boiling point range of $216\,°C$ ($C_{12}H_{26}$, dodecane) to $98\,°C$ (C_7H_{16}, heptane) covering the range of low volatility (difficult to vaporize, high boiling point) to high volatility (easy to vaporize, low boiling point).

A qualitative measurement for the preconcentrator is one that doesn't need a mass calibrated detector. For sample injection measurements where we are not finding physical properties, we open the floor to alcohols, alkenes, and other compounds on the EPA list. The idea is to show that the preconcentrator can operate effectively on a wide variety of compounds as intended. Just as a GC column does not need a mass-calibrated detector to

show separation, the same applies here. A preconcentrator does not need a mass-calibrated detector to show injection. There is one caveat. A strict, direct measurement of preconcentration factor does require mass calibration. So for that, we will once again turn to alkanes, but out of convenience to recycle our calibration data.

For the output of the preconcentrator we also have two choices and this time we use both. Figure 8.1 shows the three types of measurements that we will conduct and their relationship to the detector-only and column-detector configurations for the output of the preconcentrator. The first type of measurement is sample injection. We want to measure the native peak width from the preconcentrator without intermediate effects of the column. We will use the flame ionization detector (FID) as a detector, and care will be taken to minimize dead volumes between the outlet of the preconcentrator and the FID to avoid band-broadening calamity.

In actual separations, a temperature-programmed column will narrow the solute band of low volatility compounds while leaving high volatility compound bandwidths virtually untouched. This proves beneficial because it compensates for the behavior of the preconcentrator. For the preconcentrator, low volatility compounds are more difficult to desorb making injected plugwidths wider, while high volatility compounds rapidly desorb yielding narrow injection plugs. So we are interested in both extremes for our native plugwidth measurements.

While on the topic of volatility and its effects on various system components, we note that the sensor array detection limits are expected to be better (lower) for high boiling point compounds and worse for low boilers. Again, this helps to complement the inverted trend of desorption from the preconcentrator where high boilers are hard to get off (potentially lower preconcentration factor) and low boilers are easy to desorb (higher preconcentration factors). These opposite trends are not a coincidence.

The same fundamental physical process is at work in all parts of the WIMS μGC: that of partitioning (for a gas-liquid interface) for the column and sensor arrays, and adsorption (for a gas-solid interface) for the preconcentrator. The interfacial interaction governs their behavior so that with respect to alkane volatility, all parts have the *same characteristics*. The compensatory effect of lower detection limits for compounds with lower preconcentration factors simply comes from the *opposite process* at work: sorption for the detector and desorption for the preconcentrator.

For the desorption rate vs. time of sample injection measurements, the FID is obviously not a sorption-based detector. By using an FID, we avoid the potential pitfall of using a sensor array whose own kinetic response may change the injection plugwidth measurement just as a column would. This observation points to a general mantra if we want to measure the kinetic response of the preconcentrator: we cannot have anything downstream from the preconcentrator output that exhibits its own sorption behaviors, nor can we have anything that modifies the desorbed plugwidth from the microdevice. An example of the latter would be excessive dead volumes that are cold. To circumvent this chilling possibility, we use a Kapton encapsulated resistive heater wrapped around the valve downstream from the

1. Sample Injection (FID)

dN/dt

4τ

Result:
Desorption Rate vs. Time
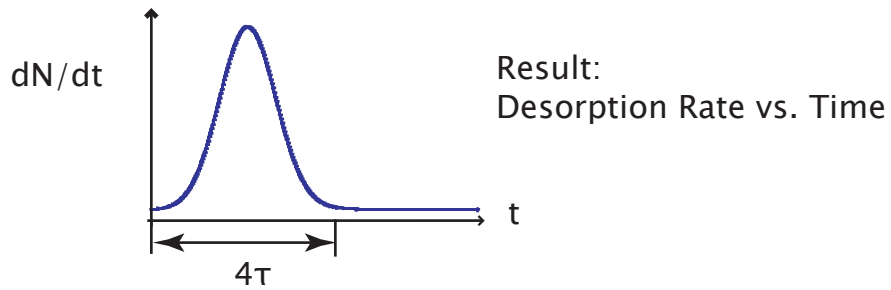
2. Complex Mixture Preconcentration (Column–FID)

Result:
Single Chromatogram

0 t_{R1} t_{R2} t_{R3}
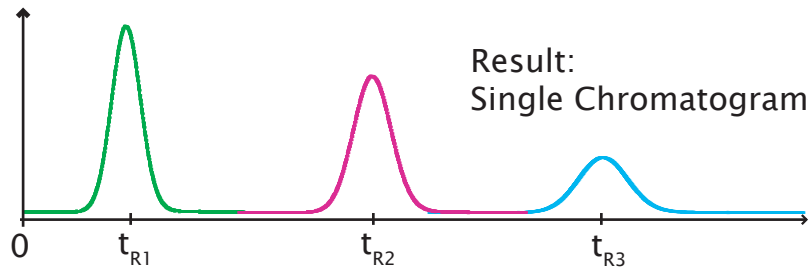
3. Breakthrough Curve (Column–FID)

A_0 A_1 A_2 A_3 ...

C/C_0

Result:
Continuous Series of
Chromatograms
→ Breakthrough Curve
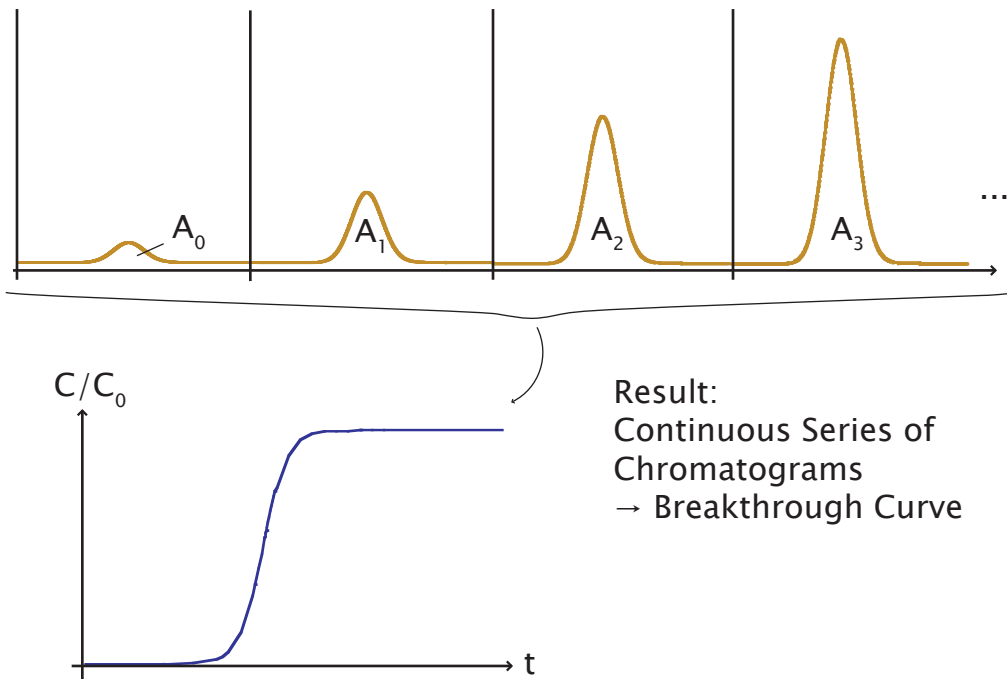
Figure 8.1. Output configurations for the preconcentrator: 1. Detector-only for desorption rate measurement, 2. Column-detector ensemble for demonstration of complex mixture preconcentration, 3. Column-detector ensemble for exhaustive extraction, breakthrough curve, and property calculations.

device. Finally, in the plot of the desorption rate vs. time, we will read off 4τ, which is the τ of Chapter 2, where finite sample injection time was put into the equation for minimum plate height and translated into system separation efficiency.
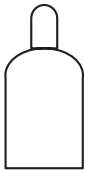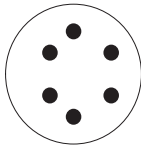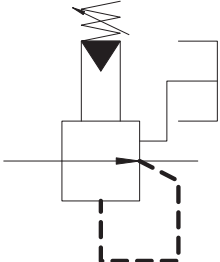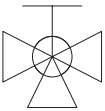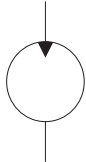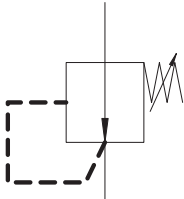
The second measurement shown in Figure 8.1 uses the column and detector, and complex mixture preconcentration is for demonstration purposes. It results in a single chromatogram where each compound has its own retention time. The idea of the measurement is to sample a known volume of low-concentration VOC-mixture into the preconcentrator and then thermally desorb (inject) it into the column via countercurrent purge, meaning that the desorption flow direction is opposite that of sampling.

The third measurement is of greatest importance to us and is the effluent curve. Measuring an effluent curve does not involve the two-step operation of sampling at room temperature and thermal desorption at higher temperature. Instead, it is a continuous measurement at a single fixed temperature. We continuously feed a step function concentration into the preconcentrator and record the output response—the effluent curve or the breakthrough curve. Knowing the breakthrough curve provides clues to the inner-workings of the microdevice. Its setup is involved because we measure it using a column and detector sampling the output at fixed time intervals. The presence of a column ensures that we can check that no other compounds exist in the source sample and gives us the flexibility of introducing multiple step functions of different compounds to the preconcentrator simultaneously. The technique itself is also involved because we want quantitative data from it to extract a fundamental material property: the adsorption isotherm. To plot the absolute concentration requires mass calibration of the detector so that the area of each chromatographic peak corresponds to a mass.

System Components

With notions of what to connect the input and output to, and an overview of the measurements, we turn to more details of the instrumentation. Figure 8.2 shows the symbols for our measurement system schematics in the pages to come. These symbols are not fictitiously created for our own purposes; they originate from a motley crew—industrial-scale process equipment to capillary GC—reflecting the variety of resources we need in order to properly interface a microdevice to a laboratory-scale GC.

The gas delivery scheme that we have constructed is common to all three setups. Practically, the house nitrogen must be scrubbed prior to use as a carrier gas. For preserving the lifetime of the GC column, we remove moisture and particulates. Hydrocarbons are removed via two traps resulting in lower baseline signals at the FID. But beyond the gas purity needs of analytical chromatography, we have a more stringent requirement. Because the preconcentrator is designed to trap trace-level VOCs from ambient air, we must perform rigorous leak checking and use measurement methods that can double-check input and output samples for inadvertent trace contamination. We are reminded of the urgency

Gas Cylinder		Six-Port Valve	
Two-Stage Pressure Regulator		Bag	
Pressure Gauge		Manual Metering Valve	
Manual Three-way Valve		Pump	
Single-Stage Pressure Regulator		Exhaust to Air	
Flow Controller		Capillary Line	

Figure 8.2. Key to gas-line and component schematic symbols.

and universality of our indoor-air analysis application. The clean air requirement steps up the level of difficulty for our work precisely because the indoor air that we breathe is not clean. Our leak detector (Model 21-070, Gow-Mac Instrument Co., Bethlehem, PA) relies on the thermal conductivity difference between the ambient (air) and the gas flowing through the device (He) to detect a leak. The He leak checking source is also scrubbed clean with a photolithography-grade all-in-one purifier for use with the system.

Single Vapor Desorption

Figure 8.3 shows a gas-line and component schematic for the single vapor desorption measurement system. The testing configuration consists of directly connecting the preconcentrator to the FID of the bench-scale GC through an external six-port valve placed inside the GC oven. This measurement makes use of two electrically-actuated three-way valves: one at the input to switch between the input sample in the Tedlar bag and the nitrogen carrier; and one at the output to switch between the sampling pump and the FID. The nitrogen carrier pushes the desorbed plug into the FID, while the sampling pump draws the input sample through the preconcentrator to load it.

The measurement sequence is:

1. Prepare the sample bag.
2. Measure the sample bag concentration with a column and FID (optional—makes use of the second FID on our Agilent 6890, but physically requires an additional 6-port valve and everything to fit into an oven with the door open).
3. Measure the flow rate through the preconcentrator.
4. Tune the manual needle valve for setting the sampling flow rate.
5. Measure the desorption flow rate through the preconcentrator.
6. Precondition the preconcentrator.
7. Sample through the preconcentrator.
8. Desorb the preconcentrator into the detector.

Figure 8.4 shows the single vapor injection profile for trichloroethylene (TCE) at a $6 \, \mathrm{mL/min}$ flow rate, splitless, and various heating rates. The sample was prepared via liquid injection into a Tedlar bag followed by dilution with zero-grade dry air. Table 8.1 shows the peak width dependence on heating rate, and the width cited in the table is equivalent to 4τ as we introduced it in Chapter 3. How does this compare with what we wanted for a $300 \, \mathrm{cm}$ Si-glass microcolumn?

The highest heating rate has $\sigma = 70.97 \, \mu\mathrm{L}$ with a flow rate of $6 \, \mathrm{mL/min}$, which is too far above the column optimal. If we use a split-flow ratio of 30 to get a column flow of $0.2 \, \mathrm{mL/min}$, then $\sigma = 2.36 \, \mu\mathrm{L}$. The good news is that this satisfies the requirement of $2.42 \, \mu\mathrm{L}$ computed in Chapter 3 for the $109 \, \mu\mathrm{m}$-radius, $3 \, \mathrm{m}$ Si-glass column. It is a coincidence that the split flow ratio to achieve the optimal column flow rate also gives

UHP HELIUM

AERONEX CE-35KF-I-4R
0.003 μm; 1 sLpm

PARKER
10 μm FILTER

TO GC
(FID MAKEUP GAS)

ALLTECH 7210
< 3ppb HYDROCARBON TRAP

SUPELCO 22445-U
HYDROCARBON TRAP

ALLTECH 8121
<1 ppm MOISTURE TRAP

PORTER 4000
0 – 60 psig

PORTER VCD 1000
110 mL/min

TO TEDLAR BAG

AGILENT 6890
6 – PORT VALVE

PRECONCENTRATOR

TO FID

VICI EH4C6WE
1/16" TUBE 0.4 mm PORTS

NITROGEN

HOKE 1300
Cv 0.024

KNF NM-9
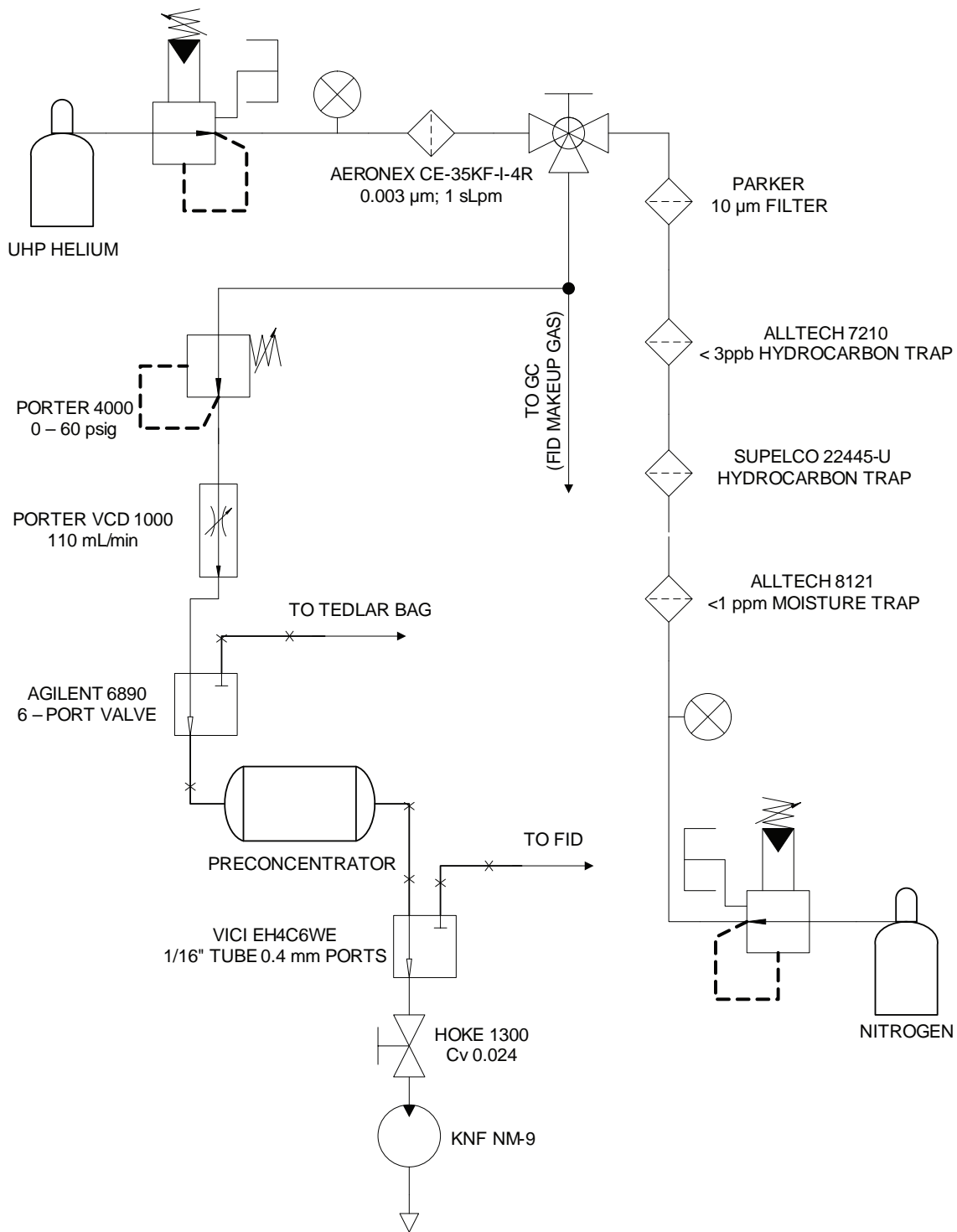
Figure 8.3. Schematic of preconcentrator single vapor desorption
measurement system.
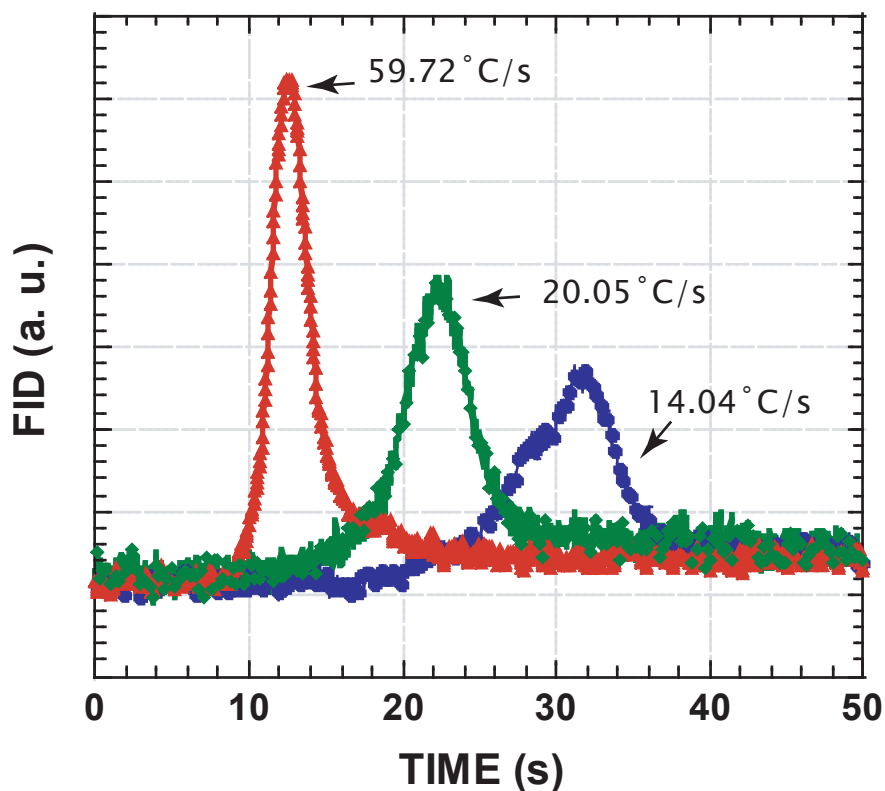
Figure 8.4. Trichloroethylene desorption peaks measured via FID with a 6 mL/min desorption flow rate, for different heating rates: $59.72\,°C/s$ (red), $20.05\,°C/s$ (green), $14.04\,°C/s$ (blue) .

a desorbed plug volume appropriate for the column. In practice, split flows need to be tuned to accommodate a variety of column and preconcentrator flows. In Gen 0.6, a single split is set by choosing the length of a capillary split-vent T-junctioned at the outlet of the preconcentrator. The length changes the pressure drop, thereby changing the effective split flow ratio.

Mixture Preconcentration

Figure 8.5 is the configuration for demonstrating complex mixture preconcentration. This configuration makes use of a GC column to separate the preconcentrated mixture so that it most resembles the actual operation cycle of the preconcentrator in the microsystem. Of course, the laboratory-scale GC is different from the μGC, but verification of preconcentration ability is important nonetheless. In this experiment, the sample pump draws the

Table 8.1. Trichloroethylene Desorption Peak Widths

Heating Rate [$^\circ$C/s]	Peak Width [s]
14.04	6.578
20.10	4.534
59.72	2.839

sample from the Tedlar bag so that the preconcentrator can extract VOCs. Then, dry air is briefly sampled through the device to purge the connecting line of residual sample. During thermal desorption, the six-port valve is switched so that N_2 carrier is pushed through the microdevice the opposite flow direction as sampling. The net result is that the thermally desorbed compounds are injected into the column-FID ensemble.

The cycle for measurement is:

1. Prepare the sample mixture.
2. Optimize the GC column and oven programming to perform the separation.
3. Measure the column flow rate.
4. Place the preconcentrator in-line with the system and tune the carrier gas pressure to match the same column flow rate for the optimized separation.
5. Tune the needle valve of the sample pump to achieve the desired sampling flow rate for the preconcentrator (dictated by the desired sample volume)
6. Precondition the preconcentrator.
7. Sample the mixture through the preconcentrator.
8. Thermally desorb the preconcentrator into the GC column.
9. Record the chromatogram.

In terms of sample injection, the chromatogram in Figure 8.6 shows the ability of this preconcentrator to trap and inject a 200 ppb mixture of acetone, trichloroethylene, and n-decane into a commercial GC. The mixture was prepared via liquid solvent injection into a Tedlar bag filled with dry, zero-grade air. During the $9.8\,\mathrm{mL/min}$, $10\,\mathrm{min}$ sampling period, the mixture is drawn through the preconcentrator which traps the n-decane in the Carbopack B, trichloroethylene in Carbopack X, and acetone in Carboxen 1000. Upon conclusion of sampling, the preconcentrator is heated using $1.8\,\mathrm{W}$ for a heating time of $45\,\mathrm{s}$ under a $1.3\,\mathrm{mL/min}$ flow of nitrogen to flush the $300\,^\circ$C thermally desorbed compounds onto the commercial GC column and FID. The chromatogram shows clear separation with the GC with the preconcentrator as its injector. Subsequent blank desorptions show no residuals. The components of this mixture have vapor pressures ranging from 1.52 to $231\,\mathrm{Torr}$, demonstrating the ability of the preconcentrator to perform sample injections of a wide range of compound volatilities for separation using GC [69].

126
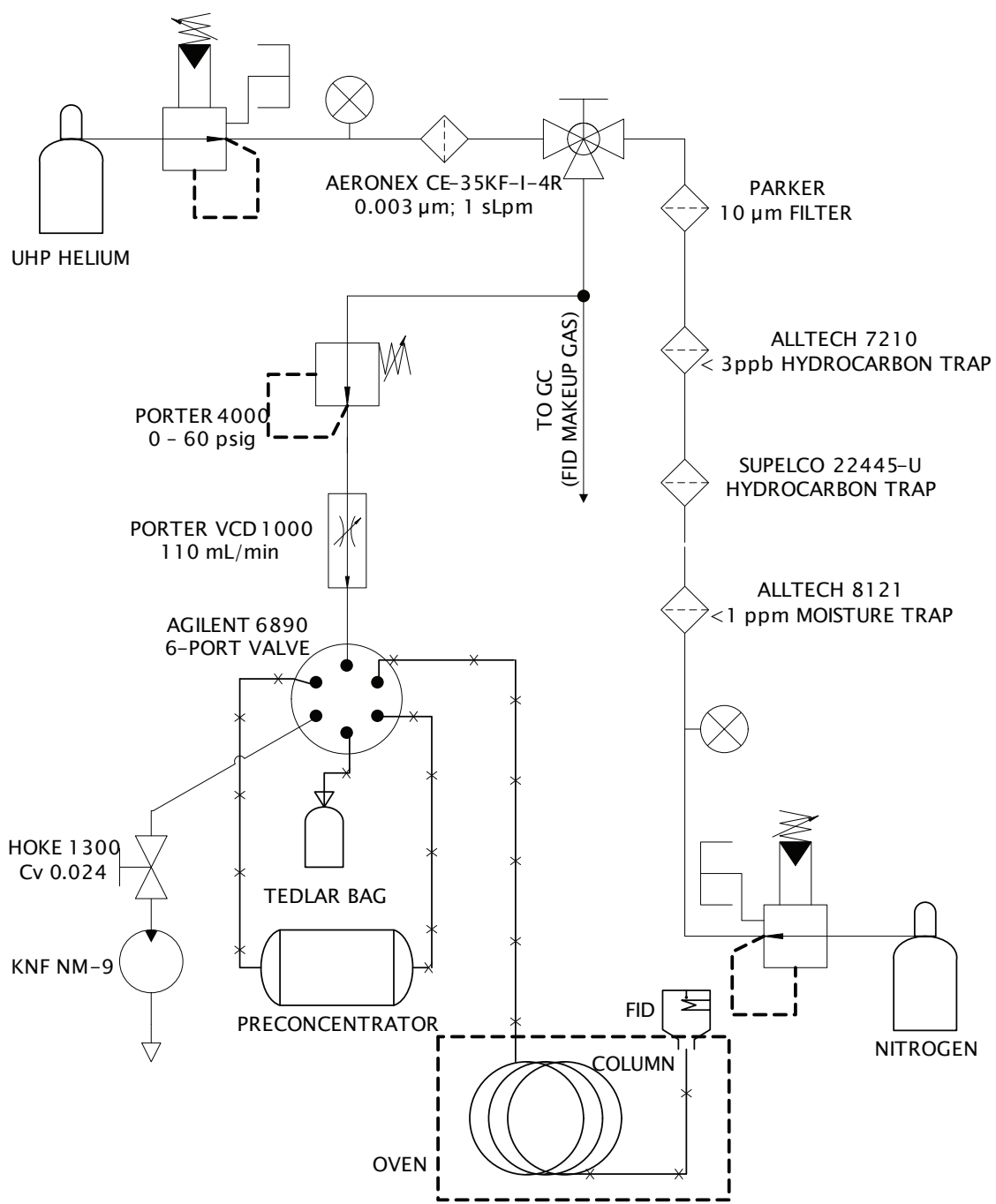
Figure 8.5. Schematic of preconcentrator complex mixture desorption measurement system.

UHP HELIUM

AERONEX CE–35KF–I–4R
0.003 μm; 1 sLpm

PARKER
10 μm FILTER

ALLTECH 7210
< 3ppb HYDROCARBON TRAP

SUPELCO 22445–U
HYDROCARBON TRAP

ALLTECH 8121
<1 ppm MOISTURE TRAP

TO GC
(FID MAKEUP GAS)

PORTER 4000
0 – 60 psig

PORTER VCD 1000
110 mL/min

AGILENT 6890
6–PORT VALVE

HOKE 1300
Cv 0.024

KNF NM–9

TEDLAR BAG

PRECONCENTRATOR

FID

COLUMN

OVEN

NITROGEN
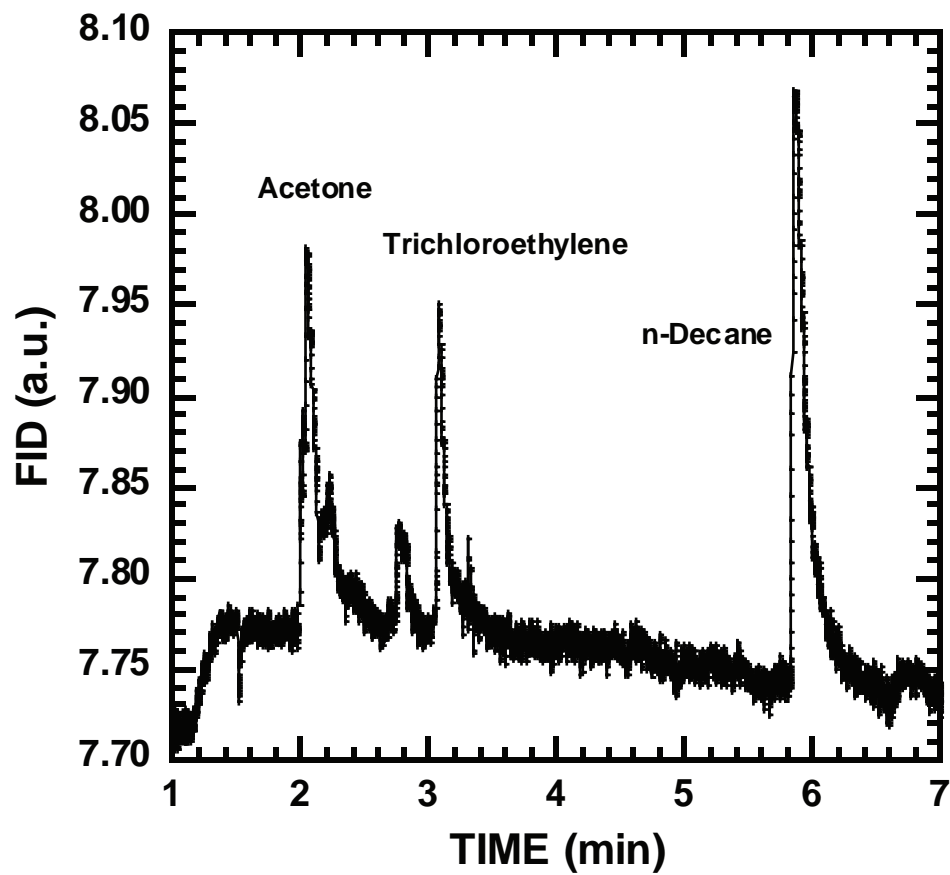
Figure 8.6. Chromatogram obtained from the preconcentration of 98 mL acetone, trichloroethylene, and n-decane at 200 ppb, 20 °C adsorption temperature, and 300 °C desorption temperature.

Breakthrough Curve

The measurement configuration for the breakthrough curve is shown in Figure 8.7. The major difference between it and that of the complex mixture desorption is that there is no reversal of flow because there is no thermal desorption step.

The configuration consists of connecting the preconcentrator to a bench-scale GC column and FID through a six-port valve. The input sample to be captured is continuously drawn from a Tedlar bag and through the preconcentrator using the sample pump. The flow path downstream from the preconcentrator includes a $100 \, \mu L$ stainless-steel sampling loop also connected to the six-port valve. The purpose of the loop is to sample the air exiting the preconcentrator for injection onto the column and FID to determine whether compound breakthrough is occurring in the device. This is achieved by switching the six-port valve at a fixed time interval ranging from 3 to $7 \, min$, depending on the time it takes to capture a chromatogram, and flushing the sampling loop for $0.5 \, min$ using N_2 onto the GC column and FID. Thus, the output effluent of the preconcentrator is sampled to detect and quantify the amount of influent present. The virtue of the six-port switching loop-preconcentrator configuration is that the influent drawn through the microdevice by the sample pump is uninterrupted during loop flushing and analysis.

The cycle for measurement is:

1. Prepare the sample mixture.
2. Optimize the GC column and oven programming to perform the separation.
3. Check the flow rate through the preconcentrator with the sample pump. Adjust the speed of the pump or the needle valve as appropriate.
4. Program the temperature of the preconcentrator for the measurement.
5. Precondition the preconcentrator.
6. Measure the bag concentration and flush the lines with dry air before commencing the breakthrough measurement.
7. Continuously sample the compound for breakthrough measurement.
8. At fixed intervals, flush the sampling loop into the column to check for presence of the input adsorbate.
9. When the output concentration is equal to the input concentration, the breakthrough measurement is stopped.
10. Check the bag concentration.
11. Connect a bag of clean dry air to being the passive desorption measurement.
12. When the output is 10% of the original breakthrough input concentration, the passive desorption measurment ends.
13. Measure the flow rates after measurement.

The device under test for breakthrough curves is a microdevice filled with $1.33 \, mg$ of Carbopack B. The upper plot of Figure 8.8 is one breakthrough curve from this device. The plot is a milestone because it is the first time that a microdevice exhibits the expected shape of an effluent curve with a step function input. Octane is used as the input sample because
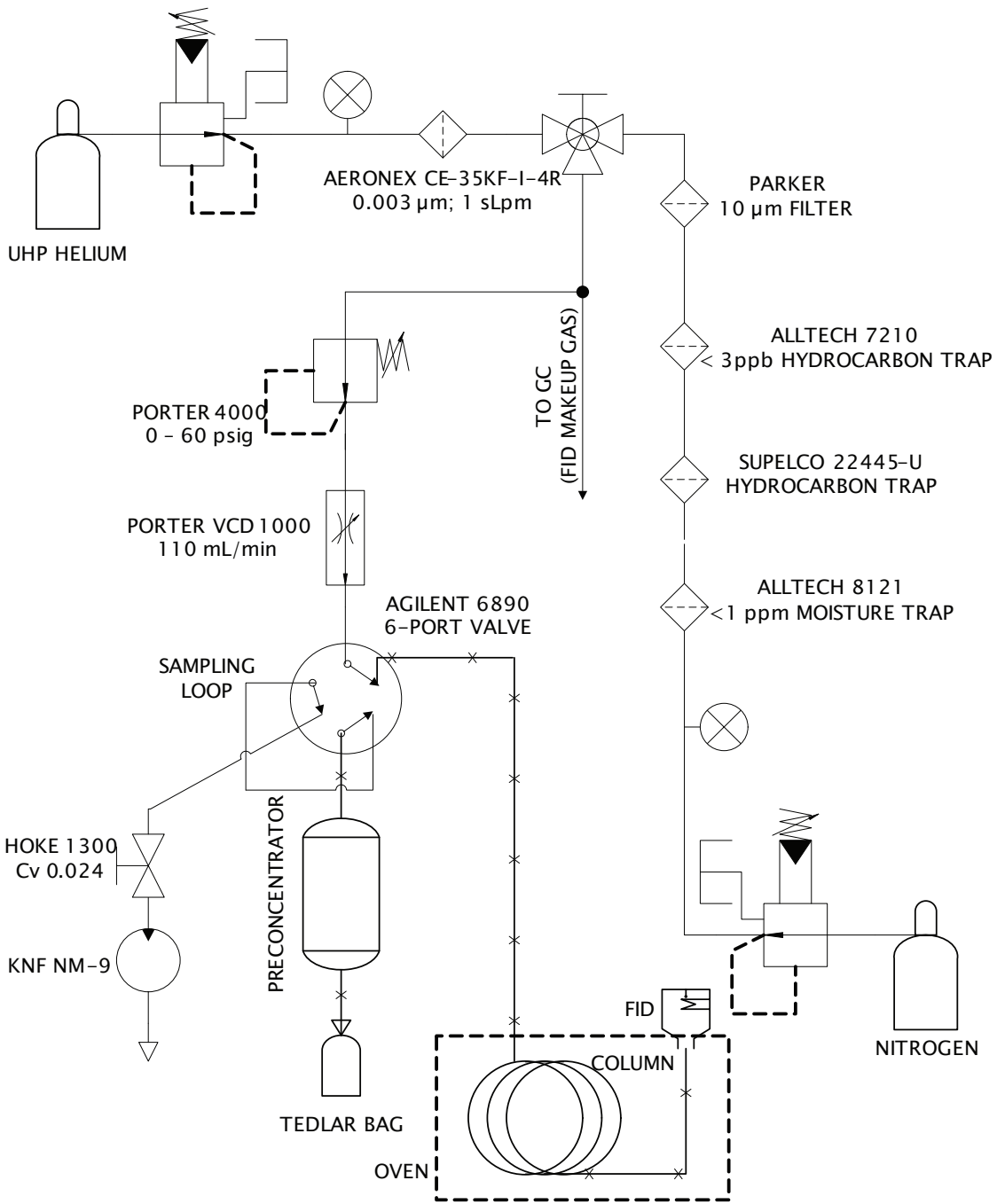
Figure 8.7. Schematic of preconcentrator breakthrough curve measurement system.

it is supposed to be "too volatile" for Carbopack B according to tube preconcentrator studies. Being "too volatile" means that Carbopack B is not expected to have large capacity or affinity for octane. Thus, it is a challenging test compound for Carbopack B. The fact that the microdevice can trap octane does not refute this general idea. It only reminds us of our reason for selecting GCBs: physisorption. Namely, there is no selectivity with respect to nonpolar compounds on Carbopack B. Therefore, even octane will stick to Carbopack B, albeit weakly as we shall see later on.

Contrast this plot to the one from the parallel-microchannel design of Figure 4.8, repeated on the lower plot of Figure 8.8, and several observations can be made. First, no influent appears for about $12\,\mathrm{min}$, and with a flow rate of $25\,\mathrm{mL/min}$, this results in an exhaustive extraction volume of $300\,\mathrm{mL}$. This exhaustive extraction volume certainly fulfills our target for the WIMS application. Where the parallel microchannel design could not exhaustively extract a single test compound, our new preconcentrator does. And even when challenged by a highly volatile adsorbate that the bed is not intended to target, the device has a large capacity. The result has encouraging implications for pursuing preconcentrators that are further scaled. The simpler cavity design does solve the problem of geometrically-fixed, variable flow-restriction paths of the parallel microchannel design. The second observation is that the curve clearly and quickly rises to the input concentration unlike the parallel microchannel breakthrough curve. One can imagine that with geometrically-fixed parallel channels of different flow restriction, the bed adsorption dynamics are different: the channel of least resistance breaks through first, followed by the one of next least resistance, etc. The lines on the lower plot of Figure 8.8 are drawn to suggest this "channel breakthrough" phenomenon.

The last observation to make is that even in the instantaneous breakthrough case of the old design, the effluent concentration does not just jump to the influent concentration of $C/C_0 = 1$. Even though the flow through the parallel microchannels is a non-optimal way to extract the adsorbate, extraction still occurs. The fact that extraction occurs can be counter-intuitive given our picture of channels with differing flow resistance. But we must remember that the influent is at *trace* concentrations, and that physisorption is an exothermic process. The adsorbate-adsorbent system is such that the influent prefers sticking to the adsorbent rather than remaining in the vapor phase.

Figures 8.9, 8.10, 8.11, and 8.12 are the first temperature-programmed effluent curve measurements from a microscale preconcentrator. The adsorptive capacity of decane at these elevated temperatures is impressive, and it points to the fact that we need a high temperature of $300\,^{\circ}\mathrm{C}$ to achieve preconcentration. The general trend is that as the concentration increases, the breakthrough time (volume) decreases; and when the temperature increases, the breakthrough time also decreases. All of the data are taken at a flow rate of $25\,\mathrm{mL/min}$, the original specification for the sampling mode of the WIMS μGC. Table 8.2 summarizes the results including measurements of octane and dodecane; large adsorbent capacities abound even with high volatility. With the presentation of these breakthrough curves, we are ready to move on to how to model them— the subject of the next chapter. The model will allow us to extract parameters that describe the relationship between input concentra-
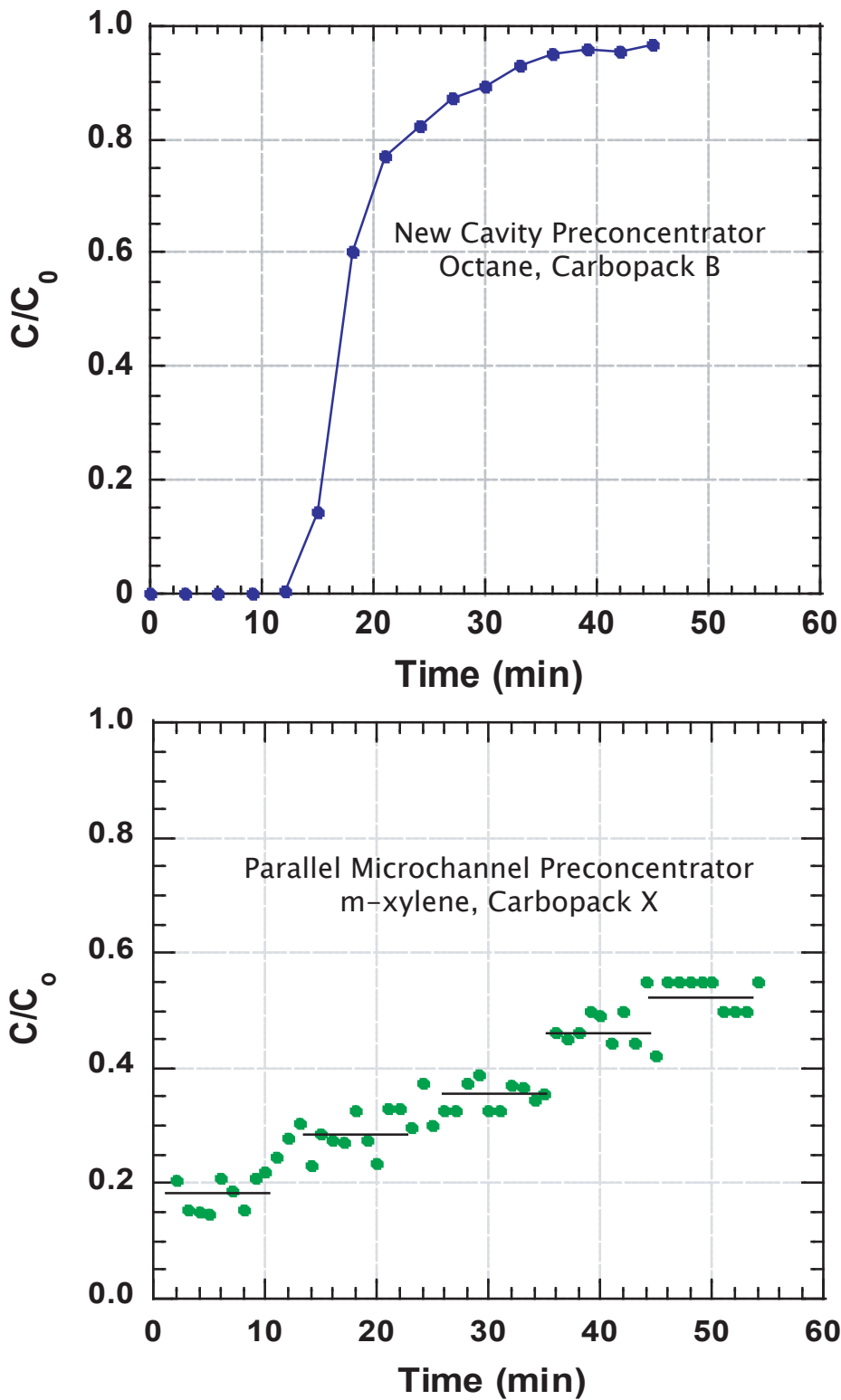
Figure 8.8. (Top) Breakthrough curve from new cavity pre-concentrator showing exhaustive extraction; input is octane, $25\,\mathrm{mL/min}$, room temperature adsorption on Carbopack B. (Bottom) Breakthrough curve of m-xylene on a Carbopack X-filled parallel microchannel des̲ ̲ ̲ ̲ighlight apparent plateaus on the plot that may be due to groups of channels breaking through depending on their flow resistance.

132

Table 8.2. Summary of Effluent Curve Measurements

Alkane	Temperature [$^\circ$C]	Concentration [$\times 10^{-6}$ g/L]	Breakthrough Volume [L]
$C_{12}H_{26}$	75	11.35	1.75
$C_{10}H_{22}$	50	18.49	1.37
$C_{10}H_{22}$	50	39.19	1.19
$C_{10}H_{22}$	75	1.14	3.08
$C_{10}H_{22}$	75	5.81	1.60
$C_{10}H_{22}$	75	6.36	1.52
C_8H_{18}	22	32.80	0.95
C_8H_{18}	22	42.89	1.13
C_8H_{18}	22	91.58	0.47

tion and adsorbed amount for a fixed temperature.
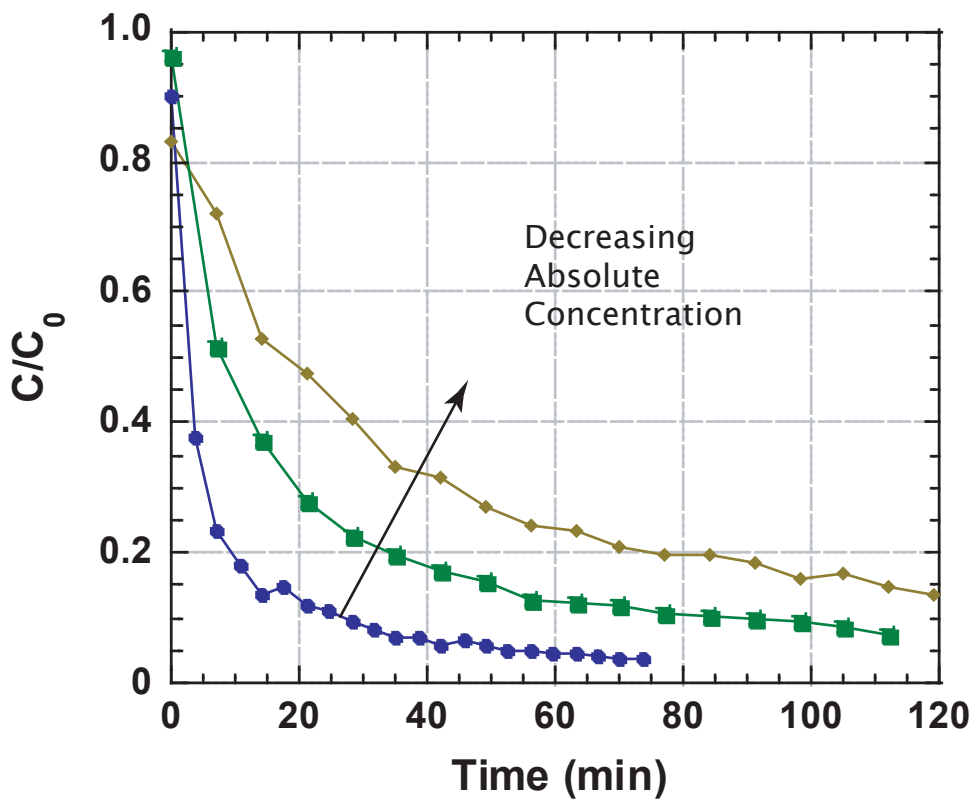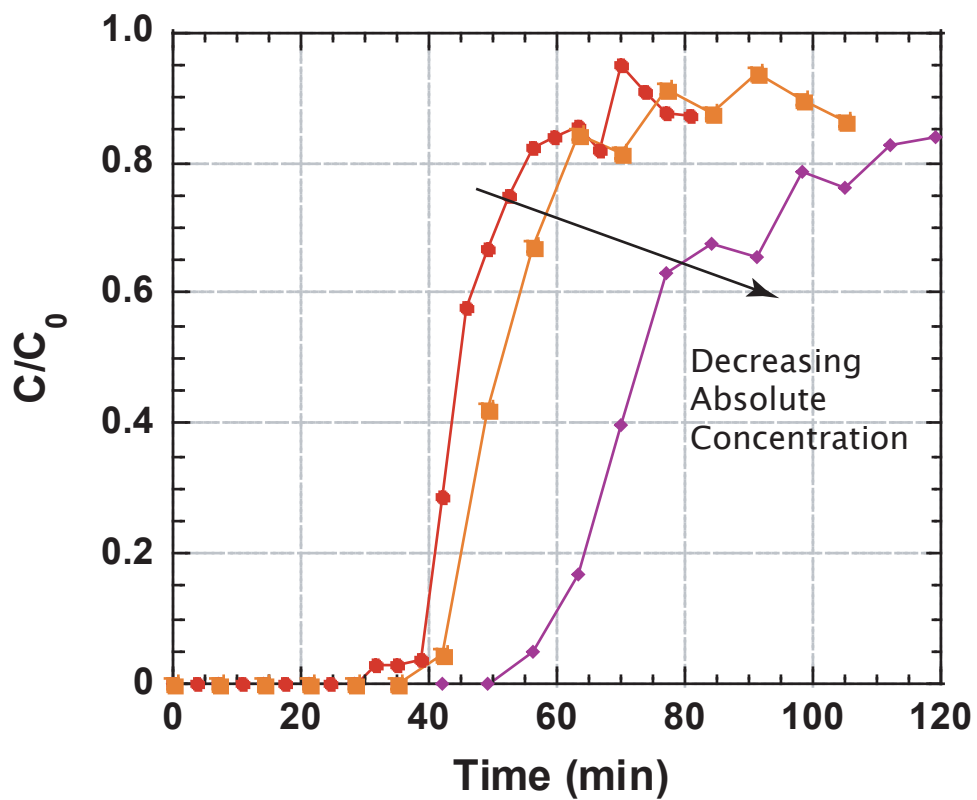
Figure 8.9. Breakthrough curves for decane at $50\,^\circ\text{C}$ on Carbopack B.

134
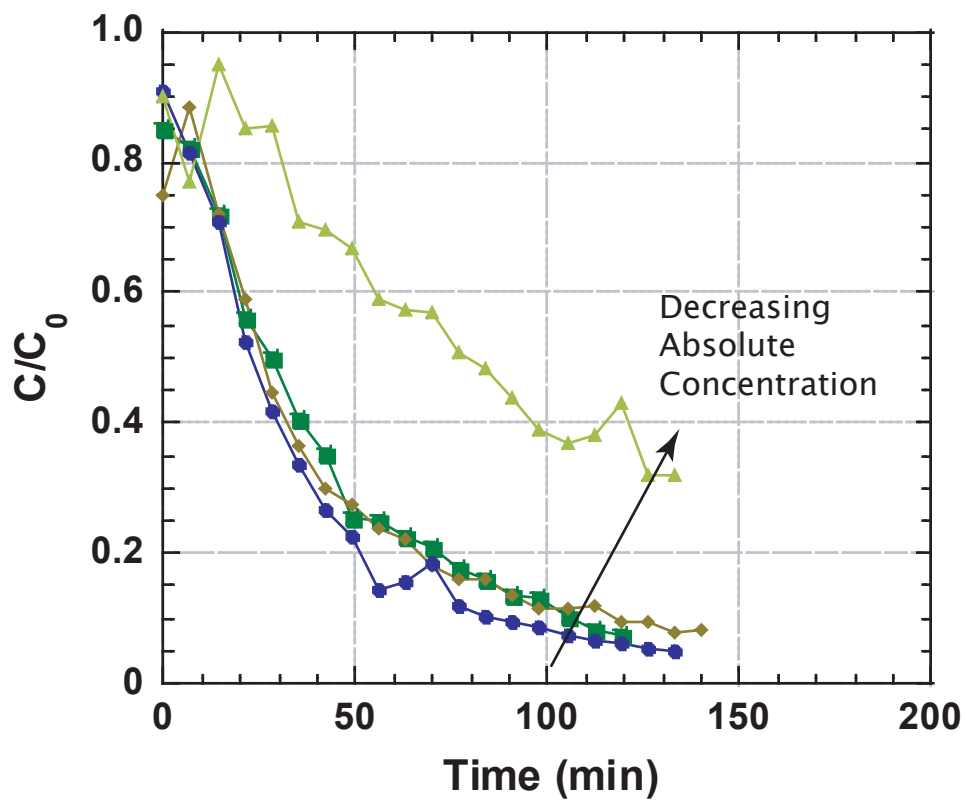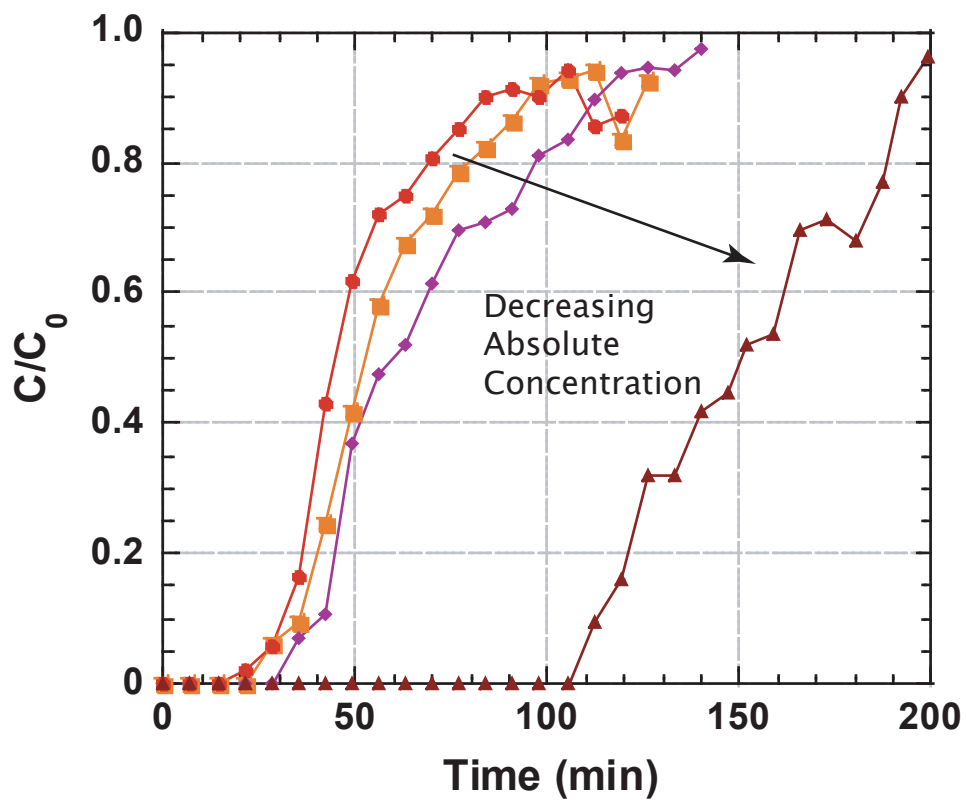
Figure 8.10. Breakthrough curves for decane at 75 °C on Carbopack B.
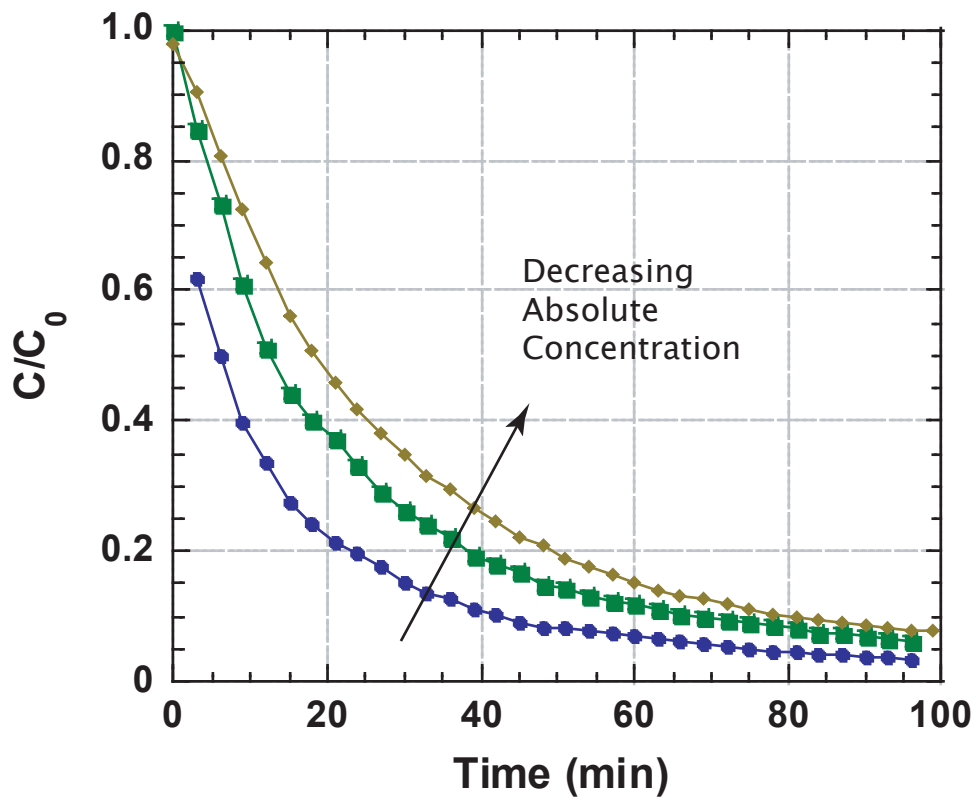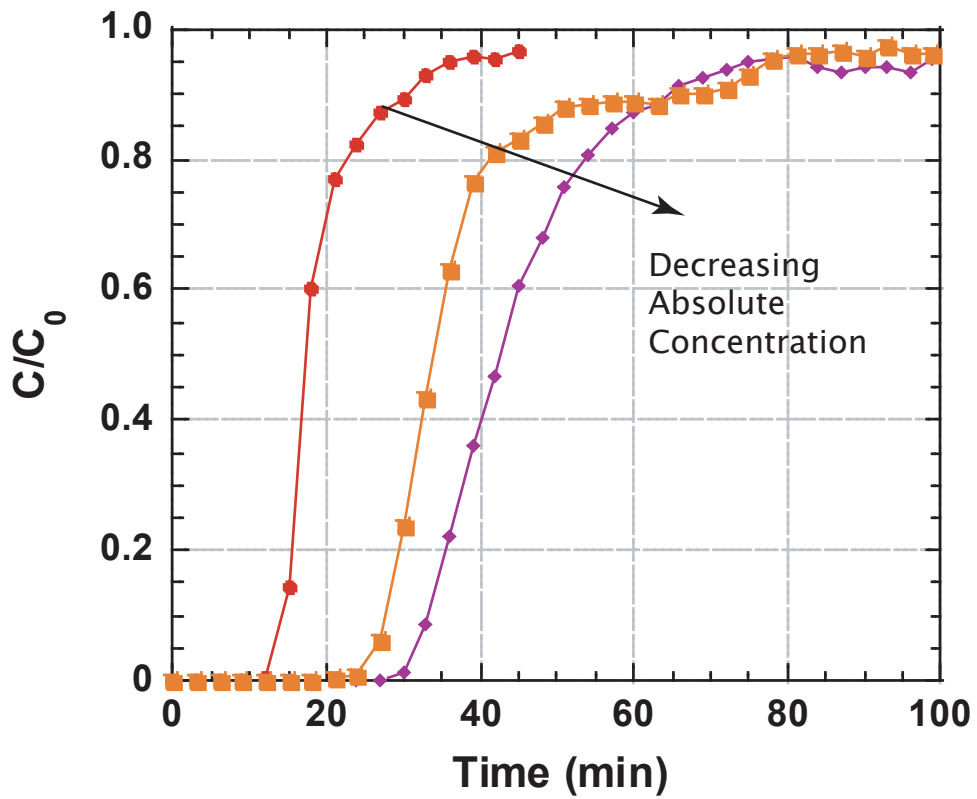
Figure 8.11. Breakthrough curves at room temperature for octane on Carbopack B 91.58×10^{-6} g/L, 42.89×10^{-6} g/L, 32.80×10^{-6} g/L.

136
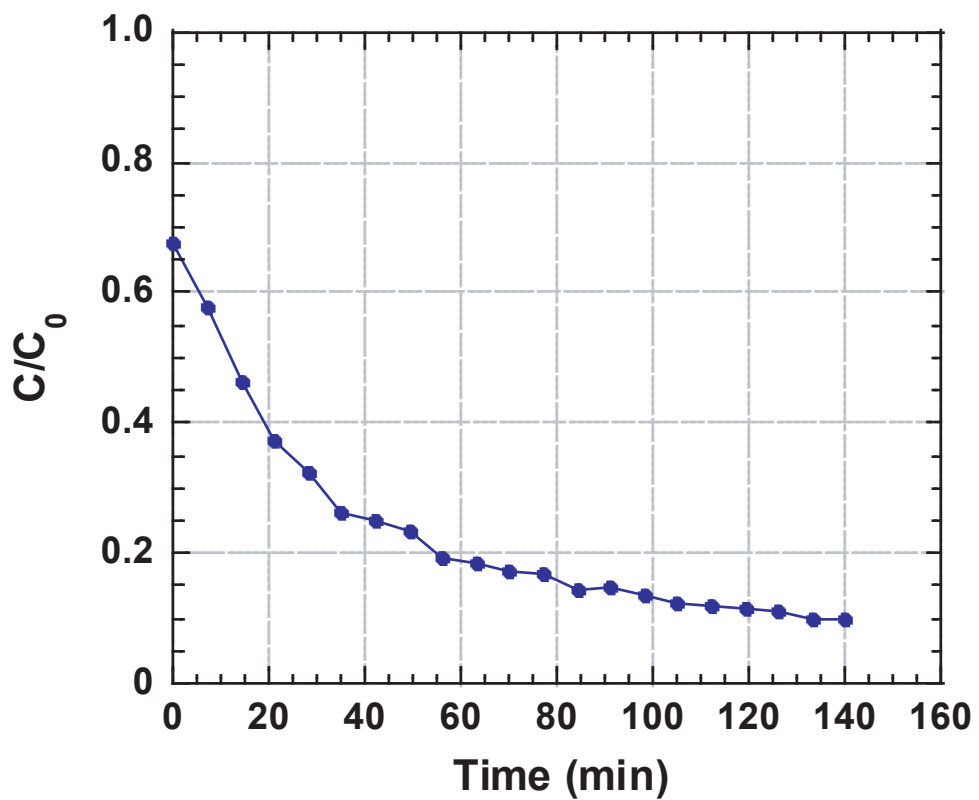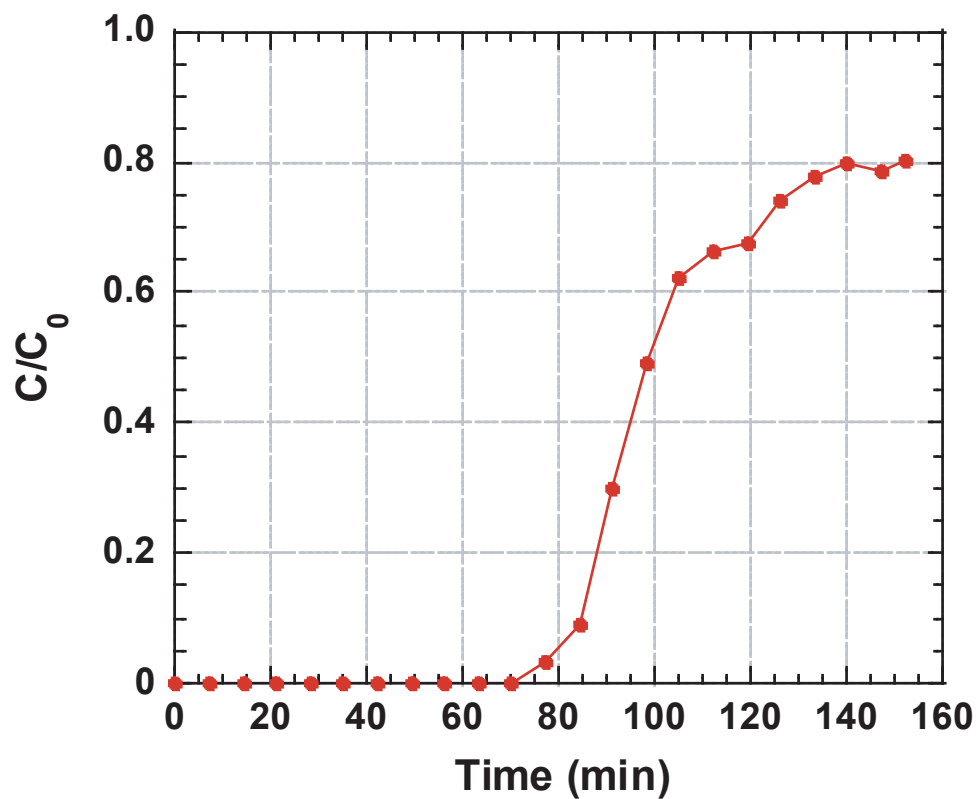
Figure 8.12. Breakthrough curve for dodecane at 75 °C on Carbopack B.

Chapter 9

MICROPRECONCENTRATOR MODELS

Picking through the alphabet soup of equations to spell out a preconcentrator model is not easy. In this chapter, we propose a simple preconcentrator model by reapplying the concepts and mathematics of GC theory as promised from Chapter 2. Though the language of partition chromatography is translatable to microscale extraction and injection, we have to hypothesize a new physical picture for microdevice operation. We will jump in with a quick survey of model choices and then go deeper to explore a simple yet physically meaningful description of how the preconcentrator acts upon a single adsorbable influent in an inert carrier.

Model Choices

What we desire is a model for the scenario depicted in Figure 9.1, corresponding to that of a breakthrough curve measurement. The input is a step function compound concentration while the effluent is monitored by the column and detector as described in the previous chapter. The upper diagram illustrates a basic physical picture of what is going on—a concentration front gradually forms in the preconcentrator and "propagates" through the adsorbent bed as time elapses.

The breakthrough curve depicted in the bottom half of the figure is an ideal textbook case where the effluent curve goes to 1 and is easily integratable. Practically, what we measure slopes towards 1 slowly and the experiment terminates before reaching 1 because of the finite amount of gas in the static Tedlar bag. The solution then, is to measure a series of curves at several concentrations, place the concentration scaling constraint into the model, and extract parameters to describe our capacities and rates. That is the new task that we attend to.

There is a plethora of packed bed reactor models for us to reapply. Many of them have come directly from large-scale preparative chromatography or gas-solid analytical chromatography. Figure 9.2 shows the three major pieces of model information required for solution (adsorption isotherm, flow model, and kinetic model) and the many choices for
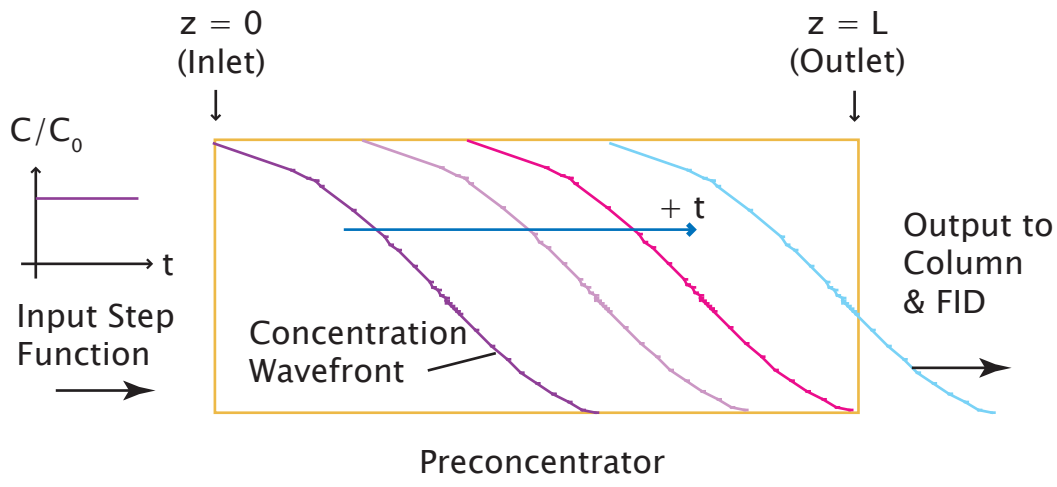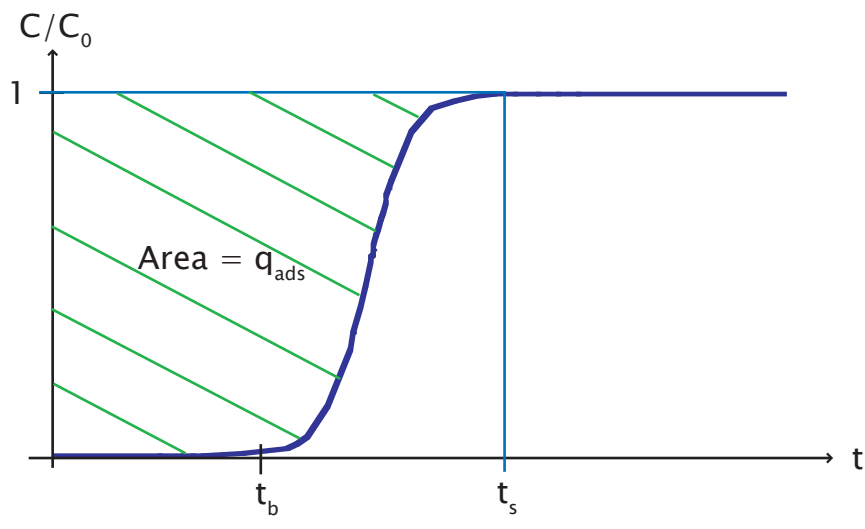
Figure 9.1. (a) Inputing a step function concentration causes a concentration wavefront to propagate along the preconcentrator. (b) The effluent is measured via the column and FID resulting in a breakthrough curve.
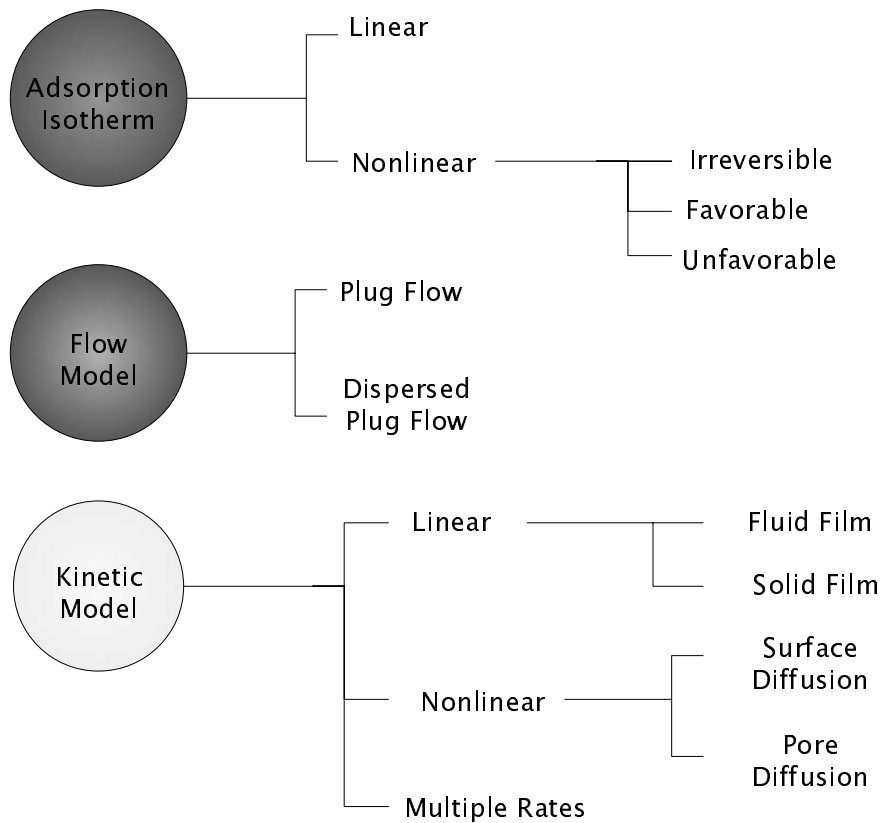
Figure 9.2. Solution tree for mass balance equation.

each. An extensive review, heavy on the mathematics, is available in [11], while another text gives more of a practical perspective [12]. To fill the gap in the literature regarding preconcentrator models requires us to select from these scenarios to describe the adsorbate in the fluid phase of our microdevice.

After careful study, we can formulate a model for the preconcentrator just like the column as we discussed in Chapter 2. Table 9.1 highlights the differences between the analytical chromatography and preconcentrator adsorption approaches to the mass balance equation. Analytical chromatography considers linear isotherms, dispersed plug flow, and linear rate kinetics. Operating at low concentrations (linear isotherms) is the interest of analytical chromatography because overloading the column causes peak distortion, reducing the resolution between peaks. In contrast, the micropreconcentrator bridges analytical and preparative chromatography. Like analytical chromatography, trace concentrations of adsorbate flow over the adsorbents during extraction. However, unlike analytical chromatography, the adsorbate is trapped on the adsorbent and since the goal is to get the adsorbate off at once, the desorption concentration is high as in preparative chromatography.

Table 9.1. Comparison of Analytical Chromatography and Pre-concentrator Adsorption Models

Parameter	Analytical Chromatography	Preconcentrator Adsorption
Type of Response	Delta Function	Step Function
Isotherm	Linear	Nonlinear
Flow Model	Dispersed Plug	Plug
Kinetics	Linear Rate	Linear Rate

As reviewed in Chapter 2, the major result of van Deemter and coworkers was to show that the effects of longitudinal dispersion and finite mass transfer were linearly additive. In essence, they corroborated the statistical random-walk models of others in the field who proposed that these effects were statistically independent. However, their results depend on a linear equilibrium relationship between the solute and the stationary phase. Translated into preconcentrator terms, the results of van Deemter would hold only if the adsorption isotherm is linear. While this is true in the region of adsorption (clean bed), it may be less applicable as the capacity of the bed is reached. So the GC rate model cannot be simply ported over to the micropreconcentrator without thought. The next section discusses the mass balance equation in more detail and following that, the remaining sections discuss the adsorption isotherm, kinetic parameters, and viable solutions for micropreconcentrators.

Fluid Phase Mass Balance

The preconcentrator can be thought of as a short GC column gone ballistic. Rapid transport and near-simultaneous firing of compounds off the adsorbents is what we want from the preconcentrator, and low mass-transfer resistance is critical. Quite a contrast to a long GC column, where we desire extensive solute-stationary phase interactions to amplify the differences between solute partitioning so as to have them come out separately. Nonetheless, though the preconcentrator and column operate in opposite manner, the physical processes that describe them are the same.

The long column and short preconcentrator share the same one-dimensional (1-D) mass balance equation. For the microdevice, this shows the adsorbate in the flowing phase of the packed bed. This is the same equation introduced in Chapter 2 on the rate theory of chromatography, which is analogous to charge balance in a semiconductor encountered in solid-state electronics. For convenience the equation is repeated below. In this case, instead of gas-liquid partitioning in chromatography, we have an adsorption/desorption term that
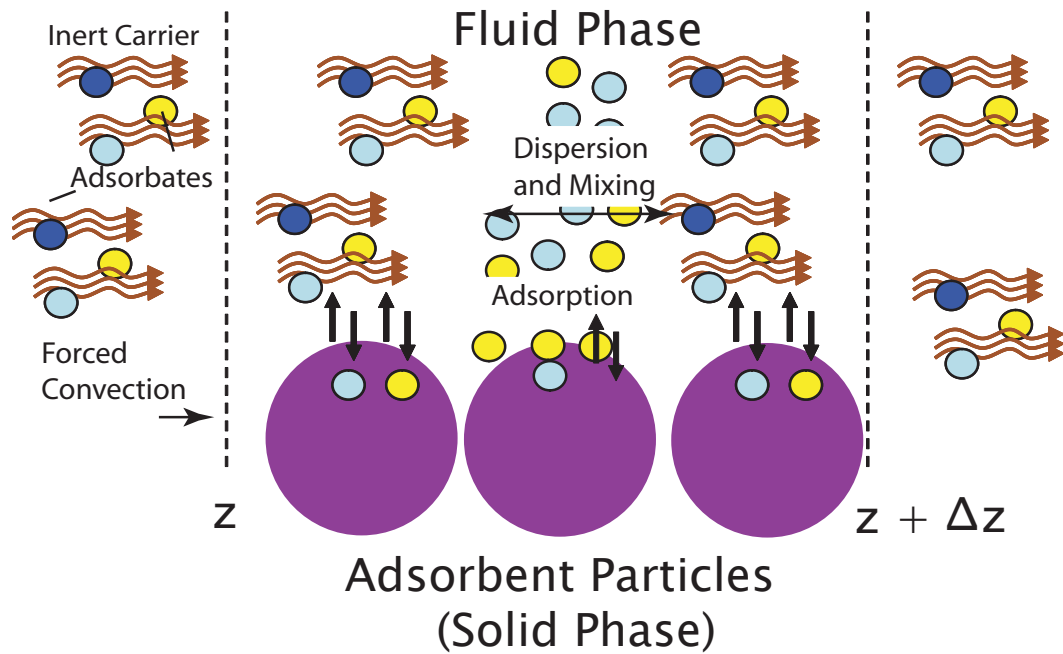
Figure 9.3. A differential length of the preconcentrator showing the mechanisms affecting the net adsorbate concentration in the fluid phase; forced convection into and out of the section, free convection (dispersion) in the center of the section due to finite diffusion (concentration gradients) and mixing in the packed bed, and adsorption into the solid phase adsorbent particles.

is quite a bit more complex:

$$-D_L\frac{\partial^2 C}{\partial z^2} + \frac{\partial(vC)}{\partial z} + \left(\frac{1-\epsilon}{\epsilon}\right)\frac{\partial q}{\partial t} + \frac{\partial C}{\partial t} = 0 \tag{9.1}$$

where D_L is the longitudinal dispersion coefficient, C is the concentration of adsorbate in the fluid phase (gaseous phase) [mol/cm^3], z is the coordinate along the length of the bed [cm], v is the interstitial fluid velocity [cm/s], q is the adsorbate adsorbed into the adsorbent granules in the bed [mol/cm^3], t is time [s], and ϵ is the adsorbent bed void fraction.

This equation elegantly captures the basic processes in the preconcentrator that affect the fluid phase adsorbate concentration. Its form is simple and the complexity of the microdevice is in the equation coefficients. Figure 9.3 illustrates the basic process in a differential section of the preconcentrator term by term: mixing or dispersion (first term), forced convection (second term), and adsorption into the particles (third term).

For the remainder of this dissertation, unless stated otherwise, we will consider a single adsorbable influent contained in an inert carrier. In other words, we are considering the case

of single vapor breakthrough. One may challenge the simplicity of this single vapor input since our application is complex vapor mixture analysis. Single vapor solutions, though overly simplistic, are a good place to begin. We speculate that the trace concentrations of the WIMS application will allow the models developed here to be simply modified for mixtures. The trace concentrations are expected to enable the assumption that different types of adsorbate do not interact; and this assumption then opens the door to the well-known multi-component Langmuir isotherm (essentially like superposition) that can then be used here to extend the single vapor description [12].

Adsorption Isotherm

The adsorption isotherm is a map that shows the equilibrium distribution of the adsorbate in the fluid and solid (adsorbent) phases. In mathematics, the adsorption isotherm, which is the equilibrium amount or concentration adsorbed onto the adsorbent q^* as a function of adsorbate concentration in the pores (C_a) for a fixed pore temperature (T_a) is:

$$q^* = f(T_a, C_a) \tag{9.2}$$

Figure 9.4 shows hypothetical examples of adsorption isotherms to highlight the differences in their shape. The shape of the isotherm influences the shape of the breakthrough curve, and the designation of favorable, irreversible, linear, and unfavorable refers to whether the concentration profile in the adsorbent bed will sharpen (favorable) or disperse (unfavorable) as it travels along the bed. The concavity of the isotherm determines the designation. An isotherm that is favorable for adsorption is unfavorable for desorption meaning that a concentration front that sharpens during adsorption will disperse during desorption.

We will use a Langmuir isotherm to describe our adsorbents because it has physical meaning at low coverages and because the GCBs are not microporous. The ppb-concentrations for our application mean that the adsorption coverage is low; the number of available adsorption sites is large. There are many other isotherms that are popular in the literature for new adsorbents such as the Dubinin-Radushkevich isotherm based on potential theory [87], [88]. The pairing of new adsorbents with D-R isotherms is natural because the development of new sorbent materials is focused on manipulating microporosity and microporous materials are the object of D-R theory. The origin of the D-R equations comes from the physical view that adsorption occurs in micropores via a mechanism similar to capillary condensation (adsorbate sticking to the walls of micropores). This description does not hold for the GCBs in this work since they have no micropores. Additionally at low coverages, the basic D-R isotherms do not reduce to a linear relationship (Henry's law region) between the adsorbed amount and the fluid phase concentration. D-R is applicable to the microporous CMS but not without modification to allow for its use at low concentrations [89]. Therefore, for the purposes of pursuing a description that physically makes sense for our work, we use the Langmuir isotherm and choose to work with the GCBs. The form of
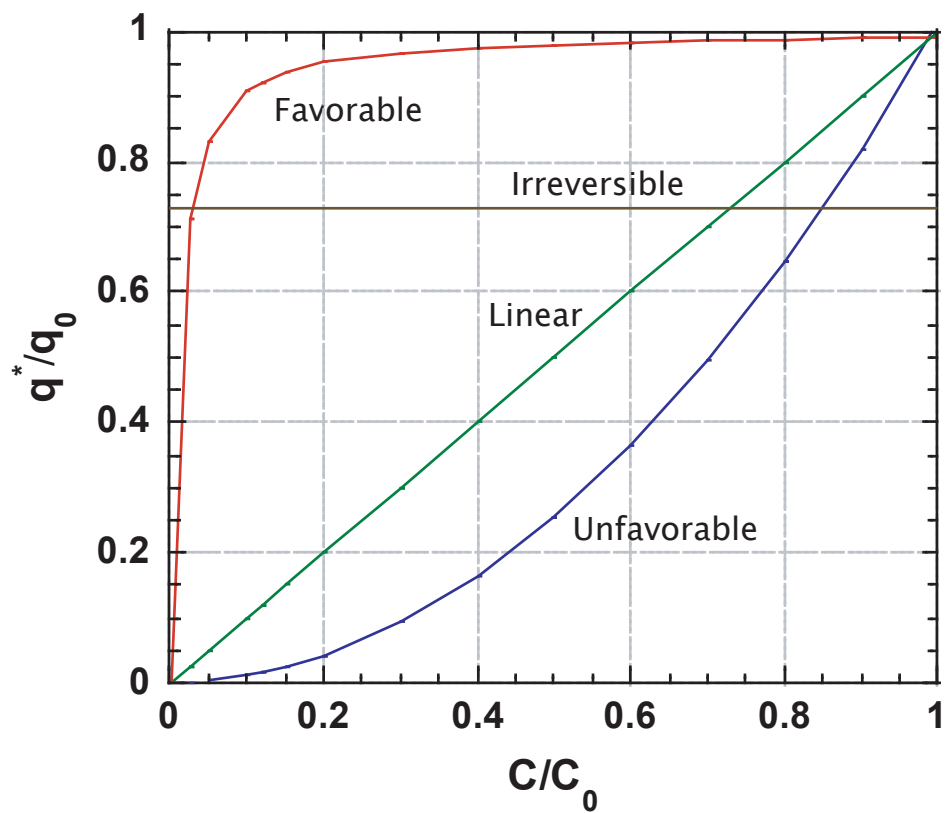
Figure 9.4. Example (hypothetical) plots of favorable, irreversible, linear, and unfavorable adsorption isotherms. The y-axis is the equilibrium adsorbed amount (q^*) normalized to the saturated adsorbed amount (q_0), and the x-axis is the gas phase adsorbate concentration (C) normalized to the concentration corresponding to the saturation vapor pressure p_0 of the adsorbate (C_0) (for a constant adsorption temperature).

the Langmuir isotherm is [90]:

$$q^* = \frac{q_{max} C}{K_{lang} + C} \tag{9.3}$$

where q^* is the equilibrium adsorbed amount per volume of adsorbent (concentration) [g/mL], q_{max} is the monolayer adsorbed concentration (maximum) [g/mL], C is the fluid phase concentration [g/mL], and K_{lang} is the Langmuir constant.

Kinetic Relationship

While the isotherm tells us the preferred location of the adsorbate (fluid or solid phase), the kinetic relationship tells how long it takes to drive the system to equilibrium and the obstacles that may slow us down. We will use a Linear Driving Force (LDF) approximation to describe the relationship between the solid and fluid phase adsorbate concentrations. The LDF approximation essentially says that a film mass transfer coefficient captures the physics of the particle-fluid adsorbate interaction that drives the system to equilibrium. In addition, we will assume no mass transfer resistance inside the particle. The resulting adsorption rate equation is:

$$\frac{\partial q}{\partial t} = k_f a(q^* - q) \tag{9.4}$$

where k_f is the effective mass transfer coefficient, a is the external surface area per unit particle volume (for spherical particles $a = \frac{3}{R_p}$), q^* is the concentration in the solid phase in equilibrium with the fluid phase (given by the adsorption isotherm), and q is the actual concentration in the bulk of the solid phase. The benefit of LDF is that it takes care of the continuity of flux at the particle-fluid boundary.

The simplicity of the LDF form of the adsorption rate equation is in having k_f for the rate of mass transfer. This means that k_f can have many forms to describe a variety of scenarios depending on the level of detail to which the adsorbate kinetics are known [12]. In our case, we know little about the adsorbate kinetics inside a particle, and we do not have the means to measure it. Therefore it makes no sense to use a complex kinetic description with more parameters. For this reason, we do not consider multiple rate constants associated with internal particle mass transfer resistances such as macro- and micropore diffusion. We only consider fluid film resistance and take advantage of the mass and heat transfer analogy (the Reynolds analogy) to estimate this film coefficient. The correlation of Wakao and Funazkri for a first-pass estimate of k_f, and this is detailed in Appendix D.

Model Assumptions

With the fluid phase mass balance equation, the adsorption isotherm, and kinetic relationship, we have the roots of our model. Returning to Figure 9.2 of the solution tree for packed bed reactor choices, we are reminded that we still need to select flow assumptions among others:

- **Isothermal** In general the heat balance equations must also be solved. However, for now we will focus on isothermal operation and not worry about temperature changes inside the preconcentrator. This is reasonable during extraction because the microdevice adsorbs trace concentrations. It is also reasonable during thermal desorption under stop-flow conditions where the clean inert influent is stopped to allow the device to reach an isothermal condition ($300\,^\circ$C).
- **Plug Flow** The velocity of the adsorbate does not change through the mass transfer region. For trace-level adsorption this is a reasonable assumption, while for desorption and continuous purge it may not be as valid. However, with stop flow it is valid since the fluid is at the same temperature.
- **Finite Longitudinal Dispersion** refers to the fate of the $-D_L \frac{\partial^2 C}{\partial z^2}$ term in the mass balance equation. Many closed form analytic solutions exist for the case where this term is ignored because then the second order term in the differential equation is gone. And while there are many clean analytical solutions for curve fitting the mass balance equation with no dispersion term, it doesn't make sense for us to ignore it. The preconcentrator cross-sectional bed diameter to adsorbent particle diameter is small so that mixing is an expectation, and the way to model this is to have a finite D_L term. Therefore, we have to grapple with the complexity that it imposes and resort to numerical methods for solutions.

To put these assumptions into context, a general model of an adsorber requires mass and heat balance inside the adsorbent, mass and heat balance outside the adsorbent (in the flowing phase), an adsorption isotherm (concentration and temperature dependent) and kinetic parameters (concentration and temperature dependent) [12]. We have reduced this considerably by looking at an isothermal micropreconcentrator: only mass balance will be considered rather than the coupled mass and heat transfer problem.

In preparation for recasting the equation into dimensionless form for numerical solution, these are the dimensionless variables that we will use:

- Gas adsorbate concentration $X = C/C_0$
- Solid adsorbate concentration $Y = q/q_0$
- Length along the bed $\zeta = z/L$
- Time $\tau = (tv)/(L\epsilon)$

Operating Conditions

There are several operating conditions for the isothermal cases of extraction (sampling at room temperature) and injection (thermal desorption at elevated temperature), and these are translated into initial and boundary conditions for our differential equations:

1. The preconcentrator is initially clean and then fed a constant concentration single vapor at the inlet.
   - i.c. is $X(\zeta) = 0$ and $Y = 0$ at $\tau = 0$
   - b.c. is $X(0) = 1$
2. It is initially loaded and then fed an inert purge gas at the inlet.
   - i.c. is $X(\zeta) = f(\zeta) \neq 0$ and $Y \neq 0$ at $\tau = 0$
   - b.c. is $X(0) = 0$.

The preconcentrator response to these conditions can be observed by looking at the outlet concentration (called the effluent curve).

Dimensionless Mass Transfer Parameters

The dimensionless mass transfer parameters are used to rearrange the mass balance equation into a convenient numerical solution form. These parameters are listed below along with a brief explanation of their physical significance [85], [91], [92]:

- The linearity of the isotherm is described by α.
$$\alpha = \frac{C_0}{K_{lang}} \tag{9.5}$$
  where C_0 is the maximum influent concentration [g/L] and K_{lang} is the Langmuir constant for the adsorption isotherm [g/L].
- The adsorption capacity is described by β.
$$\beta = \frac{q_{max}(1 - \epsilon)}{(1 + \alpha)\epsilon K_{lang}} \tag{9.6}$$
  where q_{max} is the monolayer adsorbed concentration [g/mL], ϵ is the void fraction in the bed, α and K_{lang} as defined above. The numerator is the maximum adsorptive capacity in the preconcentrator while the denominator is the adsorbate in the void volume. The breakthrough time is approximately $1 + \beta$.
- The Stanton number relates to the convection rate and is the ratio of the mass transfer rate to the convection rate.
$$\text{St} = \frac{ka(1 - \epsilon)L}{v} \tag{9.7}$$
  where k is the mass transfer coefficient that includes both external and internal resistances [cm/s], a is the surface area of the particles per volume of the bed [cm^{-1}], L is the length of the bed [cm], v is the interstitial velocity of the gas [cm/s].

- The Peclet number relates to the dispersion rate and is the ratio of the convection rate to the dispersion rate.

$$\text{Pe} = \frac{vL}{\epsilon D_z} \tag{9.8}$$

where D_z is the longitudinal diffusion coefficient [cm^2/s].

Dimensionless Equations

So far, we have discussed the main ingredients for a preconcentrator model with the goal of producing breakthrough (effluent) curves. In effect, we will now clean up the equations for fluid and solid phase mass balance by making them dimensionless to achieve two aims. First, we can have neat expressions for the mathematics of numerical methods, and second, we can use mass/heat transfer coefficient correlations with ease. The differential equation for mass balance in the gas phase in terms of dimensionless parameters is given below [91]:

$$\frac{\partial X}{\partial \tau} = \frac{1}{\text{Pe}} \left(\frac{\partial^2 X}{\partial \zeta^2} \right) - \frac{\partial X}{\partial \zeta} - \text{St} \left[X - \frac{Y}{1 + \alpha(1 - Y)} \right] \tag{9.9}$$

For mass balance in the solid (adsorbent particle) the equation is:

$$\frac{\partial Y}{\partial \tau} = \frac{\text{St}}{\beta} \left[X - \frac{Y}{1 + \alpha(1 - Y)} \right] \tag{9.10}$$

All of the coefficients can be computed for these equations based on correlations in the literature, but the ones that need model verification are k and D_z [13], [93]. These describe the kinetic behavior of the microdevice. Appendix D goes into more depth regarding the actual correlations used to estimate k_f and D_z, as well as the numerical method to solve the coupled partial differential equations.

Modelling

The effort to find the parameters q_{max} and K_{lang} that describe our system, using the newly developed model, is shown in the plots of Figures 9.5, 9.6, and 9.7. The large number of time steps requires significant computational resources; optimizing the parameters subject to the scaled-concentration constraint required several hours for each type of curve (adsorption and desorption).

It is not trivial to get the correct shape and have physically meaningful constraints such as the input concentration scaling and or fixed parameters that remain the same in the experiment. In these plots, the α's are kept in the proper ratio corresponding to the actual

Table 9.2. Model Parameters for Decane Adsorption and Desorption at $75\,^\circ\mathrm{C}$

Concentration [μg/L]	Pe	St	α	β	q_{max} [g/L]	K_{lang} [μg/L]
6.36	52.37	9.58	4.5	3.2×10^5	2.03	1.413
5.81	52.37	9.58	4.1	3.45×10^5	2.03	1.417
1.14	52.37	9.58	0.8	9.8×10^5	2.05	1.425

concentrations, and the resulting q_{max} and K_{lang} are quite close to each other. The value of the Peclet number was calculated and put into the model. The Stanton number was extracted from the numerical solution and is about a factor of four smaller than our estimation of k_f from packed bed correlations. These model parameters are summarized in Table 9.2.

The final note is the the numerical curves mostly shoot to $C/C_0 = 1$ while the experimental data have a considerably gradual slope after an initial steep rise. This is due to our simplistic representation of the uptake rate as $\frac{\partial q}{\partial t} = f(q^*)$. In reality, internal particle mass transfer resistance plays a role [92]. The inclusion of internal macro- and micropore transport resistances means that the set of partial differential equations is much more complex. Essentially the mass balance for the adsorbate in the pores of the adsorbent must be taken into account as shown in the following equation for a homogeneous pore structure [12]:

$$-D_z \left(\frac{\partial^2 C_a}{\partial r^2} + \frac{2}{r} \frac{\partial C_a}{\partial r} \right) + \frac{\partial q}{\partial t} = 0 \tag{9.11}$$

With the two mass balances, one for the fluid phase and one for the adsorbent particles, the final piece of the more sophisticated model would be to link them together via the continuity of fluxes at the surface of the adsorbent. In other words, the flux across the adsorbent surface must be continuous so we have the following continuity relation:

$$D_z \left. \frac{\partial C_a}{\partial r} \right|_{R_p} = k_c(C - C_{a,R_p}) \tag{9.12}$$

where k_c is the external mass transfer coefficient, R_p is the radius of the particle, and C_{a,R_p} is the adsorbate concentration in the fluid phase at the surface of the particle. In our case, for the design of the preconcentrator, the adsorptive capacity can be conservatively selected based on the breakthrough time predicted by the model so that the actual slope is not exceedingly important.
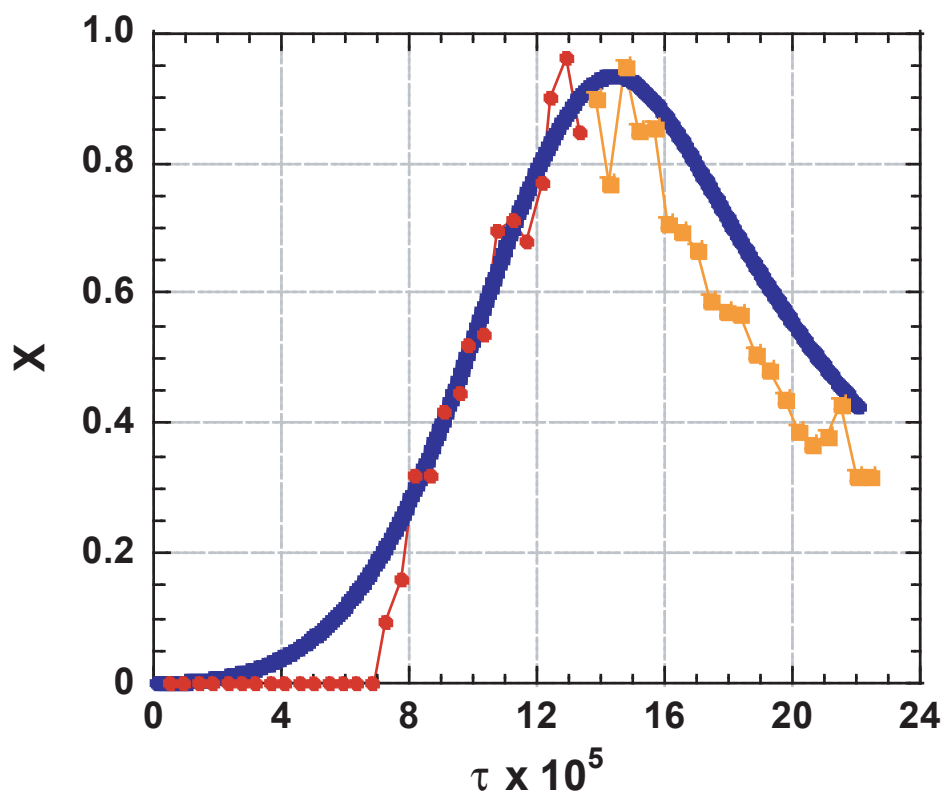
Figure 9.5. Decane adsorption and desorption at $75\,°C$ and $25\,mL/min$ flow rate. The influent concentration for adsorption is $1.14 \times 10^{-6}\,g/L$. The numerically computed breakthrough curve (blue) has the following parameters: $\alpha = 0.8$, $\beta = 9.8 \times 10^5$, $Pe = 52.37$, and $St = 9.58$. The y-axis is dimensionless concentration (normalised to the influent during the breakthrough measurement), while the x-axis is dimensionless time (normalised to the time it takes for gas to flow through a single length of the preconcentrator)
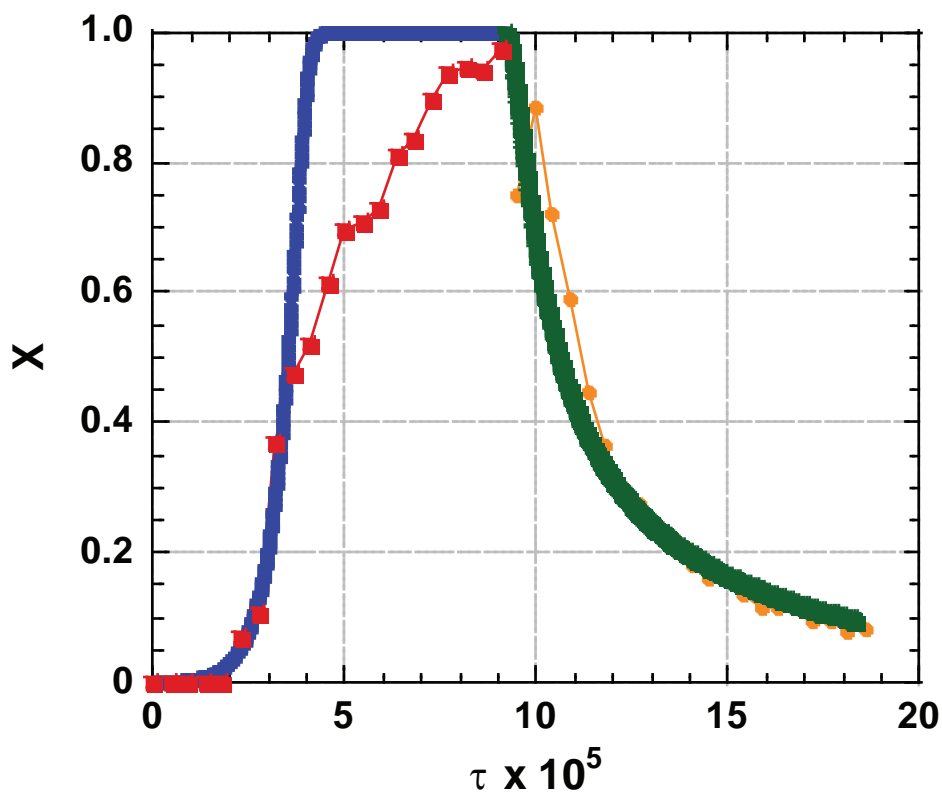
Figure 9.6. Decane adsorption and desorption at $75\,^\circ\text{C}$ and $25\,\text{mL/min}$ flow rate. The influent concentration for adsorption is $5.81 \times 10^{-6}\,\text{g/L}$. The numerically computed breakthrough curve (blue) has the following parameters: $\alpha = 4.1$, $\beta = 3.45 \times 10^5$, $\text{Pe} = 52.37$, and $\text{St} = 9.58$. The y-axis is dimensionless concentration (normalised to the influent during the breakthrough measurement), while the x-axis is dimensionless time (normalised to the time it takes for gas to flow through a single length of the preconcentrator)
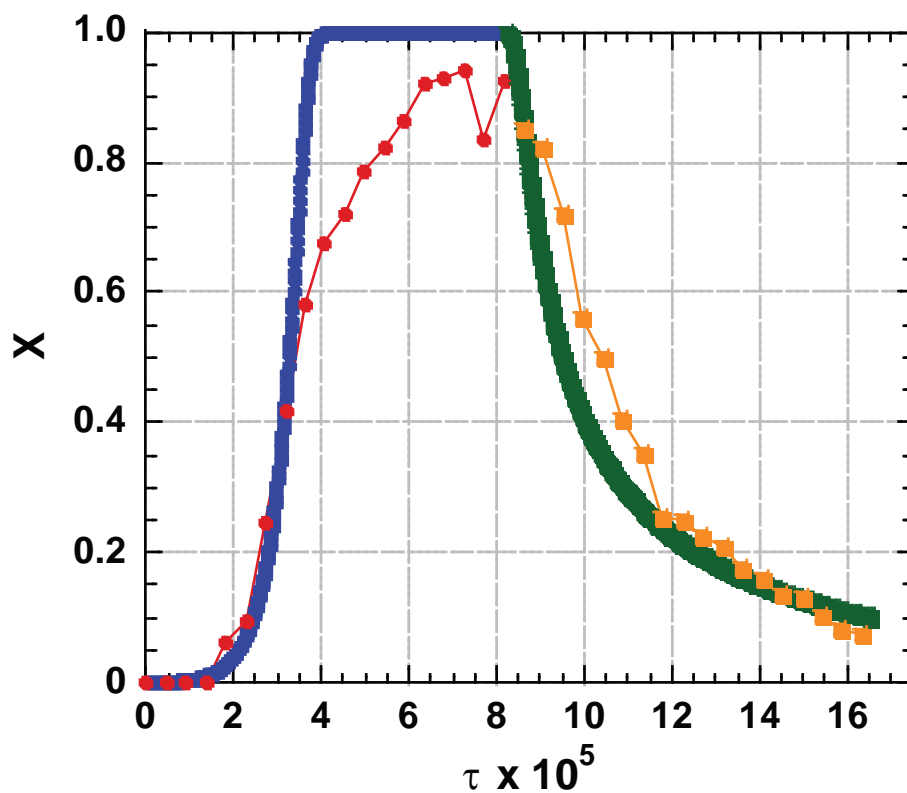
Figure 9.7. Decane adsorption and desorption at $75\,°C$ and $25\,mL/min$ flow rate. The influent concentration for adsorption is $6.36 \times 10^{-6}\,g/L$. The numerically computed breakthrough curve (blue) has the following parameters: $\alpha = 4.5$, $\beta = 3.2 \times 10^5$, $Pe = 52.37$, and $St = 9.58$. The y-axis is dimensionless concentration (normalised to the influent during the breakthrough measurement), while the x-axis is dimensionless time (normalised to the time it takes for gas to flow through a single length of the pre-concentrator)

Conclusion

The model presented in this chapter is an important first step towards optimizing the microscale preconcentrator. The fact that we have extracted q_{max} and K_{lang} from the use of this model means that we have an estimate of the adsorption isotherm for decane on Carbopack B at $75\,°\text{C}$. Where we did not have the adsorption isotherm beforehand, the new extracted estimate in conjunction with the model, means that we can change in influent concentration and predict the breakthrough time that we expect to see. We can also change the bed length, void fraction, and linear velocity to see their effects on preconcentrator behavior. The power of modeling is in prediction, and with the simple one we have constructed here, we can explore the impact of design changes with minimal resources.

The potential for modelling desorption characteristics at elevated temperatures can be seen in the hypothetical plot of Figure 9.8. In that plot, we have kept all the parameters the same as the decane $75\,°\text{C}$ case and instead have decreased β as in thermal desorption when the equilibrium adsorbed amount is very small. As expected, this hypothetical injection plug rapidly shrinks as β shrinks, and this corresponds to higher and higher desorption temperatures. In the future, the temperature dependence of the isotherm must be known in order to obtain the proper q_{max} and K_{lang} for the thermal desorption case. Once these are put back into the model, then the desorption characteristic can be modeled.
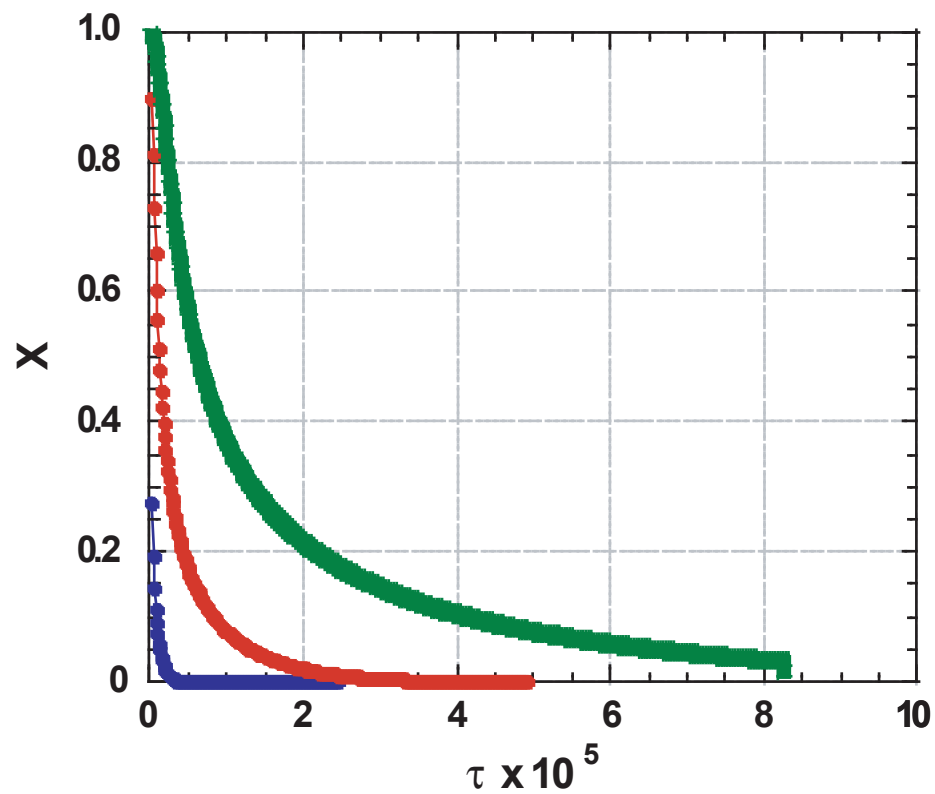
Figure 9.8. Changing β in the model amounts to modelling desorption for the preconcentrator at different temperatures. The conditions for the model are the same as for $75\,°C$ decane and $25\,mL/min$ with β decreased by a factor of 100, 10, and 2.

Chapter 10

FUNDAMENTAL TRADEOFFS

The best preconcentrator that we can conceive of can only be the best in the light of the chromatography that we want to perform. Discussing a low-power preconcentrator in and of itself means little. And likewise, talking about a scaled sensor array in and of itself has few consequences. For the column though, it *does* make sense to talk about it by itself, at least initially. Because whatever the column is—narrow-bore, standard-bore, long, short, packed, or capillary—it is what governs the chromatography and poses the fundamental constraints on separations. So in this chapter, our goal is to discuss the best preconcentrator that we can conceive of to support a μGC system based on a narrow-bore WIMS microcolumn. We ask two simple questions. What kind of separation is suitable for a $45\,\mu$m radius PECVD microcolumn? And what kind of preconcentrator do we need for this μGC? The answers to these questions bring together all of the experience and intuition that we have gained through this research: the general engineering principles that guide us through constantly evolving technology.

Thus far, our discussion has centered around μGC for complex mixture analysis. But now we will revisit Chapter 3 where we briefly alluded to narrow-bore, short-length microcolumns for high-speed separations; and we will develop concepts for preconcentrators to use with this new microcolumn.

A high-speed separation system results in drastically different requirements for sample injection. Table 10.1 shows two of the fastest separations ever accomplished using packed capillary and narrow bore capillary GC [94], [95]. It is useful to look at these two examples and to make the following observations:

- High-speed separations can be performed on packed capillary columns too, depending on the application.
- Packed capillary columns have high pressure drop so the length is generally shorter for practical purposes.
- Light hydrocarbons can be separated on packed columns while wall-coated narrow bore columns need higher boilers.
- The injection volume must be small in order to achieve high-speed separations.

In terms of sample injectors, the narrow bore capillary work used a cold trap at $-75\,^{\circ}$C with subsequent thermal desorption at a $4000\,^{\circ}$C/s heating rate for $50\,$ms using $325\,$W of power in order to achieve the required injection plug width. Certainly this puts things into per-

spective on the level of complexity and engineering constraints for our microscale injector. Were our present device to have such a heating rate with no microscale redesign, we would need to pump 208 W into it. That would require innovation in electrical interconnection.

Table 10.1. High-Speed GC Separations in the Literature

	Jonker, 1982	van Es, 1988
Column type	Packed Capillary	Narrow Bore Capillary
Length	3.2 cm	30 cm
Inner Diameter	1.19 mm	$50\,\mu$m
Stationary Phase	$10\,\mu$m Lichrosorb Si-60 particles	OV -1
Mobile Phase	He	He
Separation Mixture	C1-C4	C6-C9
Temperature	$100\,^\circ$C	$72\,^\circ$C
Injection Type	Splitless Rotary Valve	Cold Trap/Thermal Desorption
Injection Volume or Time	$1.5\,\mu$L	50 ms
Power Consumption	N/A	325 W
Separation Time	150 ms	660 ms
Inlet Pressure	63 bar	4.5 bar

A critical difference between the packed capillary and open tubular column not shown in the table is that of sample capacity. The decrease in column diameter for narrow bore columns makes their sample capacity inherently low, whereas the packed capillary column has orders of magnitude higher capacity and dynamic range. This is most clearly illustrated in Table 10.2 of data from reference [96] which also describes a recently developed multicapillary column to increase sample capacity while keeping resolving power and low pressure drop. It is easy to envision the eventual implementation of multicapillary columns in silicon since lithographic technology is reliable and mature. However, the challenge of coating a stationary phase that is uniform among the parallel microcapillaries remains in a silicon implementation.

Sample capacity is a vital limit posed for high-speed narrow-bore separations. There is one more important chromatographic descriptor to know for sample capacity, and that is phase ratio β. The phase ratio helps us visualize the relative importance between the thickness of the stationary phase, the column radius, and the retention, and is best understood in light of the distribution coefficient. The distribution coefficient K_D is a thermodynamic property that stays fixed with the solute-stationary phase pair, while the retention factor k and the

Table 10.2. Comparison of Columns for High-Speed GC

	Packed	Standard-bore	Narrow-bore	Multicapillary
Sample Capacity [ng]	200	200	1	800
Detection Limit [pg]	96	8	4	10
Plates per m	12,500	2,778	11,363	12,500
Plates per bar	90	70,000	10,000	4,000
$\bar{u}_{opt}/H$ [s^{-1}]	1,875	1,167	2,841	10,625

phase ratio β both change as a function of physical column parameters.

$$K_D = \frac{C_s}{C_m} = k\beta = k\left(\frac{r}{2d_f}\right) \tag{10.1}$$

The column radius is r, stationary film thickness is d_f, and solute concentrations in stationary and mobile phases C_s and C_m.

Looking at the phase ratio allows us to understand that the WIMS narrow-bore short-length column has a naturally suitable application: high-speed separation of trace-level, high boiling-point compounds. And the perfect sample injector would be one with low adsorptive capacity and ultra-rapid kinetics and heating. Based on existing technology, we propose a single stage Carbopack B micropreconcentrator with minimal structural mass and vertical flow configuration—an in-line micropreconcentrator. The logic behind the general statements made above is reviewed here:

- High speed comes not only from the short column lengths on the order of $25\,\mathrm{cm}$, but also from the rapid mass transport that is possible with narrow-bore (small radius) columns.
- Since the length is short, retention needs to be higher to accomplish separation. Thus, highly volatile compounds are less appropriate (they will fly through the column and coelute) while low volatility compounds are separatable.

As an illustration of the effects of the column on a new kind of preconcentrator, we consider decane with its boiling point of $174\,^{\circ}\mathrm{C}$. The molecular weight of decane is $142.28\,\mathrm{g/mol}$. A 100 ppb concentration of decane, with a $250\,\mathrm{mL}$ sampling volume gives $158 \times 10^{-9}\,\mathrm{g}$ which is fine for the standard-bore columns but not fine for the PECVD microcolumns. Assuming that stationary phase coating works for those columns, about a $100\times$ decrease in sample capacity is expected according to the values in Table 10.2, which means that the adsorbed amount can decrease by the same factor. The adsorption results on Carbopack B from the present preconcentrator indicate that $1.33\,\mathrm{mg}$ is enough for a high concentration

of decane even at $50\,°C$ since the breakthrough volume is $\approx 1250\,mL$. Our original target was $250\,mL$ which is $5\times$ less. A $100\times$ scaling for a sample size of $2.5\,mL$ is reasonable, and would mean an adsorbent mass of $26 \times 10^{-6}\,g$, essentially just a few particles.

Continuing the thought experiment, if we trap $1.58 \times 10^{-9}\,g$ of decane ($2.5\,mL$ at 100 ppb) and desorb it into $1\,\mu L$ (the plugwidth of a cold-trap/split-flow bench-scale system), then the resulting desorbed concentration (1.57 ppm) gives 15.7 as the preconcentration factor. This is quite the opposite of the present preconcentrator whose goal has is to demonstrate preconcentration factors in the hundreds as shown in Figure 10.1 where a $25\,mL/min$ flow of 151 ppb decane has been preconcentrated and thermally desorbed into a $30\,m$ column with FID detection. The concentrations have been computed from the peak areas so that column effects on the width of the eluting band play no role in the computation of the pre-concentration factor. Recalling Table 3.3 from Chapter 3 on the LODs of the sensor array, low volatility compounds need a $200\times$ preconcentration factor for a 100 ppb system LOD. In that table, chlorobenzene has a boiling point of $132\,°C$ and the sensor array's linear range for it goes from 20 to 80 ppm. Therefore the 52 ppm and $346\times$ preconcentration that we have demonstrated for decane is sufficient for our standard-bore 3-m column application.

Proposing a new preconcentrator for a high-speed system with a $15.7\times$ boost in concentration is reasonable considering that the $1\,\mu L$ desorbed volume is a formidable challenge, and the system tradeoff is that the sensor array will need to be more sensitive. Luckily, low volatility compounds support this tradeoff since they stick well to the sensor array, and their LODs are lower.

If we turn to injection plugwidths, we noted in Chapter 6 that the present preconcentrator is not optimized for low power consumption and proposed the use of stop-flow operation to compensate for the power-heating rate tradeoff. In addition, when we looked at the single vapor desorption of TCE in Chapter 8 on instrumentation, we noted that using a split-flow allows us to have a flow rate for the preconcentrator and another for the standard-bore microcolumn. Both of these techniques are implemented to demonstrate the injection plug-width of Figure 10.2 where $4\tau \approx 200\,ms$. This compares favorably to the best macroscale results that we listed in Table 10.1 while requiring only $3\,W$ of power.

The plot above highlights the potential of the model developed in Chapter 9. The almost vertical rising slope of the plug is due to the fact that in stop-flow we have essentially an isothermal bed at high temperature. The falling slope of the desorbed plug is the same falling edge that we modelled for what we called the "passive desorption" measurements in Chapter 9. The shape of the falling edge is the same, but the time is vastly different only because the temperature, and thus governing equilibrium isotherm, are different. Therefore, in the future, desorption plugwidths can be computed beforehand for single vapors provided that we know the isotherm of the adsorbent-adsorbate pair at elevated temperatures and continue to have an isothermal bed. The flow rate, void fraction, and bed length can all be input into the model to give the resulting desorbed plugwidth.

To look at enabling a preconcentrator to have a short injection plug *and* low power without stop-flow means examining the energy efficiency (or lack thereof) for the present packed-
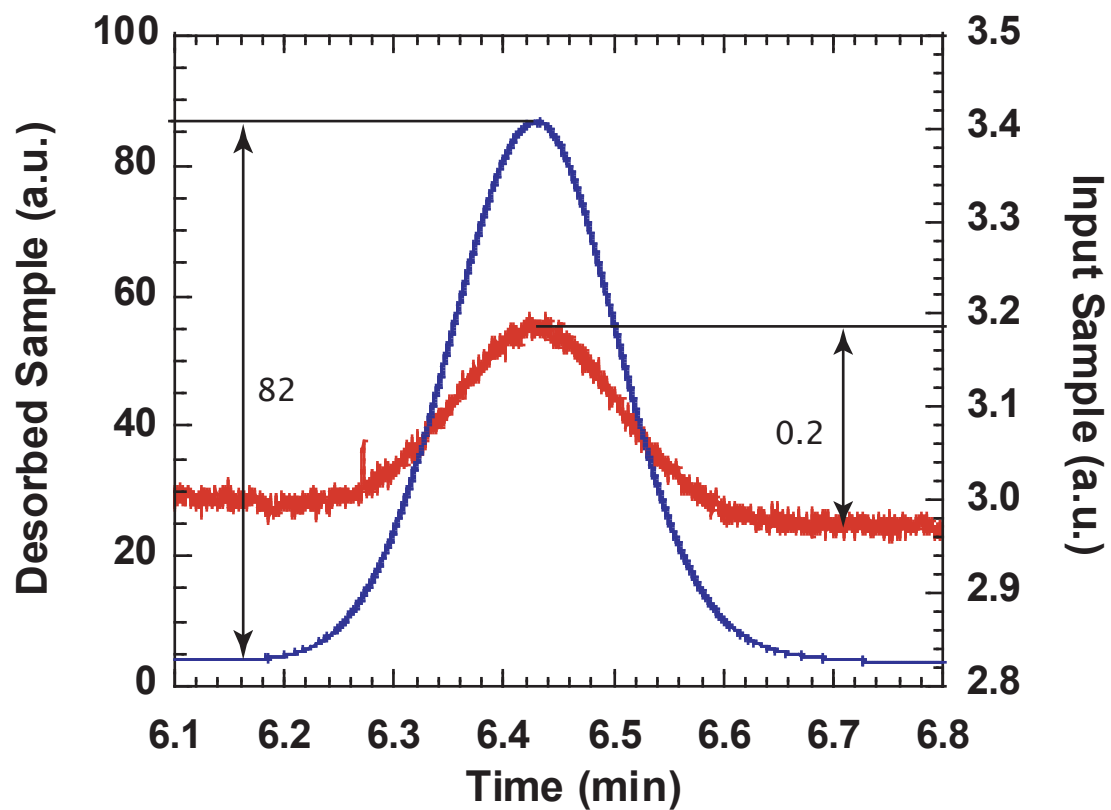
Figure 10.1. A chromatogram that shows a preconcentration factor of 346 for decane. The desorbed concentration of 346.18×10^{-6} g/L is equivalent to 52 ppm and the input sample concentration is 1×10^{-6} g/L corresponding to 151 ppb.
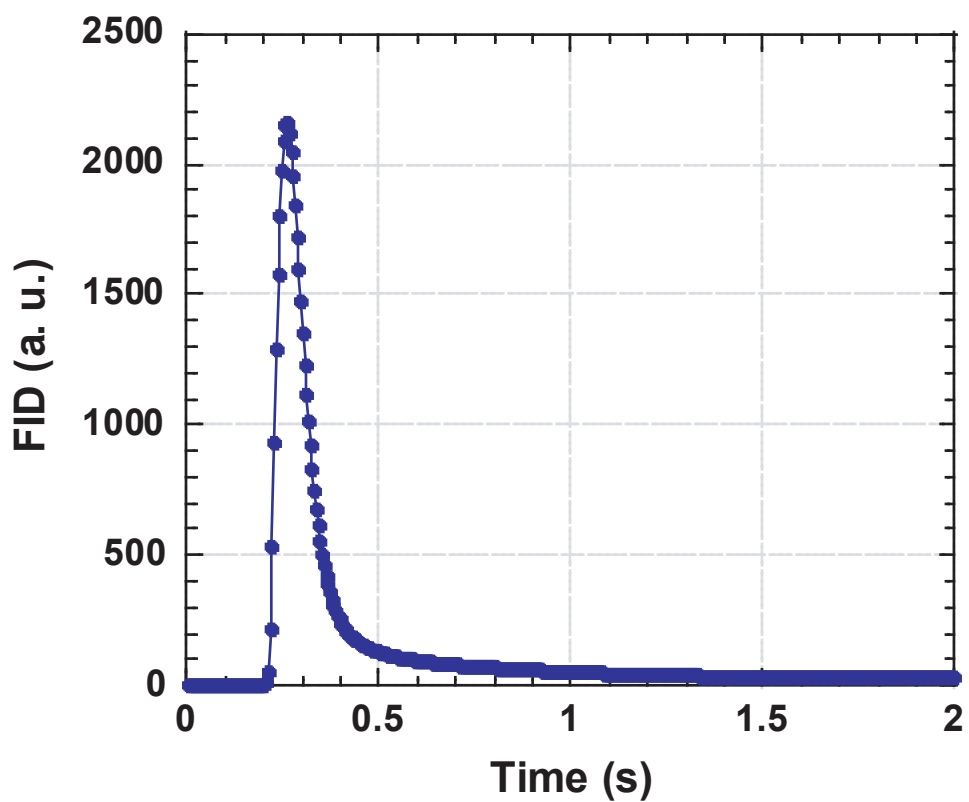
Figure 10.2. Thermal desorption directly into an FID with a 3:1 split ratio. The narrow extent of this injection can be appreciated by noting that the FID sampling rate is at its maximum of 200 Hz. This means that the distance between each data point is 5 ms. As an exercise, the reader is encouraged to count the number of data points on the rising edge of the peak.

bed design. The theoretical energy necessary to heat adsorbents is a simple function of its mass, its specific heat capacity, and the temperature difference: $Q = mc\Delta T$. To consider the rate at which we need to supply energy to accomplish heating—the power—we need only to replace the temperature difference with the heating rate.

$$\dot{S} = mc_p \frac{dT}{dt} \tag{10.2}$$

where m is the mass, c_p is the specific heat capacity, and dT/dt is the heating rate. If we want to look critically at efficiency, then we should compute the power for heating only the adsorbent. As a back of the envelope calculation, if we consider two $4\,\mathrm{mm}$ by $11\,\mathrm{mm}$ Si plates that are $150\,\mu\mathrm{m}$ thick to approximate the mostly-etched cavity and sealing portions of the preconcentrator, we have a mass of $30.76\,\mathrm{mg}$. The thermal capacitance associated with the structural mass is about $21.65\,\mathrm{mJ/K}$, which is $14.24\times$ that of the carbons. The carbons have a combined mass of $2.64\,\mathrm{mg}$ and a specific heat capacity of $577\,\mathrm{J/kg \cdot K}$ measured via differential scanning calorimetry (see Appendix C). This gives a thermal capacitance of $1.52\,\mathrm{mJ/K}$ and means that for a $30\,^\circ\mathrm{C/s}$ heating rate, $45.6\,\mathrm{mW}$ is required to heat the carbons, and $0.649\,\mathrm{W}$ is required to heat the Si structure. From our measurements in Chapter 6, the necessary power to achieve this heating rate is $1.6\,\mathrm{W}$. Therefore, 2.85% of the power goes to heating the carbons, 40.6% of the power goes to heating the Si, and the remaining power heats the surroundings.

What structure might improve on the energy efficiency and be technologically feasible to build? An alternative design structure which we call the in-line design, could allow batch loading at a wafer scale, and is shown in Figure 10.3. The technological basis for the in-line structure is the bull's eye that we have developed for the inlet and outlet gas flow ports of the present preconcentrator that was pictured in Figure 5.10. Remember that the bull's eye was for holding fused silica capillaries that interface with our device. If we wish to keep the ability to test the future device with a macrosystem, the fused silica capillaries cannot be dispensed with. Therefore, the most minimalistic preconcentrator that we can think of is one that essentially fits into a capillary, hence the name "in-line."

The concept involves taking two silicon wafers, having one to hold the granular carbons, but this time implement the heater on the other wafer so that it is inside the bonded microstructures. Now the heat lost by the heater (a thin-film resistive heater on a silicon grid) is used to preheat the gas as it enters and contacts the adsorbent. In this way, energy efficiency is improved by "recycling" the heat. For the high-speed μGC, we conveniently only need one bed of Carbopack B adsorbents to trap low volatility compounds. Otherwise, if multiple stages are necessary, a modular approach allows more of these cavities to be stacked and integrated via wafer bonding creating a "wedding cake" type configuration.

The idea for thermal isolation is to isolate the central adsorbent-containing cavity in the radial direction. The top view of the in-line configuration is illustrated in Figure 10.4. In essence, the goal of the design is to create a micro-scale thermos, or well-insulated drinking straw, with a section of adsorbent particles held in place by two silicon grids at the top and
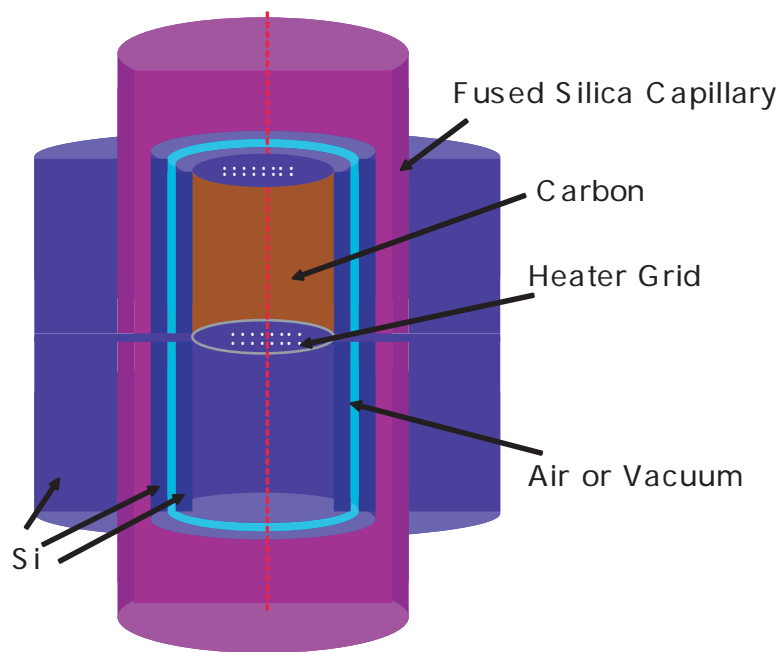
Figure 10.3. In-line preconcentrator design diagram.

Radii 215, 225, 335, 345, 445, 495, 595, 750 μm
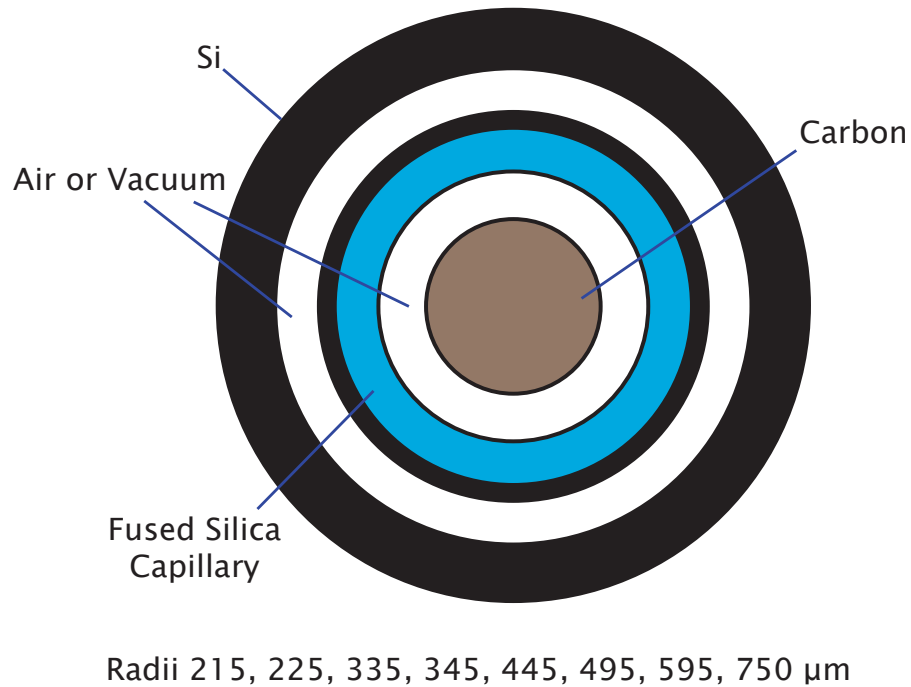
Figure 10.4. Top view of the in-line preconcentrator design showing successive isolation layers.

the bottom. Concentric rings of insulation (air or vacuum) isolate the center heated area of the device. One of the grids is heated via a thin-film metal heater and we choose to connect the heated grid-end to the micropump rather than the column.

Placing a thin-film heater inside the sealed cavity means that technologically, we need the ability to hermetically seal over metal feedthroughs. Initial work in this area is shown in Figure 10.5 where glass frit is used to bond a Si cavity over another Si substrate with $1.5\,\mu m$ Al metallization. This process has been tested for hermeticity, and its $425\,°C$ processing temperature makes it appropriate for surviving thermal desorption temperatures in microdevice operation.

The power to maintain a give steady-state temperature is plotted in Figure 10.6 for the dimensions shown in Figure 10.4. At first glance the $0.75\,W$ of power for $600\,K$ may be alarming considering that our current design, if vacuum encapsulated and gold-coated should only burn $0.47\,W$. However, this steady-state power will not be necessary in practice due to the rapid heating rate achievable with the design. And to answer the question of why the steady-state power is so great, there are two reasons. The first is that we have included the heat loss from forced flow through the device, and the second is that the fused silica
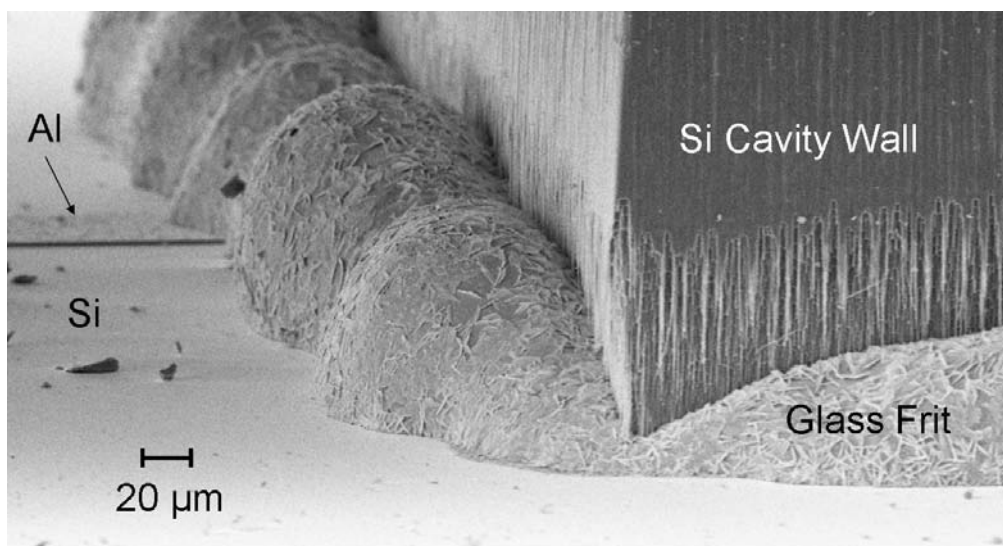
Figure 10.5. Glass frit sealing of a Si cavity over $1.5\,\mu$m Al resistive feedthroughs.

capallaries are a direct heat sink. The tubular configuration of the in-line design allows us to compute a believable loss due to forced flow since the flow path is less complex than our present horizontal configuration.

Taking advantage of the axial symmetry of this design, we have computed the transient heating power for the in-line preconcentrator with 2D axisymmetric ANSYS simulations. The boundary conditions for these simulations are specified as a function of temperature via look-up tables in the model, and are taken directly from steady-state heat transfer coefficients at those temperatures. Appendix E reviews the heat transfer coefficient computations for this design. Figure 10.7 is a comparison of different applied powers and the temperature reached by carbon at the top unheated grid. The $3\,$W case gives a necessary heating time of $200\,$ms to reach $600\,$K which amounts to a $1500\,°\mathrm{C/s}$ heating rate. Even at $1\,$W it only takes $0.75\,$s for the carbon to heat up.

Figure 10.8 illustrates the rapid rise in heating rate with applied power. At $5\,$W it only takes $100\,$ms to heat the carbon, a heating rate of $3000\,°\mathrm{C/s}$. The heating times are still short enough at $1\,$W for a brief stop-flow for actual operation if desired. The silicon grid in this design has a mass of $3.4\times 10^{-6}\,$g so that its thermal capacitance is about $6.5\times$ less than the carbon itself.

We have made the case for an overhaul of the thermal structure surrounding the carbon adsorbent. However, there is one note of caution for any new design and that is illustrated via the data we have collected for the current cavity-based preconcentrator in Figure 10.9. The two plots in this figure correspond to a binary mixture breakthrough and desorption. We mentioned in Chapter 8 how the single vapor adsorption of octane, while impressive

166
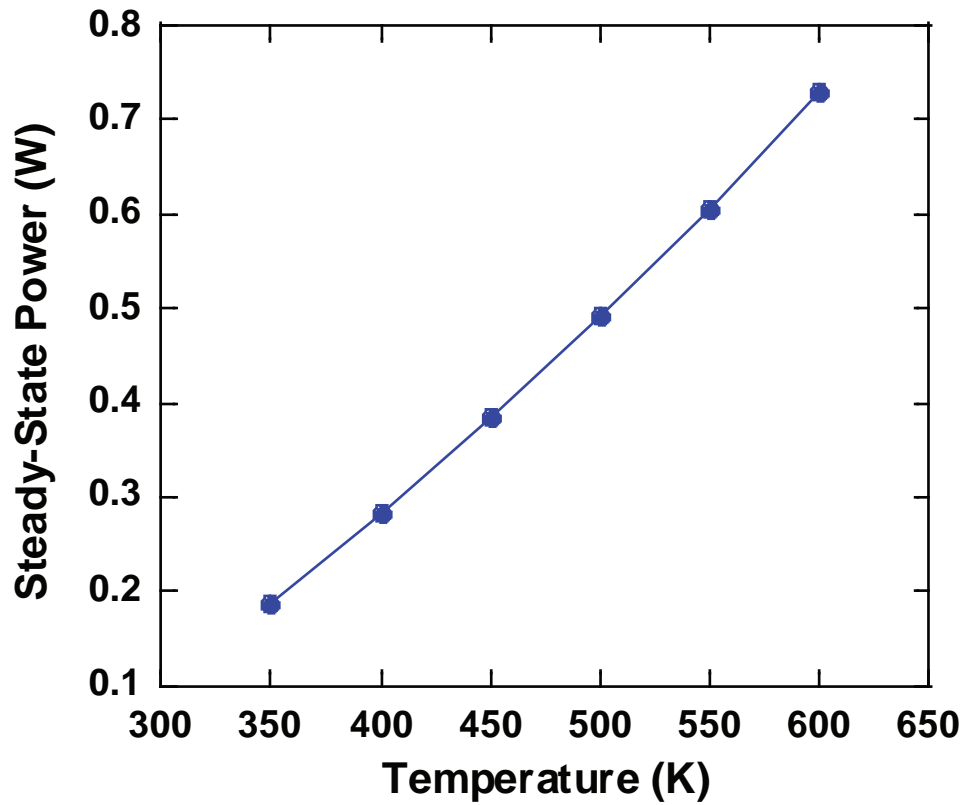
Figure 10.6. Steady-state power computed for the in-line pre-concentrator design with a grid thickness of $100\,\mu$m.
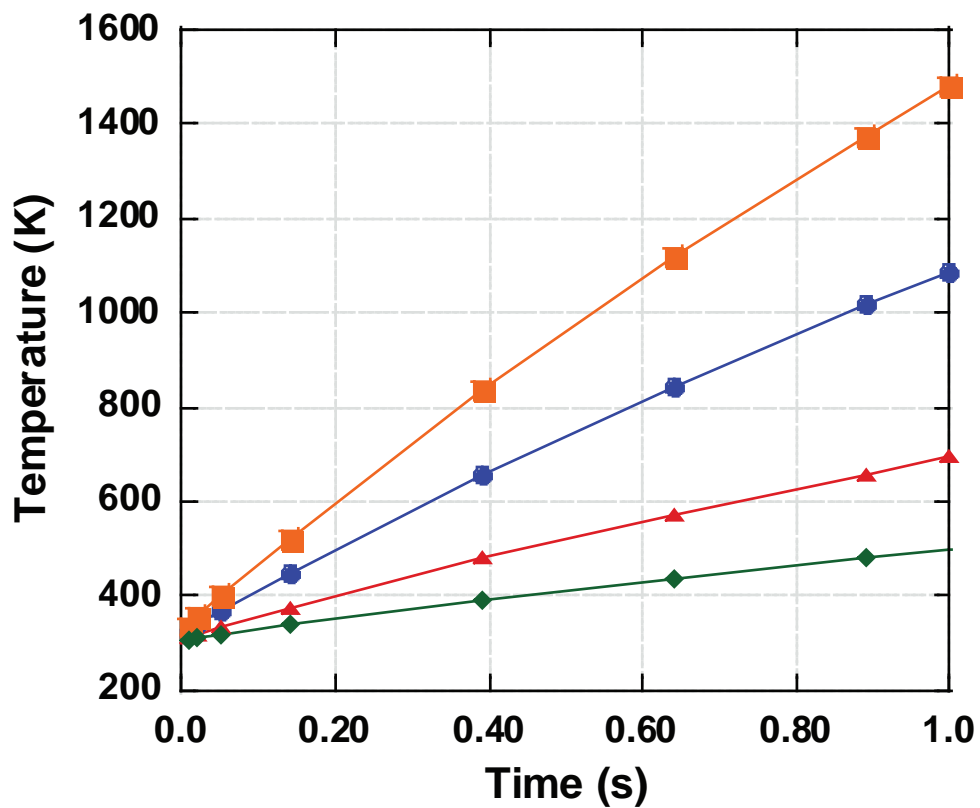
Figure 10.7. Transient heating temperature as a function of power: 3 W (squares), 2 W (circles), 1 W (triangles), 0.5 W (diamonds), and heating time for the in-line preconcentrator design for a grid thickness of 100 μm.
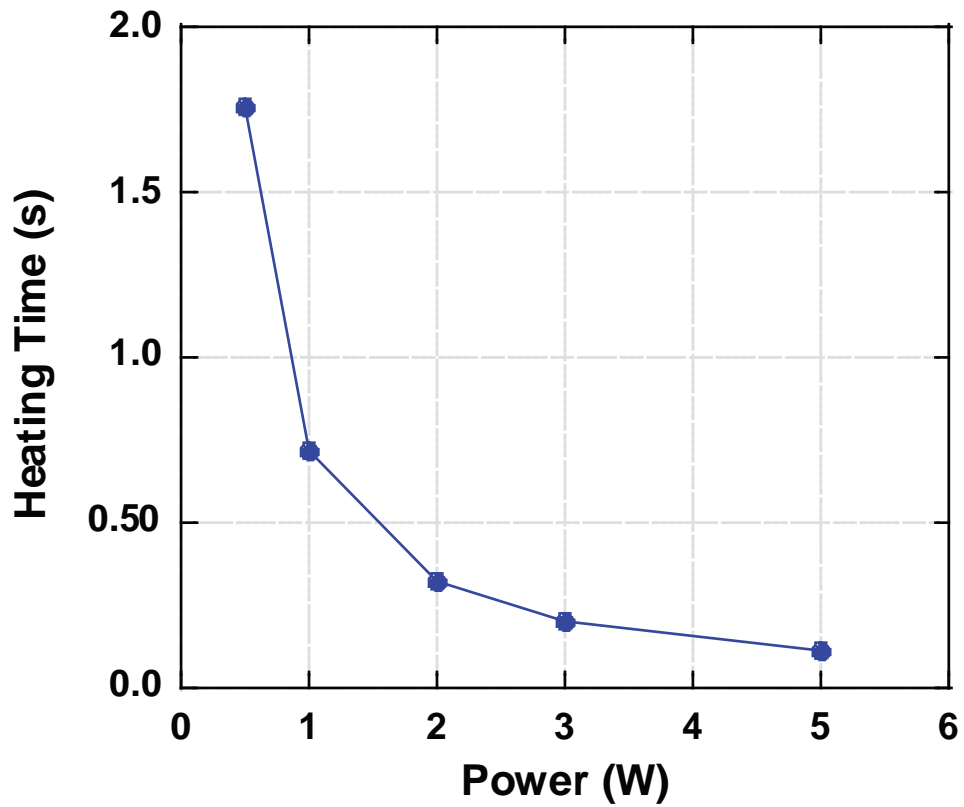
Figure 10.8. Heating time computed for a $\Delta T = 300$K as a function of applied power for the in-line preconcentrator design with a grid thickness of $100\,\mu$m.

Table 10.3. Comparison of the In-line and Cavity Designs

Parameter	Units	In-line	Cavity
Dead Volume	μL	0	1.70
Carbon Mass	mg	26×10^{-3}	2.64
Silicon Mass	mg	3.4×10^{-3}	30.76
Heating Rate for 3 W	$^\circ$C/s	1500	60

with its lone capacity, is expected to be a weak adsorption. This binary breakthrough experiment shows just that—the displacement of the initially adsorbed octane by decane, the preferred adsorbate. For modelling a new preconcentrator, we need to be aware that mixtures add a lot more computation time and complexity. The future extension of the current microdevice model is to take it to handle multicomponent adsorbable influents.

Conclusion

This chapter brought together elements that we have learned from pursuing this research to propose a next-generation in-line preconcentrator that is both energy efficient and capable of narrow injection plugwidths. The characteristics of the in-line design are highlighted in the comparison of Table 10.3. With the rapid heating ability of this in-line structure, the injection plugwidth will not be limited by the heating rate of the microstructure or carbons, as in the current design which emphasizes large adsorbent capacity and has not been thermally optimized. The decrease in adsorptive capacity for the proposed design fits in with a new system that WIMS is targeting to implement: a high-speed narrow-bore GC based on new PECVD microcolumn technology. With our understanding of how the components fit together to perform chromatography, we saw that it makes sense to pursue a single-stage Carbopack B-type in-line preconcentrator to support a lower sample capacity separation column that is suitable for lower volatility compounds. And we also noted that the system trade for a sensor array with lower detection limits is also reasonable given that sorption is also its operation principle so the low volatility compounds have better detection limits.
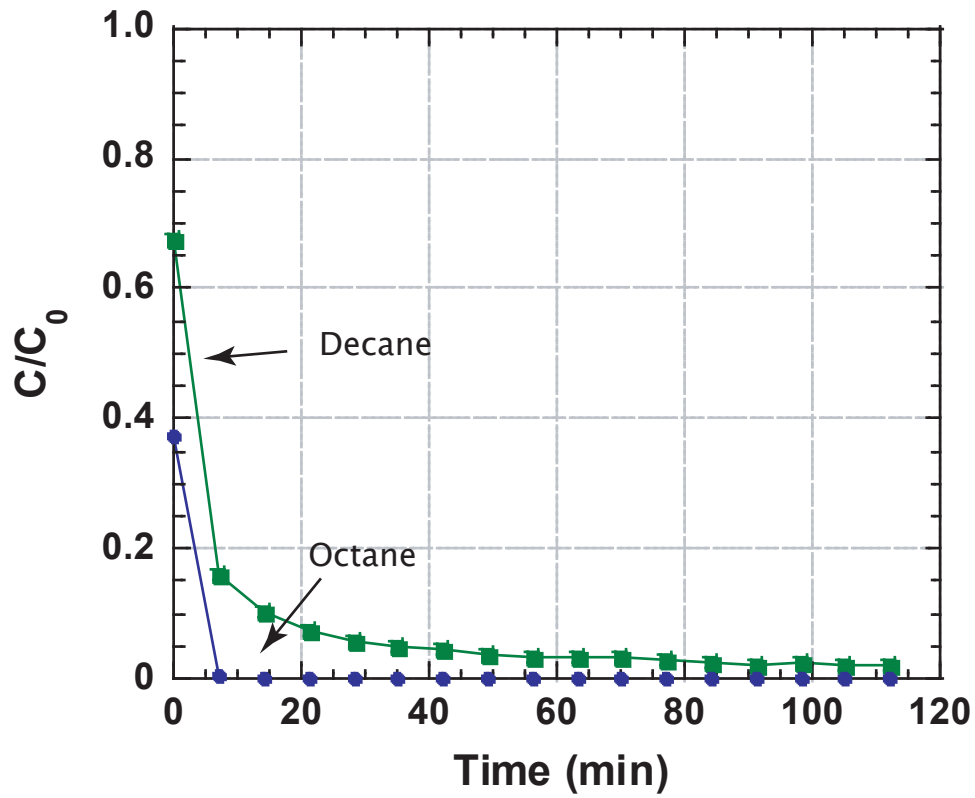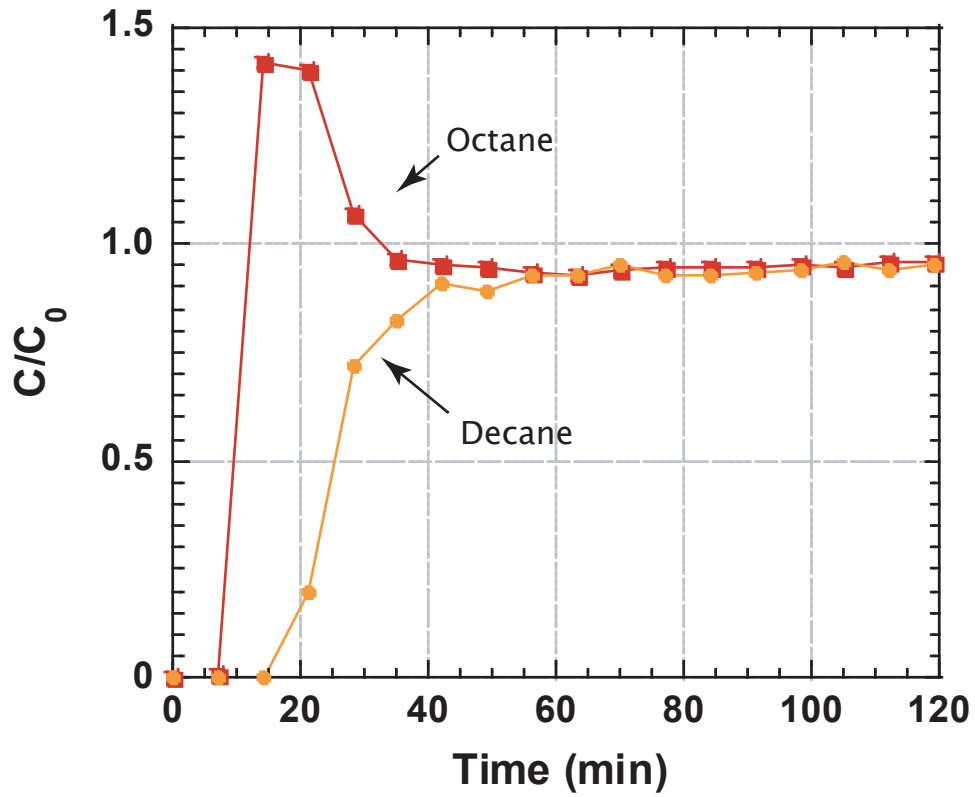
Figure 10.9. Breakthrough curve at room temperature for binary mixture of octane 38.22×10^{-6} g/L and decane 38.11×10^{-6} g/L at room temperat

Chapter 11

CONCLUSION

The irony behind dissertations is that writing about the new and novel makes it old. Often, "old" has a stigma attached to it, and undeservedly so. The power of old is how it got there, and our approach is to apply system-level thinking to solve complex multidisciplinary problems and to manage the risks of research.

The creation of a microscale preconcentrator involves holistic planning and domain-specific know-how. The previous chapters have detailed how to analyze system requirements, select an architecture, develop new technology, manufacture, test, and model a microdevice from scratch. And in addition to the tangible hardware of the microdevice, the supporting crew of test instrumentation, data acquisition, interfaces, operational parameters, and test procedures was also an output of this work. To sum up, this project has encompassed a development cycle of fabrication, integration, and verification. The next sections highlight performance accomplishments to summarize this work.

Objective

The objective for this project has been to build a microdevice that enables autonomous, real-time quantitative analysis of volatile organic compounds (VOCs), on the U.S. EPA indoor air contaminants list, using a microscale gas chromatograph (μGC).

Performance Metrics

After analyzing the system requirements, which involves understanding the discpline of gas chromatography, the performance metrics for the microdevice are breakthrough volume ($250\,\mathrm{mL}$ adsorptive capacity), preconcentration factor (200 to 600), and injection plugwidth ($\leq 1\,\mathrm{s}$).

Architecture

The architecture chosen for implementation is a preconcentrator that extracts VOCs using highly adsorptive, granular forms of graphitized carbon black and carbon molecular sieve with surface areas of 100 to $1000\,\mathrm{m^2/g}$. The 180 to $212\,\mu\mathrm{m}$-diameter carbons reside in $450\,\mu\mathrm{m}$-deep silicon cavities that have integrated heating and temperature sensing. Extraction of ppb-level VOCs happens at room temperature, while injection consists of heating the device to $300\,^{\circ}\mathrm{C}$ to thermally desorb the VOCs at ppm levels.

Existing Technology

A predecessor parallel-microchannel prototype was refabricated and re-tested to obtain a valuable starting point in understanding physical manufacturing constraints. Many challenges were identified with the parallel-microchannel approach:

- Manufacturing problem of interstage adsorbent contamination
- Inability to incorporate adsorbent mass measurement, critical to component performance characterization
- The use of off-chip devices to monitor temperature
- Absence of robust electrical and gas flow interface technology

The result of these technological challenges was that the prototypes were unable to demonstrate exhaustive extraction and sample injection, the goals of the work.

Fabrication and Integration

Each of the problem areas was solved through new technology developments in this project, building on experience in the discipline of microelectronic fabrication:

- **Adsorbent-solvent loading and wafer-level integration**
  A new adsorbent-solvent technique allowed 180 to $212\,\mu\mathrm{m}$-diameter carbons to be introduced into $450\,\mu\mathrm{m}$-deep silicon cavities in measurable (mg) quantities ($10\,\mu\mathrm{g}$ measurement resolution). Interstage adsorbent contamination was eliminated with this technique. A new solvent-tolerant wafer-level bonding process was developed with a maximum temperature of $400\,^{\circ}\mathrm{C}$, less than half of the $850\,^{\circ}\mathrm{C}$ in the rapid thermal annealing (RTA) approach of die-level predecessors.
- **Integrated temperature sensing**
  Platinum resistance temperature detectors (Pt RTDs) have been integrated onto the backside of the preconcentrator by adding an isolation oxide and evaporating the thin-film Pt.

- **Packaging**
  Two packages are developed for robust electrical and gas flow interfacing: one for functional verification with a conventional GC and one for integration into the μGC.
- **Testing platform**
  A modular, resusable testing board is developed for maximum testing-environment versatility; the testboard is used in pressure drop, forced-flow heat transfer, vacuum environment, adsorptive capacity, and sample injection test and verification setups.

Simulation and Modeling

The domains of thermal analysis and chemical engineering have been brought together in simulation and modeling of the new microdevice.

- **Mass transfer:**
  A one-dimensional mass balance is used to construct a physically intuitive model, the first for any microscale preconcentrator, to describe adsorption and desorption. The numerical description consists of centered differencing for the dispersion and convection terms, while time stepping involves the use of the Crank-Nicolson and second-order predictor-corrector schemes. The model is applied to extract Langmuir adsorption isotherm parameters q_{max} and K_{lang} from effluent curve measurements of decane adsorption and desorption at $75\,^{\circ}$C and $25\,\text{mL/min}$ with varying concentrations.
- **Heat transfer:**
  Steady-state heat transfer computations are made to categorize the contributions of radiation, convection, and conduction on device performance and to enable predictions of performance improvements. In addition, a two-dimensional axisymmetric model is implemented in ANSYS to perform simulations of transient heating for a next-generation in-line preconcentrator.

Performance Verification Highlights

The following are proven performance data that have been verified via measurements. The parenthetical notes for single-number metrics refer to improvements resulting from an apples-to-apples comparison with the predecessor prototype.

- The silicon cavity-based preconcentrator is the first to be wafer-level integrated. The maximum temperature of $400\,^{\circ}$C in this microfabrication process fulfills the constraints posed by the carbon adsorbent degradation $<477\,^{\circ}$C where previous die-level prototypes exceeded this limit by using rapid-thermal annealing for bonding at $850\,^{\circ}$C.

- Quantitative capture and injection of a wide volatility range of VOCs: 200 ppb mixture of acetone, trichloroethylene, and n-decane, and subsequent thermal desorption at $300\,°C$ and an applied power of $1.8\,W$ into a **GC/FID**.
- Large exhaustive extraction capacity (≈ 0.5 to $3\,L$) for octane to dodecane at a high flow rate of $25\,mL/min$ (brief bed-contact time).
- Preconcentration factor of $346\times$ for a decane influent concentration of $1 \times 10^{-6}\,g/L$.
- Demonstration of $100\,ms$ injections using 3:1 split-flow, $8\,mL/min$, and $30\,s$ stop-flow heating to $300\,°C$.
- $1.8\,W$ power for steady-state heating at $300\,°C$ (33% improvement).
- Transient heating energy usage of $18.75\,°C/\,J$ ($2.32\times$ better).

Lessons Learned

The process of engineering usually unearths surprises and insights. Here is a choice selection:

- The current horizontal packed bed configuration achieves exhaustive extraction that is sufficient for our quantitative analysis requirements. At elevated temperatures, the adsorptive capacity remains large.
- A 1D mass balance equation and single mass transfer resistance captures the basic behaviors of preconcentrator adsorption and desorption even without knowledge of the exact nature of flow dynamics and interparticle resistances.
- The risks associated with manipulating granular carbon adsorbents with adsorbed solvents can be mitigated to enable microdevice construction via microelectronic fabrication techniques. The risks are that typically, solvents pose problems for wafer bonding and particles are considered contaminants in a cleanroom environment.
- The horizontal packed bed design is not thermally optimized for energy efficiency. Vacuum packaging and radiation shielding can reduce two-thirds of the heat loss so that only $0.47\,W$ is required to heat to $300\,°C$.
- Microstructure energy efficiency can be improved $\approx 3\times$ to $60\,°C/\,J$ with thermal optimizations in an in-line preconcentrator design.
- To investigate mass transfer resistances and rates requires a microstructure whose flow configuration is better understood. The vertically-oriented in-line preconcentrator satisfies this need, and its axial symmetry benefits quasi-3D transient thermal modelling.

Final Remarks

The thesis is a medium by which we can contribute to a university's mission—to teach. The teaching aspect is implicitly contained in the expository nature of this dissertation.

The explicit argument in this thesis has been that making engineering progress begins with a thorough grasp of the intellectual contexts and technical constraints of the problem at hand, and then choosing the right problems to solve. This argument was first framed in Chapter 2 by observing that the "right problems" to solve are the ones that move the field forward in the cycle of invention, application, and fundamental understanding.

The remainder of this thesis has sought to show that this work has brought to bear its intellectual antecedents—gas chromatography, packed beds, and microelectronic fabrication—to create a new preconcentrator. And most importantly, the thesis argues that the robustness of the microdevice and the development of an intuitive model have propelled the field towards a fundamental understanding. The measured performance, facts and figures, reviewed above, support our claim. The hope is that while at the start of this research, preconcentrators were not hot, now the next-generation gold-coated descendents will be—based on our breakthroughs.

Appendix A

THERMODYNAMICS OF ADSORPTION

This appendix is about physisorption—the fundamental process that accounts for preconcentration. The aim is to impart a basic physical understanding of this process and its relation to material properties so that the reader's imagination can meditate on new microdevices that might benefit from modifying these relationships.

The van't Hoff and Clausius-Clapeyron equations, isosteric heats of adsorption, and chemical potential are generally discussed here as a part of a holistic account of adsorption for preconcentrators and μGCs. Concepts are explained in words and mathematical symbols, because we are talking about energy and systems in equilibrium. Here are some of the questions that we will touch upon:

- Why is it exothermic?
- What is the heat of adsorption?
- How is the heat of adsorption related to adsorbent-adosorbate (solid-gas) interaction potentials? (i.e., how we might calculate it)
- What is the relationship between temperature, pressure and the energy associated with an adsorbent-adsorbate system at equilibrium? (i.e., how we might measure it)
- Which assumptions along the way are relevant to trace-level VOC adsorption onto carbons? (i.e., how we actually use this information)

The last page gives a word on mathematical notation.

A.1   Physisorption

If a clean solid surface is exposed to a gas, the gas molecules are attracted to the solid surface via dispersion and electrostatic forces. The energy associated with this attraction is the adsorbent-adsorbate potential energy. It is expressed as a function of the distance, and for a single molecule-solid surface pair:

$$\phi \;=\; \phi_D + \phi_R + \phi_{Ind} + \phi_{F\mu} + \phi_{\dot{F}Q} \tag{A.1}$$

$$= -\frac{A}{r^6} + \frac{B}{r^{12}} - \frac{1}{2}\alpha E^2 - \mu E + \frac{1}{2}Q\frac{\partial E}{\partial r} \qquad (A.2)$$

The expression has been written out to illustrate the contribution of the Lennard-Jones 6-12 potential (nonspecific van der Waals interactions), and the last three terms which are electrostatic interactions. In carbon adsorbents, the nonspecific dispersion forces are primarily responsible for adsorption since their surfaces are nonpolar (i.e., they do not have permanent dipole or quadrupole moments). This is important because the potential of nonspecific interactions does not depend on temperature. For simple cases, ϕ can be computed. Furthermore, the potential energy associated with these forces is the heat of adsorption when the number of gas molecules is few and when the kinetic energy contribution is small, and I will come back to this later.

Physisorption as described above is observed to be a spontaneous process. This fits into the picture of molecules adsorbing onto the surface in order to minimize the energy of the gas-solid system. In chemical thermodynamics, a spontaneous process (non-equilibrium system) at constant temperature and pressure, is one where the Gibbs free energy change of the system is minimized, that is $\Delta G < 0$ so that the system tends toward equilibrium. The previous statement is quite loaded and it helps to explain it a little further because the fact that $\Delta G < 0$ for a spontaneous process comes from the laws of thermodynamics.

Recall the first law of thermodynamics, the conservation of energy:

$$dU = đq + đw \qquad (A.3)$$

where U is the internal energy of the system, q is the energy into the system via heat transfer, and w is the work done on the system. The first law tells us that energy can be converted from one form to another, and that energy is not lost in the process of conversion. This gives us the equilibrium distributions of different energies but does not indicate the preferred way for a system to get to equilibrium. In chemistry terms, it does not tell the direction of a chemical reaction. The second law of thermodynamics gives us the preferred direction of chemical reactions:

$$dS \geq \frac{đq}{T} \qquad (A.4)$$

where S is the entropy of the system, T is the temperature. The second law says that we cannot turn all of the heat we put into a system into work: some of the energy is converted to another form. For an equilibrium system which is closed and isolated, there is no heat going into it, $đq = 0$ and no change in internal energy or volume, so that the change in entropy is $dS_{U,V} \geq 0$. That is, if we perturb the equilibrium system in any way, we will increase its entropy.

A closed and isolated system is theoretically entertaining, but in the world of the practical, as in adsorption, we operate on non-isolated systems. Another limitation of the description

presented is that if we express the internal energy as a function of entropy, things will be very hard to measure! We are good at measuring temperatures, pressures, and volumes, but not entropy. Therefore, the new state functions of enthalpy H and Gibbs free energy G are defined to help recast the laws of thermodynamics into something we can relate to via experiments on the laboratory bench. I am mentioning enthalpy because it is in the definition of Gibbs free energy. Enthalpy is a state function given by $H = U + pV$ where p is pressure and V is volume. At constant pressure it is the heat absorbed by the system.

It is relatively easy to have constant temperature and pressure for a system in the laboratory, so the Gibbs free energy is useful in practice. It is given by $G = H - TS$ where H is enthalpy, T is temperature, and S is entropy. At constant T and p, the Gibbs free energy is the reversible non-pV work for a process. If we combine the first and second laws of thermodynamics with the definition of G we get:

$$dG \leq -SdT + Vdp + đw_e \tag{A.5}$$

So now, for the case of adsorption, in a non-equilibrium gas-solid system, if we hold the temperature and pressure constant ($dT = dp = 0$) and do no non-pV work on it ($đw_e = 0$), the tendency of the system is to make $dG_{T,p} < 0$ which is what I said above about the spontaneous process of adsorption.

Now that $\Delta G < 0$ has been established for physisorption, it is easy to see why it is exothermic. When a molecule from the gas phase adsorbs onto a surface it loses a degree of freedom which means that the change in entropy, $\Delta S < 0$. Therefore, it follows from $\Delta G = \Delta H - T\Delta S$ that $\Delta H < 0$ in order for $\Delta G < 0$. The enthalpy H was defined to be the heat absorbed by the system at constant pressure, so $\Delta H < 0$ means that heat is released (hence exothermic) via the process of adsorption. It is precisely the enthalpy change from the gaseous to adsorbed states ΔH that what we call the heat of adsorption ΔH_0 or ΔH_{ads}.

A.2   Heat of Adsorption

The next question is, how might we calculate ΔH_0? To tackle this question, let us look at the two phases in adsorption: the gaseous and adsorbed phases, the enthalpy associated with each of these, and hence obtain their difference, the heat of adsorption ΔH_0.

For the remainder of this article, we use the ideal gas equation of state, $PV = nRT$ to describe the gaseous phase. It is important to note that we are able to use this equation of state only because this corresponds to the adsorption of parts-per-billion levels of VOCs in air. Recall that in the ideal gas equation of state, we are ignoring the mass associated with the gas molecules and assuming that the pressure is sufficiently low so that we can say that the molecules do not interact with each other. The fact that the molecules do not interact with each other is also very important. It means that the adsorbate-adsorbate interaction

potential is assumed to be negligible. This was implied in our discussion of the potential energy of adsorption where we discussed the potential arising from interaction between a gas molecule and a surface, and did not include the potential of a gas molecule interacting with another.

Returning to how to calculate ΔH_0, the molar enthalpy of the gaseous phase is:

$$\overline{H}_g = U_g + RT \tag{A.6}$$

where U_g is the internal energy of the gas, and RT comes from the ideal gas law being substituted for pV in the definition of enthalpy (see above). Molar enthalpy just means enthalpy divided by the number of moles n. For the adsorbed phase, the molar enthalpy is:

$$\overline{H}_a = U_a + \bar{\phi} \tag{A.7}$$

where $\bar{\phi}$ is the partial molar adsorbent-adsorbate potential. This is the potential for the gas molecules of the type that get adsorbed, and the surface. (In a moment, I will digress to explain partial pressure as opposed to absolute pressure.)

The isosteric heat of adsorption is the difference in molar enthalpies between the gaseous and adsorbed phases:

$$
\begin{aligned}
-\Delta H_0 &= \overline{H}_g - \overline{H}_s \tag{A.8} \\
&= U_g - U_s + RT - \bar{\phi} \tag{A.9} \\
&= -\bar{\phi} + RT(1 + n/2) \tag{A.10}
\end{aligned}
$$

where the difference in internal energy is the difference in kinetic energy and from the equipartition of energy we have $U_g - U_s = nRT/2$. The second term is usually small so that we just have $-\Delta H_0 \approx \bar{\phi}$. This is great! We now have one way to obtain the isosteric heat of adsorption, and that is to calculate the molar adsorbent-adsorbate interaction potential $\bar{\phi}$. One useful piece of information that results from this is that $-\Delta H_0$ is temperature independent for the carbons because $\bar{\phi}$ is dominated by nonspecific interactions.

Now as promised, a digression on the key concept of partial pressures. The partial pressure of a gas in a mixture is the pressure of that single gas in a given volume as if it were the only gas existent in that volume. Dalton's law of partial pressures says that the total pressure of a gas mixture is the sum of the partial pressures of each gas. Note that this is another way of saying that the different gas molecules do not interact with one another in a mixture. In fact, this lack of molecular interaction between gase molecules had to be made in order to use the ideal gas equation of state earlier, and we said that for trace-levels of VOCs in air that this was acceptable. For adsorption, this means that if we have 10 ppb of acetone in atmospheric pressure air, we use the pressure corresponding to 10 ppb of acetone in our calculations, and not 1 atm which is the absolute pressure.

A.3   Phase Transitions

So far we have been talking about energies, and we now know the heat of adsorption as a function of distance which is not bad for a first-order calculation. However, it is hard to know the distances of all the molecules at a given instant. Therefore, it would be even better if we knew how the heat of adsorption is related to an intensive variable such as pressure or temperature.

For the case of adsorption equilibrium, we have equilibrium between two phases: a gaseous phase and an adsorbed phase. When the system is not in equilibrium, there is a phase transition between the two depending on the energy of the process.

To find the relationship between temperature, pressure, and the enthalpy of a phase transition, we take an equilibrium system, say where the gas and adsorbed phase are in equilibrium, perturb it a little in pressure or temperature to reach another equilibrium, and look at the energy difference between the two equilibrium points. For the gas phase, the infinitesimal change in Gibbs free energy as a function of dT and dp is:

$$dG_g = -S_g dT + V_g dp \tag{A.11}$$

and for the adsorbed phase:

$$dG_a = -S_a dT + V_a dp \tag{A.12}$$

We said that the initial state is at equilibrium and that the final state is also at equilibrium. This means that the Gibbs free energies of each phase should be equal, before and after, so that $dG_g = dG_a$. Therefore if we subtract the two equations we get:

$$0 = -\Delta S dT + \Delta V dp \tag{A.13}$$

and when we rearrange it, we get the general Clapeyron equation for phase transitions:

$$\frac{dp}{dT} = \frac{\Delta S}{\Delta V} = \frac{\Delta H}{T \Delta V} \tag{A.14}$$

where the last equality comes from the fact that at equilibrium $\Delta G = 0$, giving $\Delta S = \Delta H/T$. The Clapeyron equation is general for solid-liquid, gas-solid, etc. phase transitions. It tells us that we can get the relationship between temperature and pressure that describes the equilibrium coexistence of phases (many different equilibrium points) just from knowing the energies of these phases at a single equilibrium point.

In the special case of the gas-solid or gas-liquid transition, as in adsorption, if we use the ideal gas equation of state to describe the gas and make two approximations we get what is known as the Clausius-Clapeyron equation.

- The equation of state is the ideal gas law: $\overline{V}_g = RT/p$
- The change in molar volume is approximately the volume of just the gaseous phase: $\Delta\overline{V} = \overline{V}_g - \overline{V}_a \approx \overline{V}_g = RT/p$
- The molar enthalpy change is constant over temperature (second approximation)

$$\int_{p_a}^{p_g} \frac{dp}{p} = \frac{\Delta\overline{H}}{R} \int_{T_a}^{T_g} \frac{1}{T^2} dT \tag{A.15}$$

$$\ln\left(\frac{p_g}{p_a}\right) = \frac{-\Delta\overline{H}}{R}\left(\frac{1}{T_g} - \frac{1}{T_a}\right) \tag{A.16}$$

The above equation is something that we can use to find $-\Delta\overline{H}$ via experiments provided that the heat of adsorption doesn't depend on temperature which is fine to first order, not fine if we want to change the temperature a lot. What we can do is to introduce a gas of fixed pressure (or concentration) and find out how much is adsorbed at several temperatures to get the heat of adsorption. What about a temperature-dependent $\Delta\overline{H}$? If this is the case, then the molar heat capacity of the gaseous and adsorbed phases should be taken into account and put back into the Clapeyron equation.

A.4 Equilibrium Constant

So far we have looked at the heat of adsorption in terms of the potential energy associated with an adsorbent-adsorbate pair, and the temperature and pressure relationships that describe the equilibrium of the gaseous and adsorbed phases. Now we move onto a more difficult task—making a leap of abstraction to have a relationship linking the Gibbs free energy of a state or phase to something called an equilibrium constant, K which is unitless.

Why should we go through all this trouble to understand the equilibrium constant even though we are blessed with the case of working with pretty much an ideal gas (trace-level VOCs)? First of all, $RT \ln K$ is used all over in the literature even for non-ideal gases and liquids, and it may not be obvious why this is the case. Secondly, the language of chemical potential is invoked in several theories of adsorption which treat the adsorbed phase as a two-dimensional liquid. And finally, it is important to know why we can generalize the ratio of pressures into K because most of the literature on measuring heats of adsorption via gas-solid chromatography use K and not pressures (though some would say that we can just use the ideal gas equation and this is true). In chemistry, the power of the chemical potential and K is to be able to deal with the energies of n-component reactions and predict the likelihood that the reaction will happen.

We need two more tools to understand the equilibrium constant; The will now be introduced, both expressed for a single phase system. But in the end the whole idea behind the equilibrium constant is to enable chemists to deal with the energy differences of n-component systems. The first tool is the temperature dependence of the Gibbs free energy at constant pressure, called the Gibbs-Helmholtz relation, and it results from using the

chain rule:

$$\left.\frac{\partial(G/T)}{\partial T}\right|_p = -\frac{H}{T^2} \tag{A.17}$$

The second tool is the Gibbs free energy dependence on pressure with constant temperature for an ideal gas:

$$
\begin{aligned}
G(p_2, T) &= G(p_1, T) + \int_{p_1}^{p_2} V(p, T)dp \tag{A.18} \\
&= G(p_1, T) + \int_{p_1}^{p_2} \frac{nRT}{p}dp \tag{A.19} \\
&= G^0(T) + nRT\ln\left(\frac{p}{p^0}\right) \tag{A.20} \\
\mu &= \mu^0 + RT\ln\left(\frac{p}{p^0}\right) \tag{A.21}
\end{aligned}
$$

The last line is the molar Gibbs free energy and it is defined to be the chemical potential, μ. I am now going to explain in words how we make the leap of abstraction from a ratio of pressures, p/p_0 to an equilibrium constant, K which is a ratio of concentrations even if the reactants are not ideal gases.

Basically, what happens is that if we look at an n-component ideal gas mixture, Dalton's law of partial pressures says that one type of gas does not interact with the others. This means that the chemical potential of each gas is independent, and that the total chemical potential is the sum of all the chemical potentials. The total Gibbs free energy of the n-component system depends on the number of moles of each type of gas and its chemical potential so that stoichiometrically the reactant and product energies add up. The resulting function of pressures precisely has the form of a chemical equilibrium constant. The final step of magic is that when we impose the equilibrium condition, the pressure function *is* the equilibrium constant. So that is how we get the relationship between Gibbs free energy and the equilibrium constant. We began with the assumption of ideal gas equation of state and found that it gave us the form and value of the equilibrium constant at equilibrium so that in general we define the chemical potential of any gas in terms of $RT\ln K$ plus some reference state. Since adsorption is concerned with gases, I won't go into the argument for generalising this result to non-gases.

To summarise in mathematical symbols, suppose we have a chemical reaction:

$$aA + bB = cC + dD \tag{A.22}$$

where the upper-case letters are the reactants and products, and lower-case letters are the number of moles of each. Then the Gibbs free energy change is:

$$\Delta_r G = a\mu_A + b\mu_B - c\mu_C - d\mu_D \tag{A.23}$$

$$= a\mu_A^0 + b\mu_B^0 - c\mu_C^0 - d\mu_D^0 + RT(a \ln p_A + b \ln p_B - c \ln p_c - d \ln p_d) \quad (A.24)$$

$$\Delta_r G = \Delta_r \mu^0 - RT \ln \left(\frac{p_A^a \, p_B^b}{p_C^c \, p_D^d} \right) \quad (A.25)$$

where μ are the chemical potentials. At equilibrium $\Delta_r G = 0$ and we now have a chemical equilibrium constant, K:

$$\Delta_r \mu^0 = -RT \ln K \quad (A.26)$$

How do we use K practically? The Gibbs-Helmholtz relation again, now with notation indicating n-components:

$$\frac{\partial (\Delta_r G / T)}{\partial T} = -\frac{\Delta_r H}{T^2} \quad (A.27)$$

Combining these two at equilibrium, the temperature dependence of the equilibrium constant K at constant pressure is the van't Hoff equation:

$$\frac{\partial \ln K}{\partial T} = \frac{\Delta_r H}{RT^2} \quad (A.28)$$

This equation is used extensively to extract heats of adsorption from measurements. The natural log of the equilibrium constant is plotted as a function of inverse temperature, and the slope gives the heat of adsorption.

A.5   Conclusion

Through this exercise, what I have done is to work through some oft used expressions relating temperatures and partial pressures to energies. Along the way we have seen three key assumptions that are warranted for the WIMS application, and essentially they are all equivalent to the first:

- Adsorbate-adsorbate interactions can be neglected
- The ideal gas equation of state applies
- Adsorption is described via partial pressures

The relationship between the heat of adsorption and the practical, measurable equilibrium constant has been elucidated, and we are poised to use it for describing our simple two-component system in the preconcentrator. In addition, I have also gone over how to do a first-order estimation of the heat of adsorption, should it be necessary to do a sanity check for measurements.

This article was written after digesting these references [11, 97, 98, 99], and cobbling together bits and pieces that are relevant to adsorption.

A.6 Notation

This section is a quick review of the notation used in this Appendix.

- Bars over things mean molar quantities; Translation: divide by the number of moles, Example: $\overline{H}_g$ is the molar enthalpy of the gaseous phase
- Capital deltas mean the difference of a state function (independent of path) or intensive variable (variable that doesn't depend on how much of something there is, say temperature, pressure, density, specific heat) from one equilibrium state to another ; Example: ΔG
- Differentials mean small changes in state functions or intensive variables
- Inexact differentials mean small changes in things that are not state functions such as heat and work; heat and work depend on the path, Example: $đq$
- Subscripts have a lot of meanings. Sometimes they mean the phase of interest, say the internal energy of the gaseous phase U_g, or a particular reference value such as μ_0 the chemical potential at saturated vapor pressure, or they can mean that the variables are kept constant. And hopefully I make this clear in the text, as in $dS_{U,V} \geq 0$ means the change in entropy with no change in internal energy or volume.
- For more complex expressions $|_p$ means that the variable is kept constant.
- What notation is used to distinguish between the energy changes of different numbers of phases in the system? say the energy of a single phase vs. two-component vs. n-component system? Here are some examples. For a single phase with no changes:

$$G = -ST + H \tag{A.29}$$

  For a single phase with an infinitesimal change:

$$dG \leq -SdT + Vdp + đw_e \tag{A.30}$$

  For the difference between two states:

$$\Delta G = -\Delta SdT + \Delta Vdp \tag{A.31}$$

  For n-components:

$$\Delta_r G = -\Delta_r SdT + \Delta_r Vdp \tag{A.32}$$

Appendix B

MICROFABRICATION

B.1 Microcavity wafer process flow

C1. Double side polished p-type $< 100 >$ Si, $\rho = 1 - 10\,\Omega-$cm, $t = 475\,\mu$m

C2. Thermal oxidation of $2\,\mu$m for boron doping mask (backside) and cavity etching mask (frontside)

- Pre-furnace clean
- Wet oxidation B2 furnace
  Recipe name: DWDA1, Parameter table: OXIDIZE

Table B.1. B2 Parameter Table: OXIDIZE

Parameter	Value	Parameter	Value
UPGAS/A	N2-3	DRY1	00:05:00
TEMP/A	$1100\,^{\circ}$C	WET	10:00:00
TEMPRMP	MAX	DRY2	00:05:00
SETTIME	00:15:00	N2ANNEAL	00:10:00
ANLTIME	00:00:00	DOWNGAS	N2-3
PUL-600	200	SETTLE	SPKSET
LOWSET	-3	HIGHSET	+3

C3. Oxide patterning (backside)

- Frontside oxide protection
  (a) MS 1827: spin at $1.5\,$krpm for $30\,$s on the manual spinner with the Teflon/o-ring chuck (to avoid scratching)
  (b) Hardbake the PR $110\,^{\circ}$C in an oven for $20\,$min
- Lithography
  (a) MS 1827: spin at $4\,$krpm for $30\,$s, softbake $90\,^{\circ}$C for $30\,$min
  (b) EV 620 mask aligner- Exposure: $30\,$s, Development: $1.1\,$min in MF319
- Oxide patterning (removal)
  (a) Hardbake the PR $130\,^{\circ}$C for 2 to $3\,$min (to hold up in BHF)
  (b) Etch oxide in BHF for $23\,$min to remove $2\,\mu$m thermal oxide, etch rate is $0.1\,\mu$m/min
  (c) Check with SP or Nanospec before removing PR

- PR removal
  Hot PRS 2000 for $30\,\mathrm{min}$

C4. Shallow boron diffusion for Ohmic contacts (backside)
- Pre-furnace clean (2 h)
- A2 furnace for boron diffusion (16 h, two time slots) Recipe name: BORON99, Parameter table: BDEP99

Table B.2. A2 Parameter Table: BDEP99

Parameter	Value	Parameter	Value
UPGAS/A	N2-3	DOWNGAS	N2-3
TEMP	$1175\,^\circ\mathrm{C}$	LOO2FLO	150
TMPRMP	MAX	SETTIME	00:10:00
SETTIME	00:15:00	DILU	00:10:00
DEPTIME	00:45:00	DOWNGAS	N2-3
PUL-600	200	SETTLE	SPKSET
LOWSET	-3	HIGHSET	+3

C5. BSG removal leaving thermal oxide for electrical isolation for Pt RTDs
- Frontside oxide protection
  (a) MS 1827: spin at $1.5\,\mathrm{krpm}$ for $30\,\mathrm{s}$ on the manual spinner with the Teflon/o-ring chuck (to avoid scratching)
  (b) Hardbake the PR $110\,^\circ\mathrm{C}$ in an oven for $20\,\mathrm{min}$.
- Lithography
  (a) MS 1827: spin at $4\,\mathrm{krpm}$ for $30\,\mathrm{s}$, softbake $90\,^\circ\mathrm{C}$ for $30\,\mathrm{min}$
  (b) EV 620 mask aligner- Exposure: $30\,\mathrm{s}$, Development: $1.1\,\mathrm{min}$ in MF319
- BSG Removal
  (a) Hardbake the PR $105\,^\circ\mathrm{C}$ for $1\,\mathrm{min}$ prior to dry etching
  (b) PlasmaTherm RIE, Recipe #9 for 52 min, rotate 180°, etch another 52 min; thermal oxide etch rate is $0.2\,\mu\mathrm{m/min}$
  (c) Check with Nanospec before removing PR
  (d) Wet etch to finish if necessary
     i. $4\,\mathrm{min}$ HF:DI, 1:1
        End the oxide etch with BHF
     ii. or $1\,\mathrm{min}$ HF:DI, 1:1 then 3 min BHF
- PR removal
  Hot PRS 2000 for $5\,\mathrm{min}$
- Four-point probe measurement or multimeter to check the doping concentration.

C6. Lift-off lithography for Ti/Pt $100/1000\text{\AA}$ RTDs and ohmic contacts (backside)
- Lithography
  (a) MS 1827: spin at $4\,\mathrm{krpm}$ for $30\,\mathrm{s}$, softbake $90\,^\circ\mathrm{C}$ for $30\,\mathrm{min}$
  (b) EV 620 mask aligner- Exposure: $30\,\mathrm{s}$, Development: $1.1\,\mathrm{min}$ in MF319

- Evaporation of Ti/Pt $100/1000$Å in the Enerjet
- Lift-off in acetone overnight
- Annealing at $400\,°C$ for 2 h (hotplate nitrogen glove box or high-temperature oven in SEM room)
- Four-point probe measurement of V/I, PROG 1000 for 4" wafer geometry correction factor

H1. Micro-cavity etching mask patterning (frontside)
- Lithography
  (a) MS 1827: spin at $2\,$krpm for $30\,$s, softbake $90\,°C$ for $30\,$min
  (b) EV 620 mask aligner- Exposure: $30\,$s, Development: $1.1\,$min in MF319
- Oxide mask patterning
  (a) Hardbake the PR $105\,°C$ for $1\,$min prior to dry etching
  (b) PlasmaTherm RIE, Recipe #9 left chamber for $52\,$min, rotate $180°$, etch another $52\,$min; thermal oxide etch rate is $0.2\,\mu$m/min
  (c) Check with Nanospec to ensure complete oxide removal

H2. Si dry etching with STS RIE to form cavities
- Carrier wafer mounting
  (a) MS 1827 spin $10\,$s at $2\,$krpm, mount the heater wafer
  (b) Hard bake hot plate $110\,°C$ for $4\,$min (PR reflow)
- STS-RIE platen power reduction recipe and straight-sidewall recipe, etch depth is $450\,\mu$m; approximate etch time: 4 h (with two etch recipes: HC6B 2 h and H7B 2 h)

Table B.3. STS Etch Parameters for HC6B

Gas	Flow Rate	Time	Overlap	Platen Power	Coil Power
SF_6	160 sccm	13 s	-	25 W	800 W
C_4F_8	85 sccm	7 s	-	-	600 W

Table B.4. STS Etch Parameters for HC7B

Gas	Flow Rate	Time	Overlap	Platen Power	Coil Power
SF_6	160 sccm	13 s	-	25 W -0.1W/min	800 W
C_4F_8	85 sccm	7 s	-	-	600 W

- Zygo to check etching depths
- Carrier wafer removal in hot PRS 2000 for 2 h

H3. Preparation for bonding
- Oxide removal
  (a) Mount the wafer onto a clean carrier with $10\,\mu$m of 9260 to protect the backside oxide
  (b) BHF etch for $23\,$min
  (c) Rinse in DI for $5\,$min followed by SRD

       (d) Nanospec oxide thickness check
- Carrier wafer removal in hot PRS 2000 for 2 h
- Etch depth metrology, Zygo

H4. Cr/Au $500/5000\text{Å}$ evaporation for Au-Au thermocompression bonding

- Evaporation of Cr/Au $500/5000\text{Å}$ in Enerjet evaporator

H5. Loading of carbon adsorbent granules into micro-cavities using organic solution-based method

B.2   Sealing Wafer Process Flow

Bottomside means the side being bonded to the silicon microheaters; Topside means the side with the fused silica tubings.

B1. Double side polished p-type $< 100 >$ Si, $\rho = 1 - 10\,\Omega-\text{cm}$, $t = 475\,\mu\text{m}$

B2. Thermal oxidation of $2\,\mu\text{m}$ for inlet/outlet adapter etching mask

- Pre-furnace clean
- B2 thermal oxide furnace parameters: same as in step C2.
- Nanospec for oxide thickness measurement

B3. Inlet/outlet hole etch mask patterning (bottomside)

- Lithography
  - (a) HMDS, 1827 $4\,\text{krpm}\ 30\,\text{s}$ or ACS 200 $3\,\mu\text{m}$
  - (b) softbake hotplate $90\,^{\circ}\text{C}$ 30 min
  - (c) EV 620 $28\,\text{s}$
  - (d) Dev. MF319 $1.1\,\text{min}$
- PTRIE Recipe # 9 left chamber for $52\,\text{min}$, rotate $180°$, etch another $52\,\text{min}$; thermal oxide etch rate is $0.2\,\mu\text{m}/\text{min}$
- Nanospec for oxide removal confirmation

B4. Inlet/outlet capillary adapter etch mask patterning (topside)

- Lithography
  - (a) HMDS, 1827 $4\,\text{krpm}\ 30\,\text{s}$ or ACS 200 $3\,\mu\text{m}$
  - (b) softbake hotplate $90\,^{\circ}\text{C}$ 30 min
  - (c) EV 620 $28\,\text{s}$
  - (d) Dev. MF319 $1.1\,\text{min}$
- PTRIE Recipe # 9 left chamber for $52\,\text{min}$, rotate $180°$, etch another $52\,\text{min}$; thermal oxide etch rate is $0.2\,\mu\text{m}/\text{min}$
- Nanospec for oxide removal confirmation

B5. Si dry etching with STS RIE to form inlet/outlet holes (bottomside)

- Recipe: H59B, Etch Time: 2 h
- Etch depth metrology, Zygo

B6. Si dry etching with STS RIE to form inlet/outlet capillary adapters (topside)

Table B.5. STS Etch Parameters for H59B

Gas	Flow Rate	Time	Overlap	Platen Power	Coil Power
SF_6	105 sccm	14 s	0.5 s	12 W	700 W
C_4F_8	40 sccm	11 s	-	6 W	600 W

- Carrier wafer mounting, 1827 2krpm $10\,s$, $105\,°C$ hardbake on hotplate for $8\,min$
- Recipe: HC6B, Etch Time: 3 h with a $15\,min$ break after the first 1.5 h
- Etch depth metrology, Zygo
- Removal of carrier wafer in hot PRS 2000, 3 h

B7. Oxide etch mask removal

- Oxide removal

   (a) BHF etch for $23\,min$

   (b) Rinse in DI for $5\,min$ followed by SRD

   (c) Nanospec oxide thickness check

B8. Evaporation of Cr/Au $500/15000\text{Å}$ for bonding

B9. Plasma cleaning of bonding surface
March Asher for $1\,min$

Table B.6. Oxygen Plasma Clean Conditions (O2CLEAN)

Gas	Flow Rate	Pressure	Power
O_2	20%	250 mTorr	200 W

H5/B10. Bonding alignment of channel/micro-cavity and sealing wafers

- Backside of micro-cavity wafer to the "hole" side of the sealing wafer, cross-hair alignment
- EV 620 → EV 501 bonder
- Stack height determination $3800\,\mu m$

E1. Si-Au eutectic bonding using EV 501 bonder

- Temperature $400\,°C$ (meaning $425\,°C$ in the EVG 501 program)
- Graphite chuck
- Bond chamber pressure $30\,mTorr$
- Bonding Force 1000 N
- Time $45\,min$

E3. Dicing of bonded devices

- Inlet/outlet side on film so that dicing saw cooling water does not enter device
- Removal from film and precise mapping/placement into trays (orientation and position)

E4. Fused silica capillary insertion and curing

- Polyimide cure schedule: $40\,°C$ to $200\,°C$ at $5\,°C/min$, followed by $200\,°C$ 10 min
Hot plate and TC (34970A)

- Gross leak testing and flow verification with KNF pump and $50\,\mathrm{mL}$ beaker filled with DI water

E5. 16-pin hybrid package customization
- Printed circuit board cutting for large area wirebonding pads (Auto lab)
- Drilling holes in the package for capillary pass-through (micro-drill press)
- Hysol Epoxi Patch 1C or similar for affixing the PCB pieces onto the hybrid
- 24 AWG copper wire soldering to the PCB pices

E6. Device capillaries epoxied to hybrid package
Elmer's glue, air dry.

E7. Aluminum wirebonding (wedge bonder) of Pt RTDs and heating contacts from the preconcentrator to the hybrid or LCC package.

Appendix C

LABORATORY TECHNIQUES

The following list is a run-down of selected specifications for various components in the preconcentrator measurement system that we have constructed.

- Leak detector (Model 21-070, Gow-Mac Instrument Co., Bethlehem, PA)
  Minimum detectable He leak rate: $1 \times 10^{-5}\,\mathrm{cm^3/s}$.
- Solid-state flow meter (Flow Tracker 1000, Agilent Technologies)
  $\pm 5\%$ of reading from 0 to 5 mL/min flow rates, $\pm 2\%$ for 5 to 500 mL/min.
- $30\,\mathrm{m}$ GC column (HP-5ms, J&W Scientific)
  Non-polar (5%-Phenyl)-methylpolysiloxane, temperature range of -60 to $350\,^{\circ}\mathrm{C}$
- He purifier (CE-35KF-I-4R, Aeronex, San Diego, CA)
  < 1 ppb output purity for non-methane hydrocarbons, oxygen, water, hydrogen, carbon monoxide, carbon dioxide. Maximum flow rate $1\,\mathrm{L/min}$, $0.003\,\mu\mathrm{m}$ particulate filtration. This purifier is the best one available and is usable for photolithography and compound semiconductor applications. So it definitely works for keeping our GC column alive and healthy.
- $10\,\mu\mathrm{L}$ gas-tight or liquid syringe (#1801, Hamilton Co., Reno, NV)
- $5\,\mathrm{mL}$ gas-tight syringe (SGE Analytical Science, Victoria, Australia)
- 3 and 5 L Tedlar bags (SKC Inc., Eighty Four, PA)
- Diaphragm pump 0.65 to $0.85\,\mathrm{L/min}$, maximum pressure $7.3\,\mathrm{psig}$ (NMP09, KNF Neuberger, Trenton, NJ)
- Metering valve (#1300, Hoke, Spartanburg, SC)
- Flow controller for 0 to $110\,\mathrm{mL/min}$ (VCD 1000, Porter Instrument Company, Hatfield, PA)
- Pressure regulator for 0 - $60\,\mathrm{psig}$ (#4000, Porter Instrument Company, Hatfield, PA)

C.1   Specific Heat: Differential Scanning Calorimetry

Differential scanning calorimetry (DSC) is one method to determine the specific heat C_p of a material. The DSC used for the C_p of Carbopack X is a heat flux DSC (Perkin Elmer DSC-6) in the teaching laboratory of the Materials Science and Engineering Department. In heat flux DSC, the sample and a reference (in this case an empty sample pan and lid) are contained in a single furnace. A low thermal resistance plate with two islands holds the

sample and reference respectively, and a thermocouple is embedded inside each of these two islands. The furnace is programmed to ramp at a given heating rate and a temperature difference between the sample and the reference arises because of differences in their mass and specific heat. The actual measured quantity is this temperature difference, so that a prior calorimetric calibration of the instrument is necessary for the software to convert this to a heat flow [100].

C.1.1 Experiment

The determination of specific heat using DSC consists of the following:

- Verification of the existing calorimetric and temperature calibrations using a sample with known properties such as enthalpy and melting point
- A baseline scan to subtract the effect of the Al sample pans
- A reference scan to record the instrument response to a reference material with known specific heat
- The actual sample scan to compare with the reference scan for extraction of the specific heat

In this experiment, a calibration standard of In with mass of $6.312\,\mathrm{mg}$ encapsulated in an Al pan (Perkin Elmer P/N N519-0762) is placed on the sample side, while an empty Al pan is placed on the reference side. The indium verification method is used (0 mg weight, and no baseline). The expected transition temperature and energy are $156.60\,°\mathrm{C}$ and 28.45 J/g, with the verification run giving a transition temperature of $157.31\,°\mathrm{C}$ and 30.66 J/g.

To ensure best results and avoid errors due to mass difference, the same Al sample pan was used for baseline, reference, and sample measurements. (i.e., each sample can only be measured once-through with the whole procedure since the specific heat reference material must be removed before permanently encasulating the granular sample into the pan by crimping it with a lid) A microbalance is used to measure the reference and sample material masses. Care is taken not to touch any of the materials or surfaces with bare hands because contamination can result in significant desorption which would confound the measurements.

The same temperature program was used for the three scans with a nitrogen flow rate of 20 mL/min:

1. Isothermal $50\,°\mathrm{C}$ for 3 min
2. Heating from 50 to $150\,°\mathrm{C}$ at a rate of $20\,°\mathrm{C/min}$
3. Isothermal $150\,°\mathrm{C}$ for 5 min
4. Cooling from 150 to $50\,°\mathrm{C}$ at a rate of $10\,°\mathrm{C/min}$
5. Isothermal $50\,°\mathrm{C}$ for 3 min

The reference material for this particular experiment is a $17.81\,\text{mg}$ piece of Ag. The Ag is placed into the sample pan and lid without crimping and put onto the sample side, while the empty sample pan and lid remain on the reference side for the reference scan. Finally, for the sample scan, the sample (carbon) is placed into the sample pan and lid, crimped, and put onto the sample side, while the empty sample pan and lid remain on the reference side.

C.1.2 Results

The following is the relation for the extraction of the specific heat of the carbons with Ag as the reference:

$$C_{px} = \left(\frac{\ell_x}{\ell_r}\right)\left(\frac{M_r}{M_x}\right) C_{pr} \tag{C.1}$$

where the subscripts x and r denote the sample and reference respectively, C_p is the specific heat, ℓ is the height of the curve from the baseline, and M is the mass. Figure C.1 shows the graph used to extract C_{px}. At $400\,\text{K}$, or $127\,^\circ\text{C}$ the specific heat of Ag is $25.7\,\text{J/mol}\cdot\text{K}$ (atomic weight is $107.86\,\text{g/mol}$ to get $232\,\text{J/kg}\cdot\text{K}$). The average result for the 40 to $60\,\mu\text{m}$-diameter Carbopack X from the heating and cooling ramps is a specific heat of $577 \pm 65\,\text{J/kg}\cdot\text{K}$ at $400\,\text{K}$. For comparison, the specific heat of pure graphite at $400\,\text{K}$ is $267\,\text{J/kg}\cdot\text{K}$ (or $3.211\,\text{J/molK}$) so that Carbopack X is slightly more than twice the specific heat of graphite [101].

C.2 FID Calibration

Figure C.2 shows the results of a solvent-based FID mass calibration for octane, decane, and dodecane. These mass calibrations are necessary in order to complete the physiochemical property calculations (adsorption isotherm) from our breakthrough data.

C.3 Cleanroom Methodological Advice

For those who are new to cleanroom work, here are a few tips:

- Prepare before you enter the cleanroom so that you can be focused and finish your task on time. The goal of planning is to spend as little time in the cleanroom as possible.
- Write down all the conditions when you process so that you can go back to what you have done to see what has worked and what hasn't.
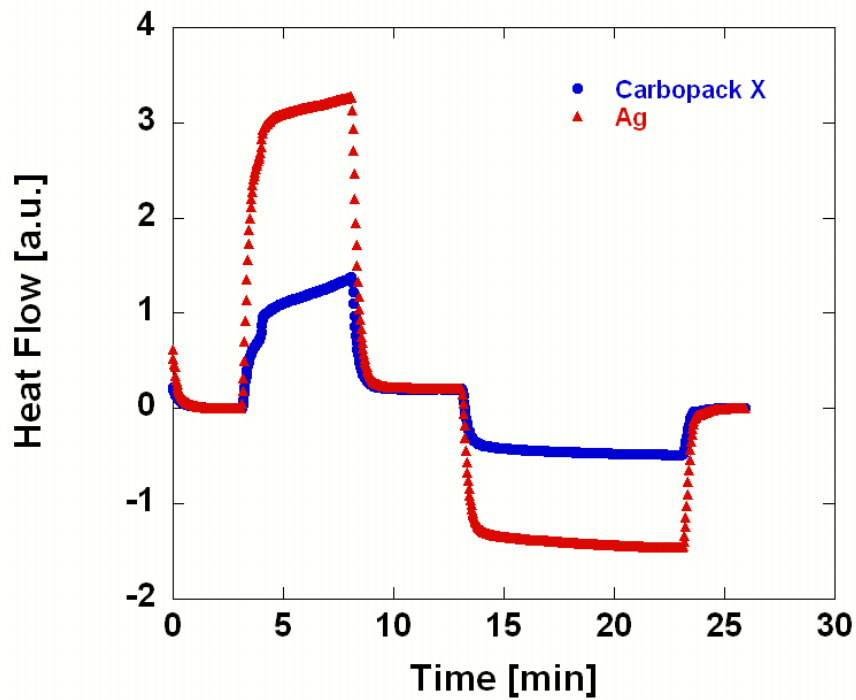
Figure C.1. Heat flow vs. time for the isothermal-ramp-isothermal-cool-isothermal DSC scans to determine the specific heat of Carbopack X at 400 K using Ag as the reference material.
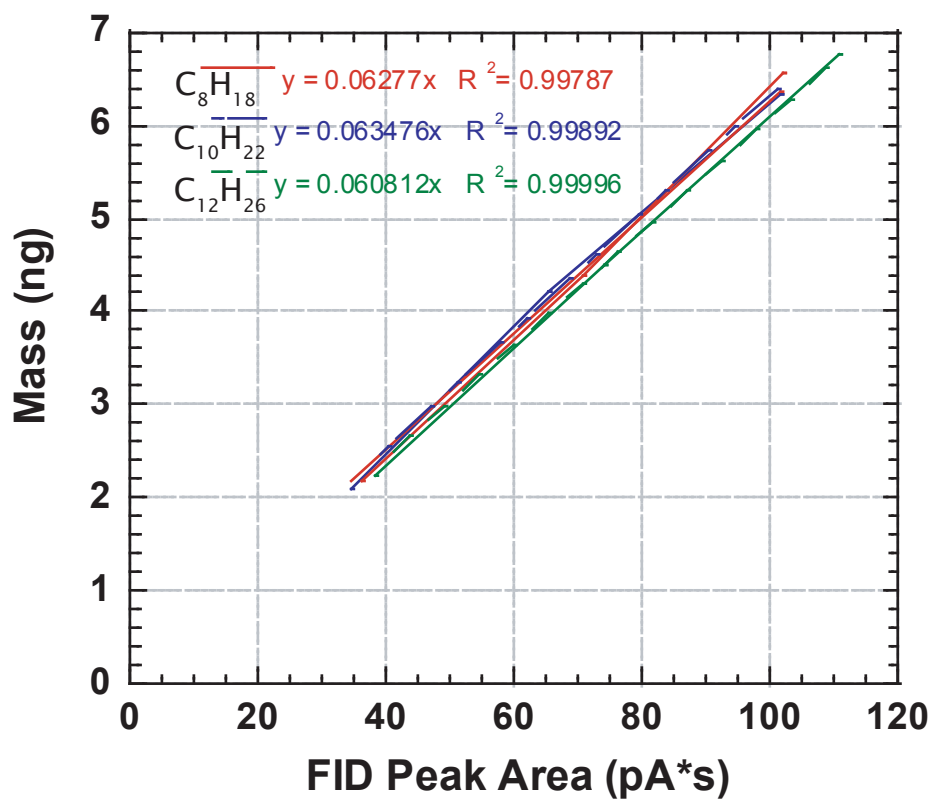
Figure C.2. FID peak area-mass calibration curves for octane, decane, and dodecane.

- Keep good track of your wafers (label them) and where they are in terms of processing.
- Examine each process step by itself and test it to get the optimal conditions necessary for your device to work.
- Make more than one wafer of the same process step so that one of them can be a calibration run. Sometimes you need many runs to perform a process step calibration.
- Perform process parameter calibrations on every process step that is new (e.g., different mask, tool, chemical, hot plate, etc.).
- Check under the microscope, Zygo, and Dektak often. Think about why the thing looks the way it does. How should it look like and why?
- Be aware of what the processing tools are doing and know the basic principles of their operation so that you can debug and discuss problems with staff knowledgeably.
- Talk to other people to find out their processing problems and solutions.
- Be patient, and pay attention to detail. If the lithography isn't perfect, the PR has particles, the temperature or humidity are non-optimal, these will screw up your later processing steps. **Do it again if it's not right.**

Appendix D

MASS TRANSFER MODEL

This appendix reviews the code and parameters for the mass transfer model in Chapter 9. The approach that we use to solve the coupled partial differential equations is to use the method of finite differences [102], [103], [104]. Solving the equation means computing the value of concentration at a given spatial location z and time t that satisfies the initial and boundary conditions given with the PDE. Many physical problems share the same forms of partial differential equations. So when we recast our equations into dimensionless form, we can use extant numerical methods and codes to solve our problem.

The finite difference method involves making two major choices: how finely we discretize the spatial and temporal variables and how to numerically compute the finite differences. Once these choices are made, we can use standard numerical solution algorithms by specifying the inputs to these functions. In mathematics, these are the independent variables (length and time) and the dependent variable (concentration). The FORTRAN code for the model using these standard methods is given below.

The dispersion and forced convection terms use centered differencing (how to compute the finite difference). The computed length z is divided into 100 equal parts (how finely to discretize in space) while 0.01 is the the time step. For time stepping, the dispersion term (second order term) is treated implicitly using the Crank-Nicholson method. The other terms, including the differential equation for Y, are treated explicitly using the second-order predictor-corrector scheme.

D.1   FORTRAN for Numerical Solution

```
c
c
      parameter (ix=101+1,iv=2,ixm2=ix-2)
      dimension y(ix,iv,2),dy(ixm2,iv,2)
c
      common /input/ope,stobe,alpha,beta,tswitch
      common /grids/odz,odz2,dt,aa,bb
c
```

```fortran
      read(5,*)ns,nmax,nprint,nsave
      read(5,*)dt
c
c y(*,1,*) is X; y(*,2,*) is Y
c ix is the number of spatial grids for the device.
c i=1 and i=ix-1 (i.e. 1 and 101) are at the boundaries.
c
      call init(y(1,1,1),y(1,2,1))
      n1=1
      n2=2
c
c
 1000 continue
      call expls(y(1,1,n1),y(1,2,n1),dy(1,1,n1),dy(1,2,n1),t)
c
      do 100 j=1,iv
        do 100 i=2,ix-1
          y(i,j,n2)=y(i,j,n1)+dy(i-1,j,n1)
 100  continue
c
      call expls(y(1,1,n2),y(1,2,n2),dy(1,1,n2),dy(1,2,n2),t)
c
      do 200 j=1,iv
        do 200 i=1,ixm2
          dy(i,j,n2)=0.5*(dy(i,j,n1)+dy(i,j,n2))
 200  continue
c
      call imp(y(1,1,n1),dy(1,1,n2))
c
      do 300 j=1,iv
        do 300 i=2,ix-1
            y(i,j,n2)=y(i,j,n1)+dy(i-1,j,n2)
 300  continue
c
      ns=ns+1
      t=dt*float(ns)
c
c perform output
      if(mod(ns,nprint).eq.0)then
        write(6,201)t,y(101,2,n2),y(21,1,n2),y(41,1,n2),
     &  y(61,1,n2),y(81,1,n2),y(101,1,n2)
c
        write(61,201)t,y(101,2,n2),y(21,1,n2),y(41,1,n2),
     &  y(61,1,n2),y(81,1,n2),y(101,1,n2)
      endif
```

```fortran
        if(t.ge.tswitch)then
          write(63,202)(y(i,1,n2),i=1,ix)
          write(63,202)(y(i,2,n2),i=1,ix)
          stop
 202      format(6e13.6)
        endif
 201    format(f8.0,6e11.4)
c
        n3=n2
        n2=n1
        n1=n3
c
        if(ns.lt.nmax)goto1000
c
      end
c
        subroutine expls(xx,yy,dxx,dyy,t)
        parameter (ix=101+1,ixm2=ix-2)
        dimension xx(ix),yy(ix),dxx(ixm2),dyy(ixm2)
c
        common /input/ope,stobe,alpha,beta,tswitch
        common /grids/odz,odz2,dt,aa,bb
c
        call bdys(xx,t)
c
        do 100 i=2,ix-1
          dxxdz=(aa*(xx(i)-xx(i-1))
     &    +0.5*(1.-aa)*(xx(i+1)-xx(i-1)))*odz
c
          dyy(i-1)=dt*stobe*(xx(i)-yy(i)/(1.+alpha*(1.-yy(i))))
          dxx(i-1)=-dt*dxxdz-beta*dyy(i-1)
 100    continue
c
        return
        end
c
        subroutine bdys(xx,t)
        parameter (ix=101+1)
        dimension xx(ix)
c
        common /input/ope,stobe,alpha,beta,tswitch
        common /grids/odz,odz2,dt,aa,bb
c
        xx(1)=1.
c       if (t.ge.tswitch) xx(1)=0.
```

```fortran
      xx(ix)=xx(ix-1)
c
      return
      end
c
      subroutine init(xx,yy)
      parameter (ix=101+1)
      dimension xx(ix),yy(ix)
c
      common /input/ope,stobe,alpha,beta,tswitch
      common /grids/odz,odz2,dt,aa,bb
c
c first, provide values for the parameters
c
c input numbers
c
c
      pe=52.37 *1.    !Peclet number
      st=38.32 /4.    !Stanton number
      alpha=0.8
      beta=9.8e5
      tswitch=1.3336e6  !time (dimensionless) to switch from case 1 to case
c
      ope=1./pe
      stobe=st/beta
c
c numerical paramters
      aa=0.
      length=1.
      dz=length/float(ix-2)
      odz=1./dz
      odz2=odz**2
c      bb=0.51  needs same dt as 0.501
      bb=0.50001 !works for dt=0.005
c
      do 100 i=1,ix
        xx(i)=0.
        yy(i)=0.
 100  continue
c
      return
      end
c
      subroutine imp(xx,dxx)
      parameter (ix=101+1,ixm2=ix-2)
```

```
      dimension xx(ix),dxx(ixm2),d(ixm2),u(ixm2),a(1)
c
      common /input/ope,stobe,alpha,beta,tswitch
      common /grids/odz,odz2,dt,aa,bb
c
      bdt=bb*dt
        do 110 i=1,ixm2
          u(i)=-(bdt*ope*odz2)
          d(i)=1.+2.*(bdt*ope*odz2)
 110    continue
        u(ixm2)=0.
        d(ixm2)=1.+(bdt*ope*odz2)
c
      do 200 i=2,ix-1
        dxx(i-1)=dxx(i-1)+dt*ope*(xx(i-1)+xx(i+1)-2.*xx(i))*odz2
 200  continue
c
      call tridm(1,ixm2,d,u,dxx, a)
c
      return
      end
c
      subroutine tridm(lv,n,d,u,x, a)
c
c
      implicit real (a-h,o-z)
c
c
      dimension d(lv,n),u(lv,n),x(lv,n), a(lv)
c
c i general
      do 10 i=2,n
        do 10 l=1,lv
          a(l)=u(l,i-1)/d(l,i-1)
          d(l,i)=d(l,i)-a(l)*u(l,i-1)
          x(l,i)=x(l,i)-a(l)*x(l,i-1)
 10     continue
c
c i=n
      do 20 l=1,lv
        x(l,n)=x(l,n)/d(l,n)
 20     continue
c i general
      do 30 i=n-1,1,-1
        do 30 l=1,lv
```

```
        x(l,i)=(x(l,i)-u(l,i)*x(l,i+1))/d(l,i)
  30    continue
        return
        end
c
```

D.2   Kinetic Parameters

This section goes over the correlations for estimating the mass and heat transfer coefficients for the adsorbent particles. The first parameter is the combined internal and external mass transfer coefficient k_f. If we treat k_f as a film mass transfer coefficient, then we can use the heat-mass transfer analogy (i.e., recycle the heat transfer coefficient correlations into mass transfer coefficients simply by using the analogous dimensionless groups).

The Sherwood number is analogous to the Nusselt number in heat transfer and gives the film mass transfer coefficient:

$$\mathrm{Sh} \equiv \frac{2R_p k_f}{D_m} \tag{D.1}$$

where R_p is the particle radius [cm], k_f is the film mass transfer coefficient [cm/s], and D_m is the molecular diffusivity of the gas [m^2/s]. The Sherwood number correlation for the case of finite longitudinal dispersion (D_z) and $3 < \mathrm{Re} < 10^4$ is as follows [105]:

$$\mathrm{Sh} = 2.0 + 1.1\mathrm{Sc}^{1/3}\mathrm{Re}^{0.6} \tag{D.2}$$

where $\mathrm{Sc} \equiv \frac{\mu}{\rho_f D_m}$ is the Schmidt number (analogous to the Prantdl number), and $\mathrm{Re} \equiv \frac{2R_p v \rho_f}{\mu} \frac{\epsilon}{1-\epsilon}$ is the packed bed Reynolds number. In their correlation D_z [cm^2/s] is given by:

$$\frac{\epsilon D_z}{D_m} = 20 + 0.5\mathrm{ScRe} \tag{D.3}$$

Looking at the previous equations, we need the molecular diffusivity of the adsorbate in the inert carrier gas D_m [cm^2/s]. Table D.1 from [106] shows values of diffusion coefficients for hydrocarbons in air at $25\,^\circ$C and 1 atm pressure.

Table D.1. Diffusion Coefficients for Hydrocarbons and Water Vapor in Air at $25\,^\circ\mathrm{C}$ and $1\,\mathrm{atm}$ Pressure

Compound	$D_{AB}[\times 10^{-6}\,\mathrm{m^2/s}]$
Methane	23.3
Octane	6.32
Nonane	6.25
Decane	5.89
Undecane	5.53
Dodecane	5.24
Water Vapor	27.1

Appendix E

HEAT TRANSFER COMPUTATIONS

This appendix goes into detail on the heat transfer computation strategies for the in-line preconcentrator. The correlations are from [83], [85], [107]. We will review the heat transfer coefficients from correlations in the literature. These heat transfer coefficients provide an estimation of steady-state power consumption and the boundary conditions necessary for transient thermal analysis. The following is an outline of the computational strategy for steady-state:

- Find the appropriate correlation for the geometry in question, usually expressed in terms of the Nusselt number, Nu.
- Check to make sure that the dimensionless parameters for the problem fall into the range of applicability for the correlation.
- Use Nu and the characteristic length of the problem to obtain the heat transfer coefficient, h.
- Use h, the area, length, and temperature difference across the boundary to compute the steady-state heat flux.

For transient thermal analyses:

- Calculate the steady-state heat flux for each boundary as a function of temperature difference.
- Use the heat transfer coefficients as boundary conditions for the finite element model.
- Take advantage of axial symmetry in the in-line preconcentrator to allow the computation of a 3D solution while only specifying the geometry and b.c.'s in the axisymmetric view.
- Heat generation is in the heater element.
- T = 300 K initial condition.
- Check temporal and spatial convergence by halving the time steps.

E.1   Natural Convection

Natural convection occurs on all of the preconcentrator surfaces and the heat transfer coefficient associated with natural convection increases with temperature difference between the

device and the ambient. To calculate the total amount of natural convection, each surface is considered in turn.

E.1.1   Outer Wall of Vertical Cylinder

The following correlation is in reference [85].

$$
\begin{aligned}
\mathrm{Nu} &= a(\mathrm{Gr}\,\mathrm{Pr})^m & \text{(E.1)} \\
&= a\left(\frac{L^3\rho^2 g\beta\Delta T}{\mu^2}\frac{c_p\mu}{k}\right)^m & \text{(E.2)}
\end{aligned}
$$

For $\Delta T = 300\mathrm{K}$, $\mathrm{Gr}\cdot\mathrm{Pr} = 4.41$ and for $\mathrm{Gr}\cdot\mathrm{Pr} < 10^4$, $a = 1.36$ and $m = 0.2$.

Table E.1. Parameters For Natural Convection on a Cylinder (Vertical Orientation)

Parameter	Symbol	Units	Evaluation Temperature	Source
Characteristic Length	L	m	-	By design
Correlation Factor	a	-	-	Tables
Correlation Factor	m	-	-	Tables
Bulk Fluid to Cylinder Temp. Differ.	ΔT	K	-	By design
Gravitational Constant	g	$\mathrm{m^2/s}$	-	-
Density of Air	ρ	$\mathrm{kg/m^3}$	Film	Geankoplis
	β	$\mathrm{K^{-1}}$	-	-
Viscosity of Air	μ	$\mathrm{kg/m\cdot s}$	Film	Geankoplis
Specific Heat of Air	c_p	$\mathrm{J/kg\cdot K}$	Film	Geankoplis
Thermal Conductivity of Air	k	$\mathrm{W/m\cdot K}$	Film	Geankoplis

E.1.2   Circular Plate

This correlation is from reference [83].

$$
\mathrm{Nu} = 0.82\,\mathrm{Ra}^{1/5}\,\mathrm{Pr}^{0.034} \tag{E.3}
$$

Ra = Gr Pr Figure E.2 shows the heat transfer coefficient for the top of the in-line design, modelled as a convection from the annulus outside the fused silica capillary.
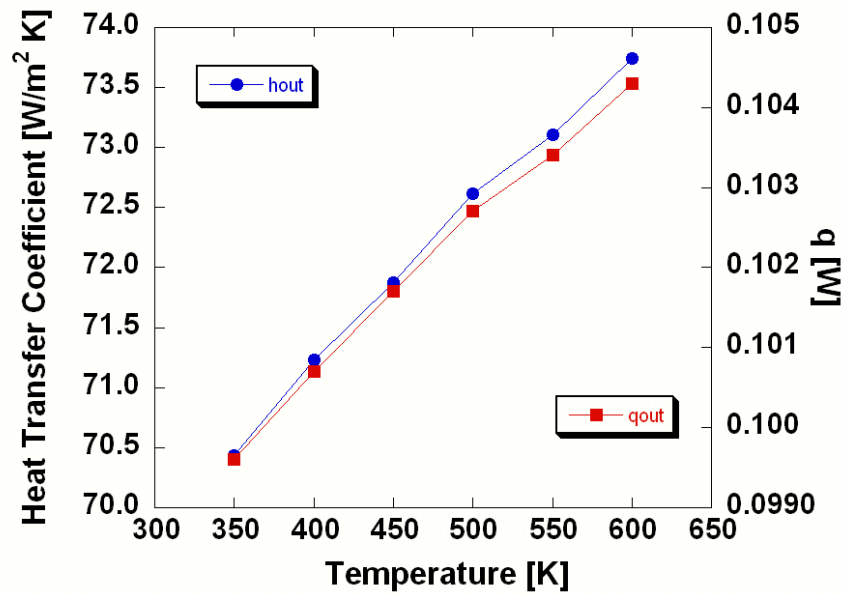
Figure E.1. Natural convective heat transfer coefficient and heat loss as a function of temperature for the vertical outer wall for the in-line design.
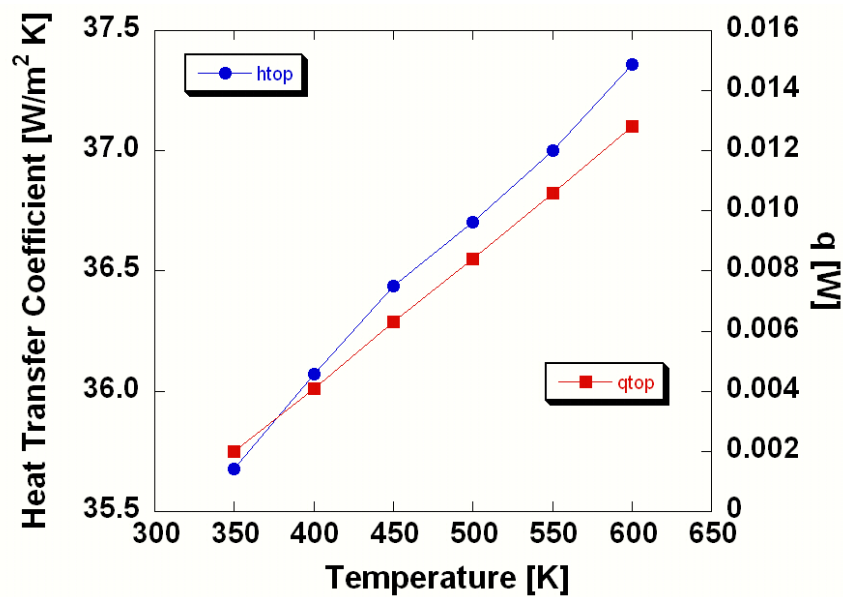
Figure E.2. Heat transfer coefficient due to convection and heat loss as a function of temperature from a circular plate as applied to the top outer annulus of the in-line design.

Parameter	Symbol	Units	Evaluation Temperature	Reference
Characteristic Length	D	m	-	By design
Prandtl Number	Pr	-	Film Temperature	Geankoplis

E.1.3   Enclosed Space (small gap) of a Horizontal Annulus

This correlation is for $0.55 < \delta/D_1 < 2.65$ where δ is the gap width $(1\,\text{mm})$, and D_1 is the core diameter $(890\,\mu\text{m})$ so that $\text{Nu} = h\delta/k$ [107].

$$\text{Nu} = \left(0.2 + 0.145\frac{\delta}{D_1}\text{Gr}\right)^{1/4} \exp\left(-0.02\frac{\delta}{D_1}\right) \tag{E.4}$$

Grashof number is:

$$\text{Gr} = \delta^3 \left(\frac{\rho^2 g\beta}{\mu^2}\right)\Delta T \tag{E.5}$$

Table E.3. Parameters For Natural Convection in an Enclosed
Annular Space

Parameter	Symbol	Units	Evaluation Temperature	Source
Characteristic Length	δ	m	-	By design
Core Diameter	D_1	m	-	By design
Density of Air	ρ	kg/m^3	Film	Geankoplis
Gravitational Constant	g	m^2/s	-	-
	β	K^{-1}	-	-
Viscosity of Air	μ	$\text{kg/m}\cdot\text{s}$	Film	Geankoplis
Bulk Fluid to Cylinder Temp. Differ.	ΔT	K	-	By design

E.2   Conduction

For conduction, we consider the pessimistic case of a heat sink 1 mm away from the pre-concentrator with the conduction path provided by a fused silica capillary. In this case the
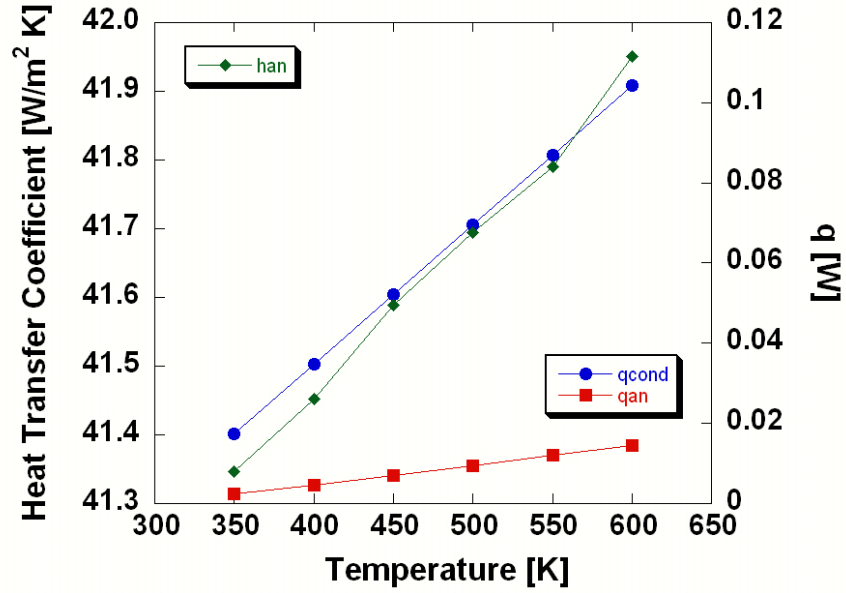
Figure E.3. Heat transfer coefficients at the bottom of the in-line design due to conduction from the fused silica capillary to a substrate 1 mm away, and natural convection in a 1 mm gap through the outer annulus.

heat transfer coefficient is straightforward:

$$h_{cond} = k/L \tag{E.6}$$

where k is the thermal conductivity of fused silica, and L is the characteristic length.

E.3 Forced Convection

Forced convection through a packed bed, Chilton-Colburn analogy between heat and mass transfer problems [107].

$$j_H = \left(\frac{h}{c_p G}\right) \mathrm{Pr}^{2/3} = j_M = \left(\frac{k_G}{G_M}\right) \mathrm{Sc}^{2/3} \tag{E.7}$$

$$j_H = \left(\frac{h}{c_p G'}\right) \mathrm{Pr}^{2/3} = 0.91\psi \mathrm{Re}^{-0.51} \tag{E.8}$$

for $0.01 < \mathrm{Re} < 50$ where the shape factor $\psi = 1$ for particles.
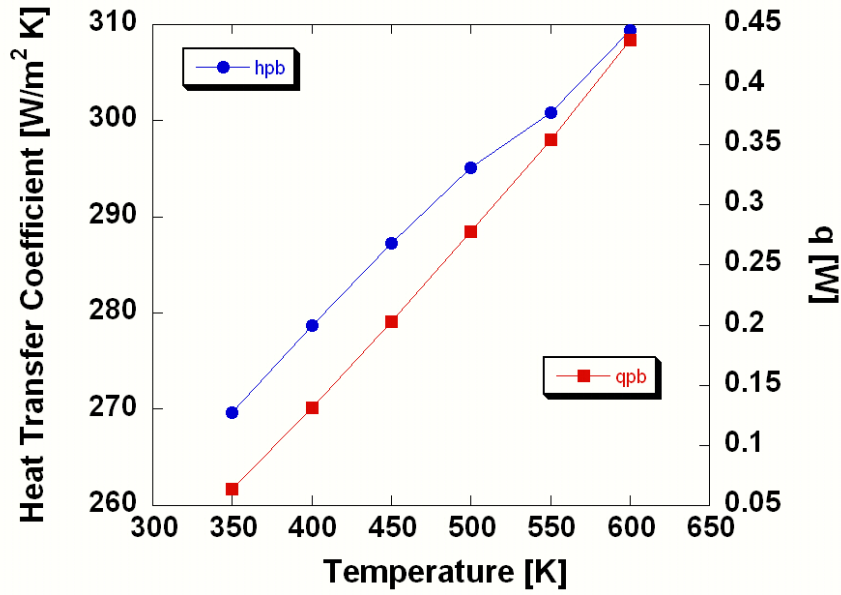
Figure E.4. Heat transfer coefficient of the packed bed and heat loss as a function of temperature from a circular plate as applied to the top outer annulus of the in-line design.

E.4 Radiation

For steady-state, the entire body is considered to be at the given temeprature so that we consider radiation from the entire cylinder. Worst-case black body radiation is calculated to provide an upper bound for radiative loss since emissivity is non-trival for silicon (temperature and doping dependent).

$$h_r = \epsilon(5.676) \left(\frac{(T_1/100)^4 - (T_2/100)^4}{T_1 - T_2} \right) \tag{E.9}$$

Table E.4. Parameters for Forced Convection in a Packed Bed

Parameter	Symbol	Units	Evaluation Temperature	Reference
Specific Heat	c_p	$J/kg \cdot K$	Film Temperature	Geankoplis
Superficial Mass Velocity	G'	$kg/m^2 \cdot s$	Bulk Temperature	Calculated
Prandtl Number	Pr	-	Film Temperature	Geankoplis
Shape Factor	ψ	-	-	Geankoplis
Reynolds Number	Re	-	-	Calculated

Table E.5. Calculation Parameters

Parameter	Symbol	Units	Reference
Emissivity	ϵ	-	-
Surface Temperature	T_1	K	By design
Ambient Temperature	T_2	K	By design
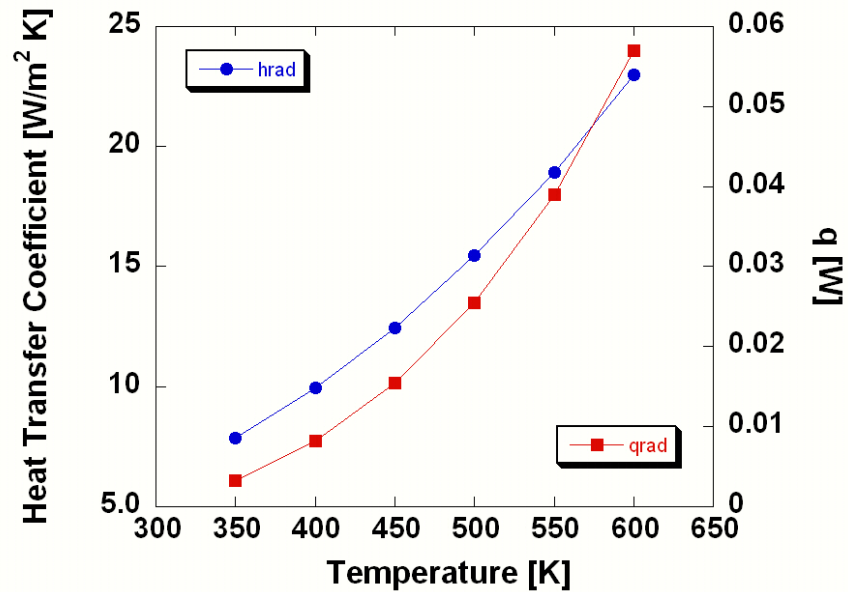
Figure E.5. Radiative heat transfer coefficient and heat loss as a function of temperature accounting the the total surface area of the in-line design.

Table E.6. Geometrical Parameters for Heat Transfer Calculations

Parameter	Symbol	Value
Outer radius	r_{out}	$750\,\mu$m
Tube length	L	$1\,$mm
Inner cavity radius	r_{in}	$215\,\mu$m
Volumetric flow rate	Q	$1\,$mL/min
Superficial linear velocity	v'	$0.1148\,$m/s
Particle diameter	D_p	$50\,\mu$m
Fused silica outer radius	$r_{fs,o}$	$445\,\mu$m
Fused silica inner radius	$r_{fs,i}$	$345\,\mu$m

References

[1] K. D. Wise, K. Najafi, R. D. Sacks, and E. T. Zellers, "A wireless integrated microsystem for environmental monitoring," in *IEEE International Solid-State Circuits Conf. Dig. of Tech. Papers,*, San Francisco, CA, 2004.

[2] G. Guiochon, "Basic principles of chromatography," in *Ullmann's Encyclopedia of Industrial Chemistry*. Weinheim: Wiley-VCH, 2005.

[3] J. Cazes and R. P. W. Scott, *Chromatography Theory*. New York: Marcel Dekker, 2002.

[4] W. K. Lewis, "The efficiency and design of rectifying columns for binary mixtures," *J. Ind. Eng. Chem.*, vol. 14, pp. 492–497, 1922.

[5] W. A. Peters, "The efficiency and capacity of fractionating columns," *J. Ind. Eng. Chem.*, vol. 14, pp. 476–479, 1922.

[6] A. J. P. Martin and R. L. M. Synge, "A new form of chromatogram employing two liquid phases," *Biochem. J.*, pp. 1358–1368, 1941.

[7] P. C. Wankat, *Large-Scale Adsorption and Chromatography, Vol. 1*. Boca Raton: CRC Press, 1986.

[8] A. T. James and A. J. P. Martin, "Gas-liquid partition chromatography: the separation and micro-estimation of volatile fatty acids from formic acid to dodecanoic acid," *Biochem. J.*, vol. 50, pp. 679–690, 1952.

[9] L. Lapidus and N. R. Amundson, "Effect of longitudinal diffusion in ion exchange and chromatographic columns," *J. Phys. Chem.*, vol. 56, pp. 984–988, 1954.

[10] J. J. van Deemter, F. J. Zuiderweg, and A. Klinkenberg, "Longitudinal diffusion and resistance to mass transfer as causes of nonideality in chromatography," *Chem. Eng. Sci.*, vol. 5, pp. 271–289, 1956.

[11] D. M. Ruthven, *Principles of Adsorption and Adsorption Processes*. New York: John Wiley, 1984.

[12] R. T. Yang, *Gas Separation by Adsorption Processes*. Boston: Butterworth, 1987.

[13] M. Suzuki, *Adsorption Engineering*. New York: Elsevier, 1990.

[14] B. Crittenden and W. J. Thomas, *Adsorption Technology and Design*. Boston: Butterworth-Heinemann, 1998.

[15] G. Gaspar, R. Annino, C. Vidal-Madjar, and G. Guiochon, "Influence of instrumental contributions on the apparent column efficiency in high speed gas chromatography," *Anal. Chem.*, vol. 50, no. 11, pp. 1512–1518, 1978.

[16] U. EPA, *TO-17 Compendium of Methods for the Determination of Toxic Organic Compounds in Ambient Air*. Washington, DC: US Environmental Protection Agency, 1997.

[17] (2004) Varian CP-4900. [Online]. Available: http://www.varian.com

[18] (2004) Agilent 3000. [Online]. Available: http://www.chem.agilent.com

[19] (2006) Short path thermal desorption system. [Online]. Available: http://www.sisweb.com/sptd/tdn.htm

[20] J. Zheng, M. Christophersen, and P. Bergstrom, "Thick macroporous membranes made of p-type silicon," *Phys. Stat. Sol.*, vol. 202, no. 8, p. 1402, 2005.

[21] ——, "Formation technique for macroporous morphology superlattice," *Phys. Stat. Sol.*, vol. 202, no. 8, p. 1662, 2005.

[22] M. Oborny, J. Zheng, J. Nichols, C. Lu, P. Bergstrom, R. Manginell, G. Frye-Mason, and E. Zellers, "Passive calibration-vapor source for a micro gas chromatograph," in *Proc. of 7th Int. Conf. on Miniaturized Chem. and Biochem. Anal. Sys. - microTAS*, Squaw Valley, CA, 2003, pp. 1243–1246.

[23] H. Kim and K. Najafi, "Characterization of low-temperature wafer bonding using thin-film parylene," *J. Microelectromech. Syst.*, vol. 14, no. 6, pp. 1347–1355, 2005.

[24] H. Kim, A. Astle, K. Najafi, L. Bernal, and P. Washabaugh, "Integrated peristaltic 18-stage electrostatic gas micro pump with active microvalves," in *Solid State Sensor and Actuator Workshop*, Hilton Head, SC, 2006.

[25] J. A. Potkay and K. D. Wise, "An electrostatically latching thermopneumatic microvalve with closed-loop position sensing," in *Proc. 18th IEEE Conf. on Microelectromechanical Systems (MEMS)*, Miami, FL, 2005, pp. 415–418.

[26] J. A. Potkay, G. Lambertus, R. Sacks, and K. D. Wise, "A low-power temperature- and pressure-programmable μGC column," in *Solid State Sensor and Actuator Workshop*, Hilton Head, SC, 2006, pp. 144–147.

[27] W. H. Steinecker, M. P. Rowe, H. Xu, Q. Zhong, C. Jin, L. Farina, Ç. Kurdak, and E. T. Zellers, "Au-thiolate nanoparticles as interfacial layers on microsensor arrays for micro gas chromatography," in *Proceedings of Eurosensors XIX, Barcelona, Spain*, 2005.

[28] Q.-Y. Cai and E. T. Zellers, "Dual-Chemiresistor GC detector employing monolayer-protected metal nanocluster interfaces," *Anal. Chem.*, vol. 74, pp. 3533–3539, 2002.

[29] S. C. Terry, J. H. Jerman, and J. B. Angell, "A gas chromatograph air analyzer fabricated on a silicon wafer," *IEEE Trans. Electron Devices*, vol. 26, no. 12, pp. 1880–1886, Dec. 1979.

[30] J. B. Pawliszyn, *Solid Phase Microextraction: Theory and Practice*. New York: Wiley-VCH, 1997.

[31] ——, "Method and device for solid phase microextraction and desorption," U.S. Patent 5 691 206, Nov. 25, 1997.

[32] J. Koziel, M. Jia, and J. Pawliszyn, "Air sampling with porous solid-phase microextraction fibers," *Anal. Chem.*, vol. 72, no. 21, pp. 5178–5186, 2000.

[33] S. A. S. Wercinski, *Solid Phase Microextraction: A Practical Guide*. New York: Marcel Dekker, 1999.

[34] Z. Zhang, M. J. Yang, and J. Pawliszyn, "Solid-phase microextraction," *Anal. Chem.*, vol. 66, no. 17, pp. 844–853, 1994.

[35] L. A. Colón and L. J. Baird, "Basic principles of chromatography," in *Ullmann's Encyclopedia of Industrial Chemistry*. Weinheim: Wiley-VCH, 2005.

[36] G. Smedje and D. Norback, "Irritants and allergens at school in relation to furnishings and cleaning," *Indoor Air*, vol. 11, pp. 127–133, 2001.

[37] G. Guiochon, "Influence of injection time on the efficiency of gas chromatography columns," *Anal. Chem.*, vol. 35, no. 3, pp. 399–400, 1963.

[38] W.-C. Tian, S. W. Pang, C.-J. Lu, and E. T. Zellers, "Microfabricated preconcentrator/focuser for a micro-scale gas chromatograph," *J. Microelectromech. Syst.*, vol. 12, no. 3, pp. 264–272, June 2003.

[39] G. Lambertus, A. Elstro, K. Sensenig, J. Potkay, M. Agah, S. Scheuering, K. Wise, F. Dorman, and R. Sacks, "Design, fabrication, and evaluation of microfabricated columns for gas chromatography," *Anal. Chem.*, vol. 76, pp. 2629–2637, 2004.

[40] E. F. Barry, "Columns: Packed and capillary; column selection in gas chromatography," in *Modern Practice of Gas Chromatography*, R. L. Grob and E. F. Barry, Eds. Hoboken, NJ: John Wiley, 2004.

[41] R. T. Yang, "Nanostructured adsorbents," *Adv. Chem. Eng.*, vol. 27, pp. 79–121, 2001.

[42] J. F. Byrne and H. Marsh, "Introductory overview," in *Porosity in Carbons: Characterization and Applications*, J. W. Patrick, Ed. London: Edward Arnold, 1995.

[43] A. Lueking and R. T. Yang, "Hydrogen storage in carbon nanotubes: residual metal content and pretreatment temperature," *AIChE Journal*, vol. 49, pp. 1556–1568, June 2003.

[44] E. W. Bittner, M. R. Smith, and B. C. Bockrath, "Characterization of the surfaces of single-walled carbon nanotubes using alcohols and hydrocarbons: a pulse adsorption technique," *Carbon*, vol. 41, pp. 1231–1239, 2003.

[45] M. Kruk, Z. Li, M. Jaroniec, and W. R. Betz, "Nitrogen adsorption study on surface properties of graphitized carbon blacks," *Langmuir*, vol. 15, pp. 1435–1441, 1999.

[46] R. R. Reston and E. S. Kolesar, "Silicon-micromachined gas chromatography system used to separate and detect ammonia and nitrogen dioxide—part I: Design, fabrication, and integration of the gas chromatography system," *J. Microelectromech. Syst.*, vol. 3, pp. 134–146, Dec. 1994.

[47] E. S. Kolesar and R. R. Reston, "Silicon-micromachined gas chromatography system used to separate and detect ammonia and nitrogen dioxide—part II: Evaluation, analysis, and theoretical modeling of the gas chromatography system," *J. Microelectromech. Syst.*, vol. 3, pp. 147–154, Dec. 1994.

[48] M. Kim and S. Mitra, "A microfabricated microconcentrator for sensors and gas chromatography," *J. Chrom. A*, vol. 996, pp. 1–11, May 2003.

[49] R. P. Manginell, G. C. Frye-Mason, R. J. Kottenstette, P. R. Lewis, and C. C. Wong, "Microfabricated planar preconcentrator," in *Solid State Sensor and Actuator Workshop*, Hilton Head, SC, June 2000, pp. 179–182.

[50] C. E. Davis, C. K. Ho, R. C. Hughes, and M. L. Thomas, "Enhanced detection of m-xylene using a preconcentrator with a chemiresistor sensor," *Sens. and Actuators B*, vol. 104, pp. 207–216, 2005.

[51] M. P. Siegal, D. L. Overmyer, R. J. Kottenstette, and W. G. Yelton, "Nanoporous-carbon films for microsensor preconcentrators," *Appl. Phys. Let.*, vol. 80, no. 21, pp. 3940–3942, 2002.

[52] R. P. Manginell and G. C. Frye-Mason, "Chemical preconcentrator with integral thermal flow sensor," U.S. Patent 6 527 835, Mar. 4, 2003.

[53] J. M. Sanchez and R. D. Sacks, "GC analysis of human breath with a series-coupled column ensembles and a multi-bed sorption trap," *Anal. Chem.*, vol. 75, pp. 2231–2236, 2003.

[54] C.-J. Lu and E. T. Zellers, "A dual-adsorbent preconcentrator for a portable indoor-VOC microsensor system," *Anal. Chem.*, vol. 73, pp. 3449–3457, 2001.

[55] ——, "Multi-adsorbent preconcentrator/focusing module for portable-GC/microsensor-array analysis of complex vapor mixtures," *Analyst*, vol. 127, pp. 1061–1068, 2002.

[56] G. A. Eiceman, *Instrumentation of Gas Chromatography*, ser. Encyclopedia of Analytical Chemistry, R. A. Meyers, Ed. Chichester, UK: John Wiley, 2000, vol. 999.

[57] J. M. Sanchez and R. D. Sacks, "On-line multibed sorption trap and injector for GC analysis of organic vapors in large-volume air samples," *Anal. Chem.*, vol. 75, pp. 978–985, 2003.

[58] J. J. Whiting, Private communication, 2005.

[59] L. A. Jonas and J. A. Rehrmann, "Predictive equations in gas adsorption kinetics," *Carbon*, vol. 11, pp. 59–64, 1973.

[60] ——, "The rate of gas adsorption by activated carbon," *Carbon*, vol. 12, pp. 95–101, 1974.

[61] W. C. Tian, H. K. L. Chan, C.-J. Lu, S. W. Pang, and E. T. Zellers, "Multiple-stage microfabricated preconcentrator-focuser for micro gas chromatography system," *J. Microelectromech. Syst.*, accepted for publication.

[62] R. E. Clement and P. W. Yang, "Environmental analysis," *Anal. Chem.*, vol. 73, no. 12, pp. 2761–2790, June 2001.

[63] J. F. Pankow, W. Luo, L. M. Isabelle, D. A. Bender, and R. J. Baker, "Determination of a wide range of volatile organic compounds in ambient air using multisorbent adsorption/thermal desorption and gas chromatography/mass spectrometry," *Anal. Chem.*, vol. 70, no. 24, pp. 5213–5221, Dec. 1998.

[64] E. Matisová and S. Škrabáková, "Carbon sorbents and their utilization for the preconcentration of organic pollutants in environmental samples," *J. Chrom. A*, vol. 707, pp. 145–179, 1995.

[65] X. Wu, K. J. Maloy, A. Hansen, M. Ammi, and D. Bideau, "Why hour glasses tick," *Phys. Rev. Lett.*, vol. 71, no. 9, pp. 1363–1366, Aug. 1993.

[66] T. Le Pennec, K. J. Maloy, A. Hansen, M. Ammi, D. Bideau, and X. lun Wu, "Ticking hour glasses: Experimental analysis of intermittent flow," *Phys. Rev. E*, vol. 53, no. 3, pp. 2257–2264, Mar. 1996.

[67] T. Le Pennec, K. J. Maloy, E. G. Flekkoy, J. C. Messager, and M. Ammi, "Silo hiccups: Dynamic effects of dilatancy in granular flow," *Phys. Fluids*, vol. 10, no. 12, pp. 3072–3079, Dec. 1998.

[68] W.-C. Tian, H. K. L. Chan, S. W. Pang, C. J. Lu, and E. T. Zellers, "High sensitivity three-stage microfabricated preconcentrator-focuser for micro gas chromatography," in *Proc. 12th International Conf. on Solid-State Sensors, Actuators, and Microsystems, Transducers '03*, vol. 1, Boston, MA, June 2003, pp. 131–134.

[69] H. K. L. Chan, M. Takei, S. W. Pang, R. A. Veeneman, and E. T. Zellers, "Microfabricated preconcentrator for quantitative analysis of low concentration organic compounds," in *Proc. 14th International Conf. on Solid-State Sensors, Actuators, and Microsystems, Transducers '05*, Seoul, Korea, June 2005, pp. 2091–2094.

[70] R. J. Furbank and J. F. Morris, "An experimental study of particle effects on drop formation," *Phys. Fluids*, vol. 16, no. 5, pp. 1777–1790, May 2004.

[71] J. Eggers, "Nonlinear dynamics and breakup of free-surface flows," *Rev. Mod. Phys.*, vol. 69, no. 3, pp. 865–929, July 1997.

[72] A. Hiraki, E. Lugujjo, and J. W. Mayer, "Formation of silicon oxide over gold layers on silicon substrates," *J. App. Phys.*, vol. 43, no. 9, pp. 3643–3649, 1972.

[73] Y. T. Cheng, L. Lin, and K. Najafi, "Localized silicon fusion and eutectic bonding for MEMS fabrication and packaging," *J. Microelectromech. Syst.*, vol. 9, pp. 3–8, 2000.

[74] R. F. Wolffenbuttel, "Low-temperature intermediate Au-Si wafer bonding; eutectic or silicide bond," *Sens. and Actuators A*, vol. 62, pp. 680–686, 1997.

[75] R. F. Wolffenbuttel and K. D. Wise, "Low-temperature silicon wafer-to-wafer bonding using gold at eutectic temperature," *Sens. and Actuators A*, vol. 43, pp. 223–229, 1994.

[76] J. S. Mitchell, G. R. Lahiji, and K. Najafi, "Encapsulation of vacuum sensors on a wafer level package using a gold-silicon eutectic," in *Proc. 14th International Conf. on Solid-State Sensors, Actuators, and Microsystems, Transducers '05*, Seoul, Korea, 2005.

[77] R. K. Shukla and N. P. Mencinger, "A critical review of VLSI die-attachment in high reliability applications," *Solid State Technol.*, pp. 67–74, July 1985.

[78] J. Kim, K. Kim, and K. Yong, "Thermal-decomposition pathway and desorption study of isopropanol and tert-butanol on Si(100)," *J. Vac. Sci. Technol. A*, vol. 20, no. 5, pp. 1582–1586, Sept. 2002.

[79] C. H. Tsau, S. M. Spearing, and M. A. Schmidt, "Fabrication of wafer-level thermocompression bonds," *J. Microelectromech. Syst.*, vol. 11, no. 6, pp. 641–647, Dec. 2002.

[80] ——, "Characterization of wafer-level thermocompression bonds," *J. Microelectromech. Syst.*, vol. 13, no. 6, pp. 963–971, Dec. 2004.

[81] M. A. Blauw, T. Zijlstra, and E. van der Drift, "Balancing the etching and passivation in time-multiplexed deep dry etching of silicon," *J. Vac. Sci. Technol. B*, vol. 19, pp. 2930–2934, 2001.

[82] B. L. Gray, D. Jaeggi, N. J. Mourlas, B. P. van Drieehuizen, K. R. Williams, M. I. Maluf, and G. T. A. Kovacs, "Novel interconnection technologies for integrated microfluidic systems," *Sens. and Actuators A*, vol. 77, pp. 57–65, 1999.

[83] J. H. Lienhard, *A Heat Transfer Textbook*. Englewood Cliffs: Prentice-Hall, 1981.

[84] A. F. Mills, *Basic Heat and Mass Transfer*. Chicago: Irwin, 1995.

[85] C. J. Geankoplis, *Transport Process and Unit Operations*. Englewood Cliffs: Prentice Hall, 1993.

[86] D. A. Weitz, "Packing in the spheres," *Science*, vol. 303, pp. 968–969, 2004.

[87] M. M. Dubinin, "The potential theory of adsorption of gases and vapors for adsorbents with energetically nonuniform surfaces," *Chem. Rev.*, vol. 60, pp. 235–241, 1960.

[88] M. Polanyi, "Section III.-Theories of the adsorption of gases. A general survey and some additional remarks," *Trans. Faraday Soc.*, vol. 28, pp. 316–333, 1932.

[89] A. Kapoor, J. A. Ritter, and R. T. Yang, "On the Dubinin-Radushkevich equation for adsorption in microporous solids in the henry's law region," *Langmuir*, vol. 5, p. 1118, 1989.

[90] A. L. Hines and R. N. Maddox, *Mass Transfer: Fundamentals and Applications*. Englewood Cliffs, NJ: Prentice-Hall, 1985.

[91] S. M. Montgomery, J. J. Linderman, D. J. Mooney, M. A. Burns, H. Y. Wang, and H. S. Fogler, "Chemical engineering fundamentals in biological systems," CD-ROM, 1997.

[92] M. A. Burns, Private communication, 2006.

[93] S. D. Faust and O. M. Aly, *Adsorption Processes for Water Treatment*. Boston: Butterworths, 1987.

[94] R. J. Jonker, H. Poppe, and J. F. K. Huber, "Improvement of speed of separation in packed column gas chromatography," *Anal. Chem.*, vol. 54, pp. 2447–2456, 1982.

[95] A. van Es, J. Janssen, C. Cramers, and J. Rijks, "Sample enrichment in high speed narrow bore capillary gas chromatography," *J. High Res. Chrom. and Chrom. Comm.*, vol. 11, pp. 852–857, Dec. 1988.

[96] M. van Lieshout, M. van Deursen, R. Derks, H.-G. Janssen, and C. Cramers, "A practical comparison of two recent strategies for fast chromatography: Packed capillary columns and multicapillary columns," *J. Microcol. Sep.*, vol. 11, pp. 155–162, 1999.

[97] D. Manolopoulos. (2005) Introduction to chemical thermodynamics. Oxford University. UK. [Online]. Available: http://physchem.ox.ac.uk/˜mano/downloads/thermo2.pdf

[98] L. K. Nash, *Elements of Chemical Thermodynamics*. Reading: Addison-Wesley, 1962.

[99] W. R. Salzman. (2001) Chemical thermodynamics: Exact and inexact differentials. University of Arizona, Tucson. USA. [Online]. Available: http://www.chem.arizona.edu/~salzmanr/480a/480ants/chemther.html

[100] E. Gmelin and S. M. Sarge, "Calibration of differential scanning calorimeters," *Pure Appl. Chem.*, vol. 67, pp. 1789–1800, 1995.

[101] H. O. Pierson, *Handbook of Carbon, Graphite, Diamond, and Fullerenes: Properties, processing and applications*. Park Ridge: Noyes Publications, 1993.

[102] H. J. Lee and W. E. Schiesser, *Ordinary and Partial Differential Equation Routines in C, C++, Fortran, Java, Maple, and MATLAB*. Boca Raton: Chapman and Hall/CRC, 2004.

[103] G. D. Smith, *Numerical Solution of Partial Differential Equations*. New York: Oxford University Press, 1965.

[104] W. F. Ames, *Numerical Methods for Partial Differential Equations*. New York: Academic Press, 1977.

[105] N. Wakao and T. Funazkri, "Effect of fluid dispersion coefficients on particle-to-fluid mass transfer coefficients in packed beds," *Chem. Eng. Sci.*, vol. 33, pp. 1375–1384, 1978.

[106] F. Haghighat, D.-S. Lee, and W. S. Ghaly, "Measurement of diffusion coefficients of vocs for building materials: review and development of a calculation procedure," *Indoor Air*, vol. 12, pp. 81–91, 2002.

[107] J. G. Knudsen, H. C. Hottel, A. F. Sarofim, P. C. Wankat, and K. S. Knaebel, "Heat and mass transfer," in *Perry's Chemical Engineers' Handbook*, R. H. Perry, D. W. Green, and J. O. Maloney, Eds. New York: McGraw-Hill, 1999.

Distribution:

1	MS 0892	Richard W. Cernosek, 1744
1	MS 0980	Jerome F. Jakubczak, 5710
2	MS 1425	Alex L. Robinson, 1744
1	MS 1425	Joshua W. Whiting, 1716
2	MS 9018	Central Technical Files, 8944
2	MS 0899	Technical Library, 4536
1	MS 0123	D. Chavez, LDRD Office, 1011

Sandia National Laboratories